THERMO-MECHANICAL FATIGUE OF POLYCRYSTALLINE, DIRECTIONALLY SOLIDIFIED AND SINGLE CRYSTAL NICKEL BASE SUPERALLOYS REPAIRED BY LASER BEAM WELDING

BY

JONATHAN DUROCHER

A Thesis submitted to the Faculty of Graduate Studies of
The University of Manitoba
in partial fulfilment of the requirements of the degree of

DOCTOR OF PHILOSOPHY

Department of Mechanical and Manufacturing Engineering
University of Manitoba
Winnipeg, Manitoba

ACKNOWLEDGEMENTS

I wish to take the opportunity to thank Dr. Norman Richards for his valuable advice and guidance over the course of this project. I would also like to thank Dr. Jack Cahoon and Dr. Lanre Ojo for the expert advice on solidification, diffusion and phase transformation theory to support this research project.

Additional thanks are due to Mr. Mike Boskwick in the Department of Mechanical and Manufacturing Engineering at the University of Manitoba for his continued assistance in the materials characterization laboratory.

I extend great gratitude to my family and friends for their support and encouragement.

ABSTRACT

The low cycle thermo-mechanical fatigue of laser beam welded conventionally cast Inconel 738, directionally solidified René 80 and single crystal René N5 has been evaluated. Results have been compared to gas tungsten arc and baseline alloy conditions. Metallographic examination of laser beam welds and the associated heat affected zone were conducted by scanning electron microscopy and energy dispersive spectroscopy. The impact of laser beam welding on thermo-mechanical fatigue properties of Inconel 738, René 80 and René N5 has been evaluated and recommendations for improvements and areas of further research have been presented.

TABLE OF CONTENTS

LIST OF FIGURES

LIST OF TABLES

1. INTRODUCTION

The repair of industrial gas turbine hot section components is of great commercial interest to operators. For a modern heavy industrial gas turbine, the replacement cost for a set of first stage turbine blades can be in the range of \$3M USD while a set of first stage nozzles can the in the order of \$2M USD. Consequently, these high cost components are at the focus of repair development initiatives in order to reduce the total operating cost of turbines in the power generation industry. The high cost of blades and nozzles is due to their complex geometry, alloy make-up, coatings and the casting processes employed to optimize the alloy microstructures.

Over the course of the evolution of gas turbine engines, improvements have been made to the alloys in use to improve high temperature mechanical properties, oxidation and corrosion resistance. In addition to thermal barrier coatings and internal part cooling, the alloy microstructure has been improved drastically. The casting process evolved from the conventional casting (CC) method where grains are equiaxed and random in orientation relative to each other and the primary loading axis. Grain boundaries in CC alloys are primarily strengthened by the $M_{23}C_6$ carbide phase to prevent grain boundary sliding but are susceptible to corrosion attack and are generally not considered resistant to creep deformation.

Second generation turbine blades featured directionally solidified (DS) cast structures where the grains are columnar. This structure offers superior mechanical properties over that of CC blades by aligning the grain boundaries parallel with the primary loading axis. Consequently, high temperature creep and transverse shear properties were improved by approximately

35ºC. The remaining grain boundaries require strengthening as in the case of CC structures and is accomplished by formation of carbides along the boundaries.

Finally, the latest generation of blades and vanes are cast as a single crystal (SX) with the [001] axis aligned with the primary loading axis. This cast structure has no grain boundaries and provides superior elevated mechanical properties over CC and DS structures. Additionally, grain boundary strengthening elements such as boron, carbon and zirconium do not need to be part of the alloy make up, further improving the performance of the alloy.

Turbine blades and nozzles are exposed to severe operating conditions such as high alternating stress, elevated temperature, thermal cycling, oxidation and sulfidation. As a result of operating conditions, critical hot section components are subject to replacement and offer limited repair opportunities. Nozzles are static components that provide high velocity gas path re-direction in order to improve power output of the turbine. They can generally be repaired by welding or furnace brazing methods followed by the re-application of oxidation resistant and thermal barrier coatings. Current repair practices are relatively economical and easy to perform allowing the components to undergo an additional service interval while significantly reducing the operating cost to the operator. However, the high strength of nickel base superalloys makes them difficult to repair by welding with matched filler alloys. Being internally cooled, these components have thick and thin sections which exacerbate the welding challenges. The majority of repairs to vanes do not restore the material's properties to 100% of original as a result of the methods employed to prevent cracking. Ultimately, all parts are retired once significant damage has occurred in a critical area or they have been deemed to be beyond economical repair condition. As a general rule, parts requiring a total repair cost of 50% of the new replacement parts are deemed non-economical to repair.

Welding of Nickel Based Superalloys

Static, non-load bearing parts such as nozzle guide vanes have tolerated GTAW and furnace brazing to repair damage such as cracks in airfoils and platforms using lower strength materials. In most cases, the vanes are manufactured from high strength conventionally cast nickel base superalloys that are susceptible to weld heat affected zone cracking. Current nickel base superalloys are strengthened by precipitation of the (Ni_3Al,Ti) coherent phase and typically contain between 6 and 8 wt. % total aluminum + titanium to precipitate the γ' strengthening $L1_2$ crystallographic structure phase. Inconel 738 and other similar alloys have been shown to be susceptible to heat affected zone cracking during gas tungsten arc welding.

Considerable research has been done to date to understand the behaviour of common gas turbine hot section nickel base superalloys. The typical pre-weld treatment for Inconel 738, a common turbine nozzle alloy, has been to solution heat treat at 1120ºC for 2 hours, followed by fan cooling to room temperature. Subsequent GTAW causes cracking in the heat affected zone as a result of strain age cracking and grain boundary liquation of precipitates present on grain boundaries. Strain age cracking is caused by the secondary precipitation of gamma prime (γ') in the heat affected during the welding process. The pre-weld heat treatment brings aluminum and titanium in solution and since gamma prime precipitation in Inconel 738 alloy occurs very rapidly, aging in the heat affected zone reduces the ductility. Strain on the heat affected zone is induced by the contracting fusion zone and ultimately leads to cracking.

Thakur et al. [1] devised a pre-weld heat treatment which over-aged Inconel 738 to significantly reduce the formation of secondary gamma prime precipitation during welding.

The pre-weld heat treatment, named UMT, is a solution cycle at 1120ºC for 2 hours followed by aging at 1025ºC for 16 hours. The UMT heat treatment over-aged the alloy to reduce strength, increase ductility, alter the morphology of $M_{23}C_6$ carbides along grain boundaries to be discrete particles and changed the character of grain boundaries from planar to serrated. The UMT developed for Inconel 738 was shown to greatly reduce heat affected zone micro-cracks during autogenous GTAW of Inconel 738. However, to date, heat affected zone cracking has not yet been completely eliminated since the GTAW process provides sufficient heat input to the base material to cause grain boundary liquation and cracking.

Another important factor at play is the liquation of low melting point phases on grain boundaries such as carbides, borides and gamma prime. During the welding process, these phases can undergo constitutional undercooling and as a result melt, which along with thermal induced strain cause grain boundary cracking in the weld heat affected zone. The heat affected zone remains fragile during the cooling phase after GTAW and is susceptible to some degree of cracking caused by the contracting fusion zone. A practical solution has been to use lower strength filler alloys such as Inconel 625 to increase the fusion zone ductility and reduce the strain on the heat affected zone. Banerjee et al. [2] studied the effect of various filler alloys on the susceptibility of HAZ cracking in Inconel 738 LC. Cracking was quantified in terms of total crack length (TCL) observed in a sample size of sufficient statistical significance. Filler alloys altered the fusion zone hardness and showed a linear relationship between the average TCL and weld hardness. Correspondingly, the weld hardness was related to the total concentration of aluminum and titanium and TCL showed good linear relationship with the Al + Ti composition of the filler alloys. Despite reducing the weld fusion zone hardness, heat affected zone cracking could not be completely eliminated. Sidhu et al. [3] evaluated the effect of aluminum concentration in filler alloys on the heat affected zone cracking of Inconel 738 alloy. The authors found that increasing the aluminum concentration in the weld filler, produced harder welds with greater heat affected zone cracking than softer alloys.

Turbine blades have not yet fully benefited from these aforementioned advancements. They are under relatively high cyclic loading and part failure can potentially involve unplanned engine shut-down and generally involves a costly subsequent maintenance event as a result of downstream damage to other components of the turbine and unplanned power outage monetary penalties. Since blade failure is a safety and reliability risk, the repairs are limited to non-critical areas of the parts. For example, minor dents, gouges and pits may be removed from industrial gas turbine blades in all areas except the fir tree where loading is at its highest. Some weld repairs are tolerated in non-critical areas such as platforms, shrouds, tips and knife-edge seals. A common practice involves GTAW or PTAW to weld low strength materials such as Inconel 625 in order to prevent microcracks but this also reduces the mechanical properties of the repaired blade due to its lower strength.

Laser beam welding (LBW) has gained popularity and widespread use and is now considered a superior alternative to GTAW and PTAW for repairing non-critical areas of turbine blades. The main advantage is that LBW significantly reduces the heat input to the part, reducing the susceptibility of HAZ cracking. Also, the LBW process offers near net build-ups, which require less post-weld processing to restore the original part profile. LBW is generally of lower heat input than GTAW and PTAW and provides highly localized heating of the filler metal and substrate.

The microstructural response of CC alloys to GTAW is well understood and despite pre-weld heat treatment (UMT for example), weld pre-heating and other techniques, heat affected zone cracking remains a concern. The low melting point phases along grain boundaries liquate as a result of the level of heat input involved with the GTAW process. Recent research has been conducted by Sidhu et al. [4, 5] using laser beam welding (LBW) in order to reduce the heat input to the base material but heat affected zone cracking was found to persist in Inconel 738 (polycrystalline) and René 80 (polycrystalline and directionally solidified).

Additional work has recently been carried out on laser beam welding of single crystal alloys. The laser beam offers a much lower heat input than GTAW and has been reported to be able to generate epitaxial growth welds by Vitek [6] and Mokadem et al. [7]. The researchers have independently shown that under the correct balance of laser beam power and welding traverse rate, the formation of stray grains can be avoided. The results were obtained under controlled laboratory test conditions and the practical implementation and commercialization of the findings have yet to be realized and reported in the literature.

Thermo-Mechanical Fatigue of Nickel Based Superalloys

To date, no research data is available on the strain controlled thermo-mechanical fatigue (TMF) life of LBW repairs using high Al + Ti (> 6%) filler material matched to a nickel base superalloy. Several papers have been published on the microstructural achievements using LBW but none provides a comparison to the baseline alloy properties and the commonly used GTAW process. Further, since turbine blades are found in conventionally cast, directionally solidified and single crystal forms, further advancements much consider the thermo-mechanical low cycle fatigue properties of each casting structure undergoing LBW repair with matched filler alloys. Thermo-mechanical fatigue has become increasingly relevant in the evaluation of nickel-based superalloys in order to evaluate their performance under representative engine operating conditions. Much of the testing reported in the literature is on the use of isothermal low cycle fatigue (LCF) tests to evaluate fatigue behaviour. However, TMF testing provides a closer simulation to the actual operating conditions of gas turbines by cycling test specimens over a temperature range rather than holding at isothermal temperatures. Components such as blades experience severe temperature gradients during engine start-up, shutdown cycles and also due to varying demands from the electrical grid. Therefore in addition to thermal fatigue, creep and oxidation factors must be considered for polycrystalline (CC), directionally solidified (DS) and single crystal (SX) alloy casting structures.

In independent studies, Coffin [8] and Manson [9] have shown that in LCF tests, cyclic plastic strain caused crack initiation, leading to the recognized Coffin-Manson law. Under the Coffin-Manson law, there exists a linear relationship between strain and fatigue life when plotted on log-log scales. Further work by Coffin [10] showed that at elevated temperatures, cracks initiate from oxide spikes occurring along the specimen surface.

Pahlavanyali et al. [11] evaluated the TMF behaviour of polycrystalline Nimonic 90 alloy over the temperature range of 400 to 850ºC. In-phase (IP) and out-of-phase (OP) tests were carried out with maximum mechanical strain ranges of 0.3% (IP) and 0.4% (OP). Under both test conditions, cracks were found to initiate from oxide spikes along grain boundaries exposed to the specimen surface. Under OP testing conditions, crack propagation was transgranular while in IP tests the cracks propagated along an intergranular path. A significant reduction in fatigue life was obtained in IP testing conditions and was approximately one third of the OP test fatigue life.

Kanesund et al. [12] evaluated polycrystalline Inconel 792 in TMF using mechanical strain control (fixed total strain range compensated for thermal expansion) in IP and OP conditions. Using maximum cycling temperatures of 750ºC (IP) and 950ºC (OP), the authors found that crack initiation in the material occurred near high plastic deformation structures such as bands and twins in IP and OP tests. The crack propagation mode for all temperature was in a transgranular mode. The initiation of cracks on specimen surfaces was not discussed in this paper.

Elevated temperature properties of nickel base superalloys such as creep and rupture strength have been significantly improved by the development of directionally solidified casting structures [13]. The improvement in mechanical properties allowed an increase in firing temperature of approximately 35ºC which increased powerplant output and efficiency. Elevated temperature tensile embrittlement of directionally solidified René 80 alloy was evaluated by Chang [14]. René 80 and other similar superalloys were found to undergo embrittlement in the temperature range of $M_{23}C_6$ stability. The $M_{23}C_6$ carbide particles have been shown to form over the range of 840-900ºC at the expense of MC along grain boundaries by the following reaction:

$$MC + \gamma \rightarrow M_{23}C_6 + \gamma'$$

This reaction has been found to cause an agglomeration of γ' along grain boundaries which, with potential interaction with oxygen and/or nitrogen leads to tensile embrittlement of the alloy in the transverse direction.

René 80 was tested under low cycle fatigue (LCF) at elevated temperature (871ºC) and high strain. Rahmani and Nategh [15] found that crack initiation and nucleation primarily occurred in the γ' denuded zone associated with oxidation near the specimen surface. Oxide spikes along grain boundaries near the specimen surface were also found to nucleate cracks in the specimens.

During high temperature LCF testing, Raguet et al. [16] found by fractographic evaluation, that crack initiation was associated with carbides and local fracture of carbide particles in DS René 80. Remy et al. [17] also found crack initiation to be associated with cracked carbide particles in the base alloy. Karamched and Wilkinson [18] used electron back-scatter diffraction analysis and measured significant thermal elastic strains around carbide particles in the order of 10^{-3} and sufficient to cause localized yielding of the MAR-M200 base material.

Much attention has been focused on the LCF and TMF properties of nickel-based superalloys in order to avoid failure during the service life of the part or component. For failure to occur, a micro-crack much grow and propagate through the part until the remaining cross-sectional area can no longer sustain the applied load. Herbig et al. [19] evaluated the three dimensional growth of fatigue cracks and found that a considerable fraction of the total fatigue life of parts is spent during the crack initiation phase. After nucleation and initiation, small cracks grew and were eventually stopped or had their growth rate significantly reduced as they interacted with microstructural defects such as grain boundaries in a polycrystalline version of CMSX-4 alloy [20]. As the crack path crossed neighbouring grains, they encountered resistance as they must propagate on different slip planes to pass the grain boundary.

Okazake et al. [21] tested DS René 80 in LCF mode to evaluate the stage I crack growth by metallurgical evaluations. The authors found that cracks initiated at micro-pores, carbide particles along grain boundaries and slip planes, although most cracks were observed from pores. In general, the growth rate of cracks (da/dN) increased proportionately with crack length but underwent periodic reductions when approaching a grain boundary due to slip deformation ahead of the advancing crack tip being blocked by the crack tip. Koss and Chan [22] have shown that failure by slip plane under cyclic loading typically appears as a brittle failure. The intersection of a surface with persistent slip bands have been studied by Feltner and Laird [23] and found to lead to crack initiation on the surfaces from extrusion points.

Chieragatti and Remy [24] conducted LCF tests on MAR-M-200 SX specimens at 650°C using a fully reversed triangular strain cycle along several crystallographic orientations. Using the total strain range, specimen orientation was found to influence the fatigue life due to variations in the Young's modulus. Using the stress range or plastic stain range, the fatigue life was insensitive to the crystallographic orientation. At higher plastic strains, cracks were found to initiate at MC carbide precipitates while at lower plastic strains, crack formed in sub-surface pores in the base alloy. The authors also evaluated the LCF of MAR-M-200 at 650°C under strain control along various crystallographic orientations.

Meyer-Olbersleben et al. [25] found that in LCF testing of CMSX-4 SX alloy, casting pores were responsible for crack initiation in tapered disc test coupons. The authors also conducted LCF testing of SX alloy SRR99 and found that oxidation and spalling occurred under low strain values. Xu et al. [26] conducted TMF tests on CMSX-4 alloy under various cycle conditions at 950°C, 1050 and 1150°C and found that crack initiation at the lower temperature occurred from casting pores with no evidence of oxidation, and from surface oxides at low strain levels. Oxidation attack was evident at 1050°C and at 1150°C surface oxidation was related to surface cracking.

SX AM1 Ni-based Superalloy was tested by Chataigner and Remy [27] over temperatures ranging from 600 to 1100°C using a diamond shape cycle. In LCF testing, major failures occurred at high strain ranges. In TMF tests under low strain values, crack initiation and failure occurred from sub-surface pores and at surface oxidation. Crack initiation was found to occur early in the tests, making up only a small fraction of the total LCF or TMF life of test specimens. Crack growth took place during the majority of the fatigue life for both test conditions.

Similarly for SX René N5, Reed and Miller [28] found fatigue cracks to initiate in casting pores while surface oxide cracks were not observed to initiate critical fatigue cracks. Hong et al. [29, 30] tested SX alloy CMSX-4 and found that at a temperature of 950°C, cracks initiated at surface scales and propagated into the base material by planar growth. The total number of surface cracks was higher in TMF specimens subjected to out of phase (OP) test conditions over those tested under isothermal fatigue testing conditions. During out of phase TMF testing, twin plates have been found to form on octahedral planes ahead of crack tip when the crack reached a certain size. This provided a preferential path for further crack propagation, particularly in the compression phase of the cyclic loading. Thus, differing modes of crack initiation tend to dominate depending on the range of temperature and cyclic conditions. Similarly, for OP TMF testing of SX alloy CMSX-4, Moverare et al. [31] found that surface crack initiation was dominant and crack propagation was found to take place by twinning plane across the entire specimen cross section. Extended ageing heat treatment of tests specimens produced fractures with extensive plastic deformation.

Fleury and Remy [32] evaluated the TMF behaviour of SX alloy AM1 and showed that two crack initiation mechanisms are possible depending on the mechanical strain range. At low strain ranges, crack initiation occurred at the specimen surface and in porosity sites, while at high strain ranges fatigue damage mechanisms dominated over crack initiation and propagation. SX alloy SR99 was evaluated under various TMF test conditions by Han et al. [33]. During IP TMF testing, the authors found that creep was the main failure damage mechanism. In contrast, under OP TMF testing, oxidation reduced the fatigue life of test specimens. Zhang et al. [34] tested several SX alloys developed in Japan, and found that under OP and triangular waveform TMF conditions, crack initiation occurred at the surface of specimens. Three stages of cracking were observed; (1) initiation assisted by oxidation, (2) growth/propagation by twinning mechanism and (3) final failure along crystallographic planes. Chen et al. [35] found that the LCF behaviour of an experimental Rolls-Royce SX superalloy varied with stress level. At low stress levels, crack initiation made up for a high fraction of the total test lives with initiation occurring at pores and surface oxidation of test specimens. At high stress levels, casting pores and their size were found to dominate crack initiation.

From this brief review of failure mechanisms in SX superalloys provides general conclusions can be drawn on the crack initiation under LCF and TMF testing conditions. At temperature less than approximately 800ºC, crack initiation will likely occur from casting pores present in the specimens as casting defects or interdendritic shrinkage porosity. This generalization holds true provided that the pores are not oxidized. At temperature above approximately

800ºC, oxidation effects take over and become the major source for crack initiation at the specimen surface.

This thesis evaluates the TMF behaviour of CC Inconel 738, DS René 80 and SX alloy René N5 via Gleeble thermo-mechanical testing and crack initiation and propagation via metallographic techniques. The research forms part of a much larger program comparing various repair techniques in Ni-based superalloys with the baseline solution treated and precipitation aged alloys.

There remains a tremendous economic opportunity with turbine blades where potential advancements could provide matched mechanical properties in a repaired component. The ability to repair blades in areas deemed critical and load bearing could bring significant cost savings potential to powerplant owners and operators.

2. SCOPE OF STUDY

The purpose of this research project is to simulate the repair to CC, DS and SX alloys by laser beam welding using a matched filler alloy. The specimen preparation is consistent with the typical preparation of a hot section component such as a turbine blade to remove relatively small cracks formed in service that render blades unserviceable.

For the present report, CC Inconel 738, DS René 80 and SX René N5 alloys were used to explain the following:

1. Metallography of the laser beam welded microstructure of a simulated crack repair

2. Explanation of the strain controlled thermo-mechanical fatigue cracking behaviour of laser beam welds

3. Evaluation of the thermo-mechanical fatigue life of laser beam weld repairs as a function of alloy structure (conventionally cast, directionally solidified and single crystal)

4. Comparison of the thermo-mechanical fatigue life of baseline, GTAW and LBW repairs on CC Inconel 738, DS René 80 and SX René N5

3. LITERATURE SURVEY

Gas Turbine Hot Section Components

Nickel based superalloys are used for nozzle guide vanes and turbine blades the hot section of aero and industrial gas turbines. Their unique properties have made them the primary choice in hot section applications of the several generations of gas turbine designs. Nickel based superalloys offer superior high temperature creep, tensile strength, ductility and oxidation resistance over other classes of material such as steels, cobalt alloys and ceramics.

Turbine blades and nozzle guide vanes are of generally complex geometry involving features such as fir trees, platforms, airfoils and shrouds. High pressure components exposed to the highest turbine outlet gas temperatures are internally cooled by delivering cool air through the hollow core of the part and discharging it over the airfoil surfaces via effusion holes and trailing edges slots. Refer to Figure 1 for a photograph of a General Electric Frame 7FA stage 1 turbine blade. These parts require a fair degree of control on dimensions and as such are investment cast to net or near-net shape. Depending on the temperature exposure of the part, the cast structure may vary based on the position of the part in the turbine from highest to lowest local exhaust gas temperature exposure; single crystal, directionally solidified or polycrystalline/equiaxed.

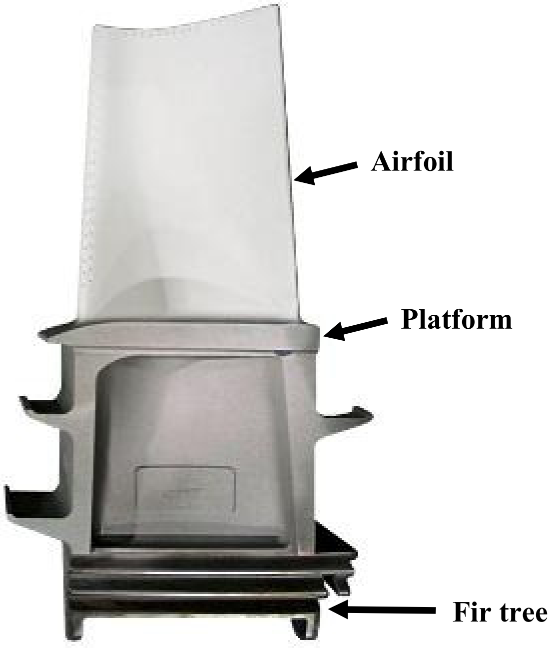

Figure 1: General Electric Frame 7FA blade, http://www.liburdi.com/TurbineServices/6FA-7FA-9FA/default.aspx. © Copyright 2012 by Liburdi Group of Companies. Reprinted with Permission.

Figure 2 shows a schematic of the three possible casting structures found in industrial gas turbine blades. For highly stressed components such as blades, the casting structure is primarily directionally solidified (DS) or single crystal (SX). With DS, the grain boundaries are aligned parallel to the primary axis of loading and are not subject to creep deformation or crack initiation as with equiaxed cast structures. Also, the concentration of grain boundary strengthening minor elements such as B, C and S can be significantly reduced and, increasing the alloy's melting point and solution heat treatment temperature. This in turn increases the volume fraction of γ' in the precipitation aged condition and increases mechanical properties such as tensile strength and creep rupture.

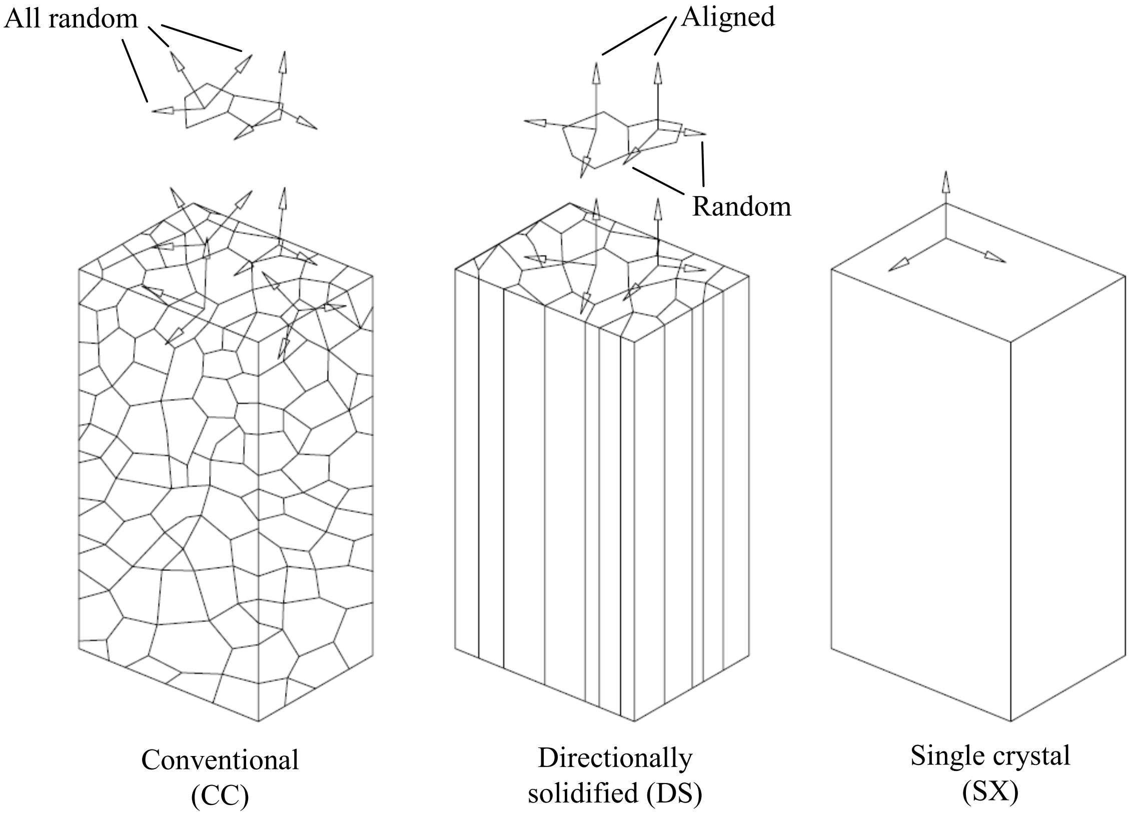

Figure 2: Schematic of casting solidification microstructures. Based on M. McLean [36].

Strengthening Mechanisms of Superalloys

The superalloys used in this study, namely Inconel 738, René 80 and René N5, are of the nickel rich austenitic type with a face centered cubic (FCC) structure. As reviewed by several authors in Superalloys II [56], nickel base superalloys are designed with the intent to optimize the mechanical properties for sustained use in the gas turbine combustion and hot section environments. They are strengthened by solid solution of select alloying element and by precipitation of the primary phase, gamma prime (γ'). Similar to solid strengthened alloys, additions of solute elements such as Al, W, Mo and Cr provide significant increase in the 0.2% flow stress of the austenite nickel rich matrix. Strength is provided by the size misfit of solute atoms as compared to the matrix, along with localized modulus misfit increase the force required for dislocations to pass through hard and soft portions of the matrix.

Considerable additional strengthening is provided the by precipitation of the coherent γ' phase having basic chemical composition of $Ni_3(Al,Ti)$. In γ', up to 60 at.% of the Al may be substituted by Ti of Nb. Characteristics of γ' precipitation affecting strength are volume fraction (f), radius of γ' (r_o), solid solution strengthening of γ' and the formation of hyperfine γ'. Gamma prime is an intermetallic phase of the Cu_3Al ($L1_2$) type maintaining its long range order over a broad range of temperature, up to near its melting point. Similar to the size and modulus misfit mechanism of strengthening of solute elements, γ' particles offer the same obstacles to advancing dislocations. Dislocations must overcome the strain field surrounding precipitated particles and pass by particle cutting or bowing. In addition, γ' particles add coherency strains, differences in stacking fault energy of particle-matrix interface. Further, gamma prime has the unique property of increasing in strength with temperature. Temperatures above approximately $0.6T_m$ increase the size of γ' and is known as ripening. As γ' grows, the mismatch with the matrix increase and affects the shape. Upon initial formation, there is least mismatch and the morphology of spherical up to a mismatch of 0.2%. In the range between 0.5-1.0% mismatch, γ' takes on a cubic shape. Beyond 1.25%, precipitates take the form of plates [56].

Alloying element in nickel base superalloys partition to various regions of the microstructure during the initial solidification of casting and subsequent heat treatments such as solutioning and ageing. Major elements partioning to the γ matrix are V, Cr, Fe, Co, Ni, Y, Mo, Hf, W and Re. Elements that partition to γ' are Al, Ti, Nb and Ta. Lastly, grain boundaries are loosely packed and offer preferential segregation of elements such as B, C, and Zr which tend to be exceedingly misfit for substitutional or interstitial solid solution in the matrix. Other elements such as Si, P, S, O and N, potentially present in superalloys are commonly known as tramp elements are strictly controlled as they have the potential to adversely affect the mechanical properties of alloys.

Carbides are important to the elevated strength of nickel base superalloys as they provide a carbon supply to grain boundaries during heat treatments and sustained elevated temperature service. Carbides improve the rupture strength by pining grain boundaries which prevents slip under applied loading. Three type of carbides are observed in nickel base superalloys; MC, $M_{23}C_6$ and M_6C [56].

MC carbides form during the initial solidification of the cast and tend to occupy grain boundary and interdendritic regions. They have an FCC crystal structure and are heterogeneously distributed throughout the casting taking coarse random and script morphologies. The most common metallic elements are Ti and Ta; thus forming TiC and/or TaC.

$M_{23}C_6$ forms from MC carbides during sustained elevated temperature exposure in the range of 760 to 980ºC. MC carbides degenerate according to the reaction $MC + \gamma \rightarrow M_{23}C_6 + \gamma'$ along grain boundaries and twin lines in the casting microstructure. The crystal structure is complex and similar to topologically closed packed phases (TCP). $M_{23}C_6$ carbides have a notable high concentration of Cr and are generally made up by the chemical formula $Cr_{21}(Mo,W)_2C_6$ [56].

M_6C carbides have a complex cubic structure and form at a higher temperature than $M_{23}C_6$ by approximately 55ºC in the temperature range 815 to 980ºC. Following a similar degeneration described above, M_6C carbides form when there is a relatively high concentration of Mo and or W in the alloy; in the range of 6 to 8 at.%. They generally have the chemical formula $(Ni,Co)_3Mo_3C$ or $(Ni,Co)_2W_4C$ [56].

Mechanisms of alloy strengthening have been briefly discussed and highlight the relevance of key alloying elements and the control of precipitated phases for increased elevated temperature properties such as creep and rupture strength. Further improvements have been realized by the control of the solidification structure achieved by the casting process. Directionally solidified and single crystal alloys are superior to conventional cast form due to the alignment of grain boundaries with the loading axis and by having the ability for higher volume fraction and more refined γ' to form in the γ matrix. These two advantages improve the high temperature ductility since grain boundaries are no longer the failure initiation site. Additionally, the alignment of grains along the [001] crystallographic orientation and the primary loading axis help resist thermal fatigue. Single crystals vary from directionally solidified casting in that the entire casting is made of a single grain with no boundaries. A starter/seed crystal is used in the mould and 'sets' the crystallographic orientation. The absence of grain boundaries alloys for a higher temperature solutioning temperature to be used, thus allowing more (up to 100% in some cases) of the secondary γ' formed during solidification cooling to be brought in solution and forming a more uniform and refined γ' throughout the microstructure during the subsequent ageing treatment. The greater volume fraction of γ' formed as a result of the increase in solutioning effect increases the strength of the fully aged alloy.

DS and SX alloys as subject to defects which may reduce their mechanical properties. DS and SX alloys, with reduced grain boundary strengthening elements, may be susceptible to grain boundary cracking during solidification cooling. Equiaxed grains and freckles form during the solidification process as a result of thermal gradients ahead of the solidification front and differences in liquid densities in the molten alloy causing dendrite tip break-off. Both conditions lead to the formation of stray grains which present a discontinuity in the alloy and no longer maintain the intended crystallographic orientation while introducing grain boundaries. Grain misalignment may occur in DS and SX alloys where the intended [001] orientation is significantly offset from the intended axis, or in the case of DS structures, off-axis grains overtake grains of preferred orientation.

Welding Practices

Although the casting processes allow the manufacture of parts with complex geometries, there exists a multi-billion dollar (USD) market in the repair of industrial gas turbine hot section components. Typically, parts require repair for renewal of coating, cracks, erosion, wear, corrosion, impact damage which inevitably requires joining processes such as gas tungsten arc welding (GTAW), electron beam welding (EB) and laser beam welding (LBW). Welding of nickel based superalloys involves the control and tolerance for characteristic defects such as distortion and micro-cracking. Consequently, much interest has been diverted to study the effect of welding on micro-cracking behaviour of nickel-based superalloys.

In industry, weld heat affected zone micro-cracking is mitigated by use of low strength, higher ductility solid solution strengthened filler alloys such as Inconel 625. This practice improves the weldability of high strength superalloys by accommodating the thermally induced compressive and tensile stress field in the weld heat affected zone [37]. Heat affected zone cracking occurs as a result of a combination of tensile stresses and grain boundary liquation of low melting point minor phases such as carbides, borides and gamma prime. Carbide and boride phases appear on the grain boundary regions due to segregation of boron, carbon and sulfur to grain boundaries and interdendritic regions during initial casting solidification and also during subsequent heat treatments. The welding kinetics (rapid heating and slow cooling) are such that only partial dissolution of these phases can occur, allowing melting of the remaining phases and formation of a liquid film on the grain boundary. Under sufficient tensile loading during the cooling stages of welding, the liquid film allows grains to separate, forming micro-cracks. This phenomenon has typically been mitigated by welding superalloys in the solution heat treated condition but due to the extremely high precipitation rate of high strength alloys, intergranular heat affected zone cracking cannot be completely eliminated.

Gas tungsten arc welding (GTAW) is the prime joining and overlay weld process for nickel based superalloys. The process is carried out manually by highly skilled welding technicians or can be automated for high volume production or long weldments. A low strength solid solution strengthened alloy such as Inconel 625 is fed to the sustained electrical arc between a tungsten electrode and the base material and provides additional reinforcement for joining operations or a build-up for dimensional restoration of parts. The process being extremely versatile has been the dominant process in the joining of superalloys and the focus on extensive research on improving the weldability of common blade and nozzle superalloys such as Inconel 738. Process parameters, pre-weld solution heat treatment and lower strength filler materials have reduced the extent of micro-cracking but further refinements are required in order to yield entirely defect free welds for highly stressed critical components such as turbine blades.

Electron beam welding (EBW) has been employed as a joining process for approximately 20 years primarily for joining shafts and discs and provides high quality welds with deep penetration in the base material with a relatively narrow weld. The process is limited by the requirement for a vacuum chamber, the inability to apply a filler material to the base material for overlay welds and the requirement for a pre-programmed weld path. EB welding is better suited for repeatable welding operations where the part to part variation is negligible and the weld path can be pre-determined by a computerized numerical control (CNC) program.

Laser beam welding (LBW) has been used in the aerospace industry for over 15 years. It was primarily introduced as an alternative to EBW with the added benefit of not requiring a vacuum chamber and allowing for application of filler alloy in wire or powder forms to the weld zone. The process has proven to be very sensitive to parameter selection and control but has been shown capable of maintaining epitaxial growth of the filler alloy along the crystallographic direction of single crystal superalloy substrates [37]. LBW has been has been used increasingly as a replacement for GTAW to join and build-up nickel based superalloys with reduced heat input to the substrate and is the subject of this thesis.

Weld Heat Affected Zone Micro-Cracking

The foundation for the present research project is based on the work done by Thakur et al. [1] on improving the weldability of Inconel 738 LC (low carbon) by the development of a pre-weld heat treatment. The researchers focused on the micro-cracking mechanisms of strain-aging (related to γ and γ') and the grain boundary structure (by grain boundary sliding and precipitate phase liquation) and evaluated the cracking response under various pre-weld heat treatments. The industry standard pre-weld solution treatment (ST) of 1120ºC for 2 hours followed by aging at 845ºC for 16 hours was used as the baseline to compare the total and average crack lengths of GTA autogenous welds on Inconel 738 LC. With regards to strain age cracking, the authors found that increasing the ST temperature, increased the cracking by dissolving a higher amount of γ' which then re-precipitated in the weld heat affected zone as secondary γ'. STA treatments with higher ST temperatures were measured to have higher strength and lower ductility which led to an increase in heat affected zone microcracking. Thakur et al. [1] have shown that solution heat treating at 1120ºC for 2 hours followed by over-aging at 1025ºC for 16 hours and water quenching provides a reduction in microhardness and changes the character of $M_{23}C_6$ carbides on the grain boundaries as discrete particles rather than a continuous film by the following reaction: $MC + \gamma \rightarrow M_{23}C_6 + \gamma'$ *(fine)*.

Additionally, the heat treatment also changed the grain boundary morphology from straight to serrated. The combined effects of increased ductility, discrete $M_{23}C_6$ carbide phase particles and grain boundary serrations proved to significantly reduce the extent of heat affected zone cracking in Inconel 738 LC autogenous GTAW. Despite the advancement in over-ageing pre-weld heat treatments, micro-cracking continues to occur and has not completely been eliminated due to the inherent heat input provided by the GTAW process. Sufficient heat is applied such that grain boundary phase liquation occurs along with micro-cracking from the thermally induced stresses in the weld heat affected zone.

Banerjee et al. [2] applied the UMT treatment developed by Thakur et al. [1] to study the effect of filler alloy selection on the tendency for heat affected zone micro-cracking in GTA welds. UMT provided a starting point whereby the micro-cracking tendency from GTAW was minimized and filler alloys were selected on their range of Al + Ti concentration. The filler alloys used in the study were Nimonic 263, René 41, FM-92 and Inconel 718 with Al+Ti concentrations ranging from 1.4 to 4.6 wt.%. The researchers assessed the extent of micro-cracking by measuring average and total crack length of GTA welds using the selected fillers. They found that the micro-cracking susceptibility of UMT Inconel 738 LC was as follows (highest to lowest): Autogenous > Nimonic 263 ≅ René 41 > FM-92 ≅ Inconel 718.

In all cases, ST resulted in a greater amount of micro-cracking. The study concluded that FM-92 and Inconel 718 reduced the strains in the HAZ due to a lower mismatch between γ and γ'. Also, being relatively slow γ' formers, FM-92 and Inconel 718 yielded a lower weld metal hardness than the other fillers (and the autogenous condition) and reduced the extend of HAZ micro-cracking by accommodating the weld stresses.

A physical understanding of the weld HAZ micro-cracking behaviour has been established and the effect of filler alloy selection has been characterized for Inconel 738 LC. Significant reductions in HAZ micro-cracking have been achieved by the over-aging pre-weld heat treatment but rely on the use of lower strength filler materials (having lower γ' volume fraction and lower hardness). Consequently, weld repairs under such conditions will be of lower strength or corrosion resistance than the base parent material and limit the extent of repairs that can be performed on damaged turbine parts.

The findings from Banerjee et al. [2] where a marked reduction in weld HAZ cracking was achieved by welding in the UMT condition using filler alloys Inconel 718 and FM-92 which undergo a slower aging response, have a lower lattice mismatch and produce softer fusion zone. This work was extended to assess the weldability of Inconel 738 LC with regards to the concentration of aluminum in the weld filler material used. Under controlled welding parameters, Sidhu et al. [3] used Inconel 625, Inconel 617 and Haynes 214 with aluminum concentrations of 0.2, 1.2 and 4.5 wt.%, respectively to weld Inconel 738LC in the ST and UMT conditions. Regardless of the pre-weld material condition and the filler alloys used, all HAZ microcracking was associated with liquation of MC carbides, $M_{23}C_6$ carbides, borides, sulfocarbides, γ-γ' eutectic along grain boundaries. Minor phase liquation provided initiation sites for micro-fissuring to occur. However, the extent of micro-cracking was found to differ between the two pre-weld material conditions. The UMT base metal was observed to have thicker liquid films, indicative of a greater amount of liquation, with a greater extent of liquid film migration. During the temperature excursion experienced by the HAZ, the thicker and more mobile liquid film along grain boundaries provided a crack arresting effect and showed a significant reduction in HAZ cracking. Also, for both the ST and UMT conditions, increasing the aluminum concentration in the filler alloy increased the volume fraction of gamma prime formed in the fusion zone (FZ) during the weld cooling phase and increased the measured total and average cracks lengths in the weld HAZ.

The importance of pre-weld condition with UMT being significantly better than the traditional ST has been demonstrated along with the effect of aluminum in filler alloys. Clearly, intergranular microcracks cannot be eliminated using the GTAW process. A pre-weld over-aging heat treatment has showed significant reduction in HAZ micro-cracking using filler alloy and autogenous welding conditions. Further, the use of low aluminum (lower γ' volume fraction and lower hardness) also reduces the extent of micro-cracking in the weld HAZ but limits welding to weaker materials with a lean mismatch in order to provide the highest quality welds.

The work of Sidhu et.al [38] evaluated the phenomenon of post-weld heat treatment cracking in Inconel 738 LC. A significant improvement on the pre-weld condition of the base metal has been achieved by significantly reducing the hardness by over-aging Inconel 738LC. This offered significant reductions in weld HAZ cracking over that of the previously used ST condition but the additional potential for cracking as a result of post-weld heat treatment (solution treat + age) remains to be evaluated.

During the solution and aging cycle, residual weld stresses act on the weld fusion zone and HAZ and a contraction of the weld metal occurs during the final aging treatment. In autogenous welds evaluated by Sidhu et al. [39], intergranular cracking occurred as a result of post weld heat treatment (PWHT) and was reported to appear larger than in the as-welded condition. The study found that the PWHT increased the TCL and ACL in the HAZ and also induced cracking in the weld FZ. Similar to HAZ cracking observed in the as-welded condition, PWHT cracking was associated with MC carbides, borides, γ-γ' eutectic and a nearly continuous film of $M_{23}C_6$ carbide.

Welding Inconel 738LC in the UMT condition was also measured to produce a narrower HAZ as a result of particle size. The over-aging treatment precipitated larger γ' particles than the ST condition and required a greater amount of heat input in order to dissolve γ' in the weld HAZ. Consequently, under identical welding conditions, the UMT condition makes it such that the base metal undergoes a reduced transformation from the heat input by the GTAW process.

In summary, the UMT treatment reduced the susceptibility of HAZ micro-cracking in Inconel 738LC. The GTAW process remains prone to inducing defects in the weld microstructure (HAZ) and further refinements are required. A similar approach to the work by Banerjee et al. [2] was taken by Sidhu et al. [39] to evaluate the effects of filler alloy composition on the PWHT cracking of Inconel 738LC. Similar to the approach taken in the previous discussion on autogenous weld, the weldability of Inconel 738LC was evaluated in the ST and UMT conditions using filler alloy Inconel 625, Inconel 617 and Haynes 214, followed by a standard STA PWHT cycle. The filler alloys were selected based on their range of concentration of aluminum. The research found that there was a general trend of increased cracking in the weld HAZ with increasing the aluminum concentration of the filler alloy used. Higher aluminum concentration in the weld metal led to a higher volume fraction of γ' formation during the PWHT cycle and increased the weld hardness. The combined effects of the change in weld metal properties showed a trend in increased cracking during the PWHT. Similar to previous findings, for a given filler alloy the susceptibility to PWHT cracking was significantly reduced by welding the alloy in the UMT condition.

Sidhu et al. [40] investigated the cracking in GTA welds in CC, DS and SX alloys by metallographic evaluation and orientation imaging microscopy (OIM). Three filler alloys with a range of Al+Ti concentration were used to apply a simulated overlay GTA weld bead repair to the CC, DS and SX cast bar specimens. The filler alloys were Inconel 625, FM-92 and Inconel 738. Total crack length and average crack length were obtained by optical metallography and were compared across the three cast forms. Inconel 738 showed the highest TCL and ACL over the DS and SX alloys for all filler alloys evaluated. Applying a second weld pass significantly increased both the TCL and ACL. As reported in previous works by the same authors, heat affected zone cracking was associated with minor phases (including γ') present along grain boundaries causing liquation and associated cracking under the local tensile stresses. Welds on the DS René 80 alloy did not exhibit cracks with Inconel 625 with 1 and 2 weld passes. One crack was observed in each of the specimens welded with FM-92 and Inconel 738 due to the increased filler alloy strength offering reduced ductility during the solidification and cooling phases of the weld process. The SX alloy did not exhibit cracking for all the filler alloys used in the study. The extent of heat affected zone cracking was in the order: CC > DS > SX, and has been explained to be as a result of a reduction in grain boundary area in the vicinity of the weld heat affected zone for the DS alloy, with a complete elimination of grain boundaries for the SX alloy. OIM analysis was conducted on the weld fusion zones and several high angle boundaries with $\Sigma > 29$ were identified for all alloy forms. The presence of high angle boundaries in the SX alloy fusion zone along with a complete absence of heat affected zone cracks demonstrated that high angle grain boundaries alone (from stray grain formation) in the fusion zone is not sufficient to lead to HAZ cracking. The state of stress in the fusion zone during solidification and cooling appear to be significant factors leading to HAZ cracking and that with the absence of grain boundaries, and subsequent liquation, the SX alloy tolerated stray grain formation in the fusion and remained crack free.

Grain boundaries present in the base material are a liability when it comes to heat affected zone cracking. It was previously generally accepted that a smaller grain size would reduce the extent of HAZ micro-cracking by reducing GB sliding and stresses by virtue of increased surface area. The once accepted rule no longer holds when it comes to welding nickel-based superalloys. Despite having higher tensile strength and coarser grain structure, DS René 80 was found to be less susceptible to HAZ micro-cracking than CC Inconel 738. This has been explained by the significant reduction in grain boundaries that are intersected by the weld fusion zone, reducing the total amount of liquid in the weld heat affected zone. In summary, the DS micro-structure is relatively coarse as compared to the CC polycrystalline microstructure and therefore reduces the likelihood that a grain boundary will be intersected by the weld fusion zone.

Low Heat Input Welding

In this thesis, the relatively high heat input from the GTAW process will be addressed by using LBW in order to resolve HAZ cracking from grain boundary liquation. Sidhu et al. [4] studied the response of laser beam welded (LBW) DS Inconel 738 to HAZ microcracking. Similarly to the investigation of GTAW on René 80 [5], HAZ micro-cracks due to grain boundary liquation of minor phases were evident along grain boundaries. The re-solidified grain boundary liquid was made up of MC carbides, γ-γ'eutectic, Cr-Mo rich borides, Zr-Ti rich sulfocarbides and γ' precipitates. In comparison to the CC form of the alloy, the extent of micro-cracking (TCL) was reduced by over half in the DS material. Therefore, the lower heat input nature of the LBW process significantly reduced the extent of grain boundary liquation and associated cracking.

In response to the limited weldability of superalloys, Tsubota et al. [41] conducted a comparative study between Nd:YG laser beam and GTA welds, studying the tensile strength and low cycle fatigue properties of specimens. Directionally solidified alloy MGA1400 was used in the study and welded using optimized welding parameters. A process parameter map was devised based on acceptable results and parameters in the centre of the map/area were used to perform autogenous welds on MGA1400DS alloy. The authors found that key processing parameters affecting weld shape and microstructural defects were (i) beam power and (ii) weld speed. Beam power was in the order of 750W and the weld speed was 15 mm/sec. Tensile strength results were comparable for LBW and GTAW. However, comparative low cycle fatigue tests showed that fatigue life of LBW specimens was three times better that that of GTAW specimens. The LCF test parameters were conducted using normal stress of 290 and 330 MPa at a constant temperature of 1173 K, with a stress ratio of 0.1. The significant improvement in the LCF results found in the LBW specimens was attributed to the improved weld microstructure. Again, by significant reduction in heat input in the material surrounding the weld metal, the LBW process provided better weld quality and improved stress controlled fatigue life under isothermal conditions.

Sekhar and Reed [42] compared the microstructural response of Waspalloy and Udimet 720Li to electron beam welding and laser beam welding. Since the 1970's EBW has been the process of choice for high quality deep penetration welds in thick sections for superalloy parts such as turbine shafts and discs. Although not considered a low heat input process, the highly localized heating and interaction with the base material of EB welding is evaluated in comparison to laser beam welding. LBW is a relatively new process and offers advantages in terms of reduced equipment complexity and the possibility of adding filler to the weld zone. The authors used a Nd:YAG laser beam power of 3 kW and a weld speed of 15.8 mm/sec for Waspalloy and 14.1 mm/sec for U720Li. The microstructural assessment provided a contrast in the shape of the welds produced by the two processes. LBW produced a weld shape of hour glass figure while EBW produced a nail head (or champagne glass) type shape. The laser beam welds were found to have 4-7% porosity resulting from repeated collapses and re-establishment of the key-hole during the welding process. In contrast, the EB welds had no porosity due to processing in a vacuum chamber which assisted in drawing out entrapped porosity in the weld metal during solidification. Using the hole drilling method, the authors measured the residual stresses in LB welds to be near the yield strength of both alloys. For Waspalloy, the longitudinal stress was 600 MPa and -300 MPa in the transverse direction. For U720Li, the residual stress in the longitudinal direction was 1200 MPa and 500 MPa in the transverse direction. The differences in residual stress between the alloys is explained to be as a result of the higher concentration on Al+Ti in U720Li allowing the alloy to harden appreciably during the cooling stage after welding as evidenced by fine precipitation of γ' in the weld fusion zone. The residual stress field surrounding the weld zone changes to compressive. Fatigue testing was not evaluated but it is postulated that the presence of porosity in the LBW would offer a reduction in fatigue life properties.

Fredirick et al. [43] investigated the mechanical properties of laser beam welds on Inconel 738 and GTD-111 (identical to René 80 in composition). The filler alloys used were Inconel 738 for the Inconel 738 substrate and René 80 for the GTD-111 substrates, both alloys being welded in the solution treated condition. Tensile specimens were tested to compare the ultimate tensile strength, yield strength and ductility of the weldments at temperatures ranging from 1200 to 1600ºF. Stress rupture testing was also carried out using an applied load of 45 ksi (310 MPa) at a temperature of 1600ºF. The mechanical properties at 1200-1400ºF were similar to those of the unwelded base alloy (baseline condition). The authors reported developing an advanced processing method to achieve similar results on repaired engine parts. The process involved the following steps: hot isostatic pressing the specimens, welding with a matched filler, sealing the surface by welding with Inconel 625, final age heat treat and mechanically re-contouring the part. This process is rather complex and requires costly equipment such as a HIP furnace. Further, the surface glazing with Inconel 625 provided healing of surface micro-cracks but did not address micro-fissuring along grain boundaries due to liquation in the heat affected zone. The approach taken by Thakur et al. [1]

as previously discussed in this report relies on changing the base material's response to micro-fissuring in lieu of surface healing micro-cracks formed in the base materials.

Laser beam welding of Inconel 718 using CO_2 and Nd:YAG lasers has been investigated by Gobbi et al. [44]. Using secondary dendrite arm spacing measurements, the authors estimated the weld cooling rate to be 15,000 K/sec for both laser wavelengths which suppressed the formation of eutectic and gamma/NbC phases in the fusion zone during the cooling stages. Low cycle fatigue properties of laser beam welds was investigated by Li et al. [45] on wrought Waspaloy having an Al+Ti composition of 4.3 wt.%. The authors used CO_2 and Nd:YAG laser systems to produce autogenous welds on 2 mm sheets of wrought Waspaloy in the annealed condition. Crack free welds were reported in both the as-welded and post-welded precipitation heat treated conditions. LCF parameters used were $R = 0.1$, $T = 450°F$, $f = 0.5$ Hz with a test run-out limit of $N = 2 \times 10^7$ cycles. LCF test results were presented on log-log plots following the Manson-Coffin relationship and show a decrease in low cycle fatigue strength of 400 MPa for the laser beam welds as compared to 400 MPa for the baseline material. Fractography analysis found that crack initiation occurred in the boundary between the weld fusion zone and the heat affected, with no cracks extending in the fusion zone. Surface analysis found MC carbides on fracture surfaces consistent with the crack initiation in MC carbides followed by propagation in the adjacent base material. The authors reported finding fractured MC carbides along fractures surface.

Rush et. al [46] investigated the effect of process parameters on liquation and PWHT cracking of laser beam welds. Using statistical analysis software, they transformed total crack length to a unitless factor representing the incidence of micro-cracking. Beam power was found to be a significant parameter on the incidence of cracking. Lower power with small beam diameters and high power used with large beam diameters reduced the incidence of cracking in the test welds. The optimal beam size for reducing cracks was 2.5 mm. Weld cracking was also related to the shape of the welds with an ideal aspect ratio (depth/width) of .25-.65, meaning shallower wide welds were less susceptible to cracking. Generally, reducing the weld fusion area reduced cracking and this is intuitive since this entails a reduction in heat input to the material. Weld micro-cracks were assessed and determined to be associated with liquation of γ’ and carbides along the grain boundaries during welding.

In another parametric study, Biela et al. [47] evaluated the effect of pre-heating on cracking in laser beam welded Inconel 600. At temperature ranging from 600 to 800ºC, weld cracking was completely eliminated. Under lower preheating conditions, extensive weld fusion cracking was observed and underwent an intergranular propagation path. Also, the authors reported that as the primary dendrite spacing increased from parameters yielding slower cooling rates, cracking was reduced.

The effect of laser welding on weld zone cracking was evaluated by Wang et al. [48] on nickel base superalloys CMSX-4 and CMSX-486 (modified CMSX-4 with additions of C, B, Zr and Hf). Using a beam power of 1000 W and a weld speed of 2.5 m/min, comparative assessment on cracking response of the alloys were carried out. Stray grains were present in the fusion zone of both alloys but were more prevalent in the CMSX-486 alloy. The authors observed that the additions of B, C, Zr and Hf grain boundary strengthening elements in CMSX-486 likely caused a depression in the solidification temperature range and thus increase the occurrence of stray grain formation which is in turn susceptible to cracking during weld cooling.

Based on the apparent increase in fusion weld cracking in single crystal alloys due to the presence of stray grains, the importance of weld fusion zone microstructure control deserves some discussion. Churchman et al. [49] compared the cracking response of a nickel base superalloy to gas tungsten arc welding and electron beam welding. The authors applied GTAW overlay using Inconel 625, FM-92 and Inconel 738 filler alloys on René N5 base material. Epitaxial growth in the weld zone adjacent to the base material was evident along with stray grains with high angle grain boundaries ($\Sigma > 29$). Despite the stray grains and high angle grain boundaries, no cracking was observed in the GTA welds. Under different welding conditions such as v or u-groove preparation, the residual stresses during weld cooling could potentially lead to cracking along high angle grain boundaries in the fusion zone. In contrast, autogenous welding with EB showed a significantly different response. Similar to GTAW, epitaxial growth and stray grain formation were present in the weld fusion zone. Cracking along high angle grain boundaries between stray grains was present in the fusion zone and was more pronounced in high depth/width aspect ratio welds. This is attributed to the weld shape and processing parameters providing a faster cooling rate and increased residual stresses on high angle grain boundaries between stray grains. With low width/depth ratio, there were no cracks in the fusion zone but this shape is not representative of actual weld shapes obtained in industrial application of this process.

A theoretical analysis of stray grain formation has been carried out by Vitek [6] where a prediction model was developed and applied to plot the solidification profile of welds under varying power and speeds. The analysis was based on material properties for single crystal alloy René N5 and assessed the shape of the weld pool by plotting the solidification temperature isotherms. The authors also derived a formula for the areal fraction of stray grain formation as a function of the thermal gradient G and the solidification speed V. Based on the extent of constitutional undercooling ahead of the solidification front as a function of weld power and speed, the model predicted an areal fraction of stray grain formation in the weld zone under various combinations of G and V. Using the process model predictions, the study found that increasing the weld power increased stray grain formation. Also, increasing the weld speed generally reduced the areal fraction of stray grains formed. In terms of processing parameter selection, low power with high speed were optimal for reducing the extent of stray grain formation.

Recent research in modelling of welds has been reported by Bonifaz and Richards [51] where a finite element analysis approach was taken to model the thermal gradient (G) and cooling rate (R) in welds under varying processing parameters. The thermal gradient is highest at the weld fusion line (high G and low R), causing the G/R ratio to be at its highest and maintain a columnar grain solidification structure. In contrast, along the weld centreline the G/R ratio is lower by up to two orders of magnitude (low G and high R). The authors proposed that further work in the field of process modelling can apply the criteria developed by Mokadem et al. [7] to predict the microstructure in the weld fusion zone (i.e. columnar, columnar to equiaxed transition & equiaxed) as a function of welding parameters and material properties.

Residual stresses in welds are difficult to accurately measure but are of great importance in terms of the final properties of a repair accomplished by welding. Residual stresses may be sufficiently high such that the fatigue life of the weld may be drastically reduced. Recent research in FEA modelling of stress and strain in weld has been investigated by Bonifaz and Richards [52]. The authors modelled the response of Inconel 738 base alloy under varying welding parameters and determined that highest residual stresses occur where the highest elastic strains occur. This highest residual stresses were at the weld fusion line while the highest plastic strains were at the centreline. Comparing the results in terms of welding parameters, the lowest welding velocity (under identical heat input) yielded the highest G/R ratio and reduced the residual stresses and plastic strains. Coupled with a reduction/prevention in stray grain formation, lower welding speeds appear to be more desirable in terms of improving the resulting microstructure’s resistance to cracking or fatigue failure.

Low Cycle Fatigue Testing of Nickel Based Superalloys

Hong et al. [53] evaluated the failure mechanism of CMSX-4 alloy under cyclic loading. Tests were conducted under constant temperatures of 750, 850 and 950ºC with alternating strain levels of 0.6-1.2% ($R = 0$). The fatigue life of the alloy at 750 and 850ºC was nearly identical but it was significantly reduced when tested at 950ºC. The facture surfaces were analyzed and the mode of crack initiation was found to differ between the 750ºC/850ºC and 950ºC tests. At the 750ºC and 850ºC temperatures, cracks originated from porosity within the material. At 950ºC, the cracks were found to initiate at the surface oxide scale layer and propagated in the base material. The study highlights the importance of oxidation protection of parts under identical loading conditions but different operating temperatures.

Cracking in multi-beam deposits has been modelled by Zhang et al. [54] to predict the location of stray grain formation based on the local thermal gradients in the weld fusion zone. The model also predicted area of high residual stresses in multi-bead deposits. The authors obtained good correlation between the model and test weld specimens using Inconel 625 powder applied to DS Inconel 738, with a weld path parallel to the microstructure axis. Actual multi-layer laser deposits exhibited cracking in the microstructure along stray grain boundaries. Using the model, the authors correlated the areas of highest residual stresses which provided the driving force for crack formation along stray grain boundaries. Therefore, stray grain formation in laser welds of DS alloys does not guarantee that cracking will occur; a sufficiently high driving force caused by residual stresses has to act on the grain boundaries in order to lead to cracking. Therefore under low residual stress conditions, stray grains may be tolerable in welds provided that the local conditions are not susceptible to residual stresses above the tensile strength of the material.

The low cycle fatigue properties of electron beam (EB) welds in GTD-222 was investigated by Feng and Nowak [55]. LCF testing was carried out under strain controlled conditions (0.1-1.5% range) at 649, 760 and 871ºC. The authors found that at low temperature, the crack initiation occurred mostly in the parent material. This can be explained by the fact that at lower temperature and strain range, the fatigue life is limited by the base material strength. At the higher temperature, the majority of cracks initiated in the weld or weld/base material interface. This change in origin of crack initiation is explained by the higher local deformation in the weld metal and interface region at high temperature and higher strain range. Stray grain formation was not considered as part of this study and it is possible that some of the cracks originating in the weld fusion zone are the result of high angle grain boundaries.

4. EXPERIMENTAL PROCEDURES

4.1. MATERIALS

Alloy cast bars 200 mm x 50 mm x 9.5 mm were purchased from PCC Airfoils. Inconel 738LC (low carbon) conventionally cast bars were obtained in the solution treated condition (1120ºC/2h, argon gas quench). The microhardness was determined to be 411 HV from the average of ten measurements taken using a Vickers microhardness testing machine. The chemical composition of the bars is listed in Table 1 below. Refer to Appendix A for a copy of the test report showing analysis methods used for each element.

Element	Weight	Element	Weight
C	0.112	**Nb**	0.90
S	0.0010	**Ta**	1.71
Si	0.04	**Re**	0.02
Mn	0.01	**Hf**	<0.02
P	<0.005	**N**	17 ppm
Cr	16.02	**O**	7 ppm
Mo	1.77	**Mg**	31 ppm
Fe	0.03	**Sn**	<10 ppm
Ti	3.44	**Ag**	<0.4 ppm
Al	3.40	**Se**	<0.5 ppm
Co	8.47	**Te**	<0.5 ppm
W	2.58	**Pb**	<0.5 ppm
V	<0.01	**Bi**	<0.3 ppm
Cu	<0.01	**Y**	n/a
Zr	0.028	**Pt**	<0.10ppm
B	0.009	**Pd**	n/a
Ni	Balance		

Table 1: Chemical composition test results for CC Inconel 738 LC (low carbon)

René 80 directionally solidified bars were obtained in the solution treated (1204ºC/2h, argon gas quench) condition with an average microhardness of 440 HV. The chemical composition of the alloy is listed in Table 2. Refer to Appendix B for the original chemical composition analysis report.

René N5 cast bars were supplied in the solution treated condition (2 hours at 1289ºC). The average microhardness was determined to be 430 HV. The chemical composition of the alloy bars as listed on the certificate of conformity from PCC Airfoils is shown in Table 3. Refer to Appendix C for the chemical composition analysis report showing methods used to analyze each element.

Element	**Weight %**	**Element**	**Weight %**
C	0.2	**Nb**	0.02
S	0.0010	**Ta**	<0.02
Si	0.04	**Re**	<0.02
Mn	<0.01	**Hf**	0.02
P	<0.015	**N**	26.1 ppm
Cr	14.01	**O**	5 ppm
Mo	3.98	**Mg**	19 ppm
Fe	0.18	**Sn**	<10 ppm
Ti	4.98	**Ag**	<0.4 ppm
Al	2.9	**Se**	<0.5 ppm
Co	9.52	**Te**	<0.5 ppm
W	4	**Pb**	<0.5 ppm
V	<0.01	**Bi**	<0.3 ppm
Cu	0.02	**Y**	n/a
Zr	0.028	**Pt**	<0.10
B	0.013	**Pd**	<0.10
Ni	Balance		

Table 2: Chemical composition test results for DS René 80

Element	**Weight %**	**Element**	**Weight %**
C	0.06	**Nb**	<0.02
S	0.0003	**Ta**	6.41
Si	0.12	**Re**	2.92
Mn	< 0.010	**Hf**	0.16
P	< 0.005	**N**	2 ppm
Cr	7.14	**O**	3 ppm
Mo	1.44	**Mg**	90 ppm
Fe	0.09	**Sn**	< 10 ppm
Ti	0.02	**Ag**	< 0.4 ppm
Al	6.14	**Se**	< 0.5 ppm
Co	7.44	**Te**	< 0.5 ppm
W	4.94	**Pb**	< 0.5 ppm
V	<0.01	**Bi**	< 0.3 ppm
Cu	0.01	**Y**	< 0.02
Zr	0.02	**Pt**	< 0.10
B	0.004	**Pd**	< 0.10
Ni	Balance		

Table 3: Chemical composition test results for SX René N5

Praxair Ni-284-1 powder was obtained as an equivalent to Inconel 738. The particle size determined sieve analysis was 270/325 μm. Refer to Table 4 for the powder chemical composition. Appendix D shows a copy of the chemical composition analysis and the sieve size test reports that were performed by the powder supplier.

Element	Weight %
Aluminum	3.27
Boron	0.009
Cobalt	8.45
Chromium	16.2
Carbon (total)	0.11
Copper	0.01
Iron	0.05
Manganese	0.01
Molybdenum	1.76
Nitrogen	0.008
Niobium	0.82
Nickel	Balance
Oxygen	0.014
Phosphorus	< 0.010
Sulfur	< 0.001
Silicon	0.04
Tantalum	1.77
Total All Others	0.06
Titanium	3.38
Tungsten	2.65
Zirconium	0.06

Table 4: Chemical composition test results for Praxair Ni-284-1 powder

4.2 THERMO-MECHANICAL FATIGUE SPECIMEN PREPARATION

Plates were sectioned from the cast bars along the [001] direction using a wire feed electrical discharge machine. Plate dimensions were 50 mm wide x 100 mm long x 3 mm thick in order to produce a specimen of suitable size for the Gleeble testing machine. The recast layer and rough surface finish were removed by grinding using silicon carbide abrasive paper with 80, 120 and 220 grit progressively.

Pre-weld heat treatments were carried in order to over-age the alloy to reduce the material hardness. Since the cast bar were obtained in the solution treated condition, only the aging cycles were required. The pre-weld heat treatment cycles applied to the materials in the present research are as follows:

- Inconel 738: heat to 1025ºC, hold for 16 hours under vacuum, water quench
- René 80: heat to 1025ºC, hold for 16 hours under vacuum, water quench
- René N5: heat to 1200ºC, hold for 16 hours under vacuum, water quench

Weld test specimens were prepared by machining a v-grove across the 50 mm width of the specimens. The depth of the 90º v-groove was 0.76 mm and the radius at the bottom was approximately 0.005 mm, representative of the preparation to remove a shallow crack from a turbine blade or vane.

A Trumph 2 kW CO_2 laser was used to weld the Praxair Ni-284-1 powder to Inconel 738, René 80 and René N5 specimens. Preliminary trials were conducted in order to obtain a weld quality suitable for low cycle fatigue testing specimens. A total of eleven trial runs were conducted using different settings for beam power, weld pass spacing, laser beam focus position and powder feed rate until the weld quality was deemed acceptable. Complete details on process parameters are listed in Appendix E.

To completely fill the v-groove, four LBW passes were applied using the following process parameters:

- Continuous beam power: 615 Watts
- Traverse rate: 6.4 mm/sec
- Weld pass spacing: 0.55 mm
- Powder feed rate: 8 grams/minute

- Shield gas: argon
- Nozzle gas flow: 40 L/minute
- Copper chill clamps located 25 mm from weld centreline
- Specimen backing: 300 grade stainless steel plate

Figure 3: Close-up of laser welding nozzle and v-notch test specimen.

After welding, the specimens were solution treated and aged (STA) as follows:

- Inconel 738: Solution heat treat at 1120ºC for 2 hours, air cooled to ambient temperature, age at 845ºC for 20 hours, air cool to ambient temperature

- René 80: Solution heat treat at 1204ºC for 2 hours, air cool to ambient temperature, age at 1052ºC for 4 hours + 843ºC for 16 hours, air cool to ambient temperature

- René N5: Solution heat treat at 1289ºC for 2 hours, air cool to ambient temperature, age at 1079ºC for 4 hours + 899ºC for 16 hours, air cool to ambient temperature

Solution heat treatment cycles were carried out using a Marshall air furnace and aging cycles were performed in a vacuum furnace.

A Lumonics 704TR Nd:YAG laser was used to cut tensile specimens to the dimensions shown in Figure 4. Prior to testing in the Gleeble thermal mechanical fatigue testing machine, the recast layer was removed from the specimen edges with a hand file.

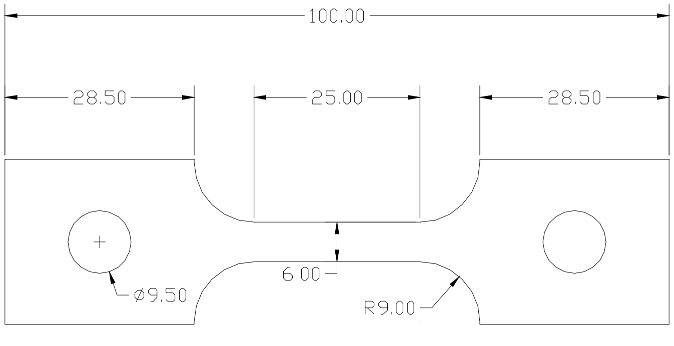

Figure 4: Thermo-mechanical fatigue specimen (dimensions in mm).

4.3 OPTICAL MICROSCOPY

A Nikon stereomicroscope was used for low magnification examination of welded thermal mechanical specimens prior to metallographic preparation. The specimen surfaces we ground smooth to remove discoloration from oxide scale and scratches in order to facilitate surface crack detection.

A Zeiss Axiovert 25 microscope was used for optical microscopy. The Zeiss microscope was equipped with a digital camera linked to Clemex image analysis software. Using the Clemex software, measurement routines were generated to measure the area fraction of porosity in the cast bars.

Specimens were prepared by sectioning using a thin-cut abrasive cutting wheel followed by hot mounting in Bakelite phenolic compound. Specimens were hot mounted in Bakelite and polished using standard laboratory preparation procedures for metallographic analysis. Grinding was carried out with silicon carbide abrasive paper on a Buehler grinding table with the following silicon carbide abrasive grits papers: 120, 180, 240, 320, 400 and 600.

Micro-polishing was done with 6 and 1 μm diamond suspension solution followed by an alumina final polish. Between grinding and polishing steps, the specimens were cleaned with cold soapy water followed by drying using filtered compressed air. The final cleaning step consisted of immersion in distilled water with ultrasonic vibratory cleaning. The specimens were air dried prior to subsequent metallographic examinations or etch treatment.

Etching for optical microscopy examination was done with Kalling’s no.2 and MTU etchants by swab etch method. Kalling’s etchant provided better etch for grain boundaries and interdendritic structures. Kalling’s tended to etch the Inconel 738 weld filler and adjacent heat affected zone more readily than the René N5 base alloy. Kalling’s etchant did not show gamma prime but was suitable for optical examinations.

Solution make up for Kalling's etchant:

- 5 grams cupric chloride
- 100 ml hydrochloric acid
- 100 ml ethanol

The MTU etchant proved to be more reactive than Kalling's. Over-etching of the specimen occurred if the solution remained on the surface for more than 5 seconds. The MTU etchant revealed the gamma prime and grain boundary structure.

Solution make up for MTU etchant:

1. 66 ml de-ionized water
2. 66 ml acetic acid, glacial
3. 66 ml nitric acid
4. 2 ml hydrofluoric acid

4.4 SCANNING ELECTRON MICROSCOPY

Specimens were prepared as described in section 4.3 with the exception that etching was electro-chemical using 12 mL H_3PO_3 + 40 mL HNO_3 + 48 mL H_2SO_4 at 5 Volts for 5 seconds, followed by rinsing in cold de-ionized water.

A JEOL JSM 5900 equipped with an ultra-thin detector window Oxford energy dispersive spectroscopy system was used for high magnification examination and semi-quantitative composition analysis. Secondary electron and backscattered electron imaging modes were used to examine the microstructure. The EDS analysis system was used to conduct point analyses, line scans and x-ray maps on features of interest.

4.5 THERMO-MECHANICAL FATIGUE TESTING

Thermo-mechanical fatigue tests were carried out on a Gleeble testing machine. Specimens were subjected to mechanical strains ranging from 0.1 to 1.5%, as measured by an extensometer over a gauge length of 10 mm. The purpose of testing over a range of mechanical strain was to obtain a range a corresponding range in the number of cycles to specimen failure.

Prior to testing under zero load, the thermal strain was evaluated by subjecting the specimen to the temperature change in the thermal cycle of 500ºC to 900°C. Therefore, the mechanical strain was derived by subtracting the thermal strain from the total strain in accordance with ASTM E2368-04. Thermal cycling was carried out in a repeated tension mode with a stress ratio (minimum to maximum stress) value of zero.

The specimen temperature was measured by a type K thermocouple resistance welded to the gauge section of the specimen undergoing thermo-mechanical cycling. Test were conducted using an in phase (IP) thermal cycle with the maximum mechanical strain occurring at the highest temperature. The thermal cycle involved heating the specimen to 500ºC followed by heating to 900ºC in 15 seconds, holding for 1.5 seconds and cooling to 500ºC in 25 seconds. After every 250 cycles, the test samples were visually examined for evidence of crack initiation and run until either a crack was visually detected, or a 20% drop in load was measured or the specimen fractured. Specimens were cycled up to a maximum limit of 10,000 cycles as it represents a practical upper limit for low cycle fatigue testing.

TMF results were plotted on log-log coordinates for applied strain as a function of cycles required for crack detection, load reduction or fracture. This representation of low-cycle fatigue data plots a straight line and is known as the Coffin-Manson relation [8, 9, 63]:

$$\Delta\varepsilon_p = \varepsilon'_f\,(2N)^c$$

Where $\Delta\varepsilon_p$ = plastic strain amplitude

ε'_f = fatigue ductility coefficient defined by the strain intercept at 2N =1

2N = number of strain reversals to failure (one cycle is two reversals)

c = fatigue ductility exponent, varying from -0.5 to -0.7 for most metals

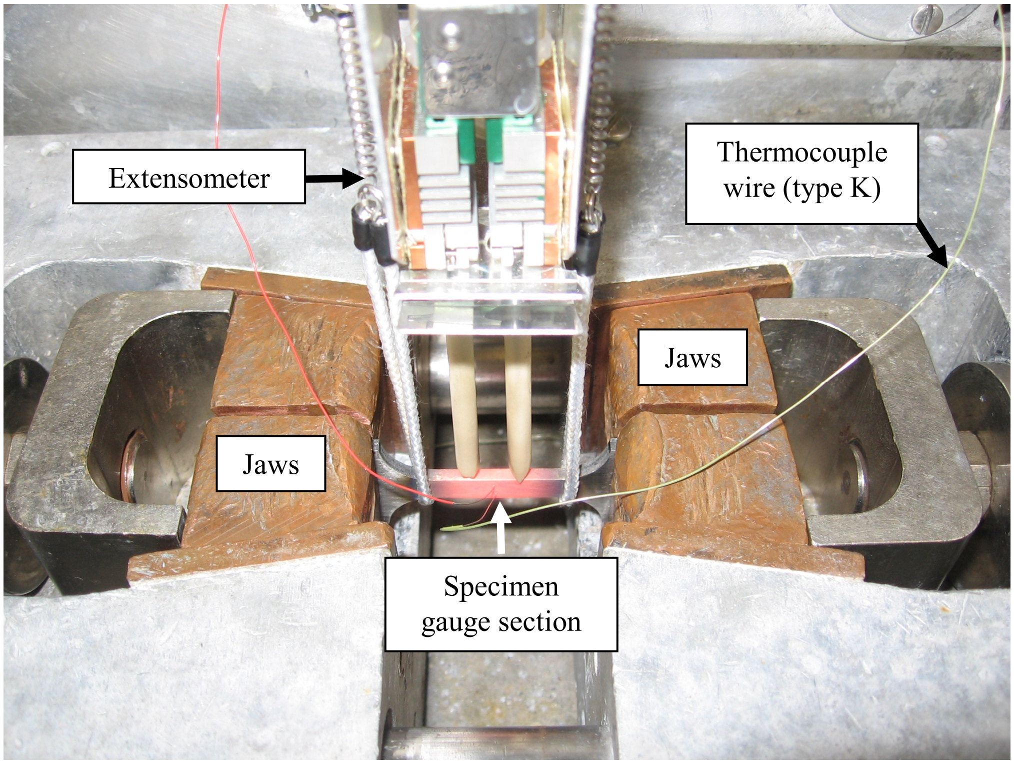

Figure 5: TMF specimen in Gleeble machine (gauge section undergoing heating cycle)

5. RESULTS AND DISCUSSION

5.1 VICKERS MICRO-HARDNESS TESTING

Micro-hardness testing was conducted on the base materials in order to compare the material hardness in each of the heat treatment conditions encountered in the study. As shown in Figure 6, the effect of over-aging (labelled as UMT), reduced the material hardness from the as-received solution treat (ST) condition for all three alloys. The greatest reduction in hardness was experienced by René 80, with a loss of 32 points (Vickers scale). Inconel 738 saw the least amount of change, with a reduction of 10 points.

Welding Inconel 738, René 80 and René N5 in the UMT condition led to increases in hardness in the weld fusion zone ranging from 18 to 32 points on the Vickers scale. The weld heat affected zone showed differing results between the alloys when comparing to the UMT pre-weld condition. René N5 was subject to an increase in material hardness while René 80 remained relatively unchanged and Inconel 738 experienced a decrease in hardness.

René 80 and René N5 both saw an increase in hardness in the post-weld heat treated (PWHT) condition. In contrast, Inconel 738 specimens were softer than in the ST and UMT condition. Several specimens were tested and confirmed the result for Inconel 738. The weld fusion zone hardness saw varying hardness values which are likely linked to the ageing response of the Inconel 738 filler alloy to the different solution and age temperatures used for René 80 and René N5.

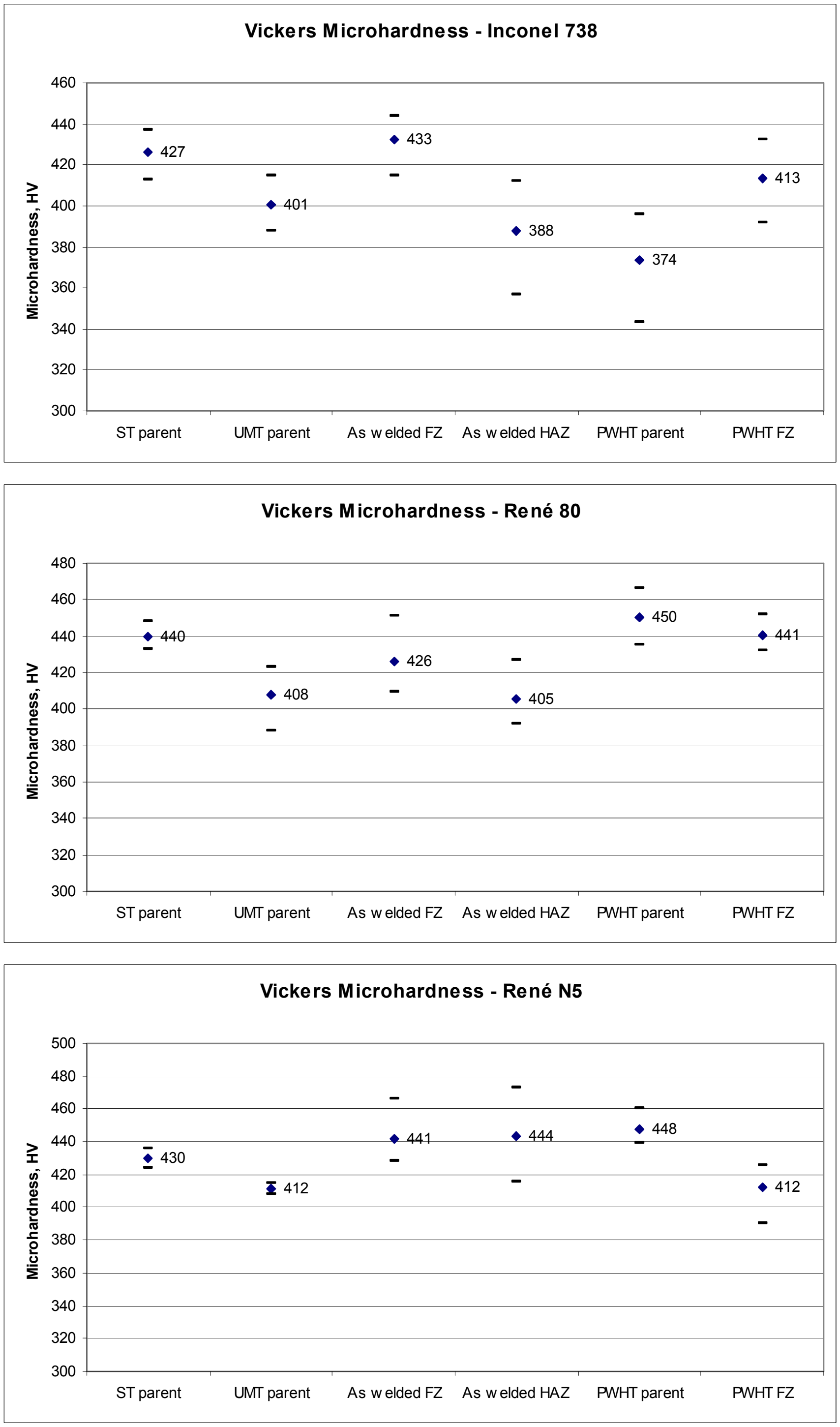

Maximum and minimum values denoted with line markers.

Figure 6: Average microhardness test results for Inconel 738, René 80 and René N5

5.2 METALLOGRAPHY OF MATERIALS IN THE AS RECEIVED CONDITION

5.2.1 Inconel 738

The microstructure of the Inconel 738 conventional cast (equiaxed) bars was of a dendritic structure. The outermost layer was made up of chill crystals with the bulk of the casting being randomly oriented dendrites. In the core structure, the average dendrite dimension was 1373 μm, as determined by the line intercept method [57].

The microstructure was dominated by the presence of the MC carbide phase, primarily located at interdendritic regions of the alloy, along grain boundaries. The morphology of the MC carbide phase was of the coarse blocky type and ranged from 5 to 40 μm in size. Porosity was apparent throughout the microstructure as shown in Figure 7. The porosity was generally spherical in shape, as a result of material shrinkage during solidification of the cast bars. The volume fraction of porosity in the as-received microstructure was measured to be 0.29%.

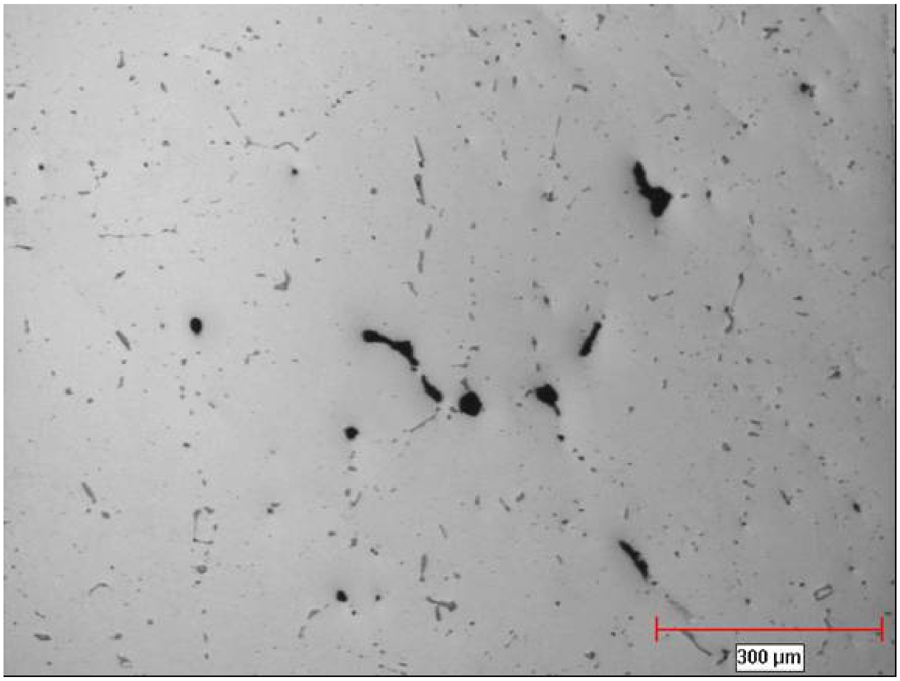

Figure 7: Optical micrograph of Inconel 738 in the as-received condition

Under SEM examination, the microstructure revealed the gamma prime phase to have a bimodal size and morphology. The primary gamma prime was cuboidal in shape and was measured to be 0.8 to 1.0 µm in size in the dendrite cores as shown in Figures 8 and 9. Fine spheroidal secondary gamma prime particles were present between primary gamma prime particles and were measured to be 0.1 to 0.2 µm in size.

As shown in Figure 10, the morphology of gamma prime in interdendritic regions was of a spheroidal type approximately 1.5 to 2.0 µm in size. Similar to the dendrite core regions, fine secondary gamma prime was evident between the primary gamma prime particles and measured 0.1 to 0.2 µm in size. Low magnification examination on the SEM revealed the presence of eutectic islands, Figure 11, surrounded by MC carbides and Cr-Mo rich borides. EDS analysis was performed on a number of carbides throughout the microstructure and were determined to be Ti-Ta-Nb rich as shown in the results of Table 5. Sulfur rich S-Ti-Zr sulfo-carbides were also observed near eutectic regions; refer to Appendix F for a linescan analysis of a typical S-Ti-Zr rich particle. A bulk analysis of the alloy composition was analyzed by EDS and the results are summarized in Table 6.

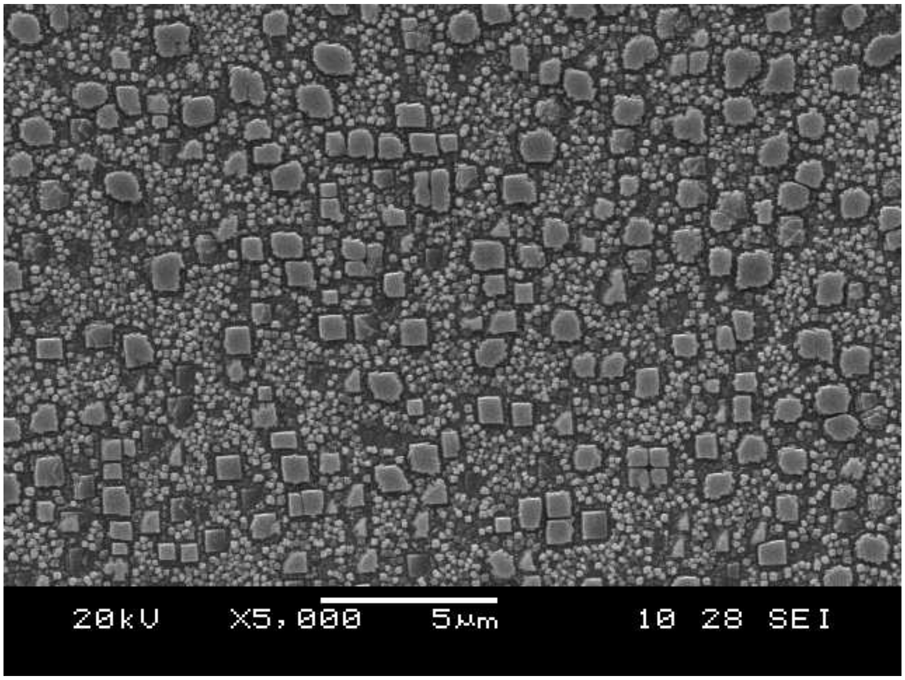

Figure 8: SEM image of Inconel 738 in the as received condition.

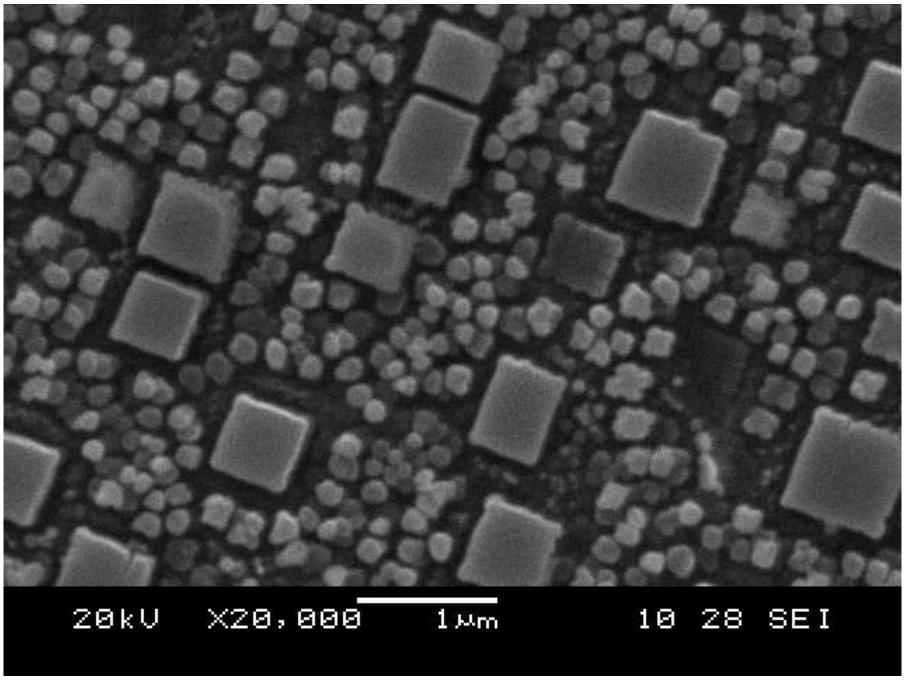

Figure 9: SEM image of gamma prime in Inconel 738 dendrite cores, as received condition

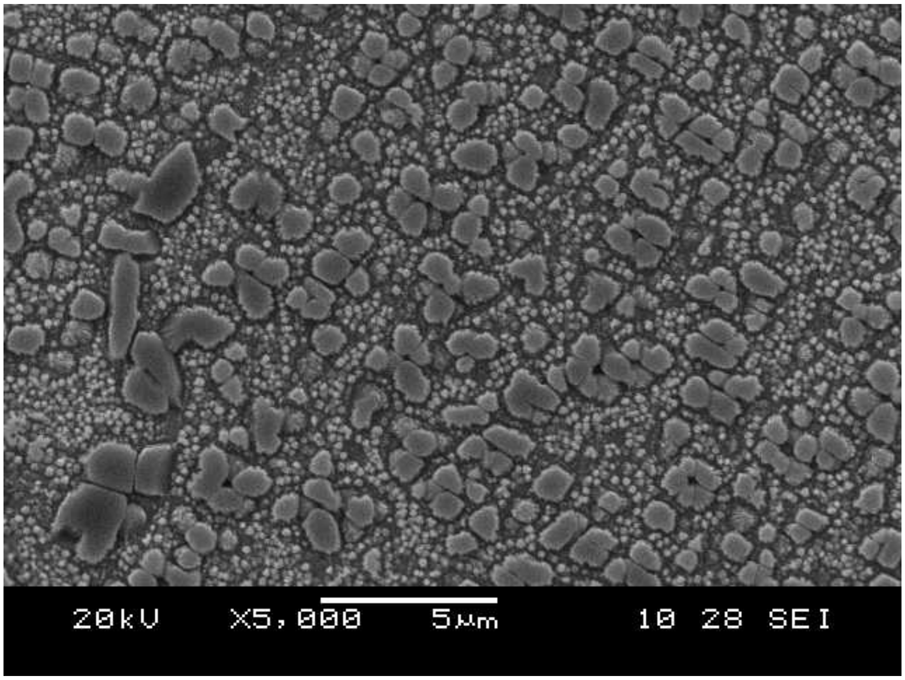

Figure 10: SEM image of gamma prime in Inconel 738 interdendritic/grain boundary region, as received condition

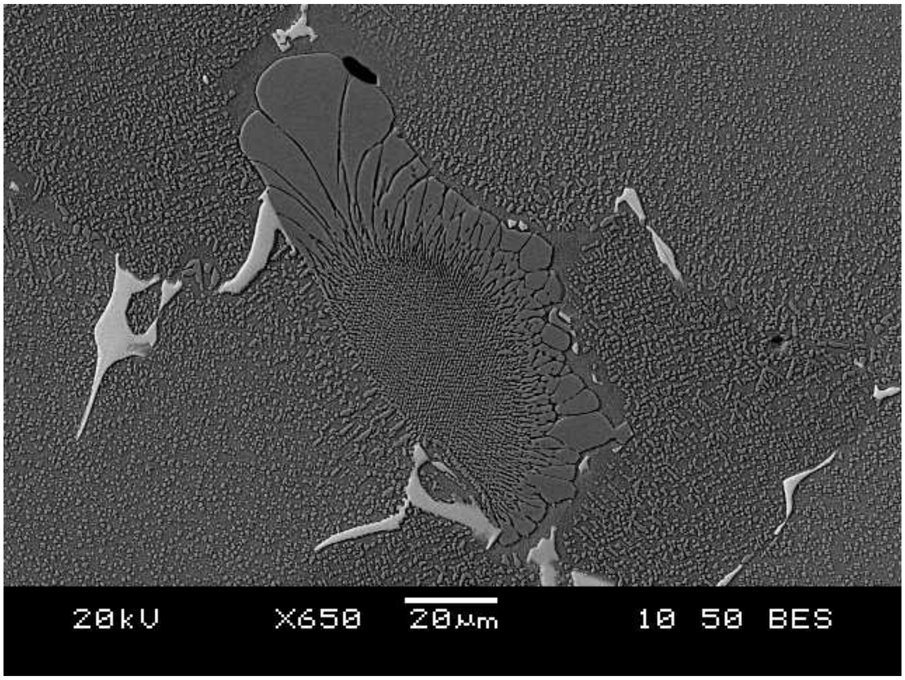

Figure 11: Inconel 738 in as-received condition, interdendritic eutectic solidification products with MC carbides and Cr-Mo rich borides

Element	Weight %	Atomic %
Co	0.32	0.31
Cr	0.77	0.8
Hf	0.58	0.56
Mo	1.9	1.7
Nb	22.0	20.8
Ni	2.5	2.6
Ta	36.9	37.8
Ti	26.3	26.4
W	8.2	8.5
Zr	0.45	0.46

Table 5: Average composition of MC type carbides in as-received Inconel 738.

Element	Weight%	Atomic%
Al	3.8	8.0
Ti	3.2	3.8
Cr	16.6	18.3
Co	8.7	8.5
Ni	59.5	58.0
Nb	0.60	0.37
Mo	2.1	1.3
Hf	0.21	0.07
Ta	1.8	0.56
W	3.5	1.1

Table 6: Average composition of alloy Inconel 738 cast bars

5.2.2 René 80

The microstructure of directionally solidified René 80 alloy exhibited a coarse dendritic solidification grain structure aligned parallel to the [100] solidification direction. The grain width in the [010] direction ranged from 100 to 300 μm in width and is shown in Figure 12. Carbides were segregated along grain boundaries and fine solidification shrinkage porosity was visible throughout the microstructure. Typical porosity is shown in Figure 13, displaying the near spherical shape of pores. Using Clemex^{TM} image analysis, several images were taken of the parent material in the as-received condition and the average porosity was determined to be 0.41%, and was the highest of the three alloys evaluated in this study.

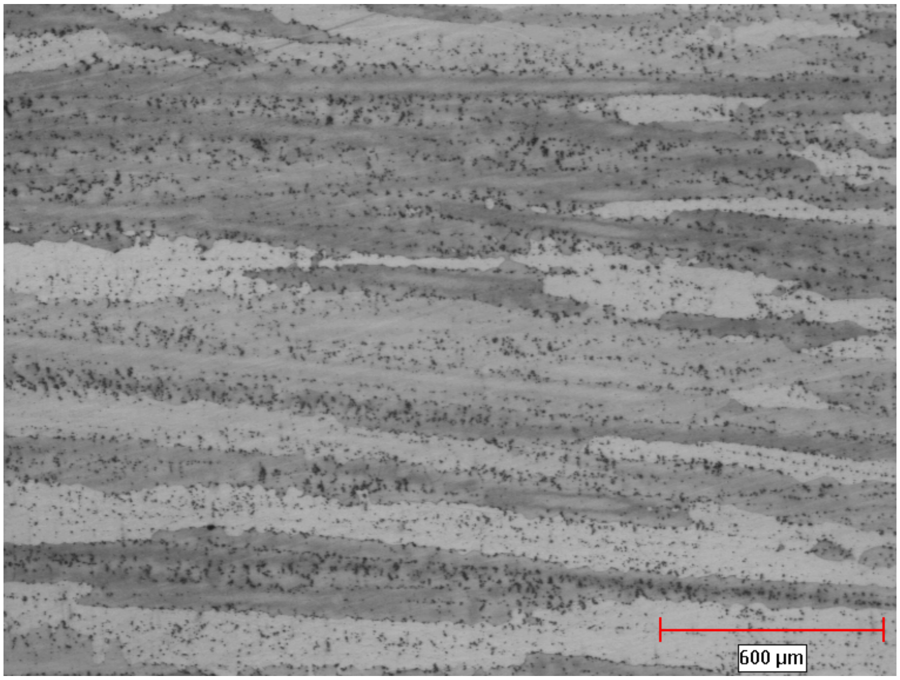

Figure 12: Low magnification optical micrograph of grain structure in as-received condition René 80

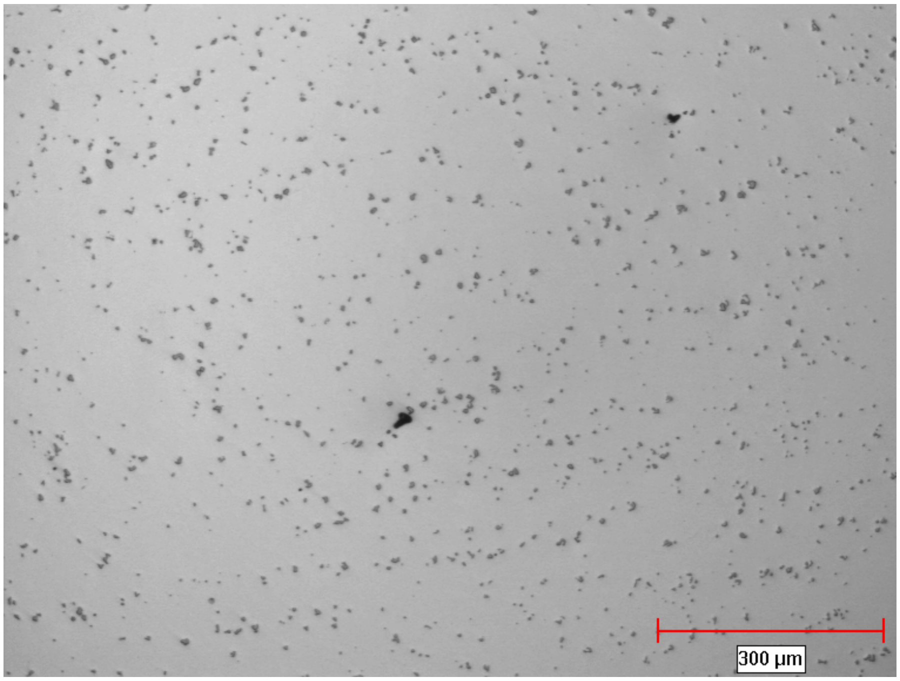

Figure 13: Optical micrograph showing porosity and carbides in René 80, as received condition

High magnification examination of the microstructure using the SEM revealed a fine unimodal gamma prime in the dendrite cores with a concave and split cubic morphology as shown in Figure 14 and were measured to be 0.32 μm in size. Along the dendrite boundaries, the gamma prime particles were primarily cuboidal in shape with a size of 0.30 μm and are shown in Figure 15. In comparison to the dendrite cores, the interdendritic gamma prime particles were marginally smaller in size with a more pronounced cuboidal morphology.

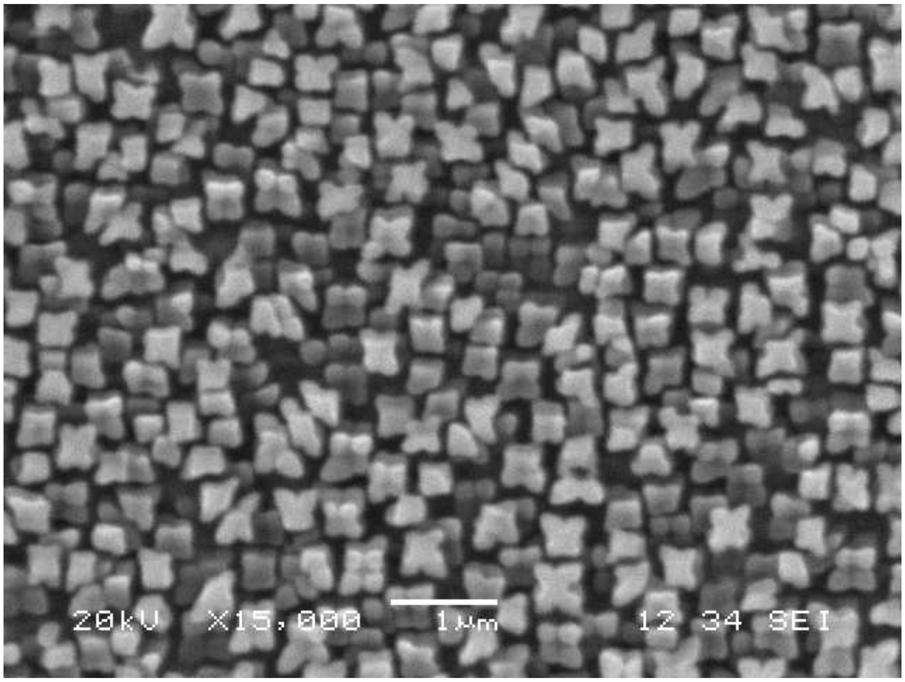

Figure 14: SEM image of concave and split cubic gamma prime in grain cores in René 80, as-received condition

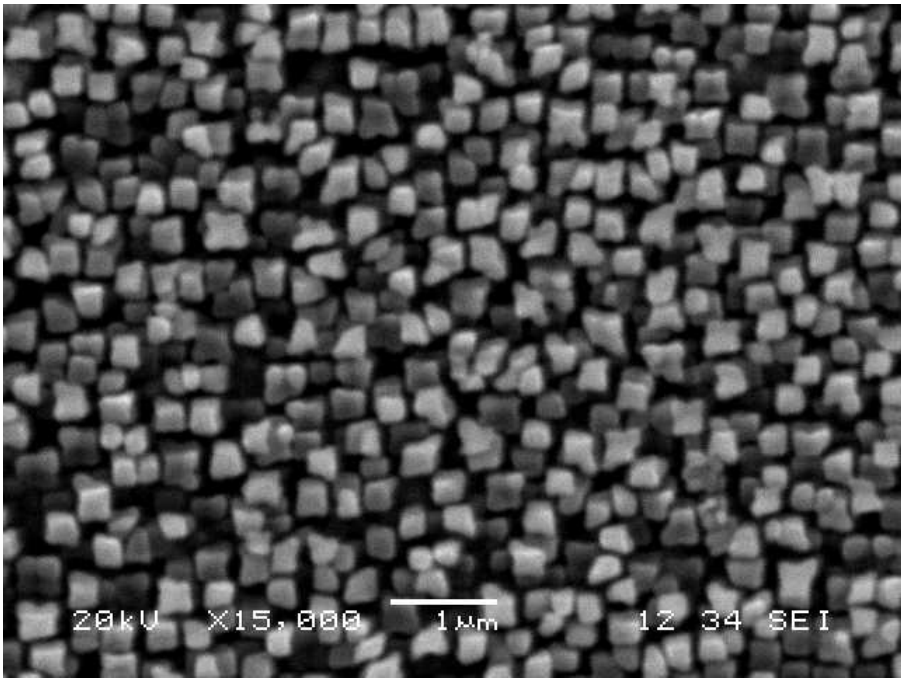

Figure 15: SEM image of typical gamma prime in René 80 interdendritic regions, as received condition

MC carbides were visible throughout the microstructure. The majority of carbides were distributed along the dendrite boundaries and were of the large, blocky type as shown in Figure 16. EDS analysis was used to determine the chemical composition the metallic constituents in several MC-type carbides with results summarized in Table 7. MC type carbides in as-received condition René 80 were rich in Ti, Mo and W. Refer to Appendix K for an EDS linescan of a typical blocky MC carbide in the Inconel 738 base alloy.

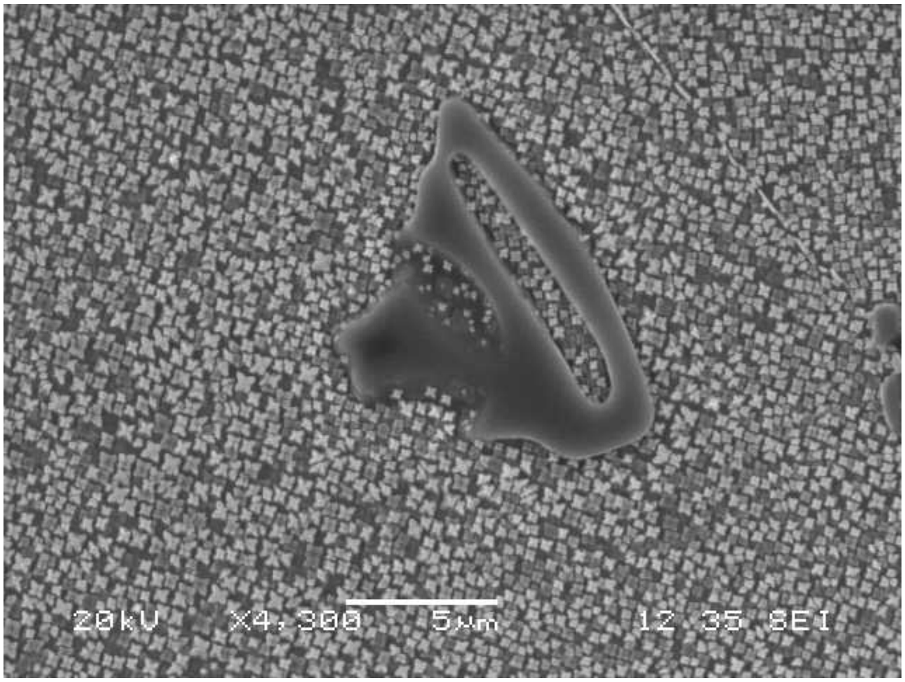

Figure 16: SEM image of blocky MC carbide in René 80, as received condition

Element	Weight%	Atomic%
Al	1.7	3.8
Ti	46.0	63.3
Cr	2.8	3.4
Co	1.3	1.3
Ni	9.7	9.8
Zr	1.1	0.8
Nb	0.69	0.51
Mo	12.6	8.9
Hf	0.19	0.07
Ta	0.14	0.05
W	24.4	8.9

Table 7: Average chemical composition of metallic constituents in MC carbides found in the as-received condition of René 80.

Several Zr-Ti rich phases were visible throughout the microstructure along grain boundaries. As shown in Figure 17, the phases were of platelet morphology in the order of 5 to 10 μm in length. EDS analysis was used to confirm the presence of S, Ti and Zr in higher concentration than the parent material composition and with the results listed in Table 8.

Refer to Appendix L for an EDS line scan across a Zr-Ti rich particle in the René 80 base alloy.

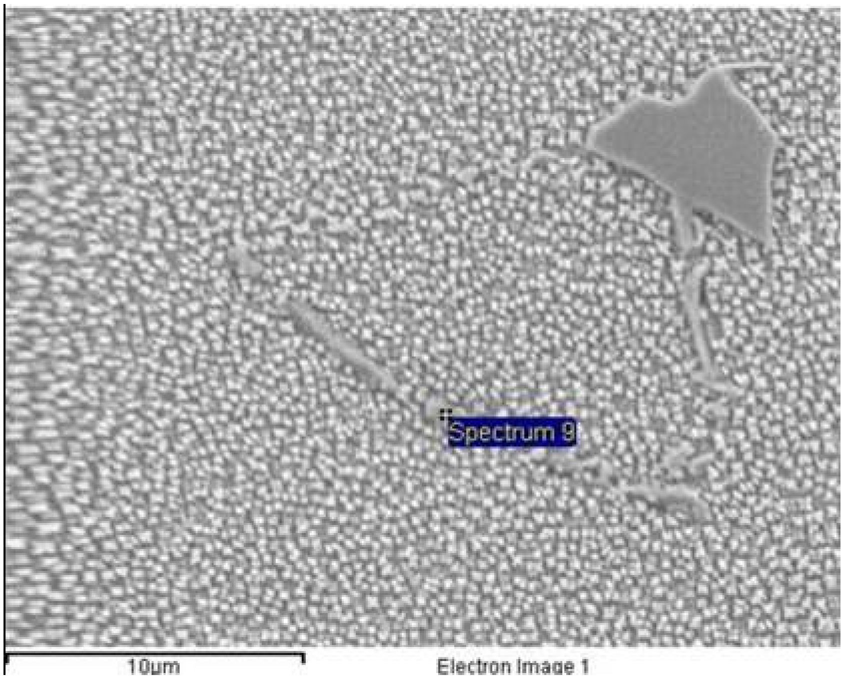

Figure 17: Ti-Zr rich sulfocarbide in René 80, as-received condition

Element	Weight%	Atomic%
Al	2.6	5.3
S	5.5	9.0
Ti	17.2	19.1
Cr	9.4	9.8
Co	8.6	7.8
Ni	50.1	46.0
Zr	1.5	0.90
Nb	0.4	0.24
Mo	3.7	2.2
Hf	0.25	0.08
Ta	0.26	0.08
W	2.6	0.77

Table 8: Average chemical composition of Zr-Ti rich sulfocarbides in René 80 in the as-received condition.

5.2.3 René N5

When observed with optical microscopy, the microstructure of single crystal René N5 was relatively featureless with the exception of the carbide particles distributed along interdendritic regions of the alloy. The carbides were in script and blocky form as shown in Figures 18 and 19, respectively.

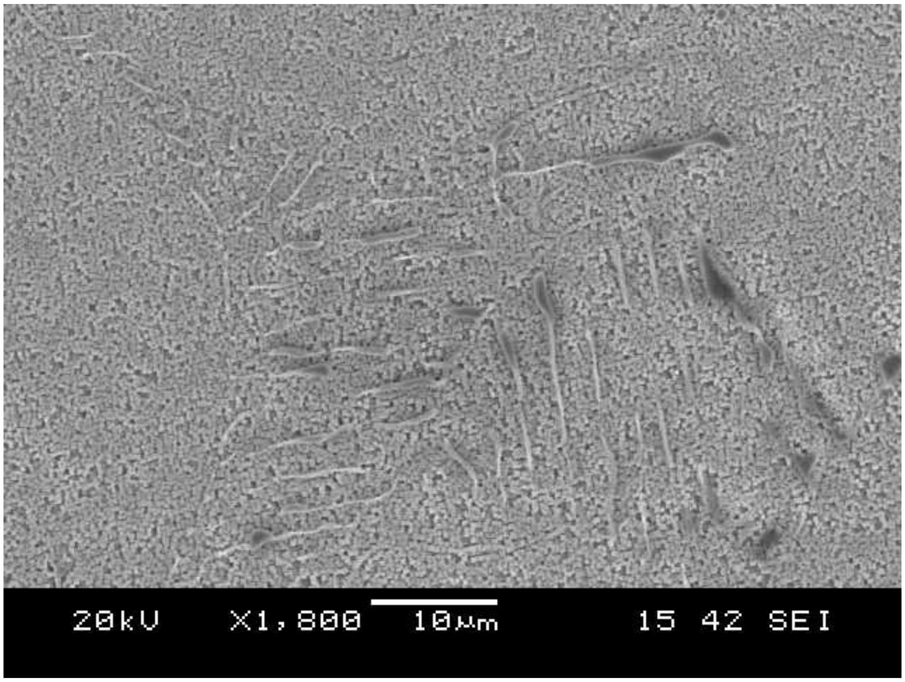

Figure 18: Script morphology MC carbides in René N5 SX cast alloy, as received condition

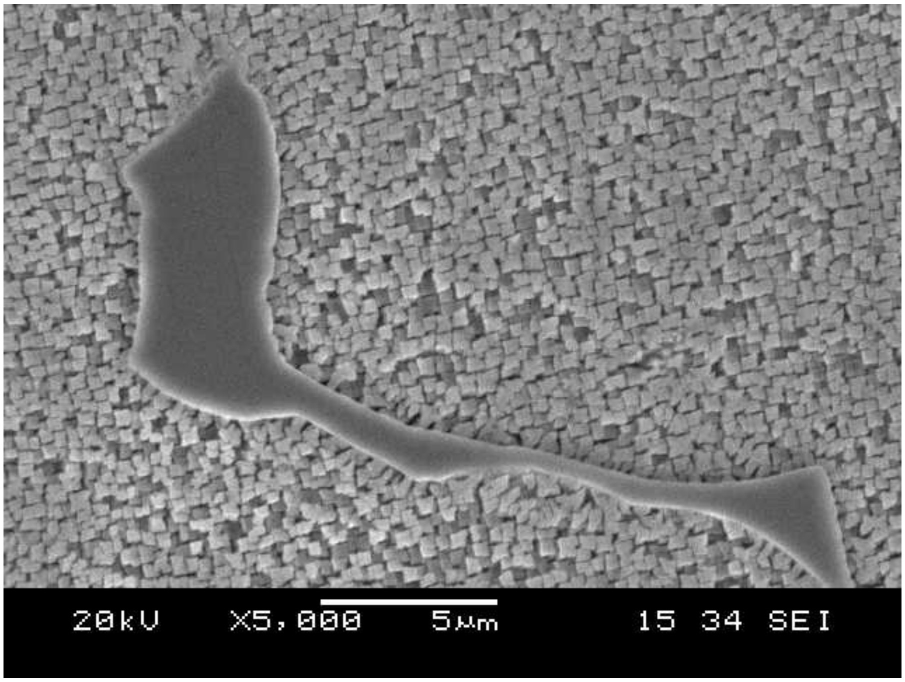

Figure 19: Blocky MC carbide in as-received René N5 SX cast alloy

High magnification examination of the alloy revealed secondary gamma prime $Ni_3(Al,Ti)$ in cuboidal morphology. The average size of gamma prime particles was 0.36 µm. The orientation of gamma prime precipitated were along the [001] direction, along the length of the bar and parallel to the solidification direction. Refer to Figure 20 for an SEM image of the as-received René N5 showing secondary precipitation of gamma prime.

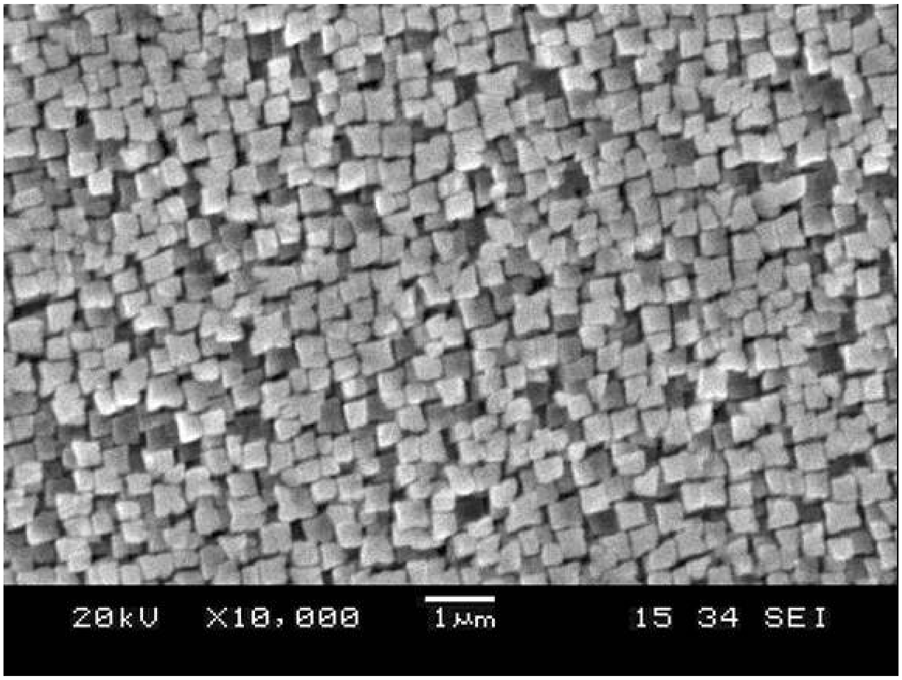

Figure 20: SEM image of typical cubic and concave cubic gamma prime in René N5, as-received condition

As shown in Figure 21, stray grains were present in the microstructure but represented less than 1% of the specimen volume, as determined by areal fraction measurement. The orientation of stray grains relative to the surrounding microstructure appeared to be random and they were surrounded by carbides similar in size and shape to those identified in interdendritic regions.

Several MC carbides were analyzed semi-quantitatively by energy dispersive spectroscopy. The primary metallic constituent was tantalum, which made up 60 to 75% of the metallic elements detected. Hafnium was detected in high concentration in all MC carbides analyzed.

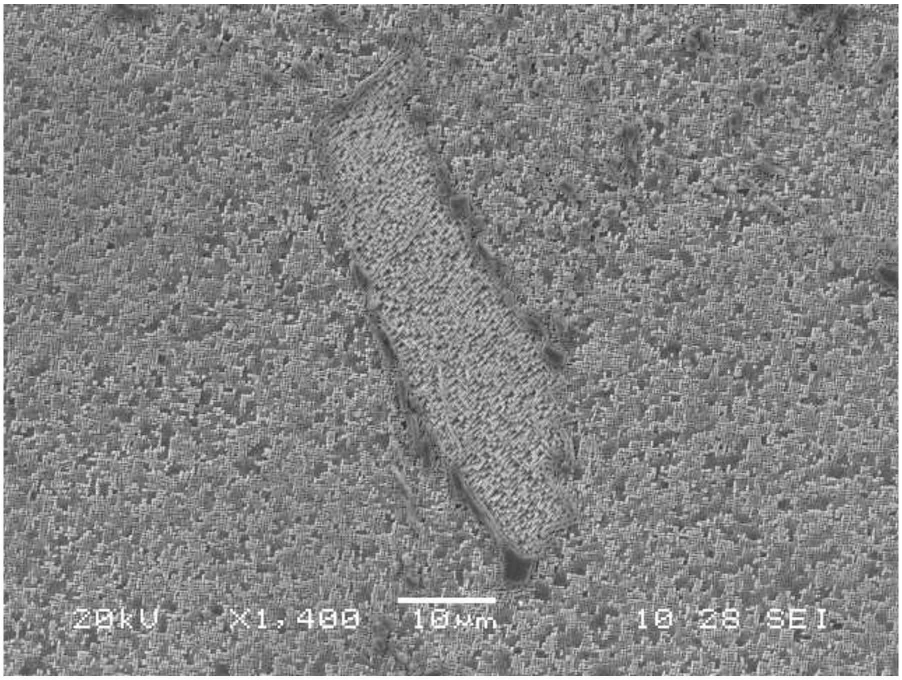

Figure 21: Stray grain in the as received condition

Although the concentration of hafnium was 0.23 wt.% in the alloy, it’s concentration in MC carbides ranged from upwards of 23 wt. % in the as received condition to 5-13 wt. % in the post-weld heat treated (PWHT) condition. In the as received condition, the principal metallic constituents of the MC carbides were Ta (63 wt.%), Hf (23 wt.%) and Zr (3.5 wt.%). The MC carbides present in the PWHT condition showed a reduction in Hf (average of 7.5 wt.%) with a corresponding increase in Ta. (average of 80 wt. %) while the concentration of Zr decreased to an average value of 1.5 wt. %.

Clemex^{TM} image analysis software was used to quantitatively measure the porosity of the alloy in the as-received condition. Areal measurements based on grey-scale sorting were used to determine the volume percentage of porosity. Ten random frames were analyzed at 100X magnification using a Zeiss Axiovert optical microscope and the average porosity was determined to be 0.14%. As shown in Figure 22 below, the morphology of porosity in René N5 alloy is related to solidification shrinkage in interdendritic regions.

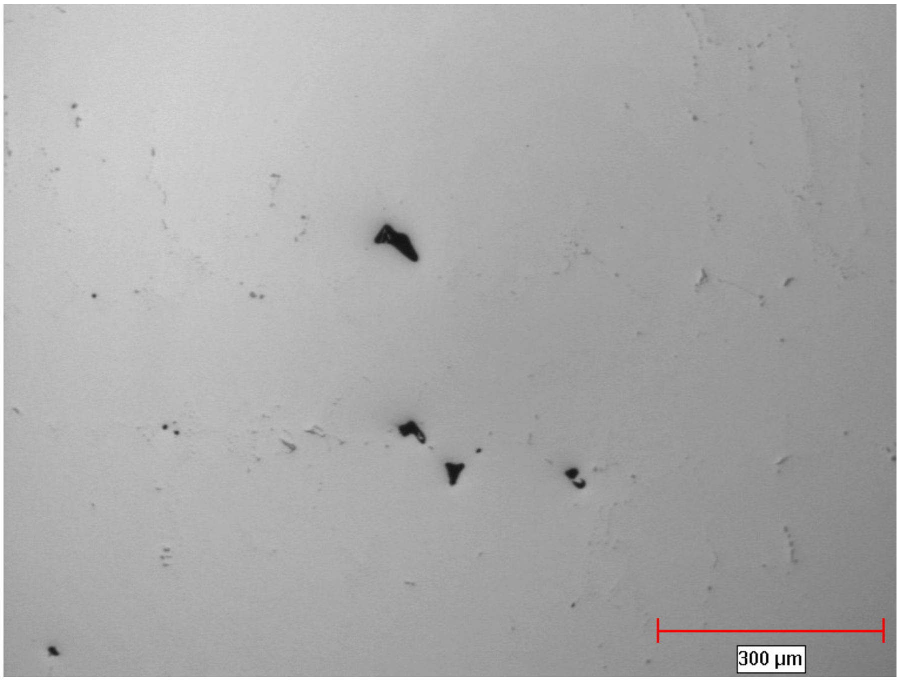

Figure 22: Typical shrinkage porosity in cast René N5 alloy, as-received condition

5.2.4 Discussion of Metallographic Results for Materials in the as-Received Condition

The metallographic evaluation of Inconel 738 (conventional cast), René 80 (directionally solidified) and René N5 (single crystal) showed similarities with regards to porosity being present in the material. Despite having been vacuum cast, some porosity remained in the castings. Based on standard processing practices for casting gas turbine nozzles and blades, a hot isostatic pressure heat treatment cycle would normally be applied to the castings in order to close shrinkage porosity and voids in the microstructure.

The cast bars were supplied in the solution heat treated condition for all three alloys. Inconel 738 was solution heat treated at 1120ºC for 2 hours followed by argon gas quenching. As evidenced by the optical micrographs presented earlier, the solution heat treatment did not fully solution the gamma prime phase as many large cuboidal particles were visible throughout the microstructure (namely primary γ'). Due to the rapid precipitation kinetics of γ', the time at elevated temperature was sufficient to allow formation of fine secondary γ' particles in the γ matrix surrounding undissolved γ' particles. This resulted in the observed bimodal size and morphology of γ' in the as-received microstructure for Inconel 738.

René 80 DS cast bars were obtained in a solution heat treated condition (1204ºC for 2 hours + argon gas quench). In contrast to the bimodal microstructure morphology observed for Inconel 738, γ' precipitate particles were cuboidal in shape and of uniform size throughout the microstructure. The γ' particles observed in René 80 in the as-received condition formed by precipitation during cooling when argon gas quenching from the solution treatment temperature. The higher solution temperature applied the René 80 cast bars accounts for the complete dissolution of γ' in the as-cast microstructure and the absence of a bimodal distribution as was observed in Inconel 738.

René N5 was solution heat treated at 1289ºC for 2 hours followed by argon gas quench, a higher temperature than the other two alloys evaluated in this study. The higher solution temperature resulted in a microstructure similar to that of René 80, being a unimodal and finer γ' size and morphology. Similar to René 80, the higher solution treatment temperature completely dissolved primary γ’ particles and only secondary γ’ was observed in the as-received solution treated condition.

Tantalum was found to be the primary metallic constituent in MC carbides found in René N5. With a bulk concentration of 6 wt.%, it accounted for up to 80 wt. % of the metallic constituent in MC carbides. René N5 alloy is strengthened by the gamma prime phase Ni_3Al as there is significantly less titanium present in the bulk alloy than in Inconel 738 and René 80. Consequently, the fraction of the metallic constituents for MC carbides in René N5 only yielded an average of 0.3 wt. % titanium, approximately one order of magnitude greater than the bulk concentration in the alloy.

Hafnium was found to be in significant concentration in all MC carbides analyzed in René N5. Hafnium is added to nickel based superalloys to increase elevated temperature properties, in particular the transverse creep [58]. Sellamuthu and Giamei [59] reported that the concentration of hafnium in MC carbides is dependent on the cooling rate of the alloy during dendritic solidification. Under slow cooling, the carbides are to form script morphology and generally yield lower levels of hafnium in MC carbides as a result of solute rejection ahead of the solidification front. Under rapid cooling, the MC carbides tended to yield higher concentrations of hafnium and exhibit an equiaxed faceted morphology.

For an interfacial temperature of T^*, the composition of solid and liquid at the interface, C_{s*} and C_{L*}, will be those given by the phase diagram under equilibrium conditions. The partition coefficient, k, is the ratio of these compositions.

$$k = C_{s*} / C_{L*}$$

Since the solidus and liquidus lines are usually more or less straight, k is approximately constant for a given system. For many systems, k has a value less than unity, so that solute is rejected from the solid as it forms, and accumulates in the liquid.

Sellamuthu and Giamei [59] report an average k_{Hf} value of approximately 0.13 for hafnium-modified MAR-M200 alloy. However, the behaviour of k_{Hf} in MAR-M200 is complex and was reported to depend on the composition of other elements such as tungsten, titanium aluminum and hafnium during solidification.

MC carbides in René N5 were present in both blocky and script like morphologies. The concentration of hafnium in MC carbides ranged from 5 to 23 wt.% and was in agreement with the findings of Sidhu et al. [40] and Churchman et al. [49]. Although cooling rates and exact solidification conditions for the alloy are not known, it is concluded that the local cooling rate was the dominant factor affecting MC morphology and hafnium concentration in SX René N5. Higher cooling rates will allow less solute rejection ahead of the advancing solidification front and reduce the concentration of Hf in the interdendritic regions available to form MC carbides.

5.3 AS-WELDED CONDITION

5.3.1 Inconel 738

The fusion zone microstructure was made up of an epitaxial solidification structure at the weld interface with the base material and stray grain in the weld core and cap. Stray grains ranged from 10 to 300 μm in size and there were no cracks along the newly formed grain boundaries. Figures 23 and 24 are optical micrographs of the weld fusion zone displaying the stray grain (equiaxed) microstructure and grain boundaries. Despite the extensive welding parameter development, a localized lack of fusion defect was apparent between the fusion zone and the base material in most of the weld specimens evaluated in this study. Figure 25 shows a typical region where lack of fusion occurred along with a fine micro-crack propagating from the cavity into the fusion zone structure. Apart from localized lack of fusion, the weld deposits were of good quality with no other visible microstructural defects.

The weld heat affected zone had grain boundary liquation corresponding to minor phase melting during the weld thermal cycle. Intergranular cracking was identified in one weld specimen shown in Figure 26 and was associated with grain boundary liquation. The total length of the liquation crack was measured to be 77 μm. Figure 27 is a higher magnification SEM image showing the re-solidified grain boundary liquation film which led to cracking during the solidification and cooling stages as a result of local stress conditions.

The chemical composition of the fusion zone was analyzed by EDS over a large sampling area and is summarized in Table 9 for major alloying elements.

Element	Weight%	Atomic%
Al	3.41	7.29
Ti	3.68	4.44
Cr	16.33	18.11
Co	8.42	8.23
Ni	59.13	58.09
Zr	0.26	0.16
Nb	1.07	0.67
Mo	2.04	1.23
Hf	0.04	0.01
Ta	2.09	0.67
W	3.52	1.10

Table 9: EDS bulk analysis of fusion zone (Praxair Ni-284-1 filler)

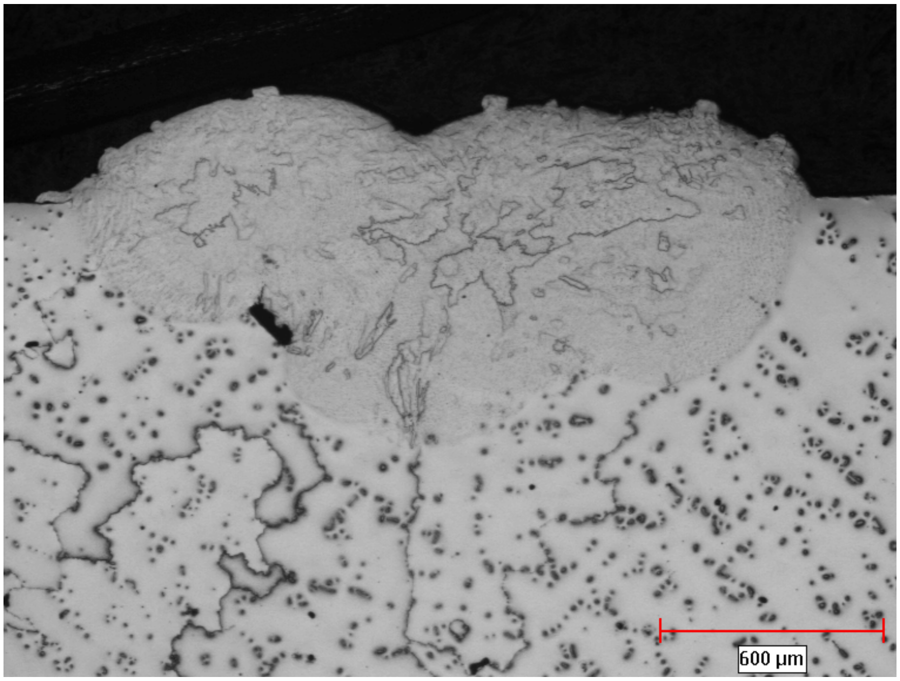

Figure 23: Optical micrograph of the weld fusion zone on the Inconel 738 specimen, as-welded condition

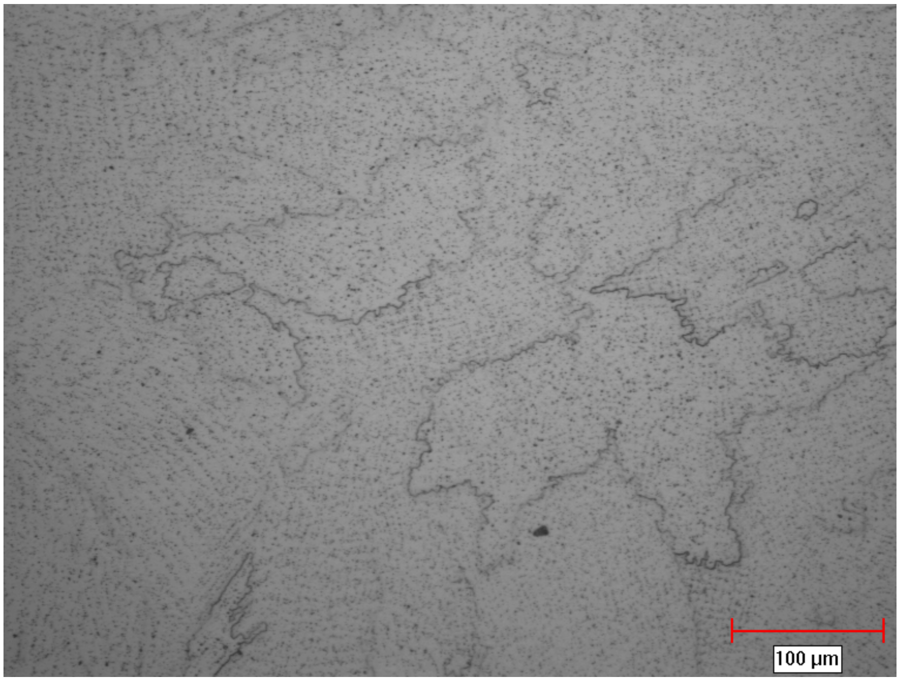

Figure 24: Optical micrograph of the as-welded fusion zone in Inconel 738 base alloy showing equiaxed grain structure

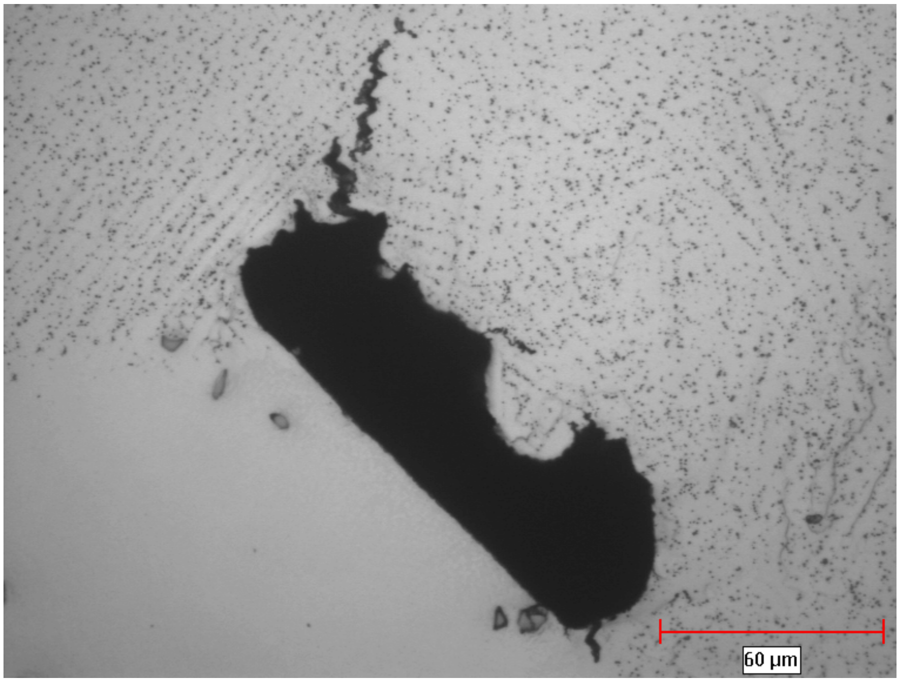

Figure 25: Optical micrograph of lack-of-fusion defect along base material machined surface in Inconel 738 as-welded condition

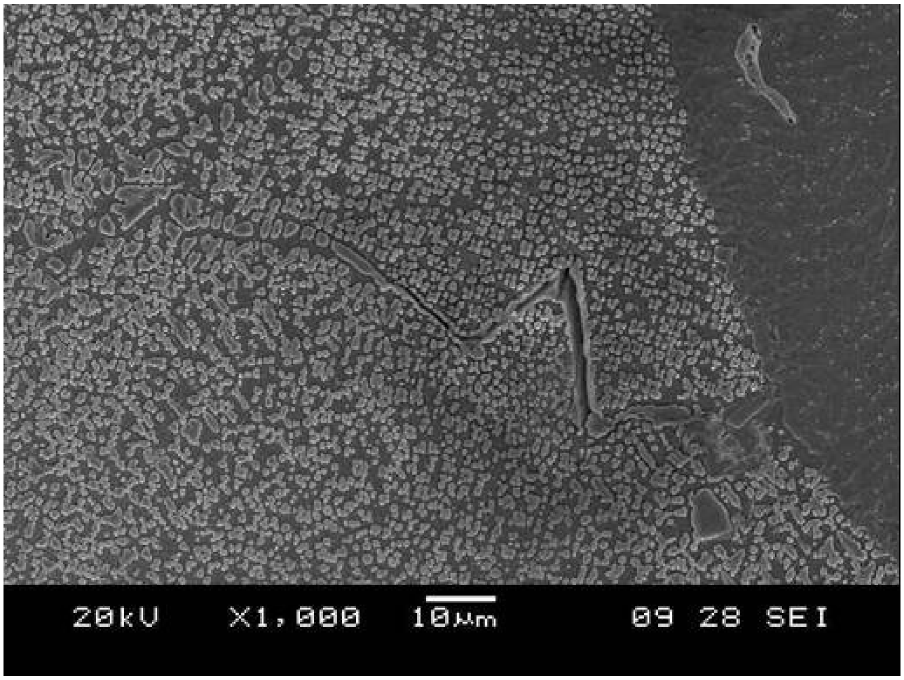

Figure 26: Grain boundary cracking in Inconel 738 weld HAZ

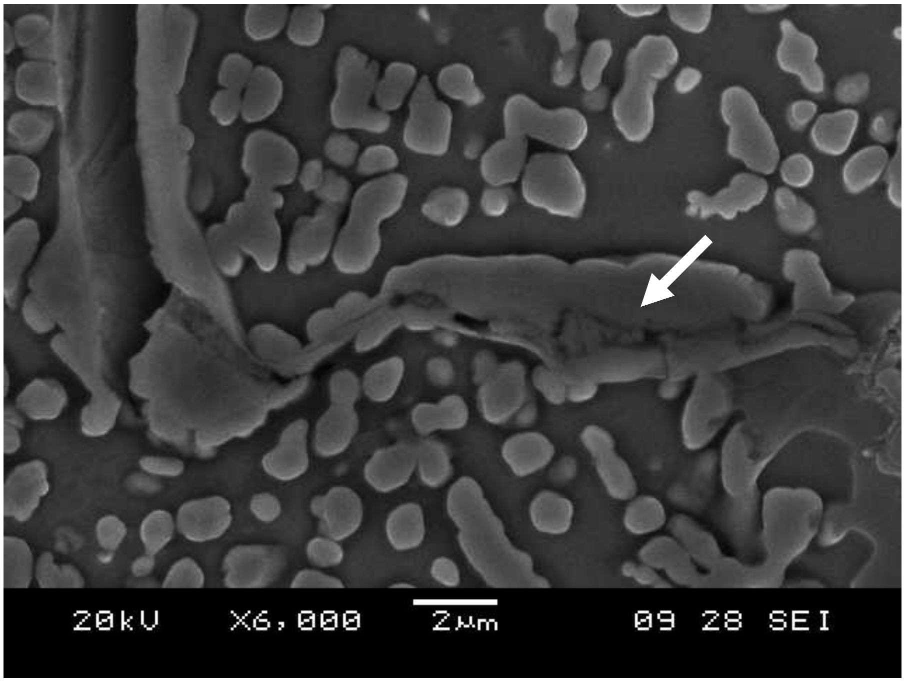

Figure 27: Grain boundary liquation cracking in Inconel 738 weld HAZ

The weld fusion zone consisted of cellular, epitaxial and dendritic stray grain solidification structures. Under SEM examination, a fine dispersed phase was apparent in the interdendritic regions of the weld fusion zone and is shown in Figures 28 and 29 (denoted by arrows). EDS line scans were taken in the weld fusion zone across dendrite arms and Ti, Mo and Nb were detected and found to segregate to the dendrite boundaries. The elemental distribution in the fusion zone is consistent with the findings of Sidhu et al. [4] and represents elemental back-diffusion segregation in the alloy during rapid weld solidification. Based on the high relative concentrations on Ti, Mo and Nb at cell/dendrite boundaries, the minor phase identified in interdendritic regions is that of Ti rich MC-type carbides. No other phases were observed in the weld fusion zone. Refer to Appendix G for an EDS line scan across the fusion zone dendritic solidification structure.

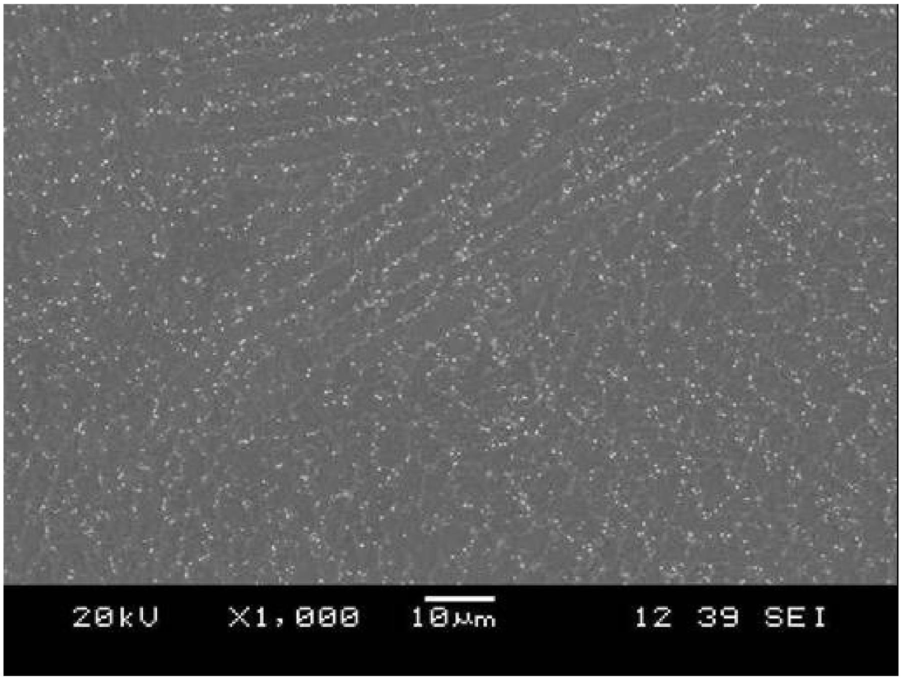

Figure 28: SEM image of Inconel 738 weld fusion zone showing carbide distribution

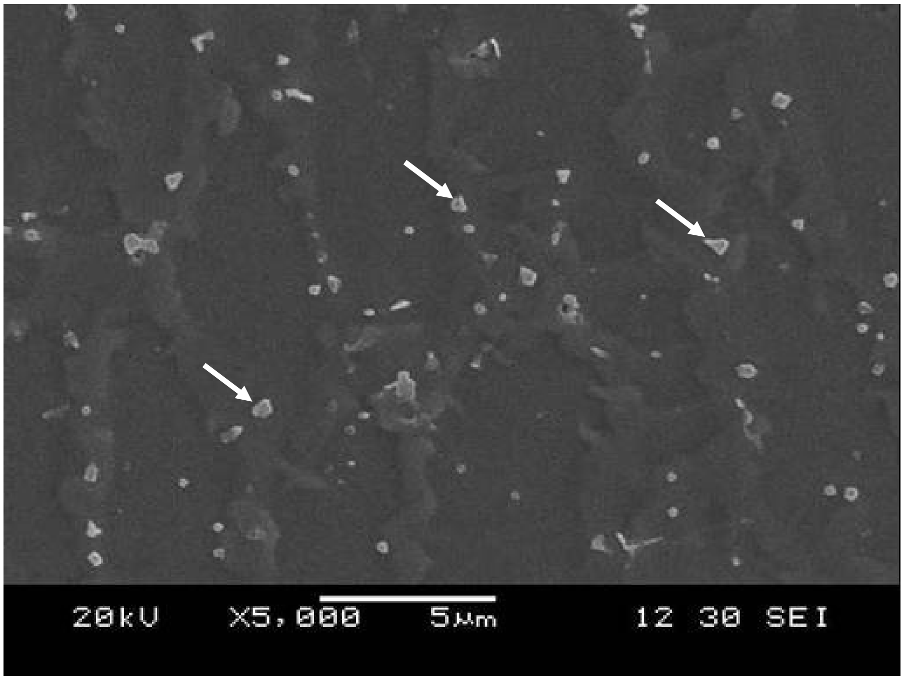

Figure 29: SEM image of the weld fusion zone solidification structure in Inconel 738 alloy

Partial liquation and cracking of MC carbides was observed along the base material grain boundaries near the weld fusion zone. As shown in Figures 30 and 31, the MC carbide particle underwent extensive cracking (five cracks) along the short axis of the particle. Liquation of the MC carbide was also observed to have occurred and a re-solidified liquation film surrounds the particles near the fusion zone boundary. There were no cracks or micro-fissures in the liquation film or base material surrounding micro-cracked MC particles in the weld heat affected zone.

Other MC carbides originally present in the base material were visible shallow in the weld fusion zone and were overtaken by the base material melting during the weld cycle. The carbides remained relatively intact, undergoing minor liquation and dissolution with the molten fusion zone. Figures 32, 33 and 34 show examples of MC carbide liquation and mixing with the weld fusion zone.

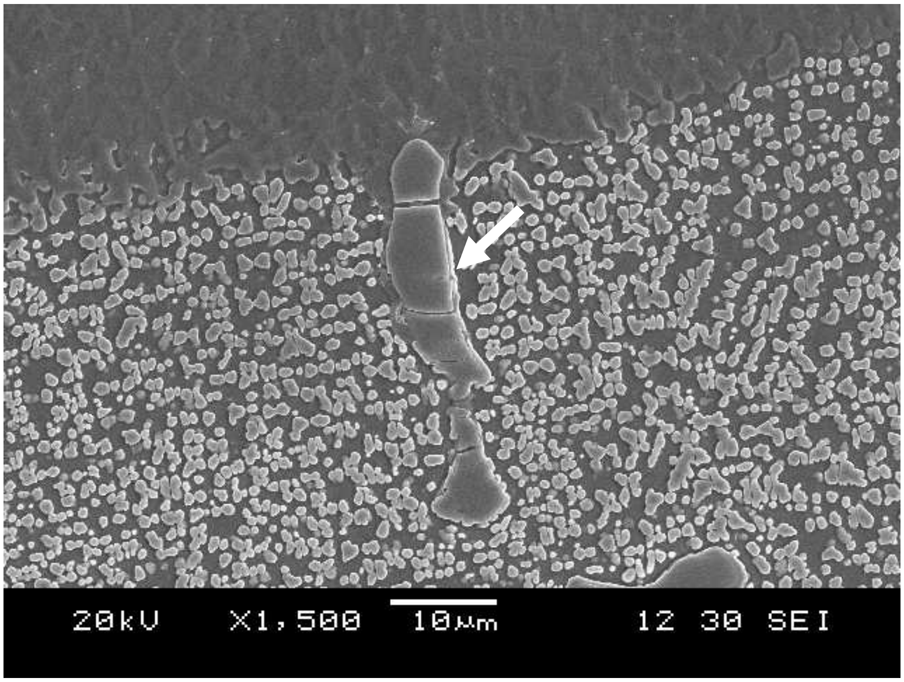

Figure 30: Carbide liquation and cracking in Inconel 738 weld HAZ

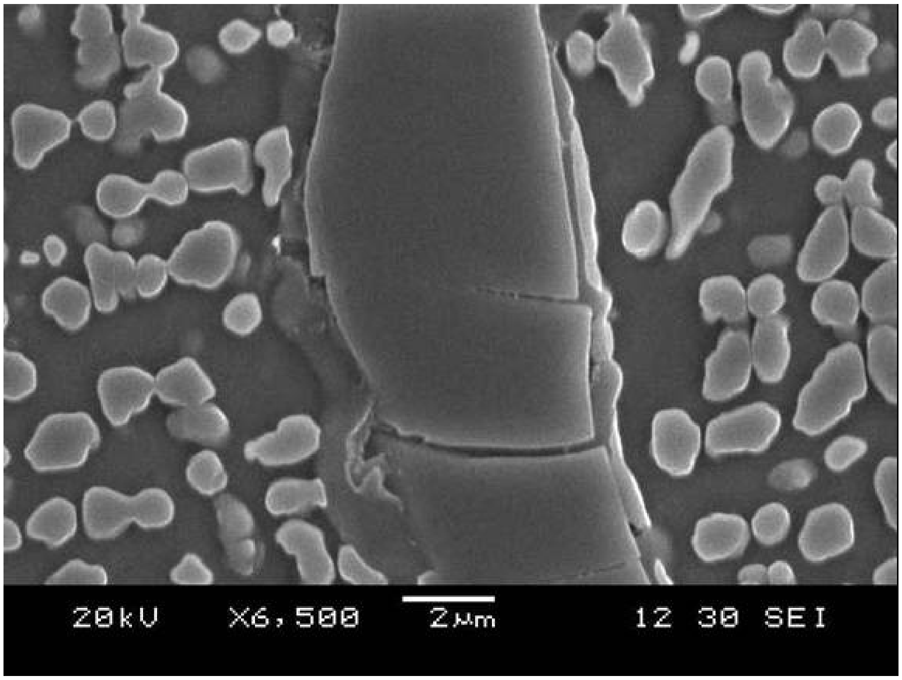

Figure 31: High magnification SEM image of carbide liquation and cracking in Inconel 738 weld HAZ

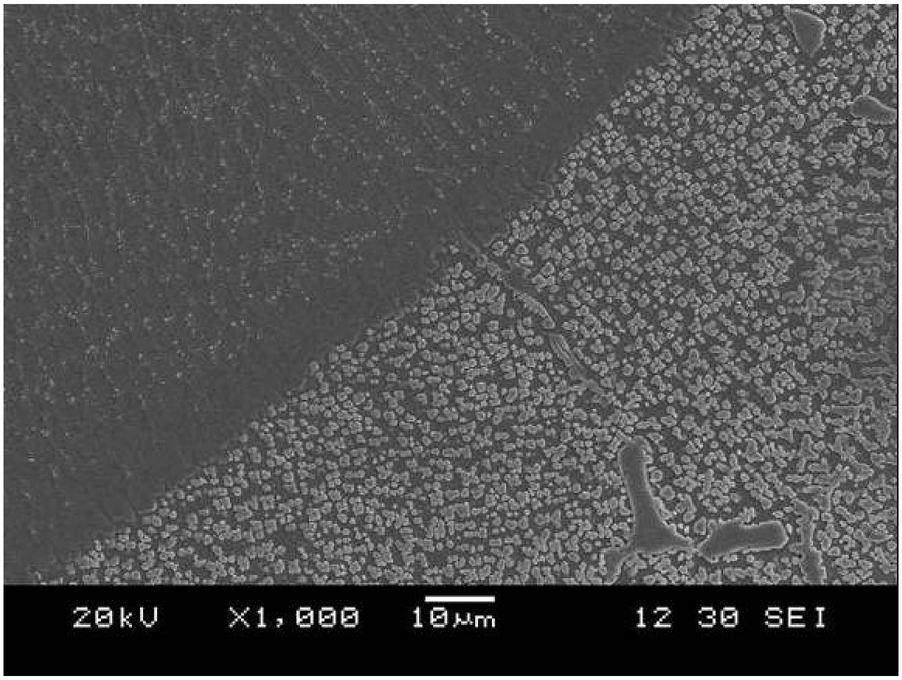

Figure 32: SEM image of the fusion zone interface with Inconel 738 base material

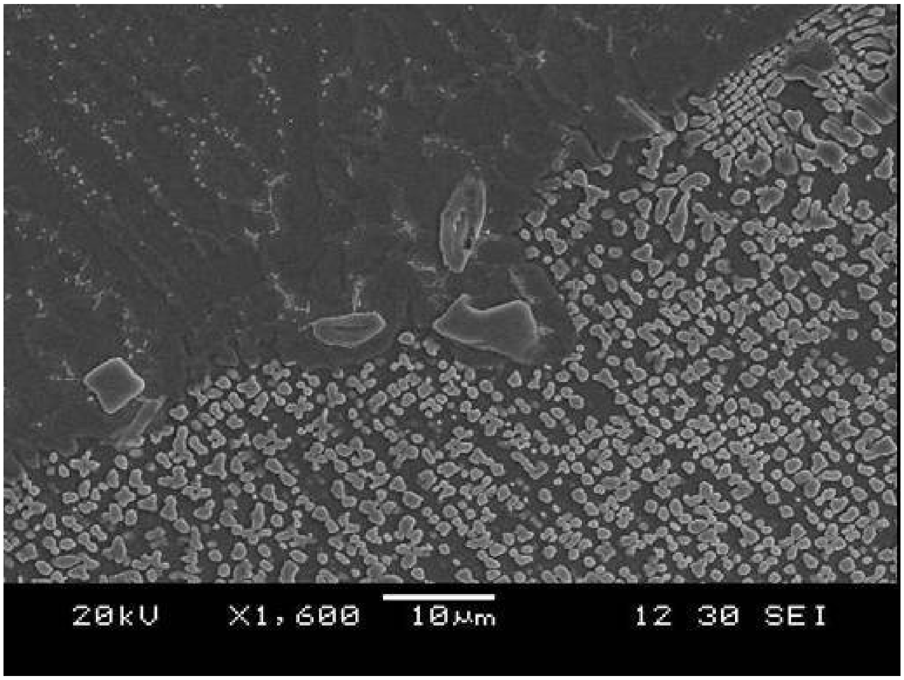

Figure 33: SEM image of liquated carbides near and within the weld fusion zone in Inconel 738 base alloy

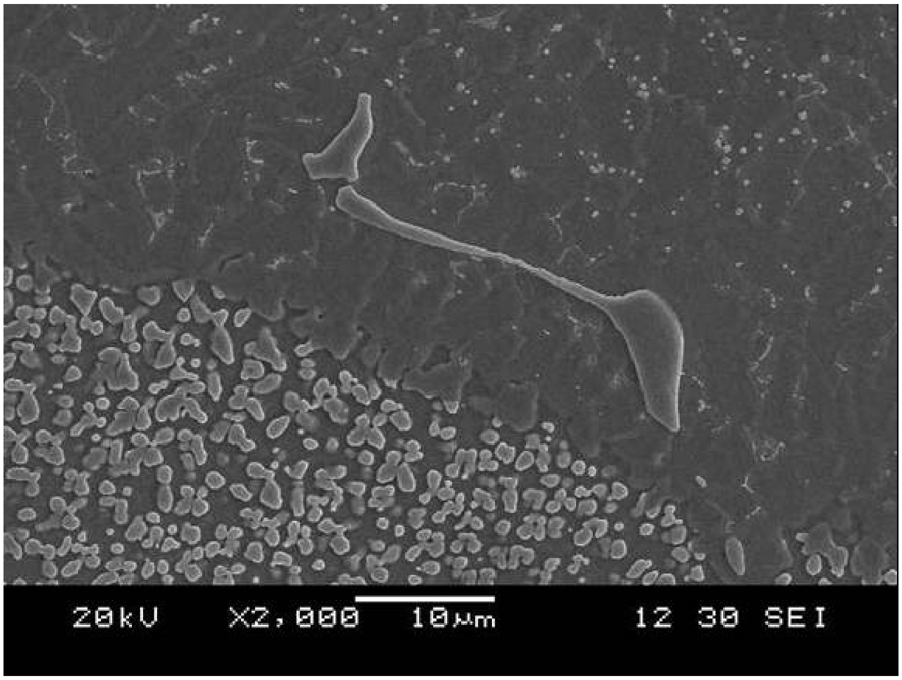

Figure 34: SEM image of liquated carbide in the weld fusion zone in Inconel 738 base alloy

The gamma prime particle size was measured over several fields in the non-HAZ core, non-HAZ interdendritic and HAZ regions of the laser beam weld. The results are summarized as follows:

- Non-HAZ gamma prime along grain boundaries: 1.1 μm
- Non-HAZ gamma prime in grain cores: 1.2 μ (Figure 35)
- HAZ gamma prime in grain cores: 1.1 μm (Figure 36)

No significant differences in size or morphology of gamma prime were found in the non-HAZ regions of the alloy subjected to the over-aging (UMT) pre-weld heat treatment. There was also no significant change in the gamma prime size or morphology in the weld heat affected zone.

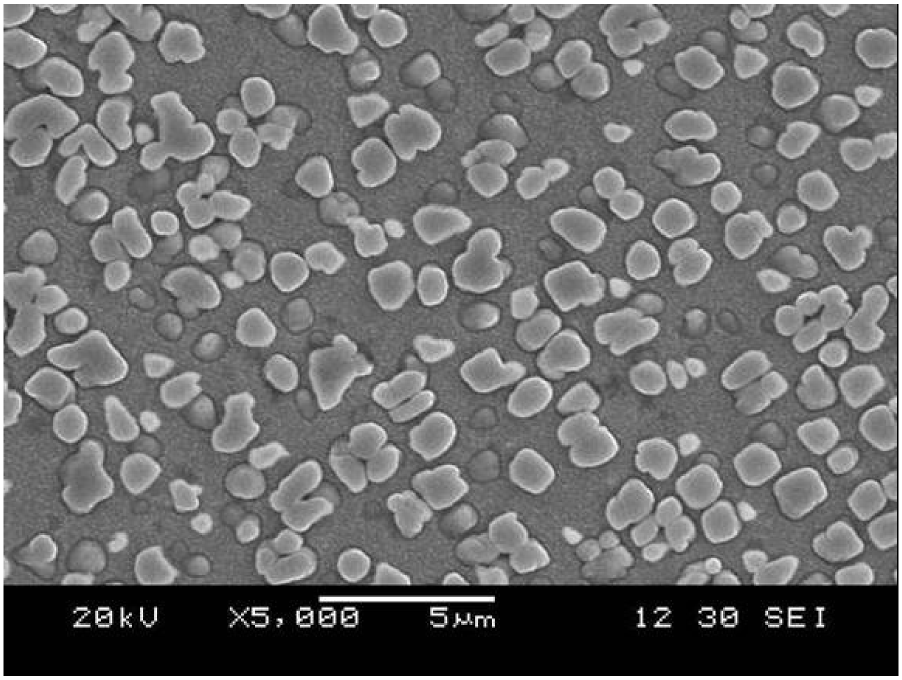

Figure 35: Non-HAZ (UMT Inconel 738) γ', dendrite core region

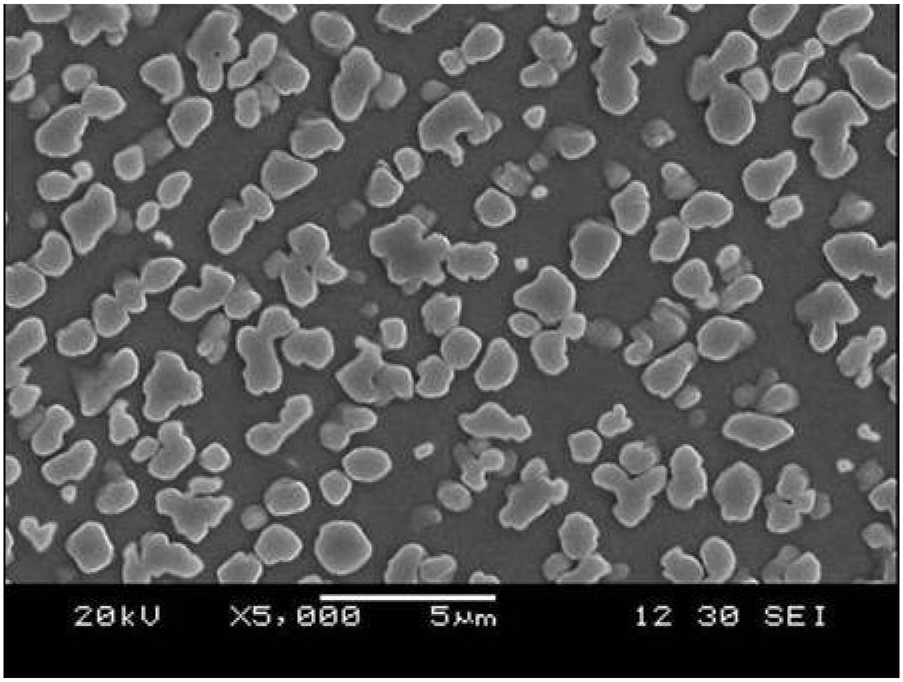

Figure 36: HAZ γ' in welded Inconel 738, dendrite core region

Carbides in the bulk alloy in non-HAZ regions were analysed by EDS for metallic constituents. The MC carbides were found to be rich in Ti, Nb and Ta rich, as summarized in Table 10 below.

Element	Weight%	Atomic%
Al	0.03	0.1
Ti	22.1	42.84
Cr	1.81	3.23
Co	0.63	0.99
Ni	3.86	6.11
Nb	16.93	16.93
Mo	4.05	3.92
Hf	0.12	0.06
Ta	40.43	20.75
W	10.05	5.07

Table 10: EDS analysis of metallic constituents in carbides in Inconel 738 in the UMT condition

5.3.2 René 80

Minor gas porosity was observed throughout the weld fusion zone and was visible in the optical micrograph shown in Figure 37. Localized minor lack of fusion at the weld root was also apparent between the initial weld deposit pass and the parent material. The microstructure of the weld fusion zone in the as-welded condition displayed a layer of epitaxial growth along the fusion zone to parent material interface with stray grains throughout the remainder of the fusion zone. As shown in Figures 37 and 38, the initial solidification occurred by epitaxial mode along the axis of the dominant (highest) thermal gradient according to local conditions and was aligned with the crystallographic orientation of the parent material along the [100] and [010] directions.

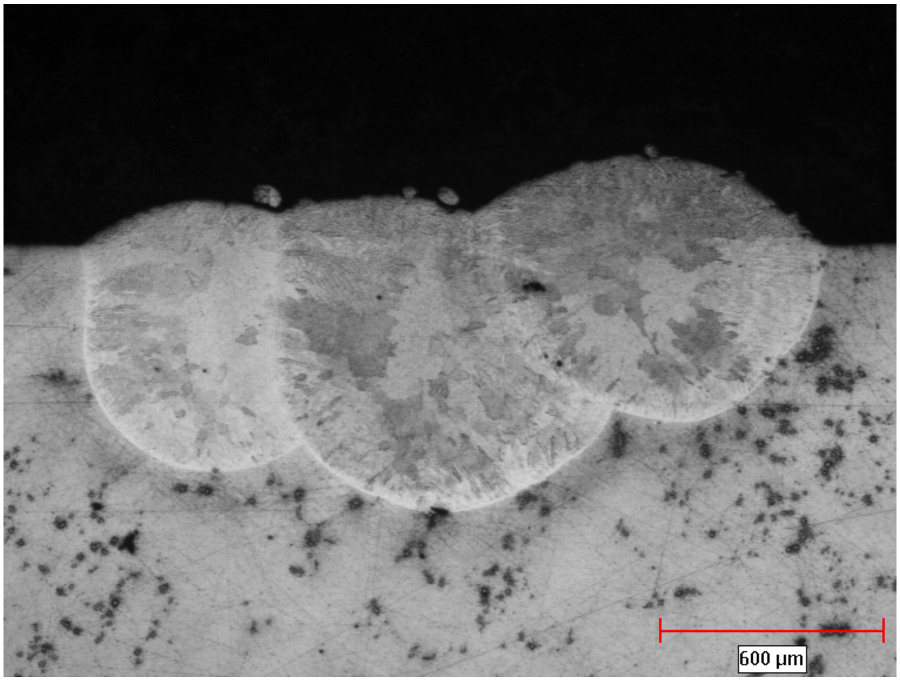

Figure 37: Optical micrograph of René 80 in the as-welded condition

The weld deposit shown in Figure 38 shows the epitaxial growth within the weld fusion zone at the interface between the deposit and the previous weld pass. Along this interface, the crystallographic direction of the solidified material is no longer aligned with the [100] parent material orientation. Stray grains make up the remainder of the fusion zone within each weld pass and are approximately 75-100 μm in size. The solidification structure changes from cellular to dendritic with stray grains as a function of the local thermal gradient and extent of constitutional undercooling.

Carbide particles were subjected to sufficiently high temperatures to cause partial liquation. As shown in Figure 39, some fragments of the carbide particle are mixed in the fusion zone to a very shallow depth. This suggests very rapid solidification with virtually no mixing near the fusion zone interface.

Figure 38 shows the transition from cellular to dendritic solidification structure in the epitaxial region of the fusion zone. Carbide liquation was observed near the fusion line and examples are shown in Figures 40 and 41. A layer of re-solidified carbide and parent material surrounds each liquated carbide. Their proximity to the fusion zone allowed sufficient parent material to liquate and links the liquid surrounding the carbides to the fusion zone. In other cases such as the liquated carbides shown in Figure 40, they were sufficiently far from the interface and small in size relative to the separation distance that it is not linked to the fusion zone. In this case, the carbide particle liquated and subsequently re-solidified in the heat affected zone layer. EDS point analyses were conducted on carbides involved with HAZ liquation and were confirmed to be rich in titanium, consistent with the MC-type, refer to Table 12 for EDS analysis results. Refer to Appendix J for an EDS linescan across the partially liquated MC carbide shown in Figure 41.

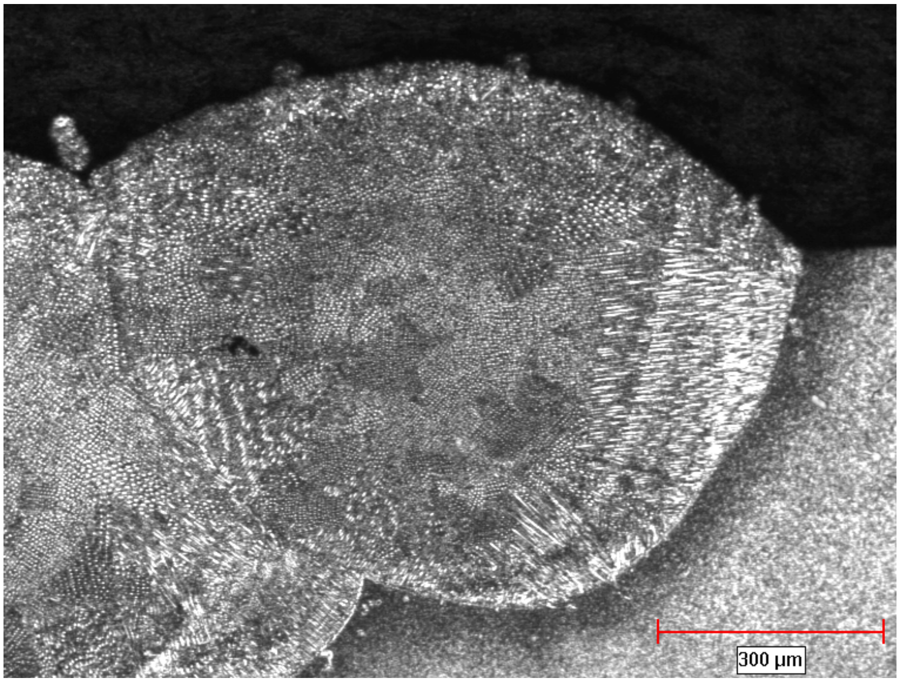

Figure 38: Optical micrograph showing solidification structures in René 80, as-welded condition

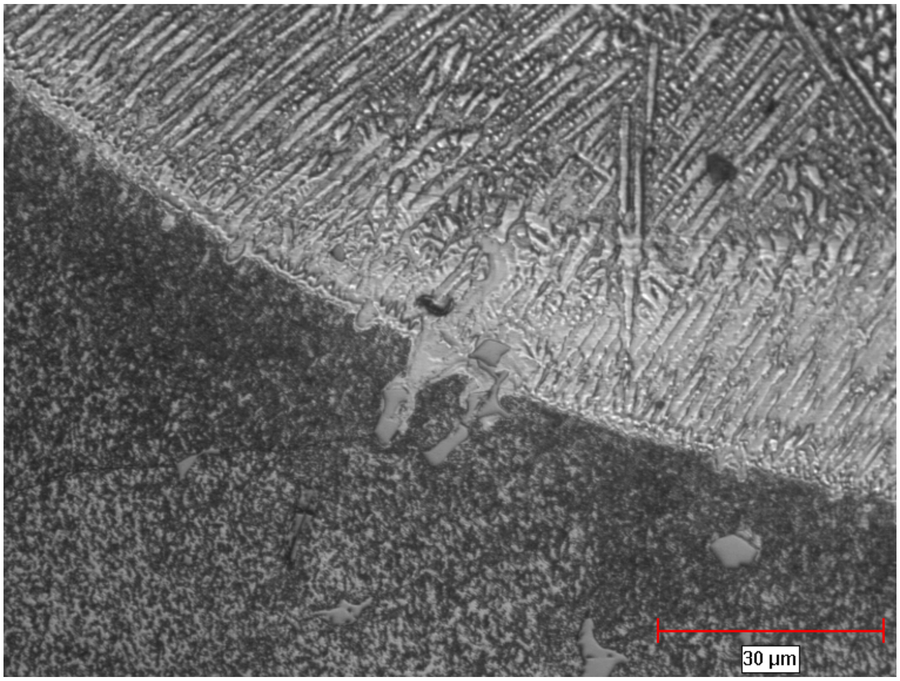

Figure 39: Optical micrograph of the weld fusion zone interface in René 80

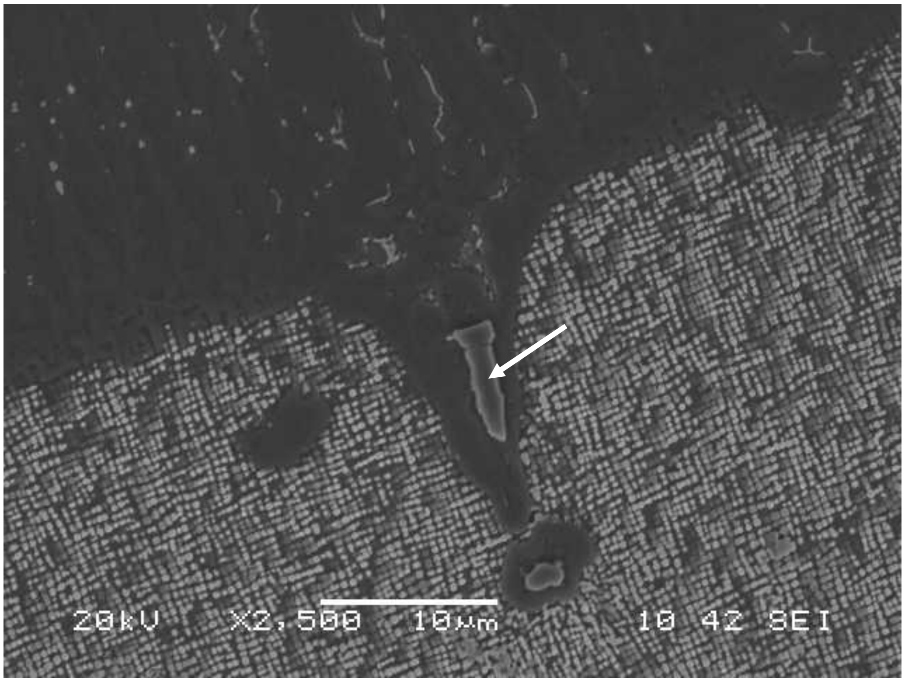

Figure 40: Liquated carbide near fusion zone, René 80 alloy in as-welded condition

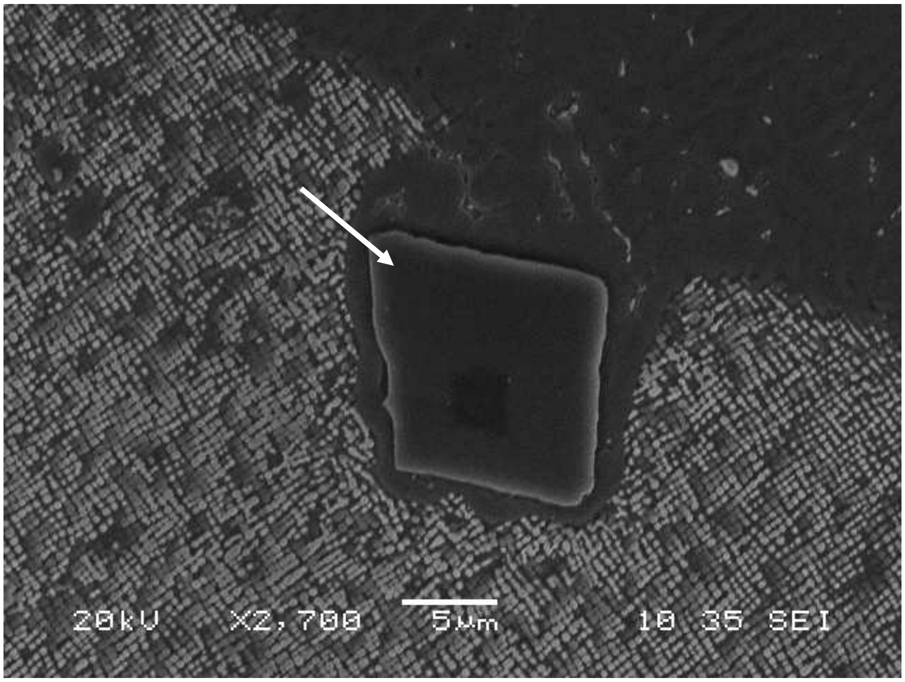

Figure 41: Liquated carbide near weld interface, René 80 alloy

Grain boundary liquation along the interdendritic region of the parent material was observed. A 1 to 3 μm thick layer of re-solidified grain boundary parent material is shown in Figure 42 and 43 with no cracking. Higher magnification imaging revealed some shrinkage porosity aligned with the grain boundary direction but this was considerably less severe than grain boundary liquation cracking found by Sidhu et al. in René 80 from GTAW [5] and similarly for Inconel 738 with LBW [4]. The grain boundary liquation in the weld heat affected zone occurs as a result of γ’ melting during the weld thermal cycle. The left side of the SEM image in Figure 42 shows the non-liquated grain boundary with γ’ particles along its surface.

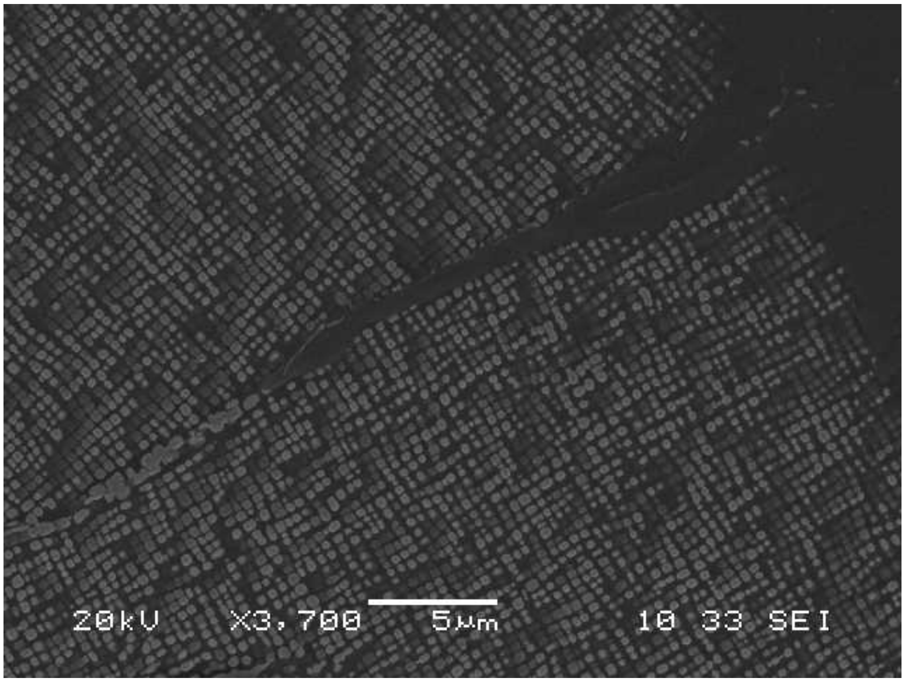

Figure 42: Grain boundary liquation near fusion zone interface in René 80

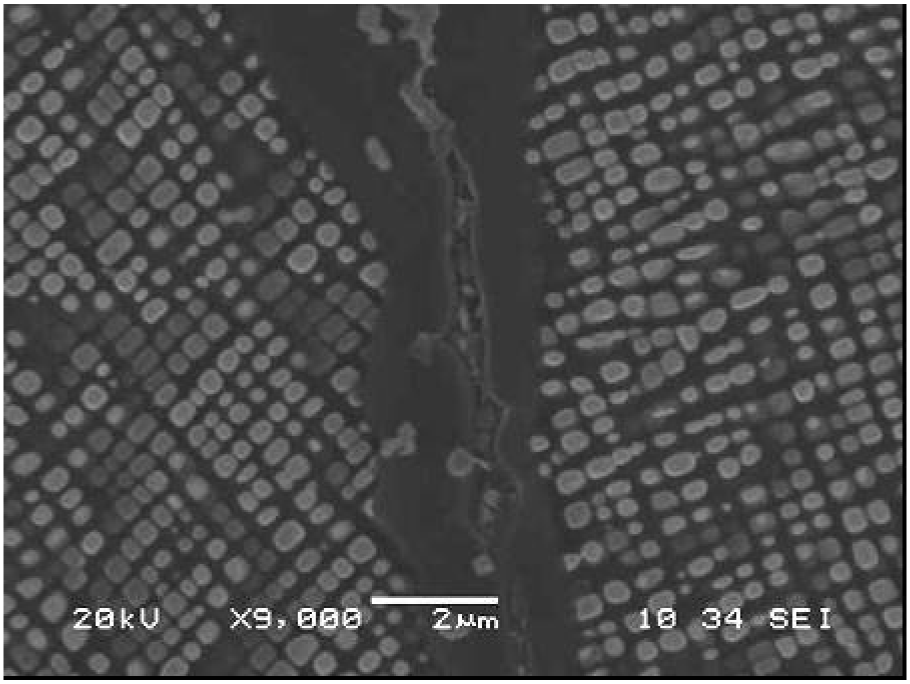

Figure 43: Liquated grain boundary from re-solidification in René 80

Under high magnification on the SEM, the fusion zone microstructure was that of cellular dendritic solidification with fine carbide segregation to the cell edges similar to that of Inconel 738 specimens. Figure 44 is an SEM image of the weld fusion zone showing the distribution of ultra-fine carbide particles. Due to being relatively small, the carbides could not be analyzed for semi-quantitative chemical composition analysis but were concluded to be Ta, Ti and Nb rich due to elemental segregation to the interdendritic regions. Dilution between the weld fusion zone and base material alloys was negligible, and the observed MC carbides are of similar composition those analyzed in the Inconel 738 base material. Table 11 lists the results of EDS map scans taken over large areas of the weld fusion zone. The results are very similar for the weld fusion zone EDS analysis on Inconel 738 (Table 9) and the certification of analysis provided by the powder supplier (Table 4), confirming that weld fusion zone dilution with the base material is negligible.

Element	**Weight%**	**Atomic%**
Al	3.19	6.84
Ti	3.99	4.82
Cr	16.02	17.83
Co	8.47	8.32
Ni	58.83	58.00
Zr	0.44	0.28
Nb	1.01	0.63
Mo	2.52	1.52
Hf	0.35	0.11
Ta	1.54	0.49
W	3.65	1.15

Table 11: Fusion zone bulk EDS analysis

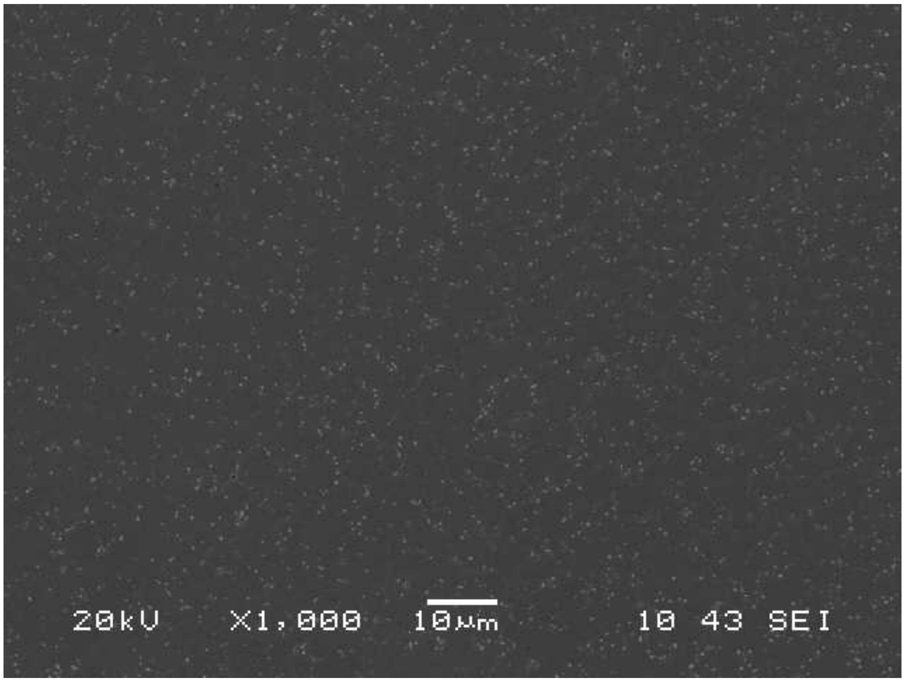

Figure 44: SEM image of fusion zone, as welded condition

The gamma prime phase was compared in the non-heat affected zone region of the parent material in dendrite cores and the interdendritic regions. In the over-aged heat treated (UMT) condition there was no appreciable difference in gamma prime morphology between the two regions. As shown in Figures 45 and 46, both regions exhibited cube shaped particles that were measured to be 0.28 µm in size. The UMT (solution + over-aging) heat treatment provided a uniform microstructure in terms of the morphology and size of the γ' precipitated strengthening phase.

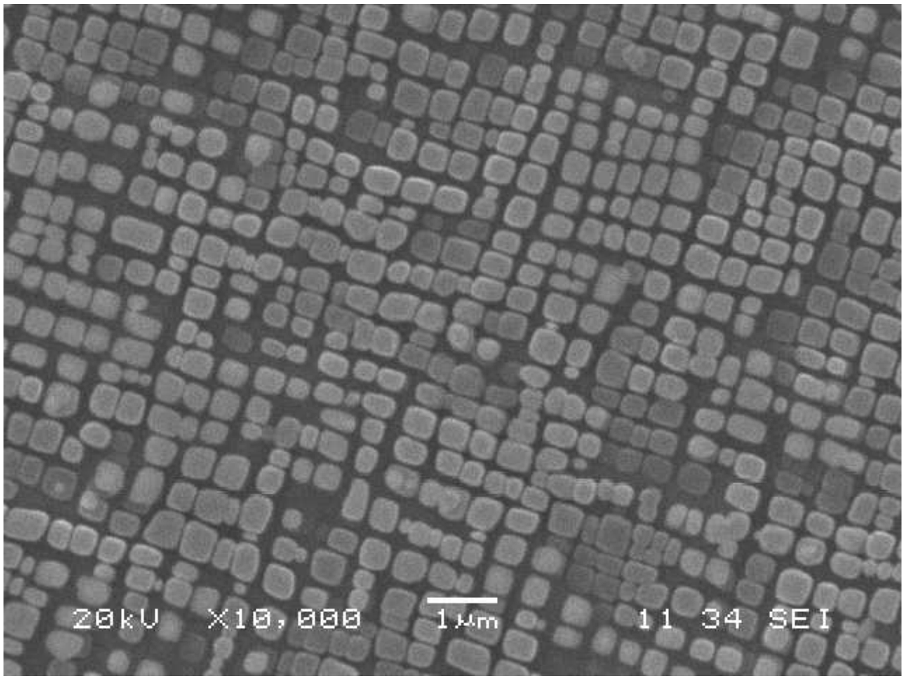

Figure 45: Gamma prime in the dendrite core region of René 80 (UMT condition)

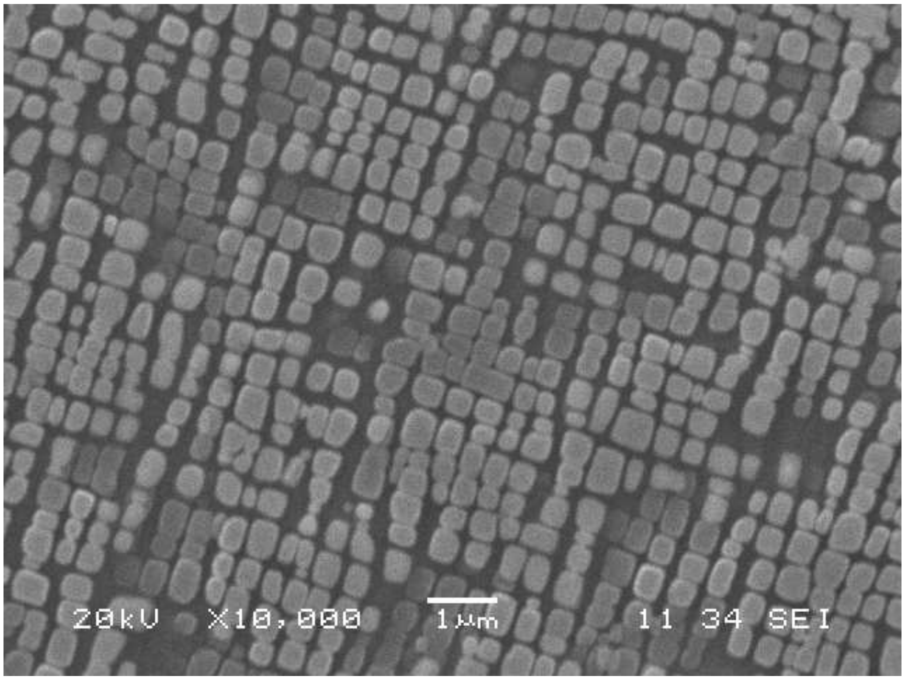

Figure 46: Gamma prime in the interdendritic region of René 80 (UMT condition)

MC carbides throughout the microstructure were examined using the SEM in backscatter electron imaging mode. As shown in Figure 47, a blocky MC carbide particle is surrounded by discrete particles of lighter shade, indicating an increase in mean atomic number relative to the adjacent MC carbide and the γ /γ' prime parent material. EDS point analysis revealed that particles surrounding MC carbides were rich in boron, chromium and molybdenum. The size, morphology and distribution of these particles along with the marked increase in concentration of boride forming elements, confirms they are Cr-Mo rich borides and is in agreement with the results reported by Sidhu et al. [5] on René 80.

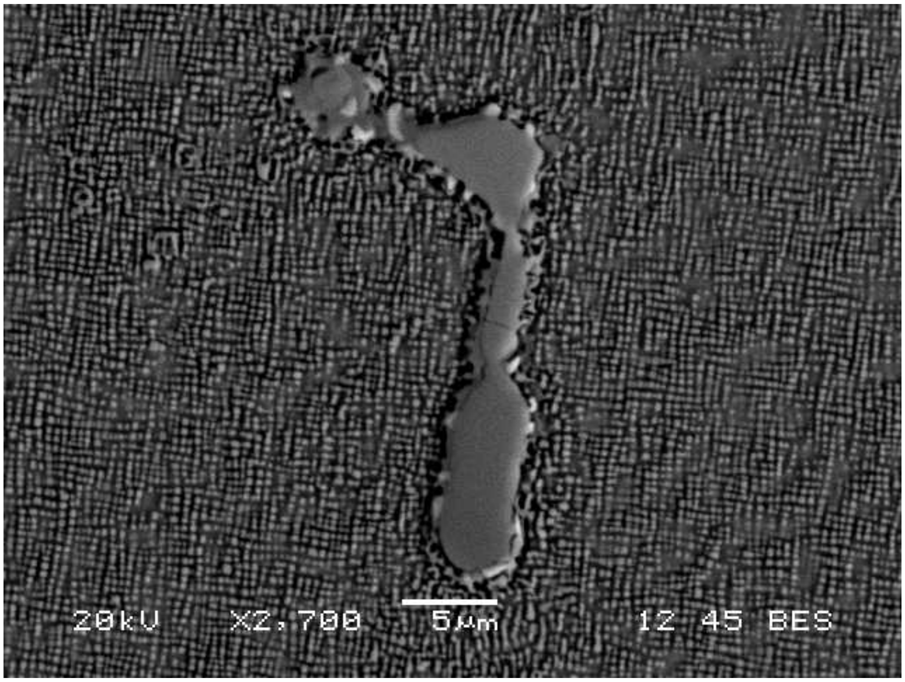

Figure 47: Boride phase on MC carbide in René 80 (as-welded UMT condition).

Element	Weight%	Atomic%
Al	0.4	0.8
Ti	52.8	72.9
Cr	1.3	1.7
Co	0.3	0.3
Ni	2.3	2.6
Zr	1.3	1.0
Nb	0.9	0.7
Mo	13.0	9.5
Hf	0.3	0.1
Ta	0.1	0.1
W	27.3	10.3

Table 12: Average chemical composition of MC carbides in René 80 (UMT condition)

5.3.3 René N5

Despite extensive LBW trials, weld defects were found in some of the specimens evaluated in this study. They involved a lack of fusion between laser weld build-up passes and centre-line cracking due to solidification shrinkage of the filler alloy. Figure 48 shows the typical region where lack of fusion with the parent material occurred. The laser welding parameters developed for the Inconel 738 powder and nickel based superalloy combination were selected based on successful trials where complete fusion was achieved while maintaining a minimal amount of heat input. This illustrates the sensitivity of this process to outside variables and factors that prevented complete fusion. During low heat input LBW, very little energy is transferred to the base material as compared to arc welding processes such as GTAW or PTAW. In LBW, a significant portion of the laser beam energy is absorbed by the powder that is fed axially in the beam path. Since laser radiation only penetrates metals to a very shallow depth, the energy transfer to the base material is by conduction from the molten weld puddle.

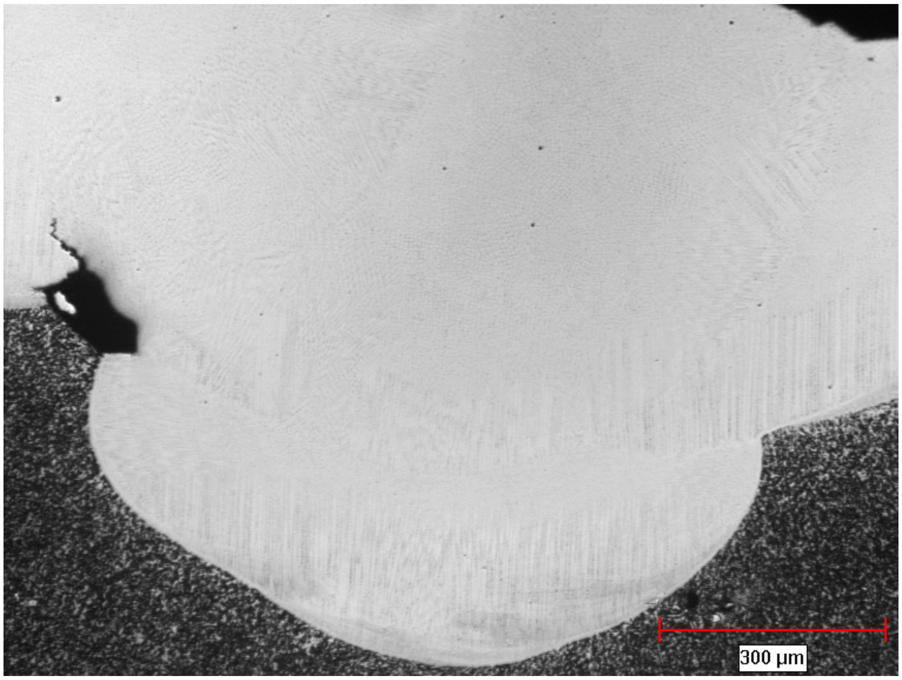

Figure 48: As-welded condition of IN738 filler on UMT René N5, MTU etchant.

Epitaxial growth of the fusion zone was aligned parallel to the axis of thermal gradient between the weld pool and substrate at base of the v-preparation. On the weld edges, near the specimen's surface, the solidification direction is perpendicular to that of the bottom of v-groove, indicating preferred growth parallel to the local thermal gradient. Figures 49 and 50 are optical micrographs showing the transition from epitaxial cellular and dendritic solidification structures in the weld fusion zone.

Stray grains were observed in all weld deposits (all base materials) appearing in the upper portion of the fusion zone (weld cap) and were surrounded by an epitaxial columnar solidification structure. Typical stray grains observed in the weld fusion zone are shown in the upper left portion of Figure 49. Similar to the laser welds in Inconel 738 and René 80 alloys, there were no cracks associated with the presence of stray grains in the welds.

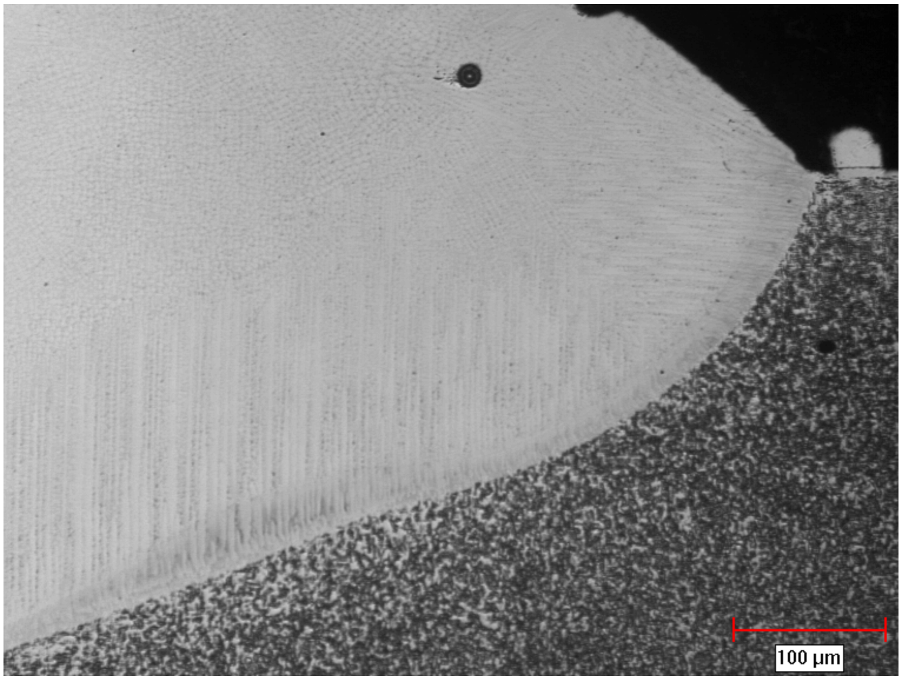

Figure 49: Epitaxial growth and stray grain formation in the fusion zone of René N5, MTU etchant

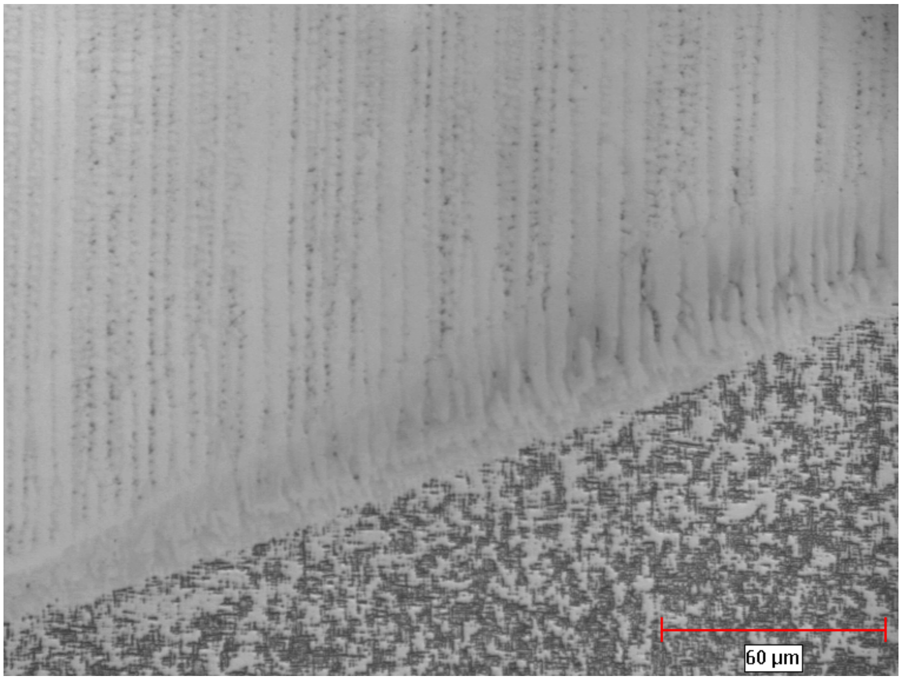

Figure 50: Cellular and dendritic solidification in the weld fusion zone, René N5 base alloy, MTU etchant

As shown in Figure 50, the fusion zone underwent a change from a cellular to dendritic solidification structure near the parent material interface as a result of thermal gradient change over the course of weld pool solidification. Centreline cracking as a result of fusion zone shrinkage after solidification was observed in one specimen and is shown in Figure 51. The crack was contained to the weld fusion zone and was aligned parallel to the primary dendrite trunks, along the solidification direction. High magnification examination on the SEM revealed a cellular dendritic microstructure in the fusion zone.

As shown in Figure 52, MC carbides formed along interdendritic regions in the weld fusion zone. EDS was used to analyze the metallic constituents of the carbide phase present in the fusion zone and it was determined to mainly be tantalum. EDS analysis results are summarized in Table 15 and are in agreement with the findings of Sidhu [4].

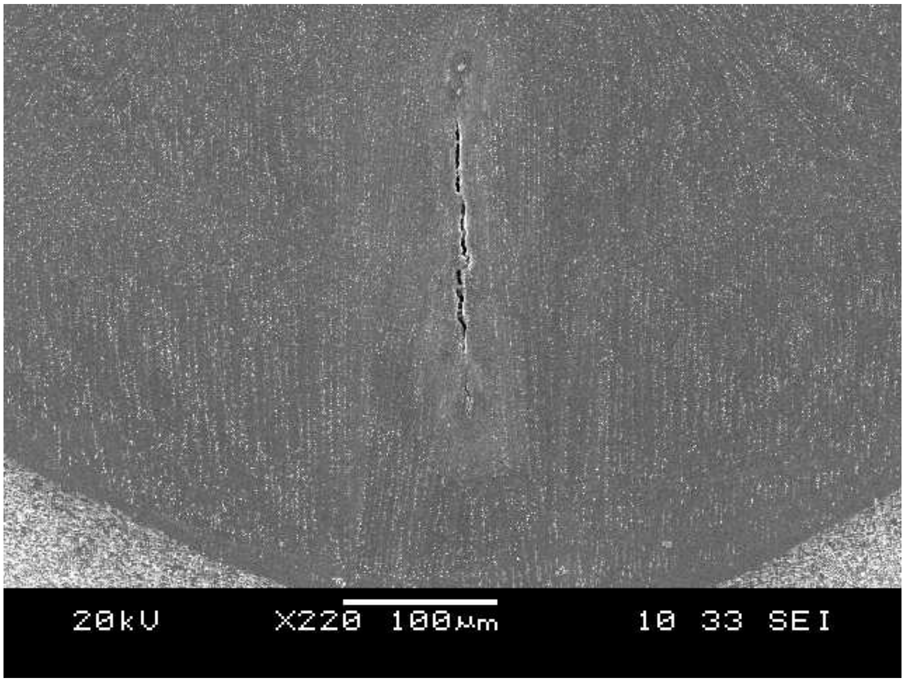

Figure 51: Centerline cracking in fusion zone of a René N5 weld, γ' etchant.

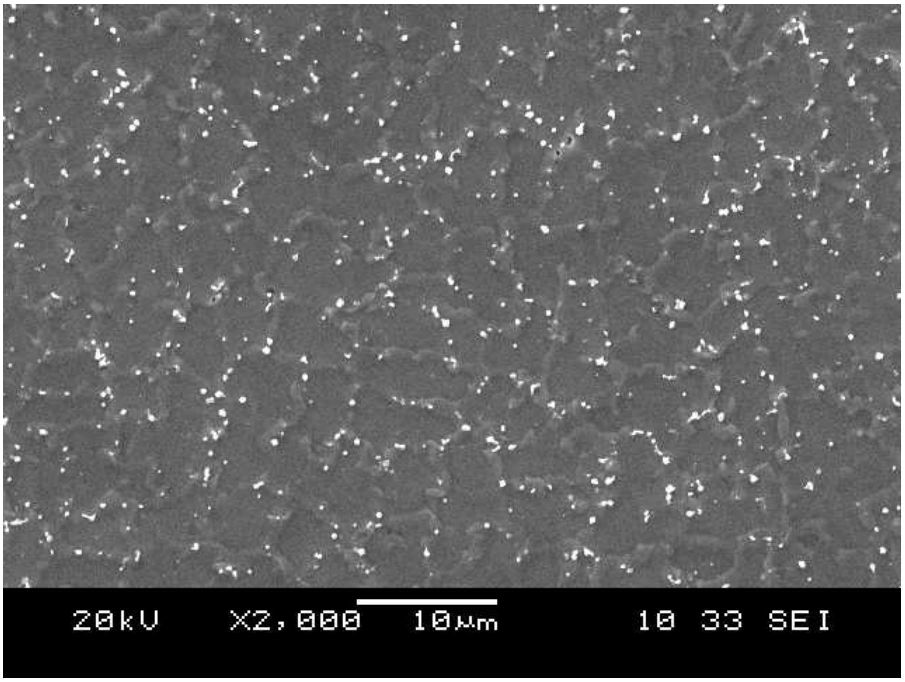

Figure 52: Cellular dendrite fusion zone microstructure, γ' etchant.

Figure 53 is an SEM image showing the morphological change of γ' along the fusion zone to parent material interface. The γ' particles show evidence of having undergone melting along the solid-liquid interface. In the molten alloy, a cellular solidification structure was observed and tended to grow directly from the partially liquated γ' layer. The cellular solidification structure extended for 10 to 20 µm from the solid-liquid interface and changed to a dendritic structure for the remaining solidification until overtaken by stray grains in the weld pool.

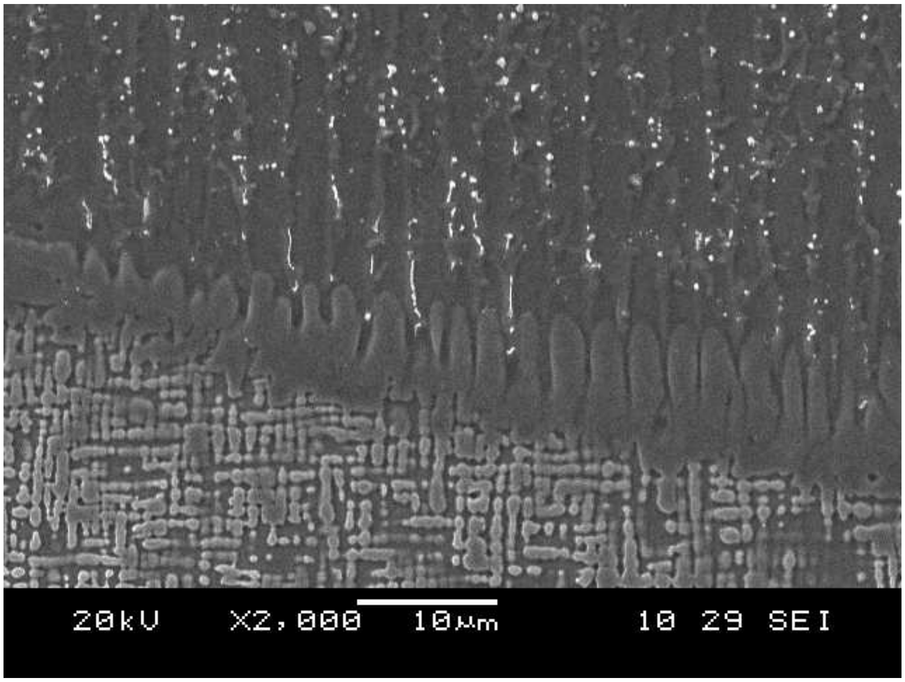

Figure 53: Fusion zone interface showing transition from cellular to dendritic solidification structures, gamma prime etchant.

Using the SEM image analysis tool, several measurements of γ' particles were taken in the specimen axial and transverse directions. In the heat affected zone, the average γ' dimension was 1.0 µm (st. dev 0.2 µm) as compared to 1.3 µm in the non-HAZ regions of the base material. In the weld heat affected zone, the secondary γ' particles were fully dissolved while the primary γ' underwent partial dissolution, accounting for the measured reduction in particle size. Refer to Figure 54 for an SEM image showing the morphological and size changes in the weld heat affected zone. In the base material non-HAZ material, the γ' phase is bimodal having large spherical primary γ' with fine secondary γ' in the surrounding regions. See Figure 55 for an SEM image of the René N5 base material in the over-aged heat treated condition (non-heat affected zone).

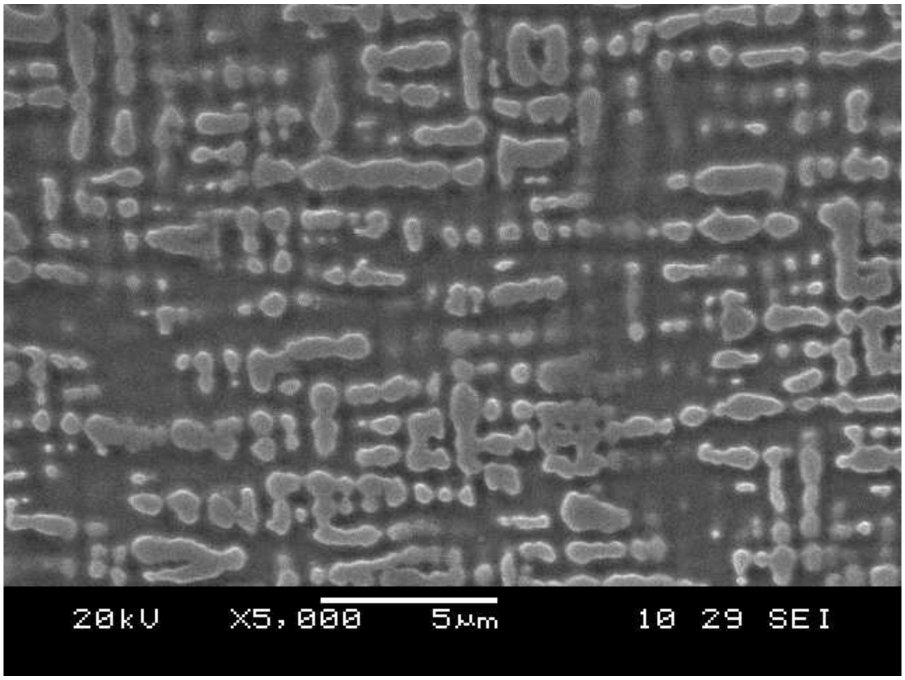

Figure 54: SEM image of γ’ in the weld heat affected zone of René N5, as-welded condition

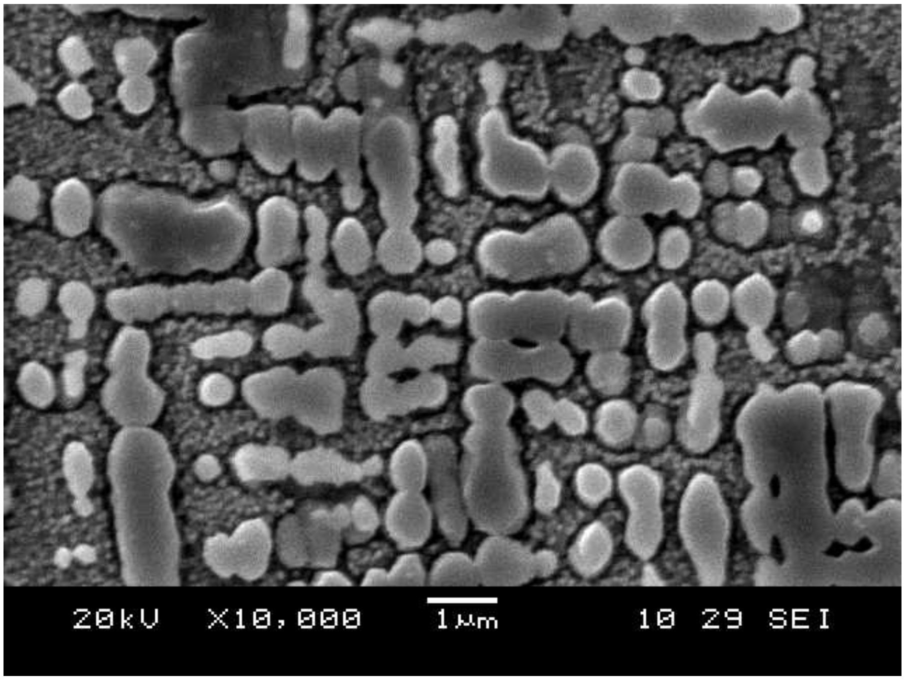

Figure 55: SEM image of the γ’ in the non-HAZ region of the base material.

Energy dispersive spectroscopy was used to assess the chemical composition of the weld fusion zone and heat affected zone with the results being summarized in Tables 13, 14, 15 and 16.

Element	Weight%	Atomic%
Al	4.71	10.12
Ti	2.03	2.45
Cr	13.13	14.63
Co	8.15	8.01
Ni	61.42	60.62
Zr	0.28	0.18
Nb	0.55	0.34
Mo	1.93	1.17
Hf	0.13	0.04
Ta	2.98	0.96
W	4.69	1.48

Table 13: EDS map scan analysis of the fusion zone, Praxair Ni-284-1 (Inconel 738) powder

Element	Weight%	Atomic%
Al	7.05	15.20
Ti	0.01	0.01
Cr	6.96	7.78
Co	7.82	7.72
Ni	65.76	65.15
Mo	1.18	0.71
Ta	6.52	2.09
W	5.42	1.72

Table 14: EDS map scan analysis of weld HAZ in René N5

Element	Weight%	Atomic%
Ti	0.37	1.19
Cr	0.66	2.00
Co	0.79	2.10
Ni	4.25	11.33
Zr	1.35	2.31
Nb	0.35	0.59
Mo	1.28	2.08
Hf	6.16	5.40
Ta	85.07	73.52

Table 15: EDS point analysis of metallic constituents in MC carbides in fusion zone of René N5 alloy, near the fusion interface

5.3.4 Discussion of Results for the As-Welded Condition of the Weld Fusion Zone

Extensive weld trials were conducted in order to develop laser welding process parameters capable of fusing the Ni-284-1 (Inconel 738 equivalent) powder to the v-notch prepared specimens while minimizing heat input. Several rounds of trials were carried out, each followed by a metallographic assessment of the weld quality until acceptable parameters were achieved (see Appendix E for a summary of laser welding trials).

As discussed in the preceding sections, a lack of fusion defect was found at the interface region between weld passes and the base material v-notch. In general welding practice, increasing the beam power will reduce or possibly eliminate the lack of fusion condition but would increase the heat input to the base material. Therefore, it is reasonable that a sufficient increase in heat input via higher laser beam power would eventually provide heat to the base material comparable to GTAW and lead to grain boundary liquation cracking.

In all laser welds, the solidification microstructure was initially cellular along the base material interface, changed to epitaxial-dendritic followed by stray grains in the core and upper portions of the weld pool. For all three materials, whether in equiaxed, directionally solidified or single crystal alloy form, epitaxial growth was achieved along the direction of the thermal gradient and the local base material crystallographic orientation was maintained. The solidification structure changed as a function constitutional undercooling ahead of the solidification front in the weld pool. Vitek [6] has shown that welding parameters can be controlled such that epitaxial growth in a power beam weld can be maintained while preventing the formation of stray grains. In a later paper, Mokadem [7] extends the analysis to account for off-axis dendritic growth and its effect on stray grain formation. The work by Mokadem shows that off-axis growth adversely affects the G/V ratio and leads to a greater fraction of stray grain formation in the weld. The revised equation for off-axis columnar growth is as follows:

$$\frac{G^n}{V_{iso}} = (\cos \Psi)^{n+1} \geq K_{CET}$$

Where G is the thermal gradient at the solid/liquid interface, V_{iso} is the velocity perpendicular to the solidification front, Ψ is the angle between the dendritic growth and the heat flow axis, n is a material constant of 3.4 for René N5, as reported by Vitek [6].

$$K_{CET} = a \left\{ \left[\frac{-4\pi N_o}{3 \ln(1-\phi_c)} \right]^{1/3} \frac{\Delta T_o}{n+1} \right\}^n$$

where a is a material constant (1.25×10^6 s $K^{3.4} m^{-1}$ for René N5), N_o is the nucleation site density, ΔT_o is the equilibrium liquidus-solidus temperature interval.

Both research groups concluded that the rate of stray grain formation can be reduced by reducing the weld solidification rate by decreasing the weld speed and using lower beam power. The effect of off-axis solidification has been illustrated to increase stray grain formation with increasing values of Ψ.

The beam power used in this thesis was 615 Watts with a welding speed of 6.4 mm/sec. Also, the weld deposit was applied in four consecutive passes with little time for cooling between passes, likely causing a pre-heat effect in the weld specimen for the next weld pass. Therefore, the first weld pass experienced the greatest degree of temperature difference between the base material (room temperature) and the weld pool. The G term was at its highest value for the first weld pass providing conditions least favourable for stray grain formation. The residual heat input from the first weld pass provided a pre-heating effect for the second weld pass and will decrease the G term, favouring the formation of stray grains in the fusion zone. Similarly, the third and fourth weld passes were affected by the pre-heating effect of previous weld passes.

As shown in the preceding sections for Inconel 738 and René 80, weld passes 1, 2 and 3 exhibit epitaxial solidification structures both in parallel and off-axis orientations with respect to the weld beam. For both alloys, the epitaxial solidification structure is overtaken by stray grains in the weld deposit core and upper region (cap). The fourth weld deposit was not readily discernable from the first weld pass as it appears to be completely made up of stray grains. The optical micrographs also suggest significant re-melting of the first weld pass deposit by the fourth weld pass.

The René N5 weld deposit showed similar behaviour with the exception that the epitaxial growth in weld passes 1, 2 and 3 was significantly more pronounced, accounting for approximately half the weld deposit volume. Stray grains dominated the upper (cap) regions of weld deposits 1, 2 and 3 similar to the Inconel 738 and René 80 welds. Also, the fourth weld pass in the René N5 weld deposit was nearly all stray grains.

Based on the research by Vitek [6] and Mokadem [7], the parameters for the welds performed in this study would require an increase in the thermal gradient (G) term along with a decrease in the solidification front velocity (V). This suggests increasing the laser beam power and decreasing the weld speed. Also, since the weld deposit was made up of four consecutive build-passes, sufficient time and cooling must be allowed in order to eliminate the pre-heating effect of preceding weld passes such that the thermal gradient is altered and begins to favour stray formation.

Despite showing extensive stray grain formation it the weld fusion zone, only one of specimens (René N5) exhibited a solidification crack during cooling from the weld thermal cycle. Interestingly, the crack occurred in the epitaxial dendritic solidification region of the first weld pass in the René N5 specimen. During the cooling portion of the weld thermal cycle, sufficient stresses were present and acting on the weld fusion zone imparting tensile stresses perpendicular to the dendritic solidification structure and caused the crack measuring 180 μm in length. Generally, thermal stresses in welds are reduced by pre-heating the base material or by reducing the heat input of the weld process. As discussed, both pre-heating and reducing the heat input during welding will decrease the thermal gradient (G) and favour the formation of stray grains in the weld fusion zone. Clearly, the control of microstructure response under a fixed weld geometry/configuration is highly complex and optimization for crack free and completely epitaxial welds requires additional extensive work such that process maps are devised for each case. Finally, despite the extensive stray grain formation in the welds, there were no cracks along grain boundaries.

For all three alloys, the fusion zone along the base material interface was of a cellular solidification structure. The initial solidification structure was directly affected by the local condition between the base material and molten weld pool. The SEM image shown in Figure 53 reveals that the initial solidification structure was of the cellular type (cells) during the onset of solidification up to a range of distance of 5 to 10 μm from the interface. During the initial stage of solidification, the rate of solidification was at it's lowest due to thermal effects (heat input from the weld pass is localized in the fusion zone and underlying substrate). Upon further solidification distance, the velocity of the solidification front increases and the structure change to dendritic as a result of change in the G/R ratio [51]. Referring to Figure 56 below, the solidification structure observed in the laser welds begins in the lower right region of the diagram and moves toward the center. Accordingly, the solidification structure changes from planar to cellular, dendritic and equiaxed dendritic (stray grains) as the thermal gradient G decreases and the growth rate V increases.

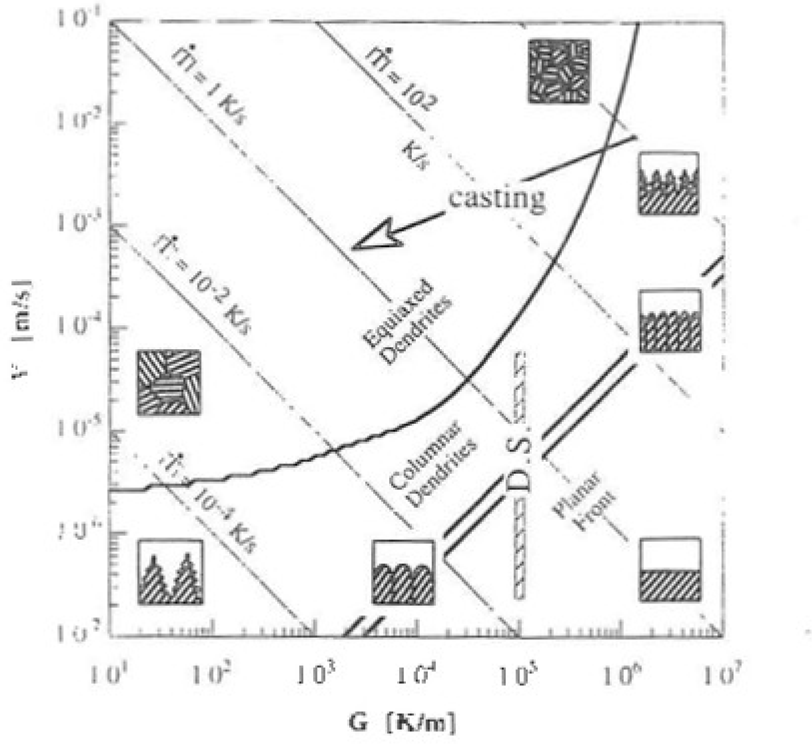

Figure 56: Solidification profile for structures. © Used with permission by Trans Tech Publications [60].

5.3.4.1 Weld heat affected zone

The over-aging pre-weld heat treatment applied to Inconel 738 in conjunction with the relatively low heat input of the laser welds produced deposits that were nearly crack-free. One grain boundary in an Inconel 738 specimen was observed to have a crack in the weld heat affected zone along a grain boundary. High magnification examination of the crack revealed the nature of the crack was as a result of grain boundary liquation of the γ' phase. No other phases were observed to be associated with the liquation and subsequent cracking during the cooling portion of the weld thermal cycle. The crack only extended to a total length of 78 μm beyond which there was liquation of the grain boundary. Other grain boundaries along the fusion zone underwent liquation but did not experience cracking. Similarly, the René 80 specimens showed evidence of grain boundary liquation in the heat affected zone and complete absence of cracks. The René N5 specimens, having a single crystal microstructure with no grain boundaries, did not experience grain boundary liquation and were free of cracks in the weld heat affected zone and fusion zone.

The pre-weld heat treatment reduced the base material hardness of Inconel 738 and René 80 by 10 and 32 Vickers Hardness respectively, from the as-received solution treated condition. The work carried out by Thakur et al. [1] developed a pre-weld heat treatment for Inconel 738 which (1) reduced the material hardness, (2) formed discrete carbide particles in lieu of a continuous film along grain boundaries and (3) changed the grain boundaries from planar to serrated. As shown in Figure 23, the optical micrographs for Inconel 738 in the over-aged (UMT) conditions show the discrete carbide particles along serrated type grain boundaries. Therefore the combination of changing the material susceptibility to heat affected zone cracking with the use of a low heat input process provided a significant improvement in the weldability of Inconel 738 and René 80 in comparison to previous work done by Sidhu et al. [4, 5] on the same alloys. The principal difference between the previous studies and the present research is the significantly reduced heat input of the laser beam welding process employed.

Although the weld heat affected zone grain boundary liquation cracking phenomena has largely been eliminated by the low heat input of the laser beam welds carried in the present study, sufficient heat is applied to the base material such that γ’ liquates along grain boundaries. The over-aging heat treatment reduced material hardness, changed the grain boundary shape and changed carbide into discrete particles. This unfortunately leaves the carbides, γ’ and other low melting point phases present along grain boundaries susceptible to liquation and potentially cracking under sufficient tensile stresses during weld cooling. Further reduction in weld heat affected zone cracking may be realized by pre-heating the base material prior to welding but this will reduce the thermal gradient at the solidification front and further promote the formation of equiaxed dendrites (stray grains) in the weld fusion zone. Therefore, a reduction in HAZ cracking would likely come at the expense of weld fusion zone mechanical properties by allowing stray gain formation while using a weld pre-heat approach. Further experimentation using a range of beam power and weld speed are required in order to (1) satisfactorily produce a weld deposit without stray grains and (2) and assess the resulting impact to the heat affected zone and minor phase liquation along grain boundaries.

5.4 POST-WELD HEAT TREATED CONDITION

5.4.1 Inconel 738

After undergoing the solution and ageing post-weld heat treatment, the fusion zone maintained the mixture of epitaxial columnar and dendritic solidification structures. Throughout the weld fusion zone, the equiaxed dendrites (stray grains) were of comparable size and distribution as was observed in the as-welded condition. Figure 57 shows the post-weld heat treated (STA) microstructure of a Inconel 738 thermo-mechanical fatigue specimen prior to testing. No heat treatment related cracking was visible along the grain boundaries intersected by the fusion zone or within the weld fusion zone. A typical grain boundary intersection with the fusion zone is shown in Figure 58.

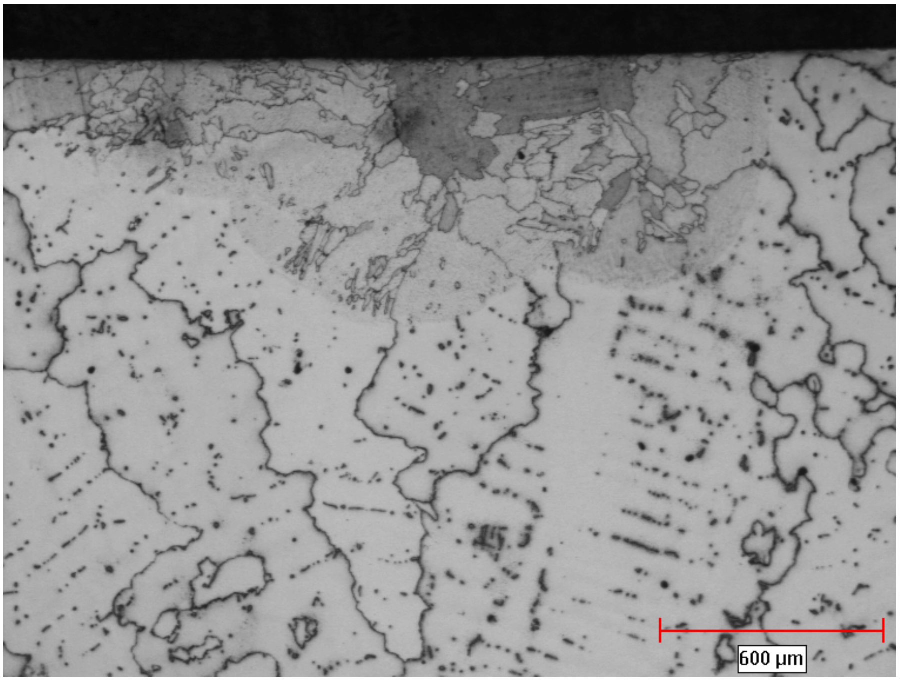

Figure 57: Optical micrograph showing the weld cross-section of Inconel 738, post-welded heat treated condition

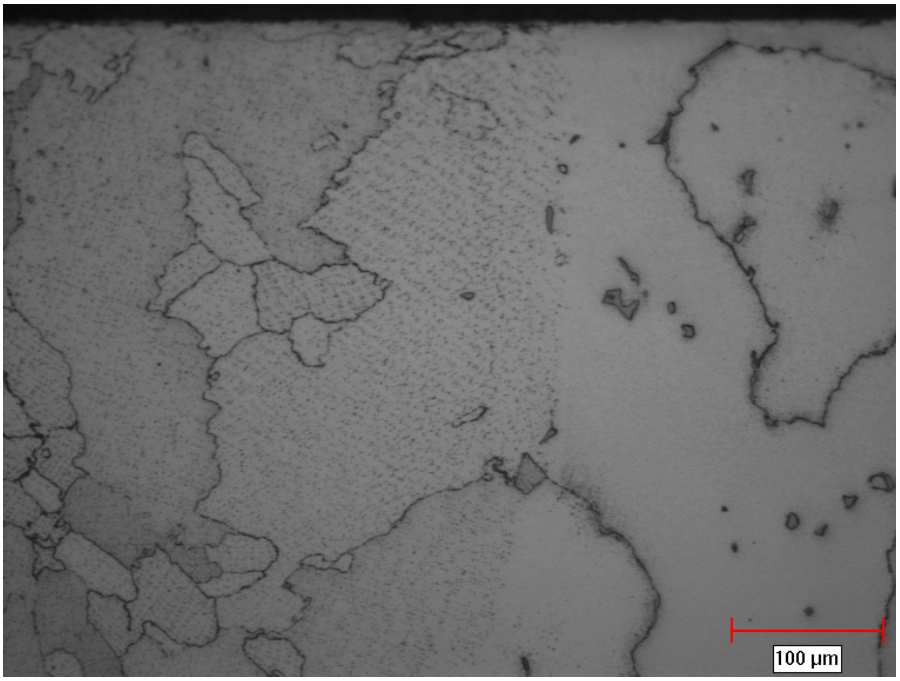

Figure 58: Optical micrograph of weld fusion zone (left) and base material (right) in Inconel 738, post-weld heat treated condition

SEM examination of γ' in the weld fusion microstructure revealed a predominantly spherical morphology 0.5 µm in size, shown in Figure 59. Coarse γ' particles were present along grain boundaries in the fusion zone.

In the base material, the γ' morphology was bimodal, consisting of primary γ' as diced cubes 1.0 to 1.5 µm in size with a fine dispersion of secondary γ' as shown in Figure 60. There was no appreciable difference in the size and morphology of γ' in the HAZ and non-HAZ regions of the base material.

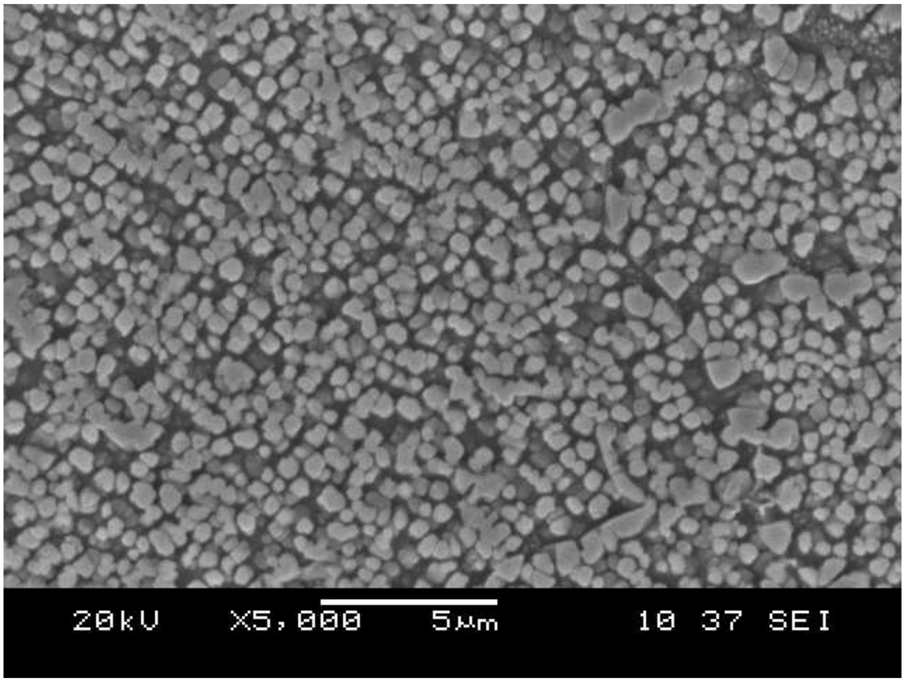

Figure 59: Fusion zone gamma prime in PWHT Inconel 738 specimen

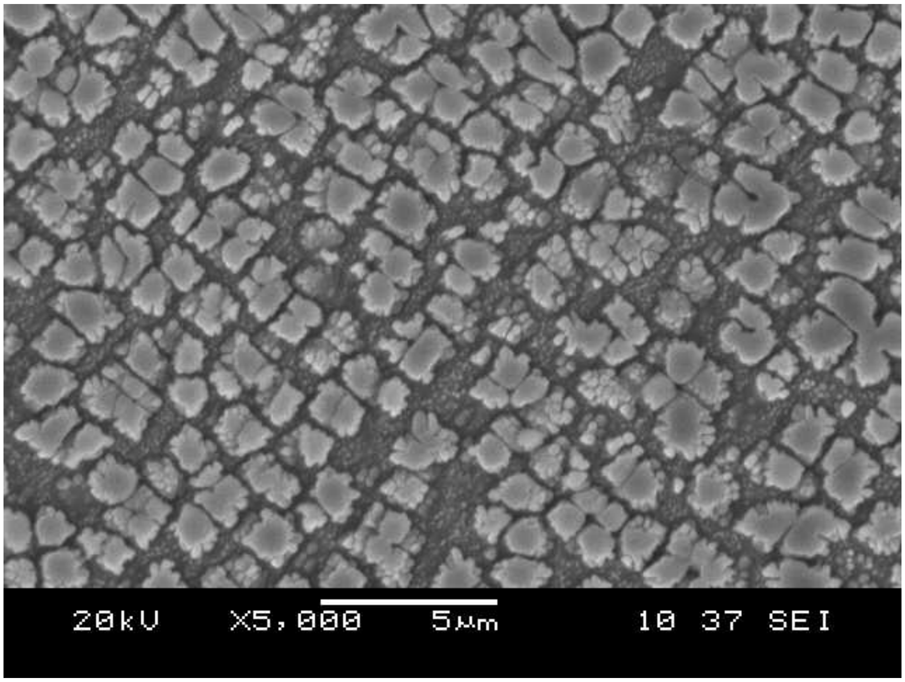

Figure 60: Gamma prime morphology in Inconel 738 base alloy taken in dendritic core locations (non-HAZ)

The interface between the fusion zone and base material was discernible by contrast in the size and shape of γ' in the microstructure. Figure 61 is an SEM image of the weld fusion zone to heat affected zone interface. Despite being similar in composition, the Inconel 738 base alloy and Praxair Ni-284-1 (Inconel 738 equivalent) powder show a vastly different aging response with finer γ' particles being formed in the Inconel 738 weld fusion zone during the post-weld heat treatment.

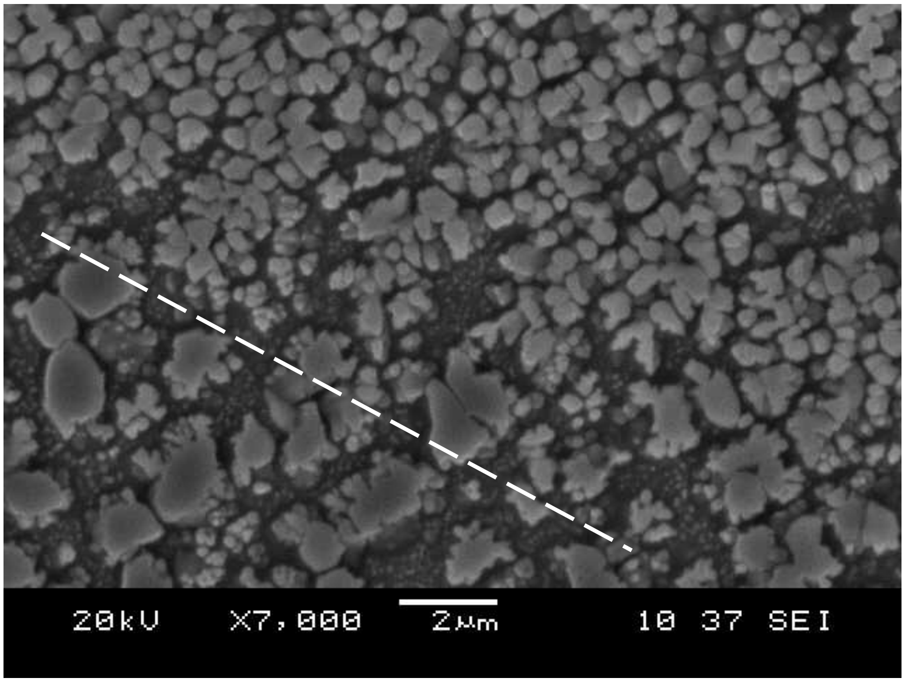

Figure 61: Fusion zone (top right) to parent material (lower left) interface in Inconel 738 base alloy

As discussed in the preceding section for the as-welded condition, carbide particles appeared as having been partially liquated and frozen in the solidified welding fusion zone microstructure. Figure 62 in an SEM image of a carbide phase particle spanning across the interface between fusion zone and base material. The gradient in brightness across the particle (dark core and lighter boundary) indicated a gradient in chemical composition of the particle (from core to its edges). Fine cuboidal gamma prime is visible around the perimeter of the carbide particle and illustrates the partial dissolution during the elevated temperature solution and aging treatment (STA). MC type carbides were analyzed by EDS and found to be rich in Ta, Ti and NB, consistent with MC type carbide in nickel base superalloys [56]. A summary of EDS analysis of carbide in the post-weld heat treated Inconel 738 is provided in Table 16.

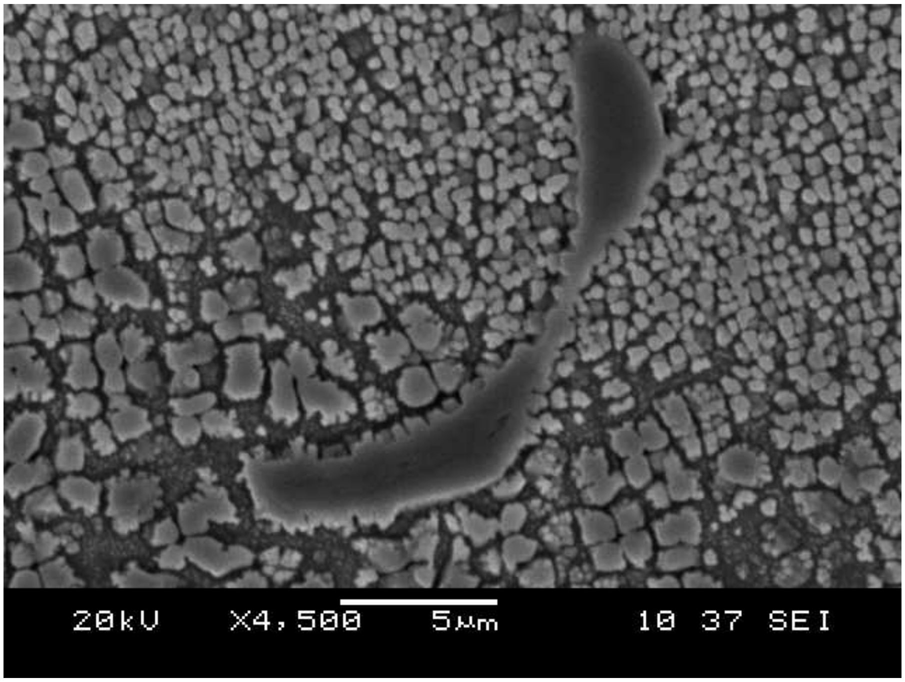

Figure 62: Carbide particle along fusion zone (top) and Inconel 738 parent material (bottom) interface.

Element	Weight%	Atomic%
Ti	25.3	47.6
Cr	0.8	1.3
Co	0.4	0.6
Ni	2.4	3.7
Nb	23.4	22.6
Mo	3.9	3.9
Hf	0.4	0.2
Ta	39.4	19.8
W	9.2	4.6

Table 16: Chemical composition of metallic constituents in carbides in non-HAZ region in PWHT Inconel 738

5.4.2 René 80

Examination of the weld microstructure in the post-weld heat treated condition revealed the presence of recrystallization in an area surrounding the weld fusion zone. As shown in Figure 63, the weld fusion zone appeared as a darker zone with the rounded profiles of three weld passes being visible. Within the fusion zone, a combination of epitaxially oriented grains and equiaxed stray grains make up the microstructure. In the heat affected zone regions surrounding the fusion zone, large recrystallized grains ranging from 300 to 500 μm in size were discernable from the base material microstructure. Higher magnification examination, as shown in Figure 64 shows good fusion with the parent material with no heat affected zone cracking along the newly formed grains boundaries. Under optical microscopy examination, the newly formed grain boundaries are generally linear in appearance, consisting of facet type interfaces between joining recrystallized grains.

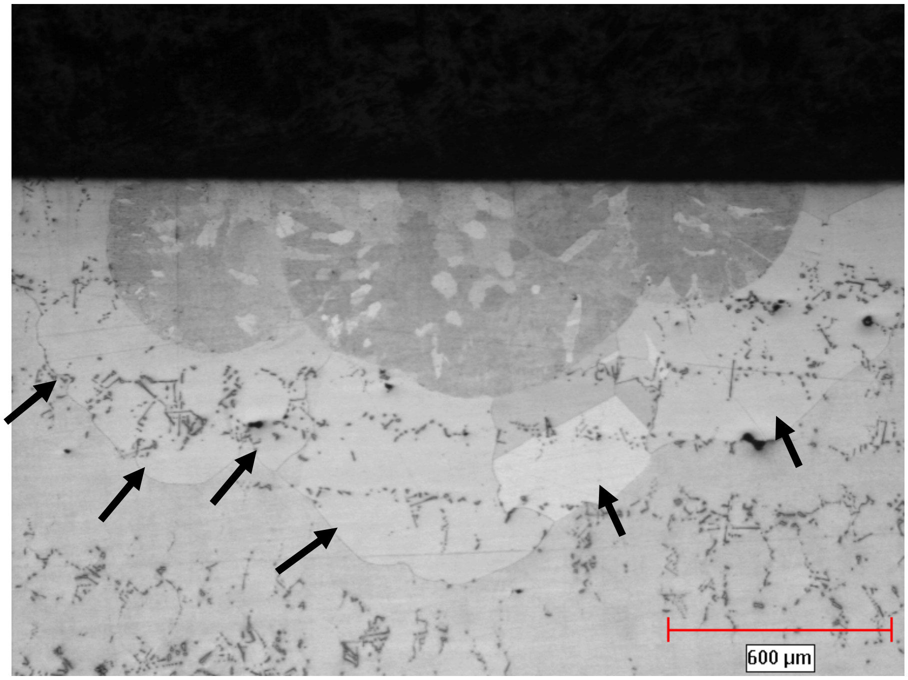

Figure 63: Optical micrograph of LBW in René 80 specimen in the post-weld heat treated condition

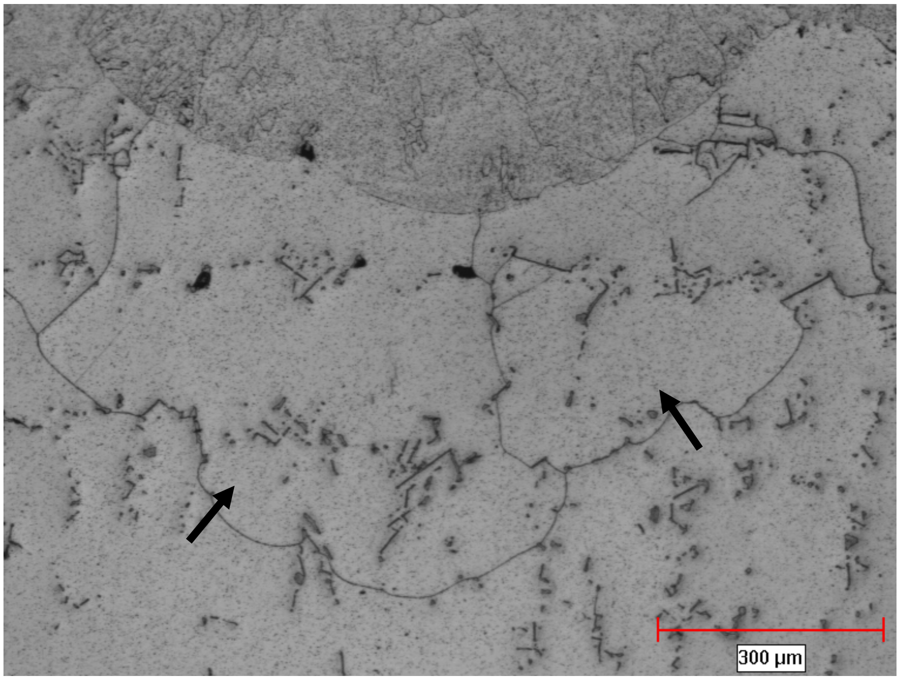

Figure 64: Optical micrograph of recrystallization grains at weld root of René 80 specimen (bottom of v-preparation).

Similar to the welds on Inconel 738 base material, SEM imaging of the weld fusion zone on René 80 showed a fine gamma prime of predominantly spherical shape less than 1 μm in size. Also, a coarse layer of γ’ was apparent along grain boundaries in the fusion zone and is shown in Figure 65.

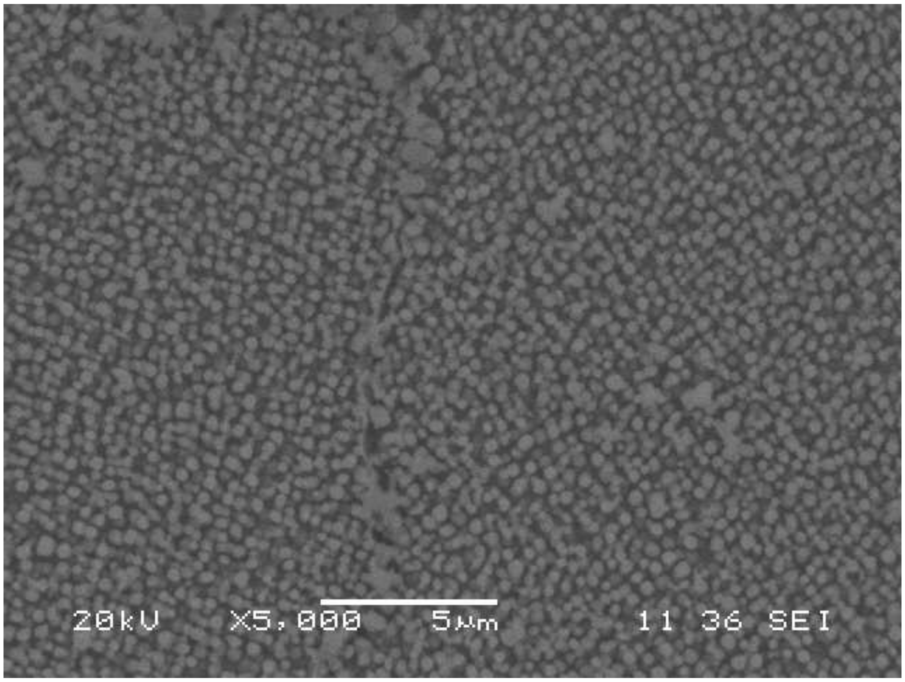

Figure 65: SEM image of γ’and grain boundary in the weld fusion zone, René 80 LBW specimen

The γ’ structure in the parent material non-heat affected zone microstructure was evaluated and determined to be cuboidal in morphology. The size distribution suggested a mild increase in size at the interdendritic regions over that of the dendrite cores. The size of gamma prime in the dendrite core was in the order of 0.2 to 0.3 μm and was in the range of 0.3 to 0.4 μm in the interdendritic regions and is shown in Figure 66.

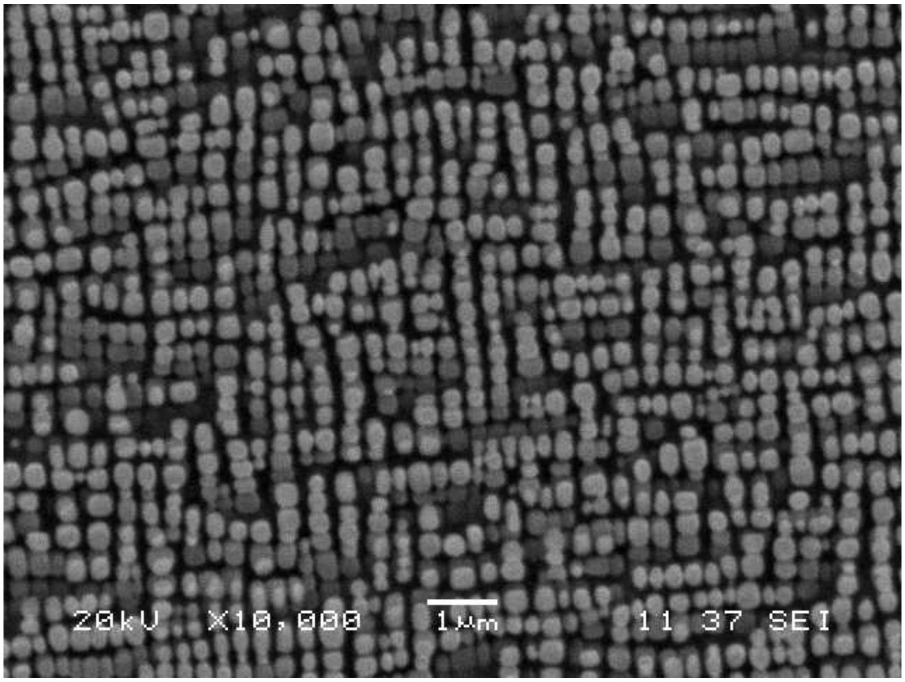

Figure 66: SEM image of typical γ' in René 80 base material, PWHT condition

Carbides in the parent material microstructure were examined by SEM and found to have undergone partial dissolution as a result of post-weld heat treatment. As shown in Figures 67, 68 and 69, γ' particles appear on the surface of grain boundary and grain boundary carbide particles. EDS analysis was conducted on a thick region of carbide dissolution along a grain boundary and as summarized in Table 17, the high concentration of titanium is consistent with MC carbides in nickel based superalloys [56]. Refer to Table 18 for EDS analysis of carbides in the non-HAZ regions of René 80 after PWHT.

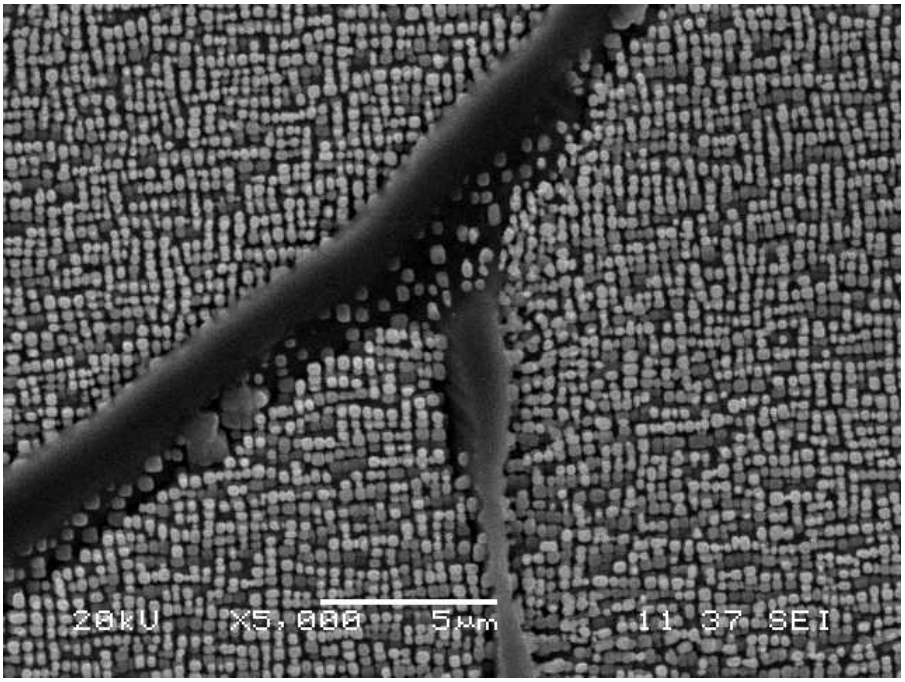

Figure 67: SEM image of carbide degeneration in along recrystallized grain boundary in PWHT René 80

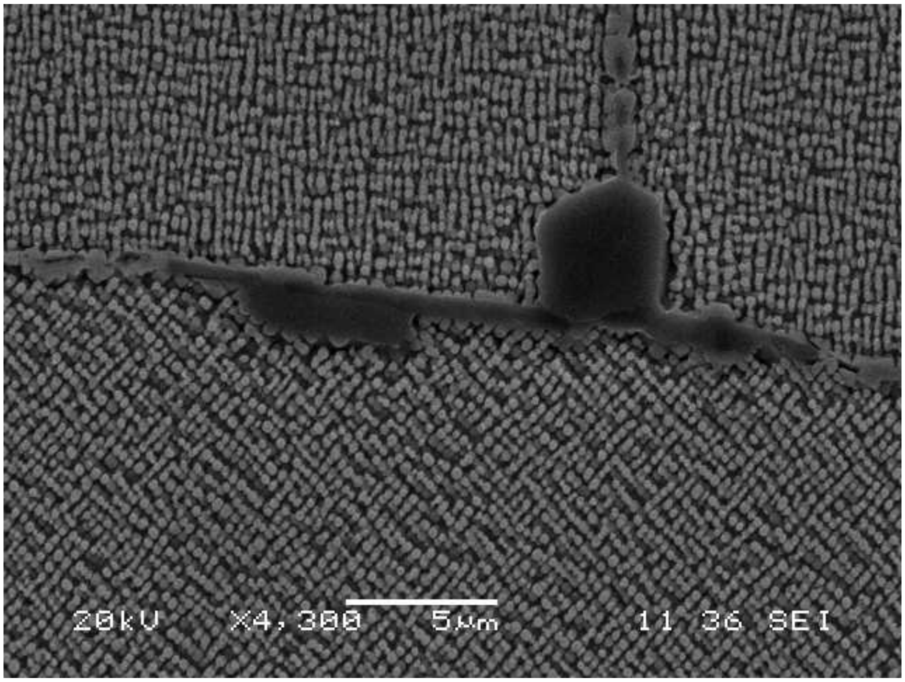

Figure 68: SEM image of recrystallized grain boundaries with carbide phase dissolution in PWHT René 80

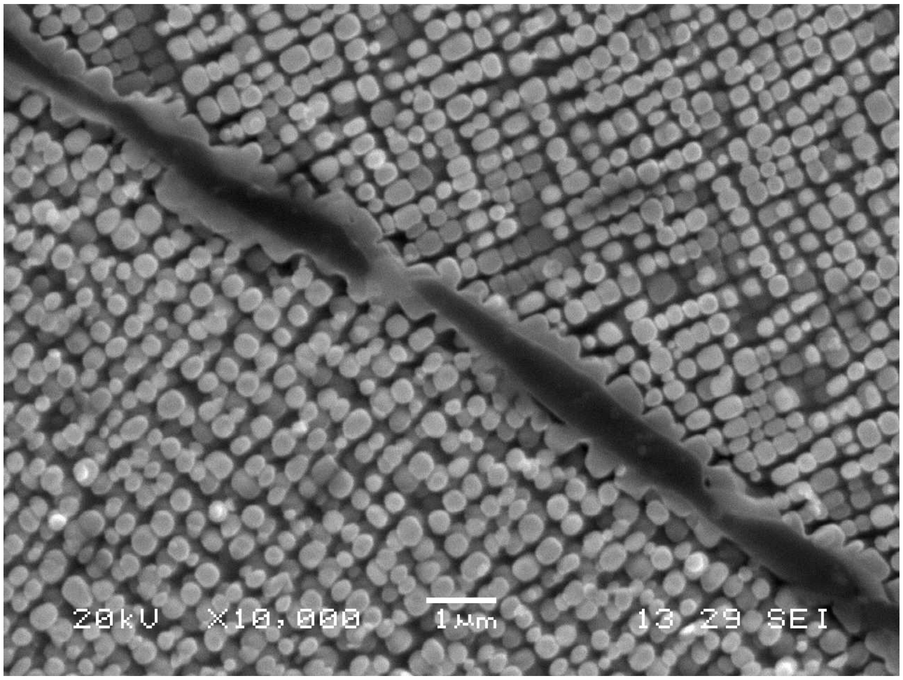

Figure 69: Carbide phase dissolution along recrystallized grain boundary in PWHT René 80

Element	Weight%	Atomic%
Al	0.95	2.24
Ti	29.21	38.73
Cr	5.92	7.23
Co	2.77	2.99
Ni	21.60	23.37
Zr	6.23	4.34
Nb	2.98	2.04
Mo	26.99	17.87
Hf	2.04	0.73
Ta	0.38	0.13
W	0.93	0.32

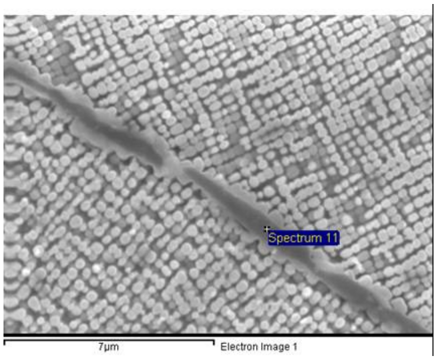

Table 17: SEM EDS point analysis of metallic constituents in a carbide film along a recrystallized grain boundary in René 80 HAZ

Element	Weight%	Atomic%
Al	0.1	0.4
Ti	40.9	62.1
Cr	2.5	3.5
Co	0.5	0.6
Ni	4.2	5.2
Zr	1.7	1.4
Nb	1.0	0.8
Mo	18.1	13.7
W	30.9	12.3

Table 18: SEM EDS analysis (average) of metallic constituents in carbides in René 80 parent material (PWHT condition)

The heat affected zone microstructure was analyzed by EDS along stray grain boundaries. As shown Figure 70, the boundaries of recrystallized grains in the fusion zone formed a coarse and porous layer of γ', as determined by EDS analysis. Refer to Appendices M and N for EDS linescans across the grain boundary between adjacent recrystallized grains in the René 80 base alloy.

A noteworthy observation in the weld heat affected zone recrystallized microstructure has been the formation of grain boundary twins. Figure 71 is an SEM image showing a twin grain boundary between two recrystallized grains in the weld heat affected zone. In contrast to other ‘normal’ grain boundaries in the weld microstructure, there are no carbides or other phases present along the twin boundary. Its formation is as a result of significantly high strain energy in the weld heat affected zone being released during the solution portion of the post-weld heat treatment.

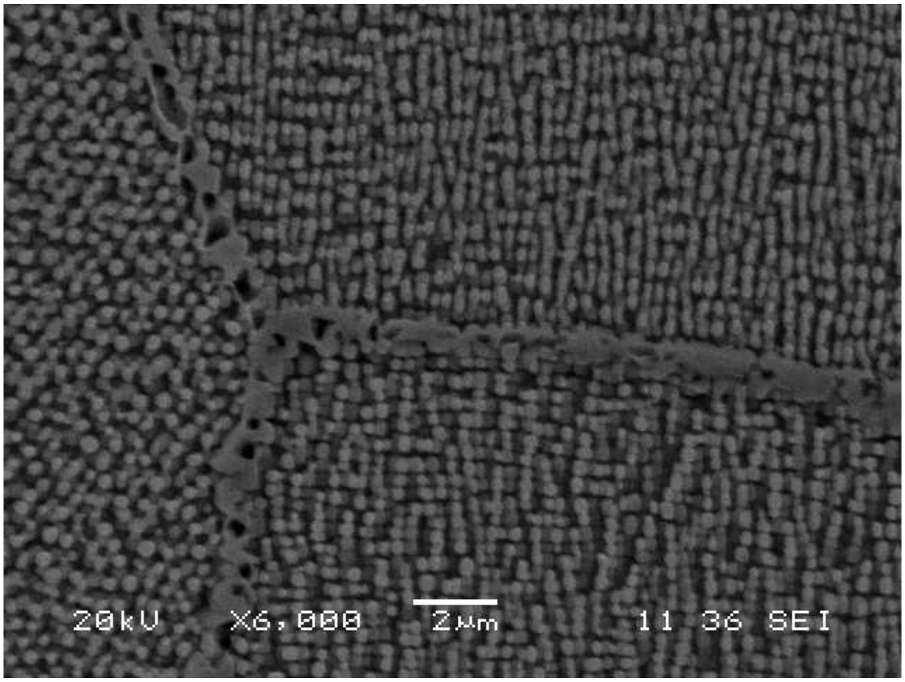

Figure 70: Recrystallized grain boundaries in PWHT René 80 HAZ

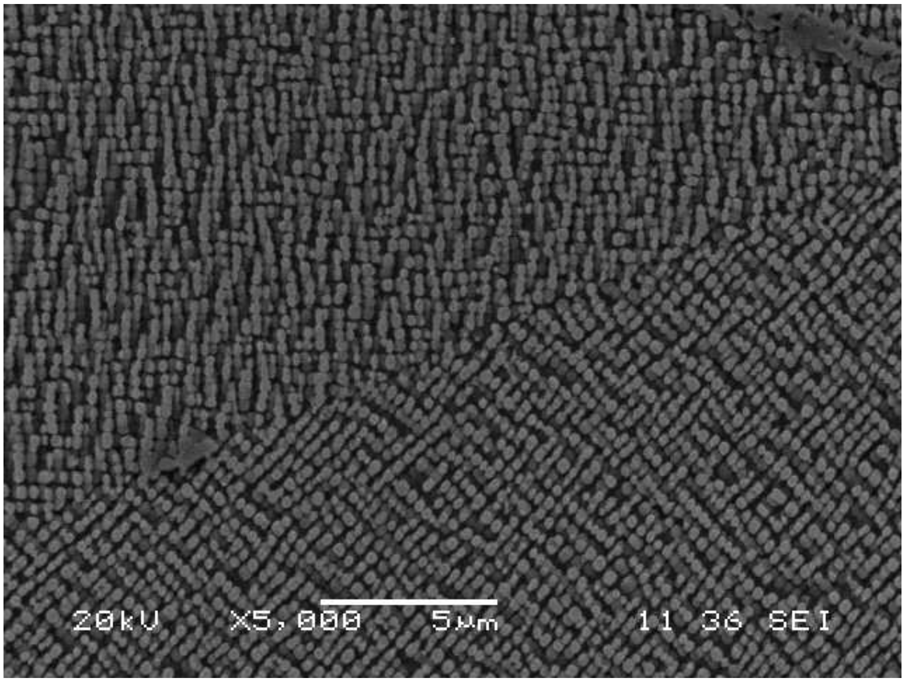

Figure 71: Grain boundary twin in the recrystallized zone of PWHT René 80

5.4.3 René N5

Examination of the weld heat affected zone in the solution treated and aged condition revealed a change in microstructure. As shown in Figure 72, recrystallized grains formed in the heat affected zone along the root of the weld (denoted by arrows). Examination at high magnification with the scanning electron microscope revealed a continuous and coherent layer of gamma prime completely surrounding each new grain. The gamma prime layer was relatively thick, in the order of approximately five times thicker than the average gamma prime particle size and exhibited a blocky/jagged edge structure against the neighbouring grains.

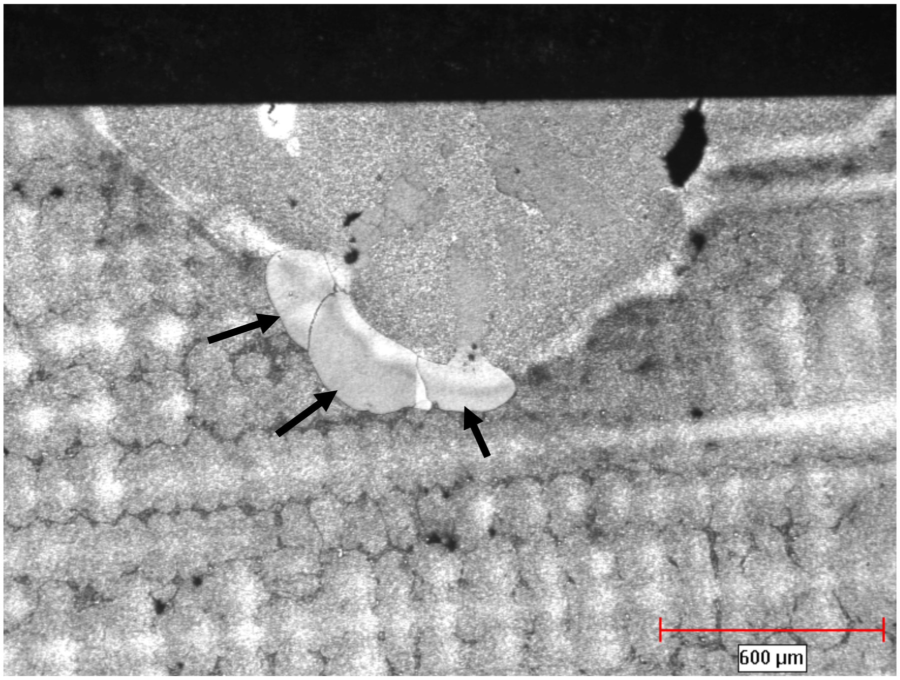

Figure 72: Post-weld heat treated Inconel 738 filler on SX René N5 specimen

Energy dispersive spectroscopy was used to analyze the chemical composition of the layer surrounding recrystallized grains. The results are summarized in Table 19 and show a marginal increase in aluminum concentration of 1 at.% as compared to the base material bulk composition. Since the grain boundary layer was typically 1 µm in width, the sampling volume by the electron beam was larger than the feature of interest and included a significant portion of the surrounding parent material in the assay results. This resulted in an approximation of the bulk material composition. The morphology of the grain boundary layer was consistent with the cubic structure of γ'. Under high magnification examination, gamma prime particles were seen to grow out of the grain boundary layer and form a coherent interface with the surrounding microstructure.

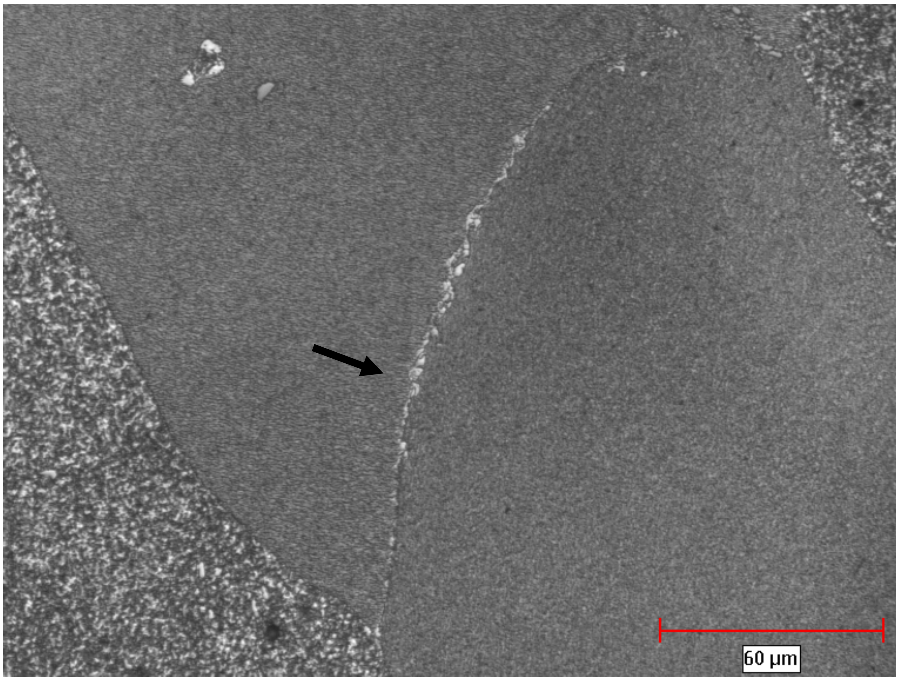

Figure 73: Gamma prime layer between recrystallized grains in the weld heat affected zone of René N5 base alloy

Element	Weight%	Atomic%
Al	8.06	17.85
Ti	0.00	0.00
Cr	3.65	4.20
Co	5.71	5.79
Ni	64.93	66.08
Zr	0.02	0.01
Mo	1.07	0.67
Hf	0.56	0.19
Ta	9.69	3.20
W	6.42	2.09

Table 19: EDS point analysis of the gamma prime grain boundary layer

Figure 74 is an SEM image showing the thick gamma prime layer that formed between the recrystallized grains and the surrounding heat affected zone material. The gamma prime particles immediately adjacent to the layer show alignment with the blocky structure of the intergranular layer. Fine dispersed particles were visible along the grain boundary. As shown in Figure 75 (denoted by arrows), the particles appear brighter (white), indicating a relative higher average atomic number than the surrounding microstructure. EDS point analyses were conducted on the grain boundary particles and showed enrichment in Cr, Mo and W. Tantalum was in lower concentration than the base alloy by approximately 1 wt.%.

EDS elemental line scan were run for extended sampling periods (>1200 seconds) and showed a distinct increase in boron concentration across the grain boundary phases. Corresponding to the point analysis results, the line scans showed increased concentration for Cr, Mo, W while it showed lower Ta. Refer to Appendix P for an EDS line scan across the Cr-Mo rich borides along the grain boundary γ’ layer between recrystallized grains. In contrast to these results, the elemental line scan across the intergranular gamma prime layer alone did not show an increase in boron concentration.

Based on the increase concentration in Cr and Mo, low Ta content and sharp spike for boron, it was suggested that the observed phase along the intergranular layer are Cr-Mo rich borides. Boron is known to have low solubility in nickel and tends to segregate to grain boundaries and this would explain the presence of borides along the newly formed grains. It must be noted however that the boride phase was not observed in the alloy in the as-received condition.

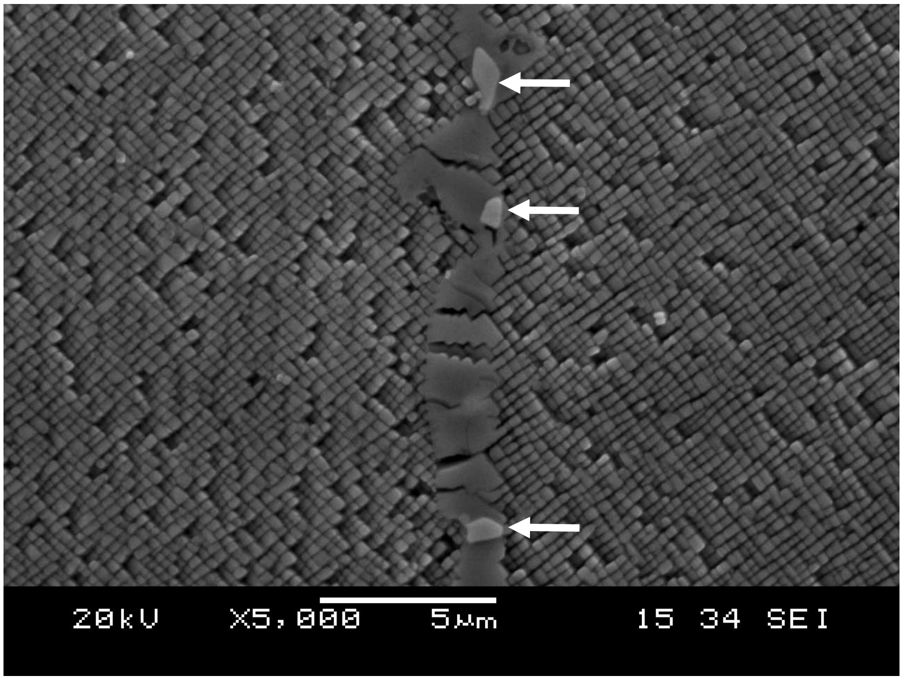

Figure 74: Cr-Mo-B rich particles along grain boundary between a recrystallized grain (left) and heat affected zone (right) in PWHT René N5

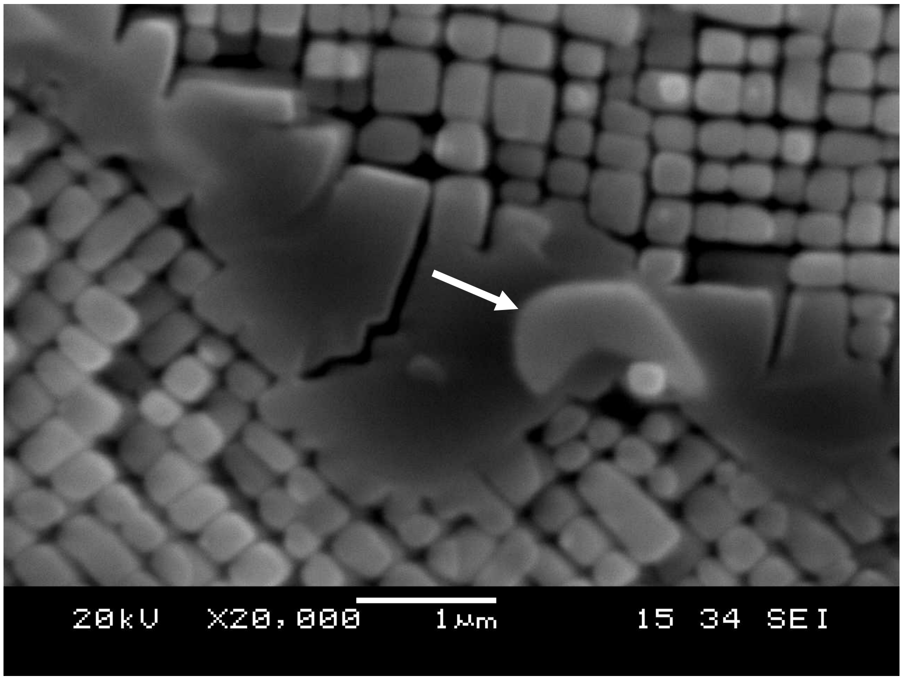

Figure 75: Cr-Mo-B rich phase at recrystallized grain (top) and heat affected zone (bottom) boundary in PWHT René N5

High magnification images were taken on the SEM to show the difference in γ' morphology between the base alloy and the filler material in the post-weld heat treated condition. As shown in Figure 76, the γ' morphology in the filler zone is near spherical with an approximate size of 0.5 μm. The gamma prime structure in the base alloy is shown in Figure 77 as cuboidal and measuring 0.3 μm in size.

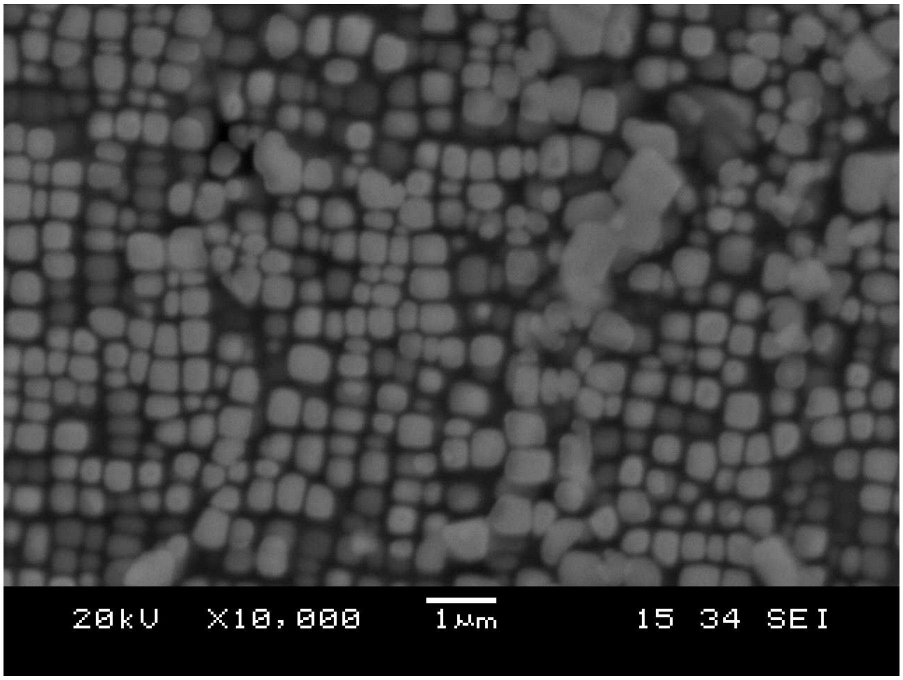

Figure 76: Typical gamma prime in the weld fusion zone (Praxair Ni-284-1 filler alloy) in a René N5 specimen

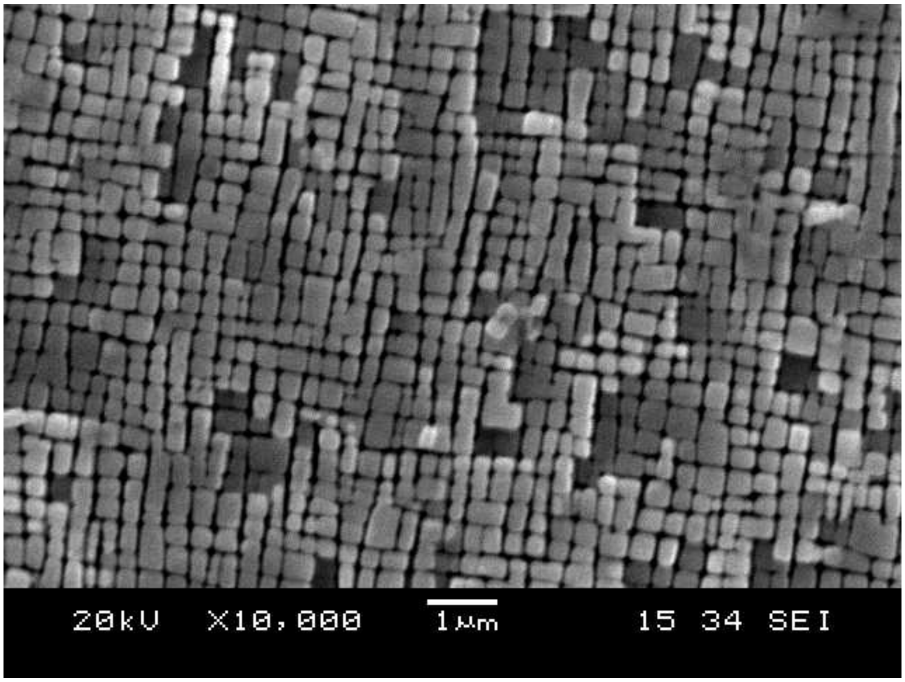

Figure 77: Typical gamma prime in PWHT René N5, non-HAZ

5.4.4 Discussion of Result for Post-Weld Heat Treated Condition

Recrystallization of the base material in the weld heat affected zone occurred during the solution and age heat treatment for alloys René 80 and René N5. As shown in the optical micrographs and SEM images in the preceding sections, large grains formed surrounding the weld fusion zone. In contrast, the HAZ microstructure of equiaxed (conventionally cast) Inconel 738 did not undergo recrystallization.

In order for recrystallization to occur, sufficient strain energy was stored in the material and the material was subjected to a sufficiently high temperature for the nucleation of new grains. Burgel et al. [61] studied the recrystallization of CMSX-11B, PWZ1483, SRR9 and CMSX-6 nickel based superalloys after applying low strain levels. CMSX-11B with 1% compressive strain underwent partial recrystallization during a solution heat treatment. Under the low strain condition, all new grains intersected the specimen surface. Under 2% compressive strain, the alloy underwent complete recrystallization during the post-weld solution heat treatment. Similar results were obtained with strains applied in tension. The authors explained that two conditions must be met in order for recrystallization to occur: (1) γ' must be dissolved in the area of new grain nucleation and (2) a free surface must be available. The need for a free surface is based on the activation energy for nucleation and no interface energy has to be generated by the system. Lastly, the dislocations present in the microstructure (from plastic strain) supply the mechanical energy required for recrystallization once γ' dissolved during the solution heat treatment cycle.

In the present study, the recrystallized grains were contained to the weld heat affected zone along the fusion zone. The interface created by the base material and the weld fusion zone effectively provided an internal discontinuity (similar to a surface) and reduced the interface free energy required for recrystallization. The expression for free energy associated with cellular recrystallization is as follows [62]:

$$\Delta G_{RECRYTALLIZATION} = \Delta G_{MECHANICAL} + \Delta G_{INTERFACE} + \Delta G_{CHEMICAL}$$

where $\Delta G_{MECHANICAL}$ (-'ve) represents annihilation of dislocations, $\Delta G_{INTERFACE}$ (-'ve) and represents microstructure coarsening and creation of high angle grain boundaries and $\Delta G_{CHEMICAL}$ is deemed negligible as there is no change in the chemical composition before and after recrystallization of the alloys.

In the laser welds applied in this study, the residual stresses and plastic strain were sufficiently high to provide the stored mechanical energy for new grain nucleation in the directionally solidified and single crystal alloys. As previously discussed in the literature review section of this report, Sekhar and Reed [42] measured the residual stresses in laser beam welded Waspalloy and Udimet 720Li. The authors reported a longitudinal stress of 600 MPa and a transverse direction stress of and -300 MPa for Waspaloy. For U720Li, the residual stress in the longitudinal direction was 1200 MPa and 500 MPa in the transverse direction. These residual stresses values are near the yield strength of nickel based superalloys [56] and provided the driving force for nucleation of new grains. Bonifaz and Richards [52] used finite element analysis to model residual (Mises) and plastic strain in Inconel 738 after GTA welding. The authors found that the highest residual stresses and plastic strain were located along the weld centreline were in excess of 800 MPa and 2.6%, respectively. In comparison to the work done Burgel et al. [61], the predicted residual plastic strain in GTA welds would be sufficient to initiate grain nucleation, growth and potentially complete recrystallization of the affected section.

In the present study, the recrystallized grains grew to a relatively large size and formed a thick layer along the newly formed grain boundaries and the adjacent base material microstructure. In René 80, the grain boundary films were determined to be MC carbides undergoing decomposition and γ'. As shown in Figure 70, the intergranular γ' was irregular and porous. In contrast, a thick coherent γ' layer formed between new grains in the René N5 alloy along with boride particles.

Burgel et al. [61] subjected recrystallized specimens to low cycle fatigue testing at 980ºC and a total strain range of 0.7% and found no change in the number of cycles to crack initiation when compared to the baseline CMSX-11B alloy. However, a higher density of cracks were notes in the specimen gage length. Li and Han [62] evaluated the stress rupture properties of IC6SX nickel based single crystal superalloy in the recrystallized condition. Similarly, the authors found no significant difference as compared to the baseline SX alloy.

5.5 THERMO-MECHANICAL FATIGUE TESTING

Thermal mechanical fatigue test results were plotted on log-log scales comparing the fatigue life of laser beam welded Inconel 738, René 80 and René N5. As shown in Figure 78, results for LBW René 80 and René N5 were similar and both tolerated higher strains than Inconel 738 at equivalent N_f (no. of cycles to failure) values. The comparative TMF life of CC

Inconel 738 is significantly lower than that of DS René 80 and SX René N5. These results are as would be expected since grain boundaries are crystallographic defects that reduce the mechanical properties of the material under loading. Consequently, turbine blades have evolved from polycrystalline cast structures to directionally solidified and single crystals in order to improve elevated temperature mechanical properties and component life [56]. Refer to Appendix R for the TMF test results.

As shown in Figure 78, the data generally followed a linear relationship according to the Manson-Coffin relationship [8, 9]. GTAW welding and thermo-mechanical fatigue testing of CC Inconel 738 and DS René 80 evaluated by Abrokwah [69] are included in Figures 80 and 81 for comparisons with LBW. Linear regression was used and a fitted line is plotted in for baseline, GTAW and LBW thermal fatigue testing results. The regression model for the TMF results is calculated in the form [63]:

$\Delta\varepsilon_p = \varepsilon'_f\,(2\,N)^c$

where:

$\Delta\varepsilon_p$ = mechanical strain amplitude

ε'_f = fatigue ductility coefficient defined by the strain intercept at 2N = 1

(approximately equal to the true fracture strain ε_f for many metal.)

2N = number of strain reversals to failure (one cycle is two reversals)

c = fatigue ductility exponent, which varied between -0.5 and -0.7 for many metals.

Generally, smaller values of c correspond to large values for fatigue life.

Refer to Table 20 for a summary of fatigue ductility coefficients and exponents for Inconel 738, René 80 and René N5 in the baseline, GTAW and LBW conditions.

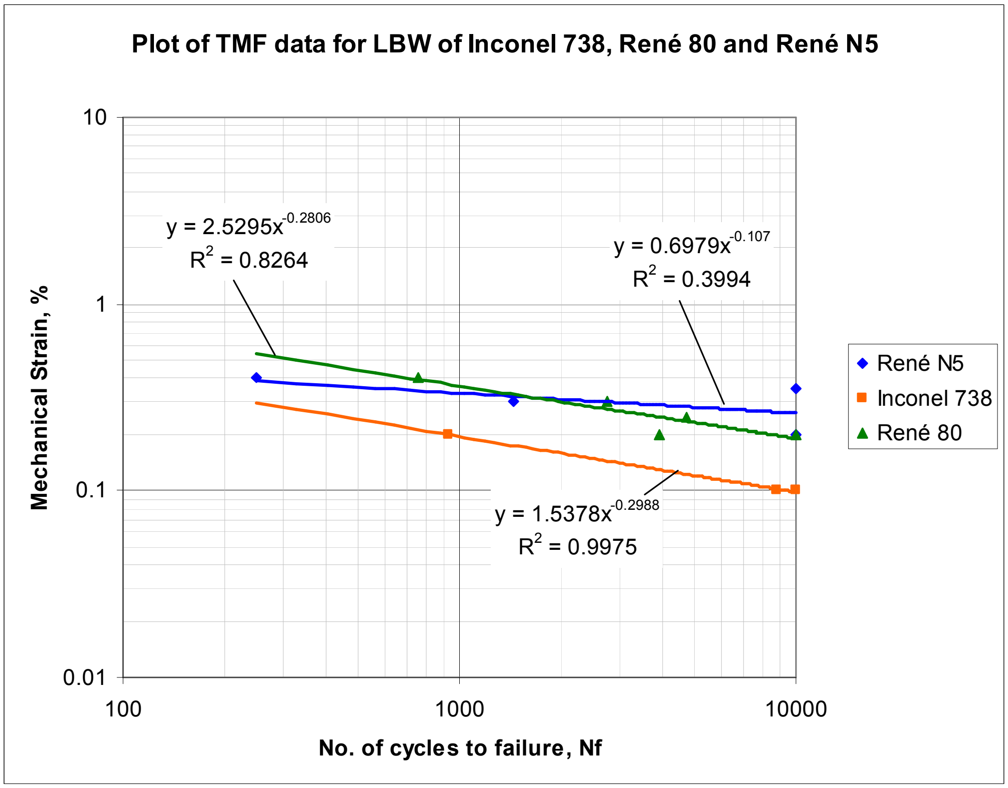

Figure 78: TMF test results for LBW specimens

	ε'_f	c	R^2
Inconel 738 baseline	5.1	-0.46	0.99
Inconel 738 GTAW	4.1	-0.39	0.92
Inconel 738 LBW	*1.5*	*-0.30*	*0.99*
René 80 baseline	1.9	-0.16	0.89
René 80 GTAW	2.6	-0.26	0.90
René 80 LBW	*2.5*	*-0.28*	*0.83*
René N5 baseline	3.3	-0.18	0.99
René N5 GTAW	0.6	-0.02	0.01
René N5 LBW	*0.7*	*-0.11*	*0.40*
$\Delta\varepsilon_p = \varepsilon'_f (2N)^c$			

Table 20: Fatigue ductility coefficient ε'_f and exponent c for TMF results.

The TMF life of Inconel 738 was not significantly affected by GTAW and LBW. As shown in Figure 79, the line plots for baseline, GTAW and LBW are relatively close and suggest that welding under the conditions described in this thesis did not introduce fatigue life reducing defects. Therefore, the equiaxed grain and epitaxial growth structures in the fusion zone did not have an adverse effect of the TMF properties of polycrystalline Inconel 738. However, it must be noted that altering the welding parameters and the pre-weld material condition may reduce the TMF life of the alloy relative to the baseline condition.

The TMF life of baseline specimens exceeded that of GTAW and LBW specimens for DS René 80 and SX René N5. The results plotted in Figures 80 and 81 clearly show that GTAW and LBW significantly reduced the TMF life of René 80 and René N5. Figure 80 shows the TMF test results for DS René 80 with a significant difference in fatigue life between all the baseline, GTAW and LBW conditions. The TMF life of baseline specimens is distinctively greater than those of GTAW and LBW specimens, with LBW being the lowest for René 80.

The TMF results for SX René N5 are shown Figure 81. It must be noted that the GTA welds on the single crystal alloy were of relatively poor quality and likely do not provide a conclusive representation of TMF properties under these test conditions. However, a significant decrease in fatigue life is apparent with LBW of René N5 as compared to the baseline conditions.

Based on the TMF plots shown, the following general observations are made:

- By using the welding parameters and material conditions described in this thesis, the TMF life (N_f) of polycrystalline Inconel 738 was not significantly reduced by GTAW and LBW.
- The TMF life (N_f) of DS René 80 and SX René N5 in the baseline condition exceeded that of GTAW and LBW specimens.
- The TMF life (N_f) of DS René 80 and SX René N5 exceeded that of CC (polycrystalline) Inconel 738.

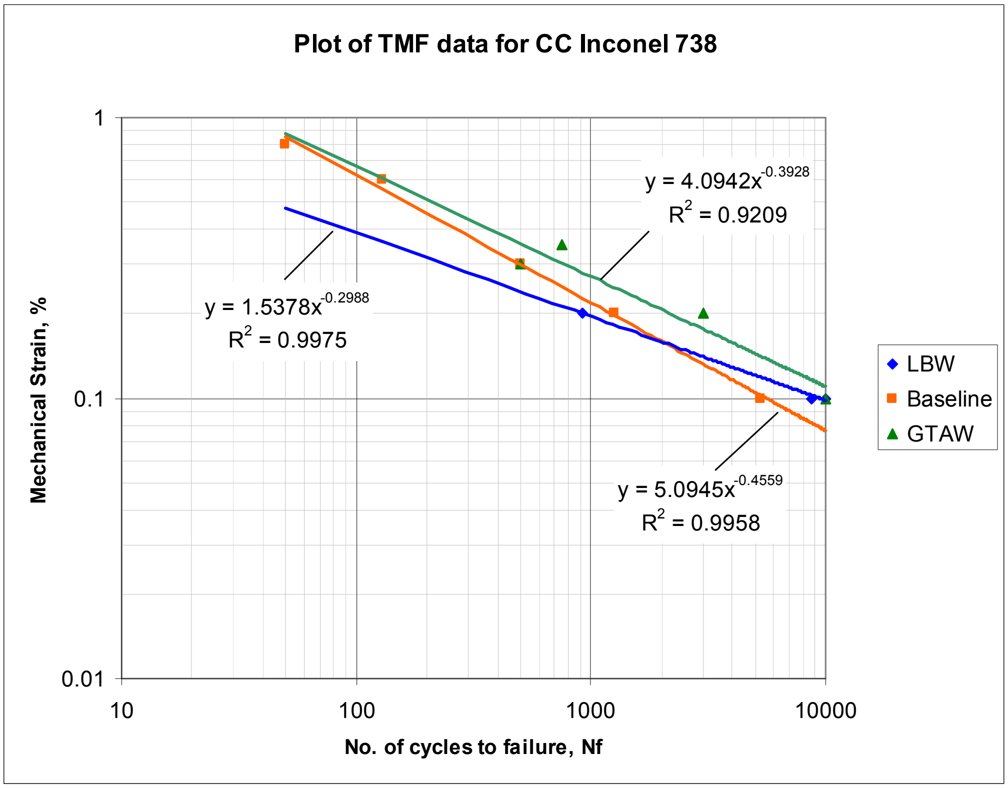

Figure 79: TMF test results for baseline, GTAW and LBW Inconel 738 specimens.

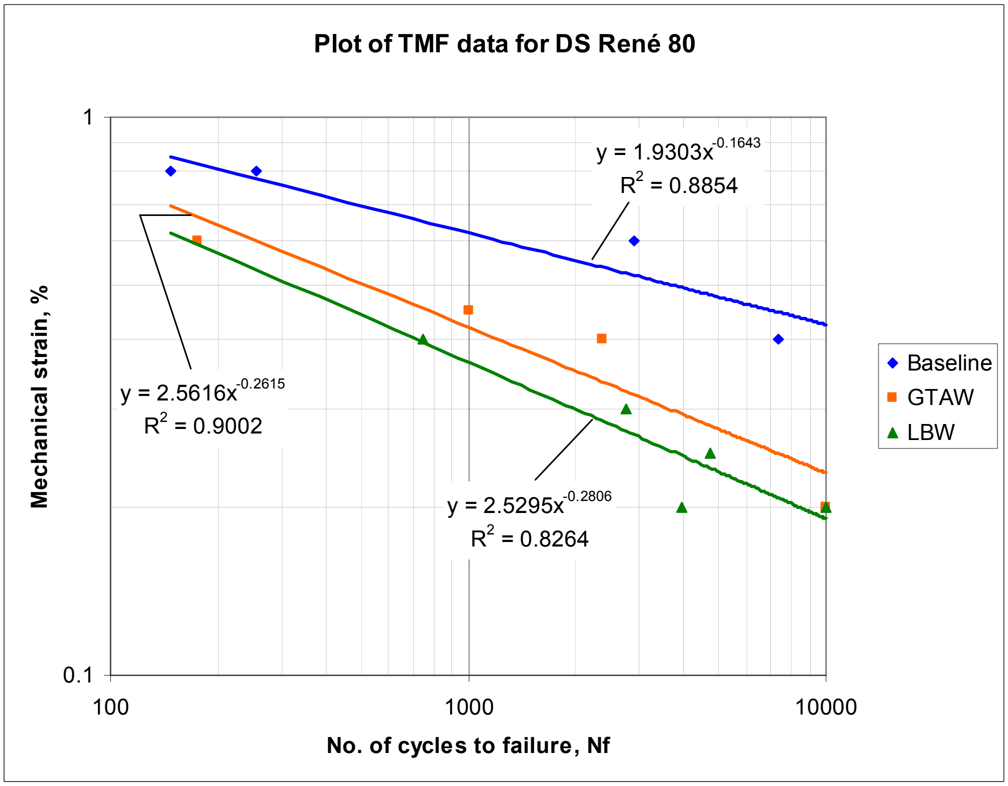

Figure 80: Test results for baseline, GTAW and LBW TMF René 80 specimens

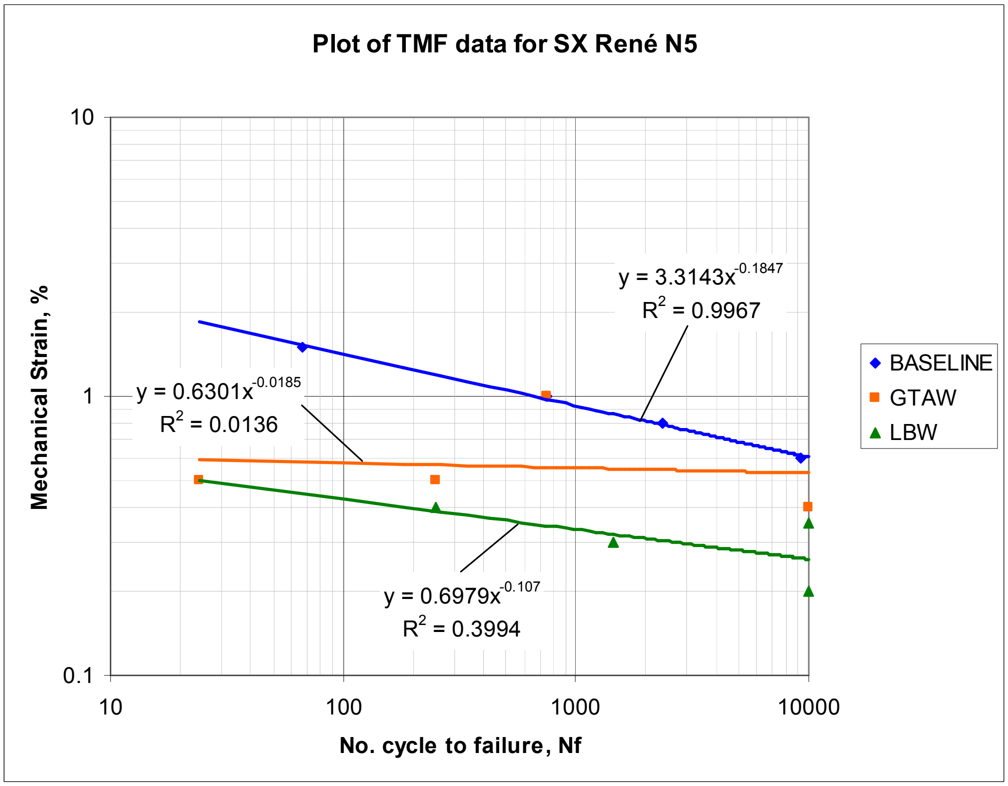

Figure 81: Test results for baseline, GTAW and LBW René N5 specimens

5.6 FRACTOGRAPHY

5.6.1 Inconel 738

0.1% MECHANICAL STRAIN

Two specimens were tested and ran for a total of 8750 and 10,000 cycles without fracture. The 8750 cycle test was stopped due to visual crack detection. Figures 82 and 83 are optical micrographs taken with a stereomicroscope showing the edge and top views of TMF specimens. When viewed with the unaided eye, cracks were observed to extend within the weld fusion zone, perpendicular to the loading axis. Surface cracks (branch cracks) were also visible along the specimen edges.

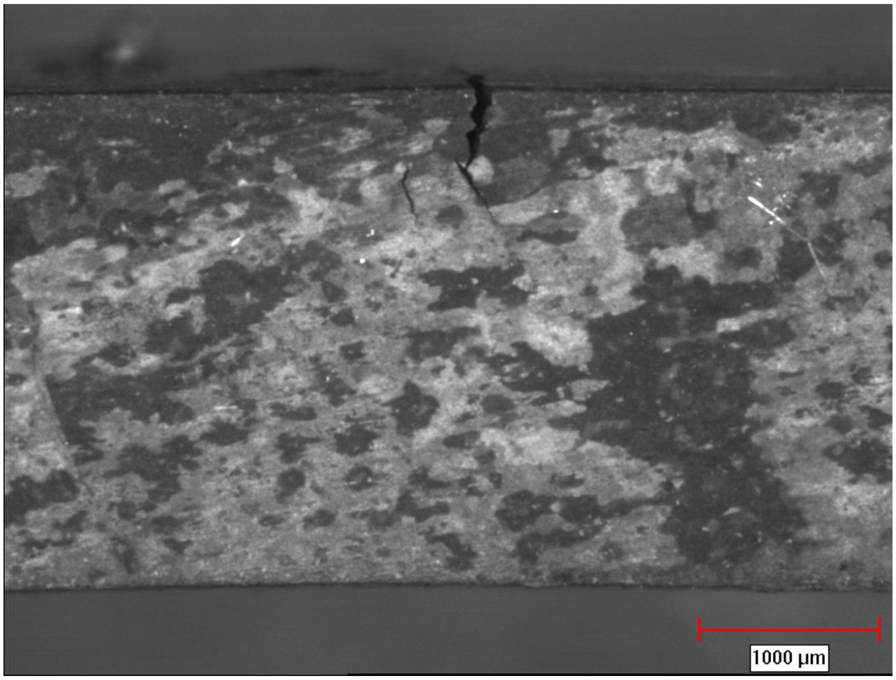

Figure 82: Edge view of Inconel 738 specimen tested under 0.1% mechanical stain after 8750 cycles

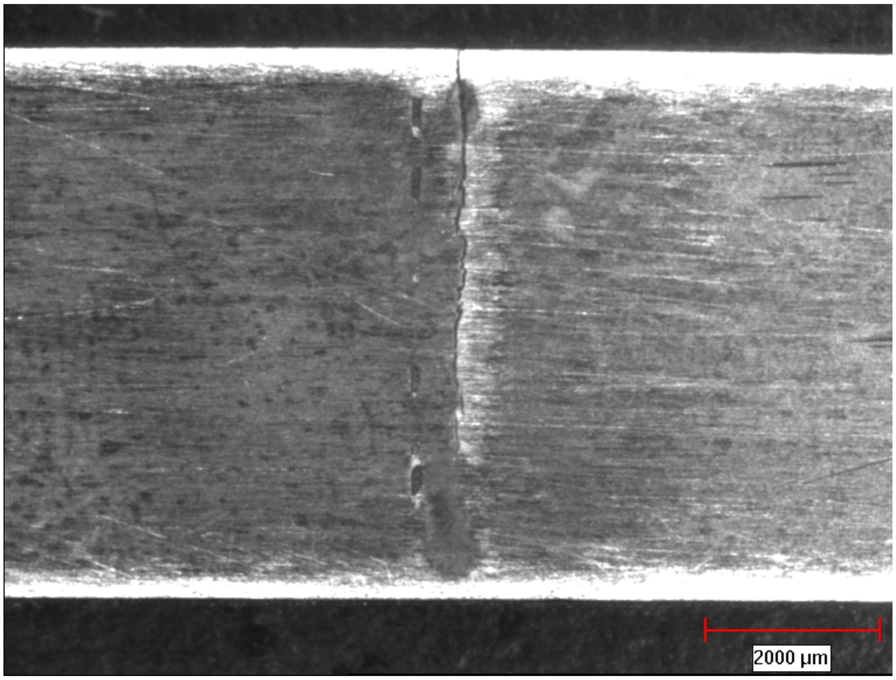

Figure 83: Top view of Inconel 738 specimen tested under 0.1% mechanical strain after 10,000 cycles

Higher magnification using optical microscopy and SEM revealed several cracks in the weld microstructure. The specimens showed a primary crack forming in the weld fusion zone, presumably at the surface, and propagating perpendicular to the loading axis through the weld fusion zone and extending in the base material. Figure 84 is an SEM image of the weld fusion zone cross section showing the propagation of the primary crack through the fusion zone. Additional secondary cracks are visible in the weld fusion zone and the base material heat affected zone.

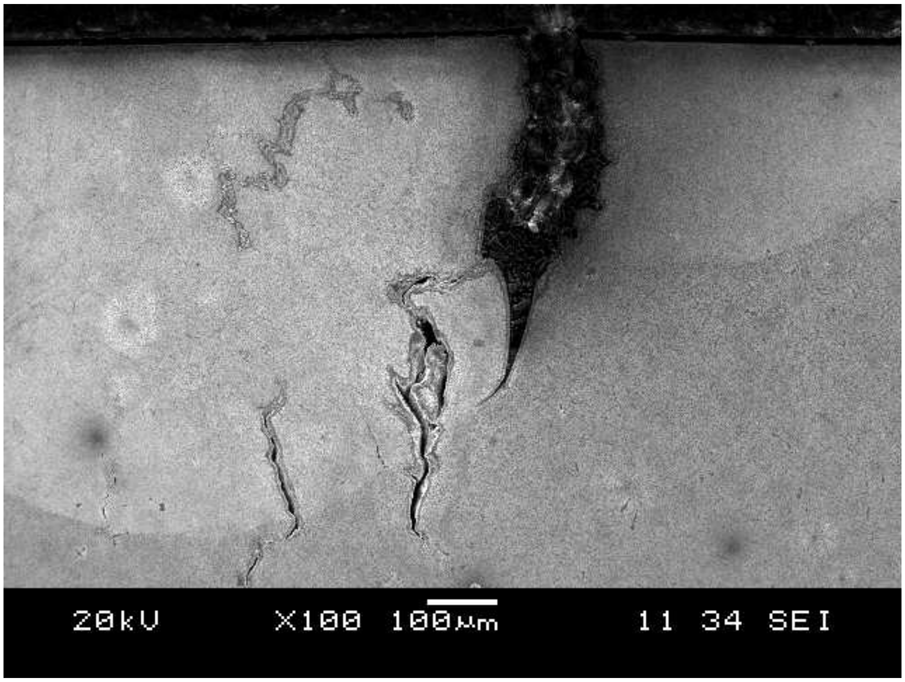

Figure 84: Cracks through fusion zone and Inconel 738 parent material, 0.1% mechanical strain after 8750 cycles

The crack tips appeared sharp with oxidation along the surfaces. Figure 85 shows an SEM image of a crack tip extending along the fusion zone to the base material interface and redirected in the fusion zone. A surface oxidation layer is visible along the entire length of the crack along with a zone devoid of the γ’ phase. EDS analysis of the surface scale and adjacent layer reveals the presence and segregation of Ti and Al displaced by diffusion to the surface oxidation of the base material surfaces exposed to the oxidizing atmosphere. The diffusion of Al and Ti to the oxide layer and precipitates corresponds to the region with no visible gamma prime under the SEM. Figure 86 is an SEM image of the crack tip extending through the base material. In contrast to the fusion zone cracking (shown in Figure 85), an increase in oxidation precipitates was visible immediately below the surface scale. Oxide precipitates were aligned perpendicular to the crack surface and parallel to the diffusion flux/direction. Using EDS analysis, the surface scale in the base material was determined to be rich in titanium while the precipitates are rich in aluminum. Similar to the cracks in the weld fusion zone, a layer devoid of gamma prime was visible along the crack surfaces in the parent material. Refer to Appendix H for an EDS line scan across a crack propagating through the weld fusion zone.

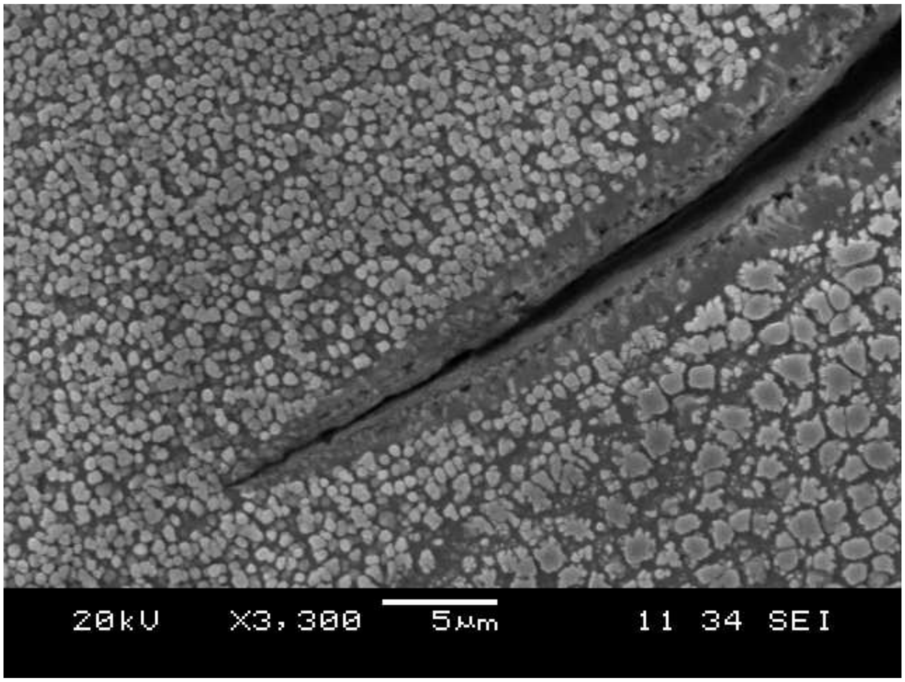

Figure 85: Crack tip in fusion zone on Inconel 738 specimen, 8750 cycles

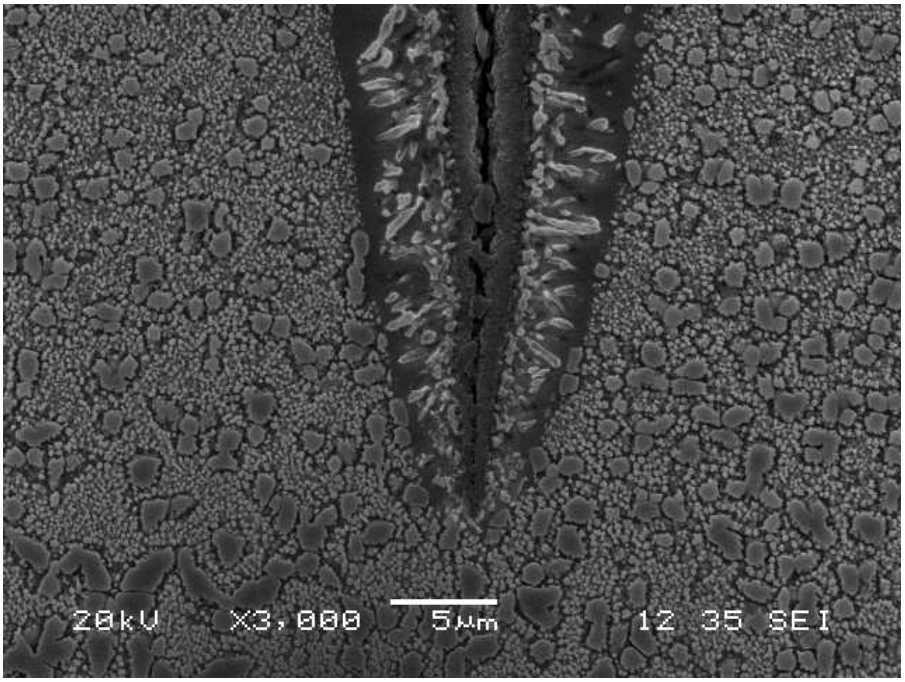

Figure 86: Crack tip in Inconel 738 base material, 10,000 cycles

The thickness of surface oxidation scale and the corresponding layer devoid of gamma prime decreased in thickness from the crack opening to the crack tip. As shown in Figures 87 and 88, the layer free from gamma prime is in the order of 10-15 μm near the specimen surface where the cracking first occurred. The surface scale in the vicinity of the crack opening is approximately 3-4 μm and irregular in shape, indicative of extensive growth over a significant portion of the thermal mechanical fatigue test. In contrast to the crack opening, the surface oxide scale and γ' free zone are relatively thinner and in the order of 2-3 μm in thickness. The reduction in oxide scale thickness and γ' free zone is as a result of the reduced exposure to oxidizing atmosphere during the TMF test. Therefore, the change in surface microstructure along the crack length is indicative of gradual crack growth during the test. Refer to Appendix I for an EDS linescan along the edge of the crack extending in the Inconel 738 base material.

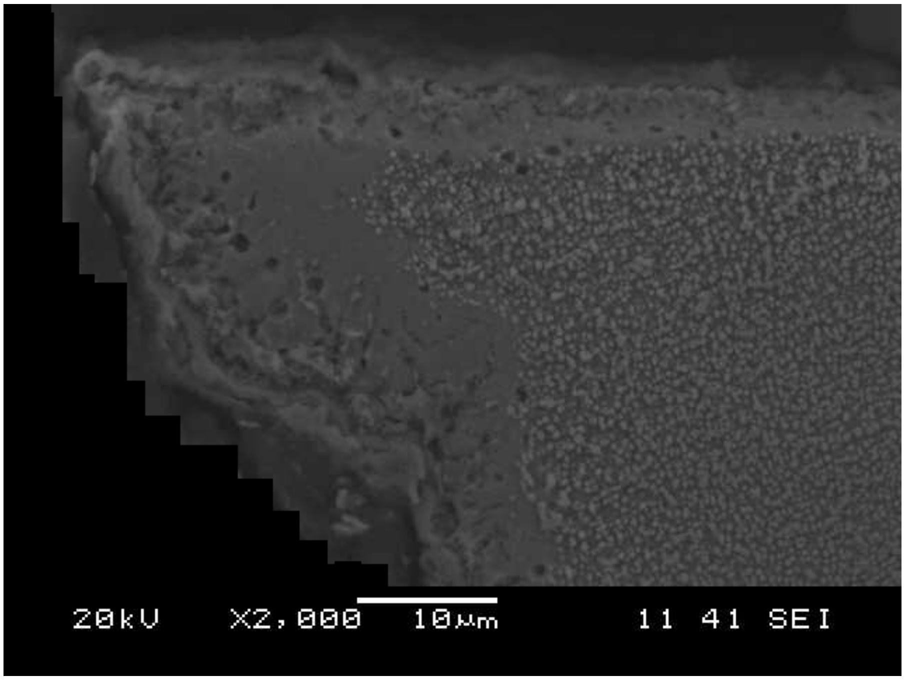

Figure 87: Crack opening on Inconel 738 specimen, 8750 cycles

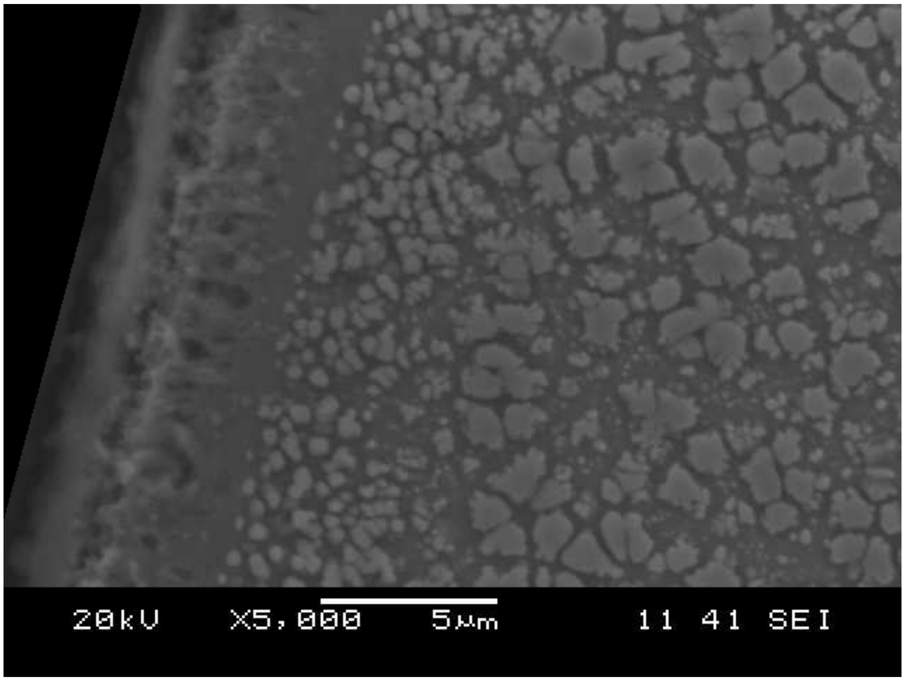

Figure 88: Crack surface on Inconel 738 specimen, 8750 cycles

The gamma prime in the weld fusion zone of TMF specimens was predominantly spherical in shape, similar to that of the post-weld heat treated condition. As shown in Figure 89, no appreciable changes in particle size was noted. In contrast, the gamma prime phase in the Inconel 738 parent material exhibited changes. As compared to the PWHT condition, the volume fraction of the primary gamma prime phase shows a significant decline. Figure 90 is an SEM image of the typical microstructure in the parent material (non-heat affected zone region) showing the increased distance between remaining primary gamma prime. As previously presented in this report, the spacing between primary gamma prime particles in the PWTH condition was typically less than 1 μm. The morphology of the remaining gamma prime particles changed from cuboidal to spherical shape. New, fine spherical secondary gamma prime particles approximately 0.2 μm in size are visible between primary gamma prime particles.

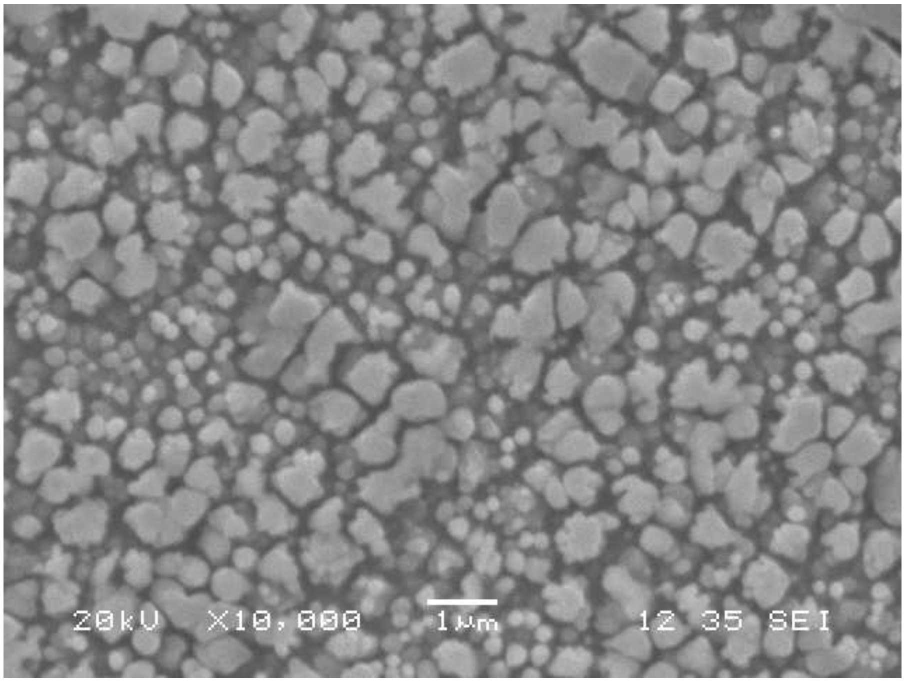

Figure 89: Fusion zone gamma prime in 10,000 cycles, Inconel 783 specimen

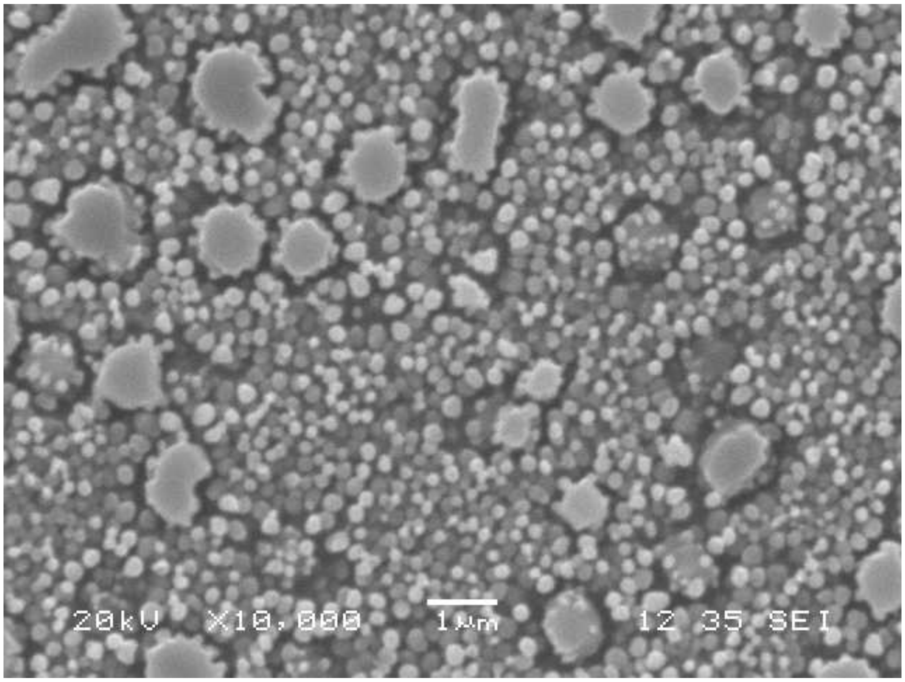

Figure 90: Non-HAZ gamma prime after 10,000 cycles, Inconel 738.

0.2% MECHANICAL STRAIN

The 0.2% strain TMF specimen fractured after 925 cycles. A shown in Figure 91, the specimen's top surface has a linear fracture across the entire width of the weld fusion line consistent with brittle cleavage type fracture. In contrast, Figure 92 shows the bottom surface of the fractured TMF specimen with a cup and cone shape normally associated with ductile fracture. Based on these observations, it can be concluded that cracking initiated along on the fusion zone side of the specimen, propagated in a brittle fashion until the load carrying capacity of the remaining cross-section was exceeded and terminated in ductile fracture.

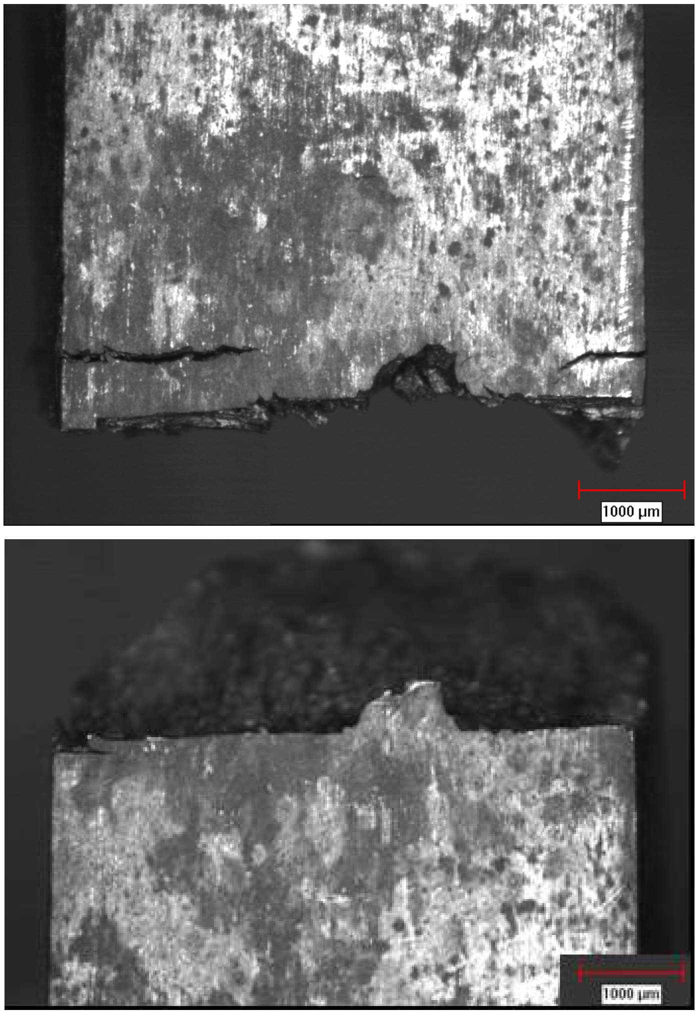

Figure 91: Top view (fusion zone side) of fractured 0.2% mechanical strain Inconel 738 specimen

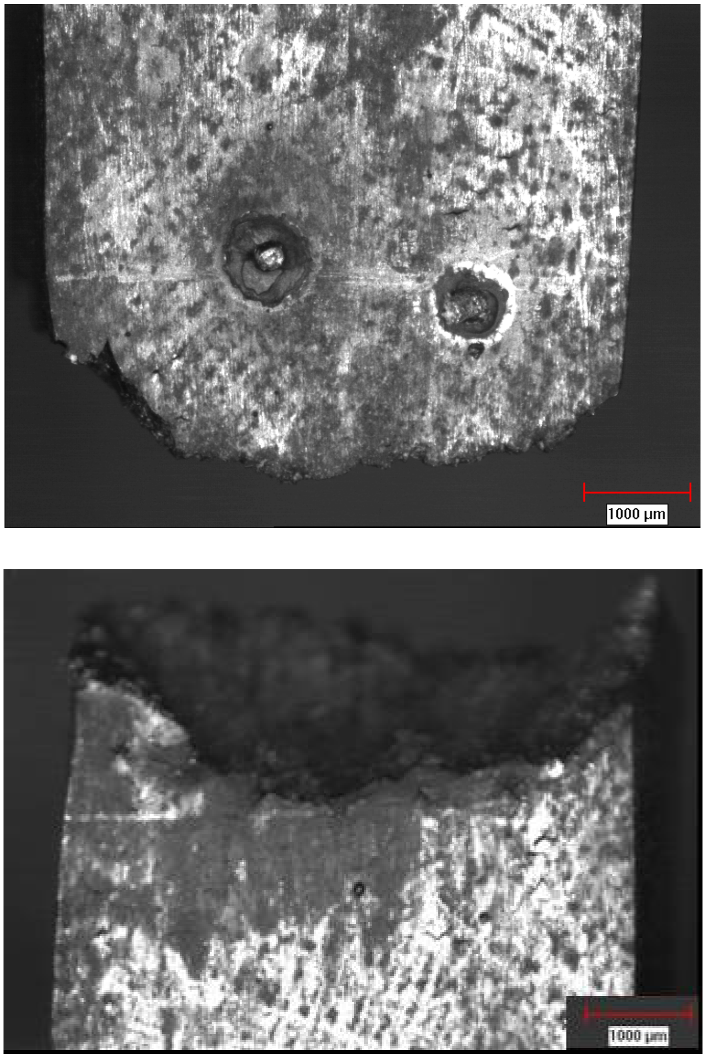

Figure 92: Bottom view of fractured 0.2% mechanical strain Inconel 738 specimen

The mating fracture surfaces were viewed end-on under the optical stereomicroscope and are shown in Figure 93. In both views, the weld fusion zone is visible in the upper quarter of the exposed surface. Under higher magnification, the surface texture appeared relatively smooth over the weld fusion zone and transitioned to a rough/facetted structure in the parent material.

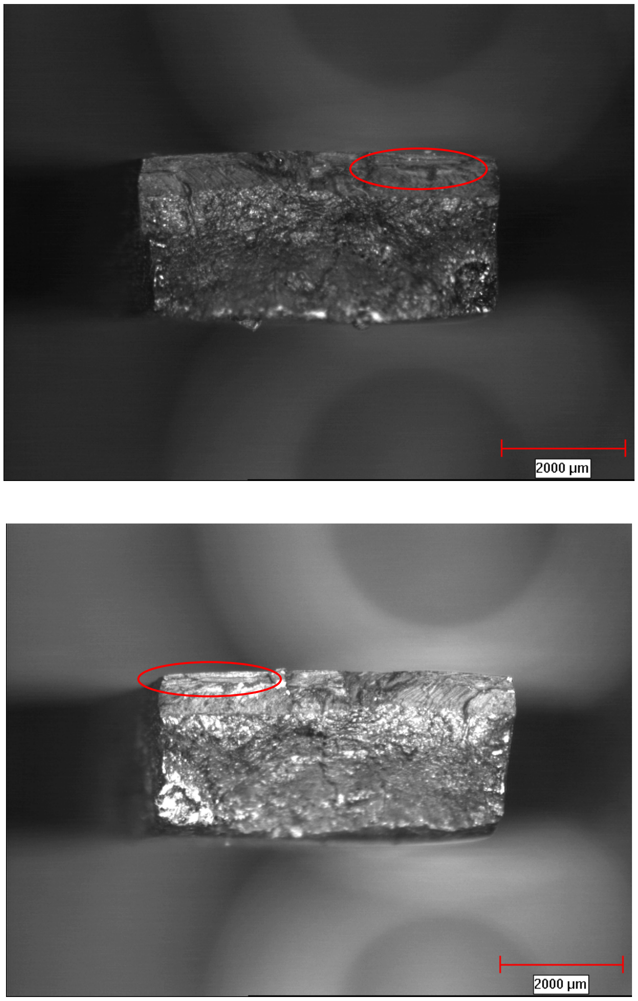

Figure 93: Fracture surfaces on 0.2% mechanical strain Inconel 738 specimen

Figure 94 is a higher magnification view of the area circled in Figure 93 and shows the likely crack initiation site along the top surface of the TMF specimen. An area approximately 1000 µm long by 200 µm stands out from the surrounding fracture surface and shows the beach marks associated with cleavage crack propagation. Figures 94 and 95 are images showing a crack initiation area taken from the specimen's corner and suggests multiple crack initiation sites along the fusion zone top surface.

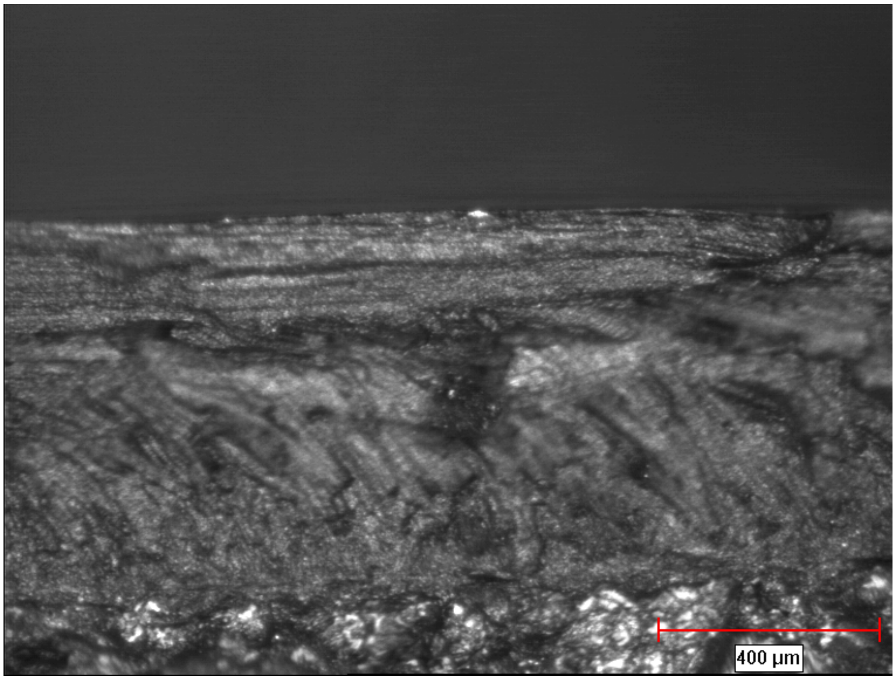

Figure 94: Beach marks in weld fusion zone near surface of 0.2% mechanical strain Inconel 738 specimen

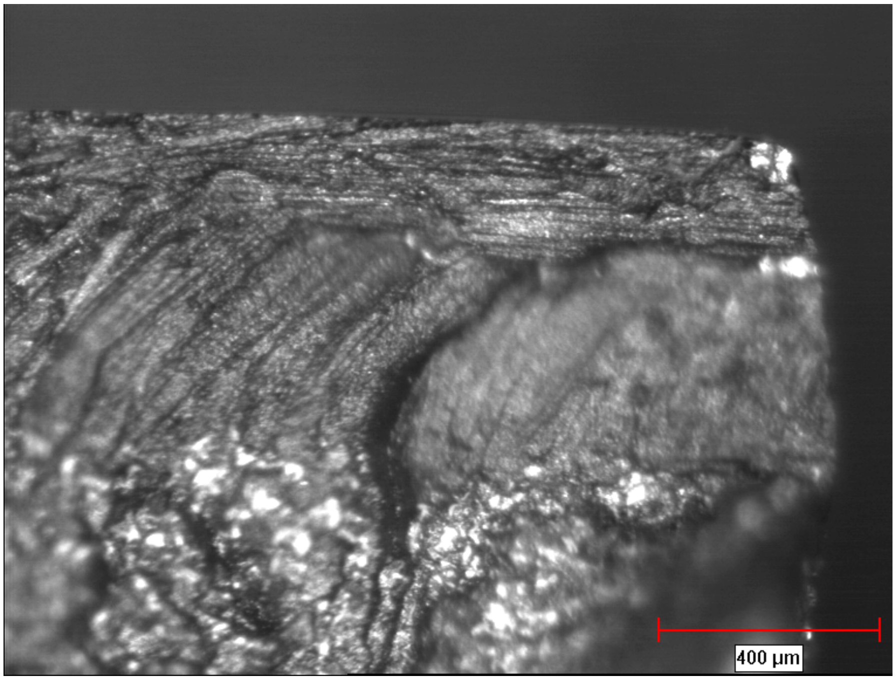

Figure 95: Beach marks in weld fusion zone near corner of Inconel 738 specimen tested under 0.2% mechanical strain

Under optical microscopy examination, several cracks were visible in the weld fusion zone near the fracture surface. For example, Figure 96 shows the fracture surface along with intergranular cracking in the adjacent fusion zone microstructure. The fracture surface exhibited a thinner oxidation layer that the 0.1% mechanical strain specimens which ran for considerably longer in the test chamber (8750/1000 cycles versus 925) with a typical thickness of 0.5-1.0 μm. Likewise, the layer devoid of gamma prime as a result of local de-alloying by surface oxidation was approximately 0.5-1.0 μm in thickness. The marked decrease in oxidation layer thickness and de-alloying are directly related to the reduced exposure time in the test chamber atmosphere, being approximately 10% of the total exposure time as the 0.1% mechanical strain specimen.

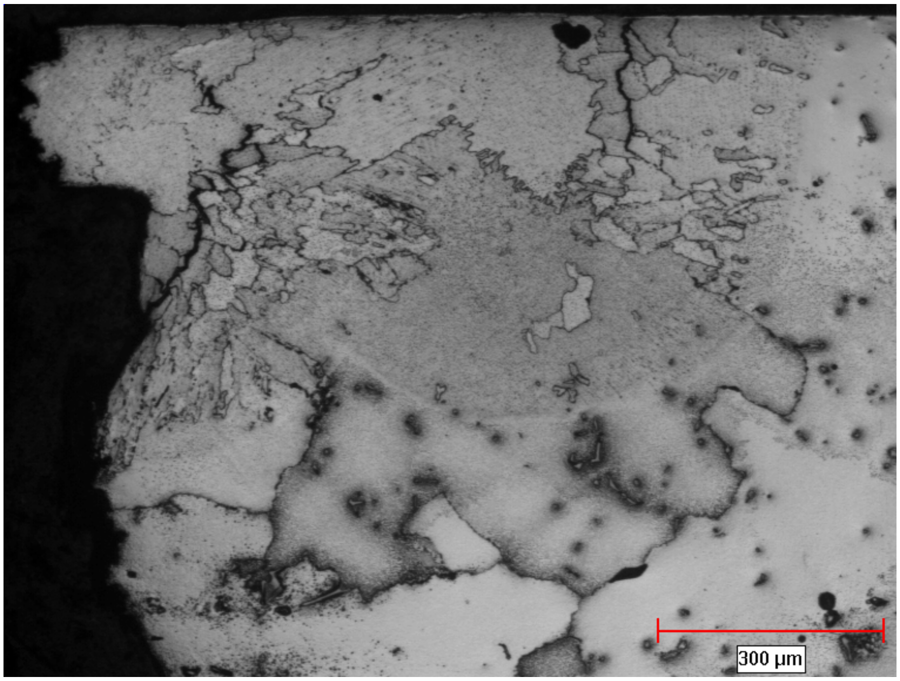

Figure 96: Optical micrograph of fracture and cracking along the fusion zone in Inconel 738 specimen

The specimen’s surface was examined by SEM in order to evaluate surface cracks and determine the initiation mode. As shown in Figure 97, small cracks were found to propagate along grain boundaries in the weld fusion zone. The cracks showed evidence of oxidation along the surface and de-alloying of the grain boundary ahead of the crack tip. The parent material responded to the combined effects of elevated temperature oxidation and cyclic tensile loading by forming micro-cracks where grain boundaries intersect the specimen’s surface. Figure 98 shows oxidation of a carbide particle along a grain boundary at the specimen’s surface. Left of the particle and near the surface, a micro-crack has formed and is approximately 6-7 μm in length. In Figure 99, a micro-crack initiated at the specimen surface but was not associated with a grain boundary or a readily identifiable carbide particle. In this instance, it is likely that the tensile loading on the specimen exceeded the tensile strength of the surface oxide film and induced surface cracking which, in turn exposed the underlying parent material. The parent material readily formed an oxide layer locally depletes the surface material of aluminium and titanium, locally reducing the materials tensile strength, and alloying further crack growth under cyclic loading.

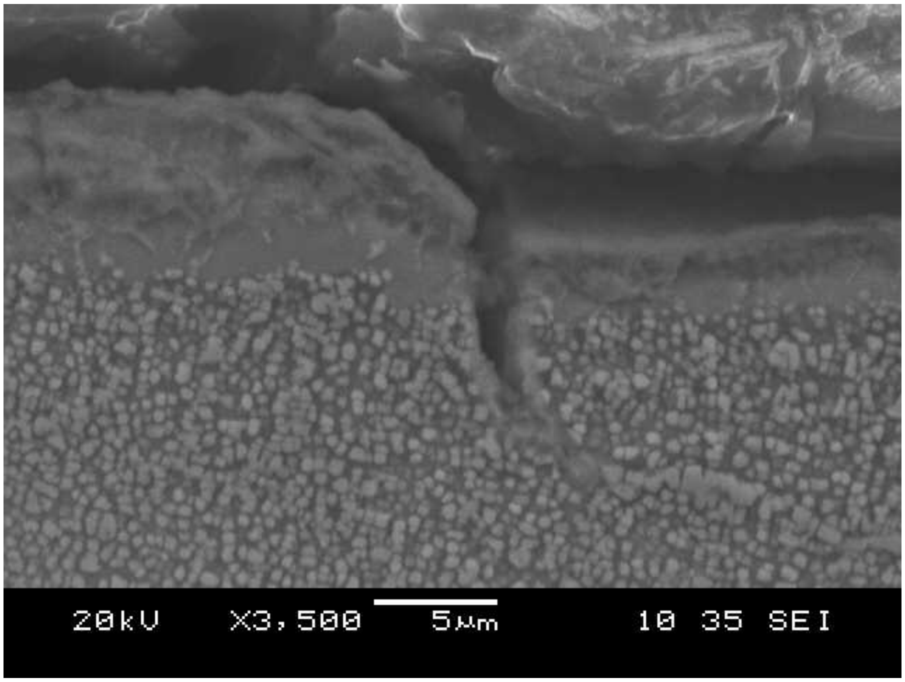

Figure 97: Surface crack in fusion zone along grain boundary, Inconel 738 specimen

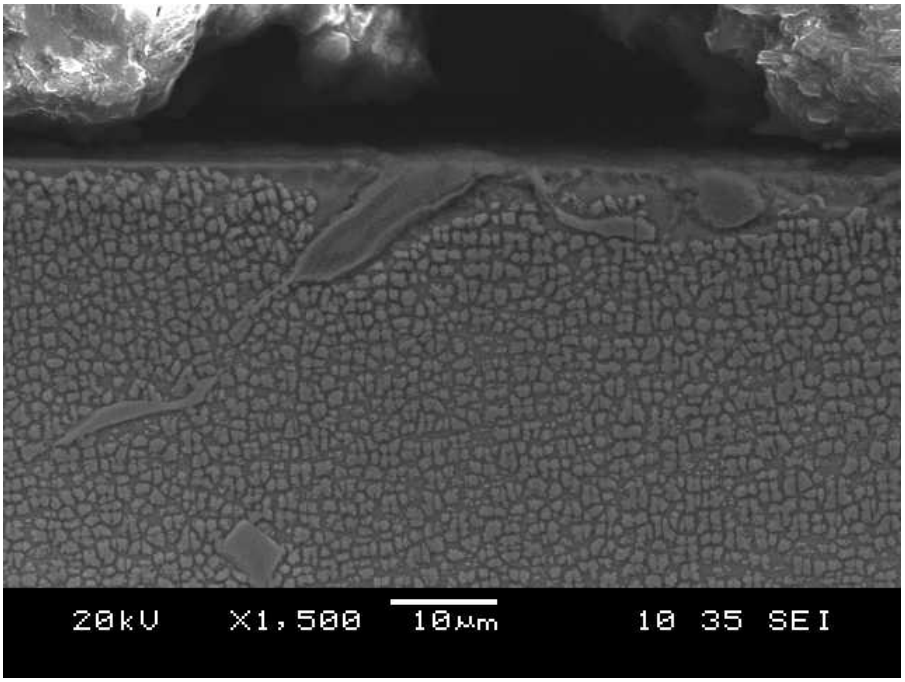

Figure 98: Carbide oxidation at Inconel 738 parent material surface and grain boundary intersection

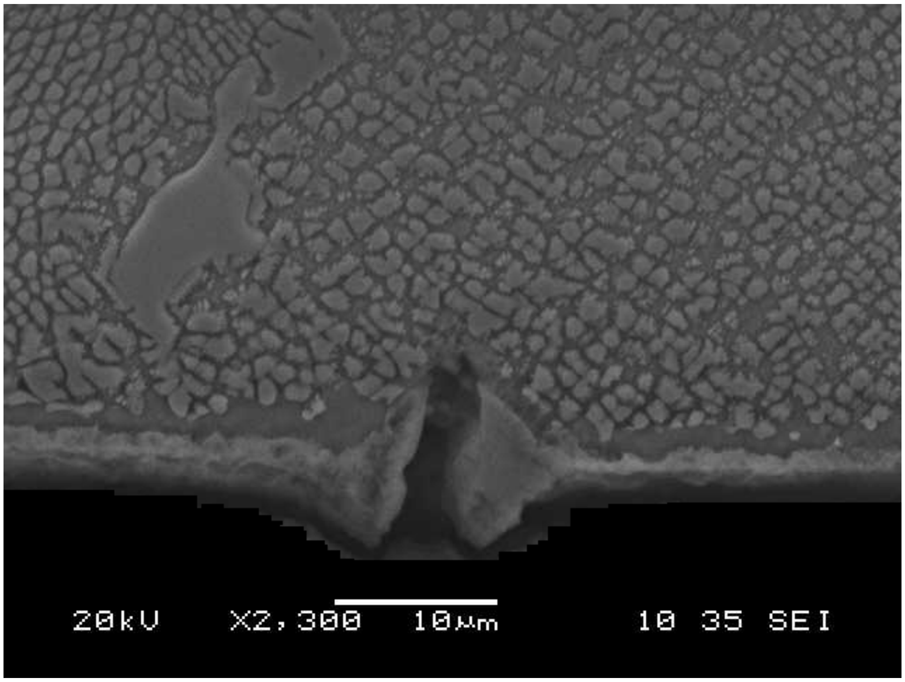

Figure 99: Crack and associated oxidation along surface of Inconel 738 specimen

5.6.2 René 80

0.2% MECHANICAL STRAIN

Two LBW René 80 specimens were tested under 0.2% strain. One fractured at 3950 cycles while the other ran for the maximum of 10,000 cycles as defined by the upper boundary of testing undertaken in this study. Figure 100 is a photograph of the fractured specimen taken in the as-tested condition. The specimen's gauge section, where heat was applied by resistance heating, exhibited surface oxidation as evidenced by the dark grey/black colour and the blue to straw transition toward to the specimen tabs where copper grips provided cooling. The specimen showed sign of deformation or necking near the fracture.

Figure 100: Fractured René 80 TMF specimen, 0.2% strain

End view macroscopic examination of the specimen fracture surfaces revealed three distinct microstructural zones. The upper zone, shown in Figure 101 represents the weld fusion zone. Immediately beneath the fusion zone, a coarse and faceted layer is visible and represents the recrystallized grain microstructure. Finally, the third zone shown in the lower half of the factures represents the unaltered parent material.

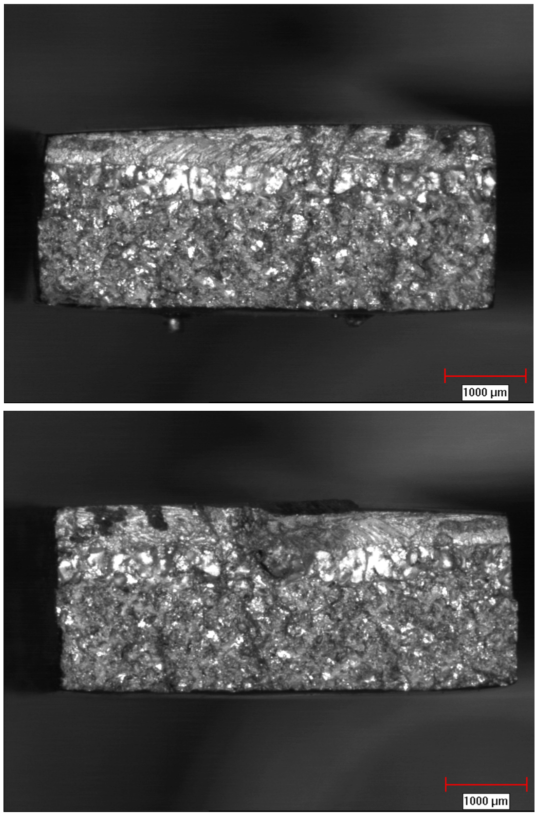

Figure 101: Mating fragments of fracture surface of René 80 TMF specimen, 0.2% strain

Figure 102 is an SEM image of the fracture surface showing the fusion zone (upper half) and recrystallized grain region (lower half) near the specimen edge. The fusion zone fracture surface shows mild evidence of beach marks near the upper surface of the specimen suggesting a likely crack initiation site. The lower portion of the fusion zone visible in Figure 103 shows a stepped structure at approximately 45 degrees to the specimen width corresponding to the dendritic structure being oriented towards the direction of laser beam travel as described by the three-dimensional model developed by Vitek [6].

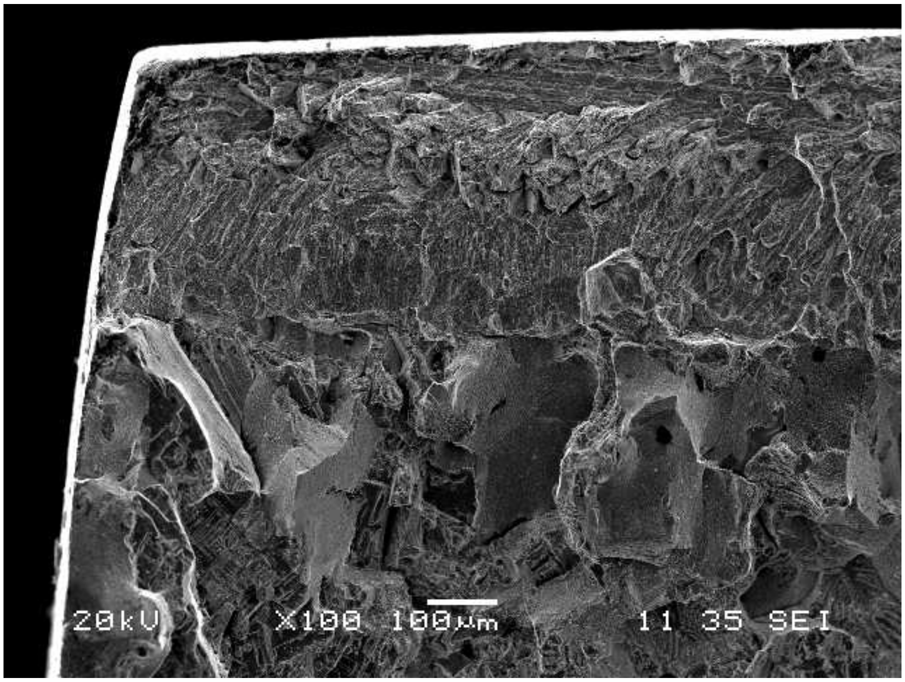

Figure 102: SEM image of fracture surface through the fusion zone and recrystallized grains, René 80 specimen, 0.2% strain

The parent material beneath the fusion reveals a coarse microstructure with appearing as large grains with a facetted fracture surface. Figure 103 is an SEM image showing the recrystallized zone in the central portion of the image. As shown in greater detail in Figure 104, the interface between the recrystallized grains and the parent material displayed cracking along the entire width of the specimen. The exposed grain surfaces along the fracture surface secondary intergranular cracking regions were relatively smooth with surface oxidation being the only notable feature as shown in Figure 104.

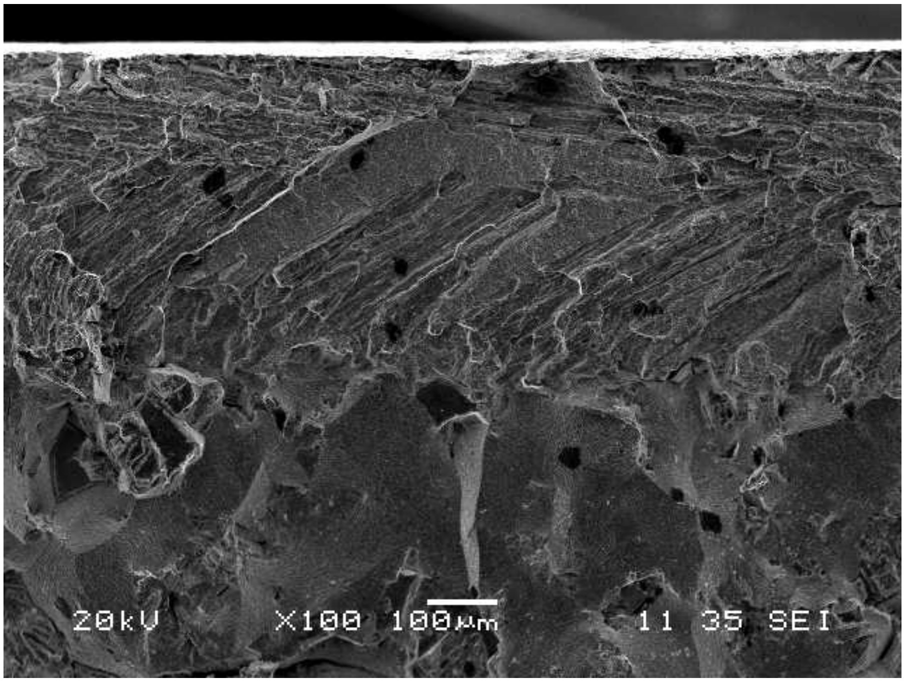

Figure 103: SEM image of the fracture surface in the fusion zone and recrystallized grains in René 80, 0.2% strain

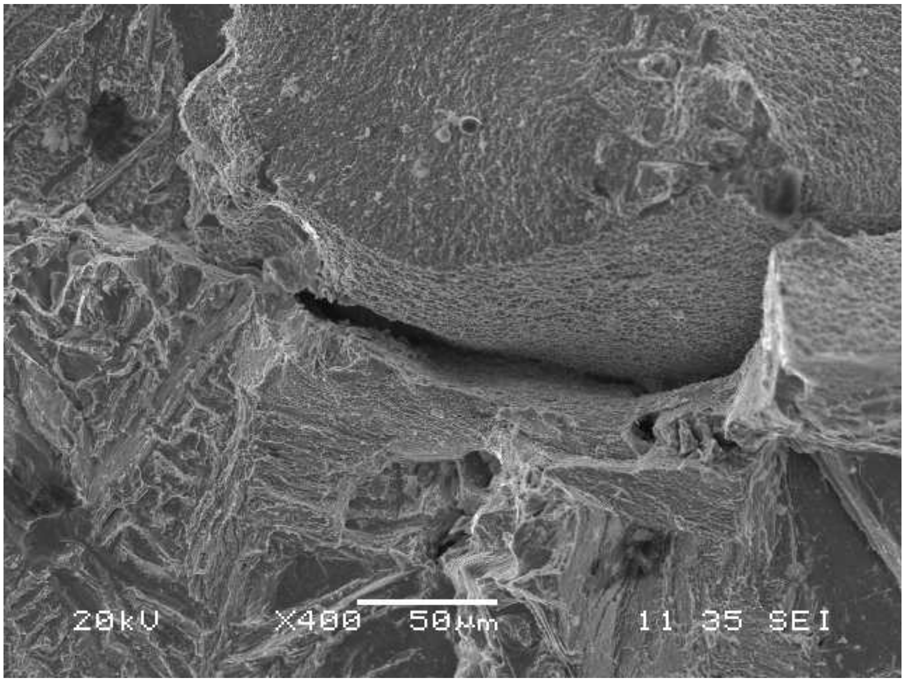

Figure 104: SEM image of intergranular cracking between the recrystallized grains in René 80 base material, 0.2% strain

The fracture surface in the recrystallized region is shown in Figure 105 and appeared relatively smooth as compared to the underlying untransformed base material. As shown in Figure 106, the remaining fracture surface along the unaltered parent material region was generally rough in texture. The fragments were examined by optical microscopy and confirmed to have undergone cracking through the weld fusion zone, extending in the recrystallized grain region followed by the parent material. Figure 107 shows matched optical micrographs of the fragments showing the fracture path along the microstructure. The cracking mechanism through the weld fusion zone appears to be intergranular. Minor secondary cracking in the weld fusion zone also occurred by intergranular fashion.

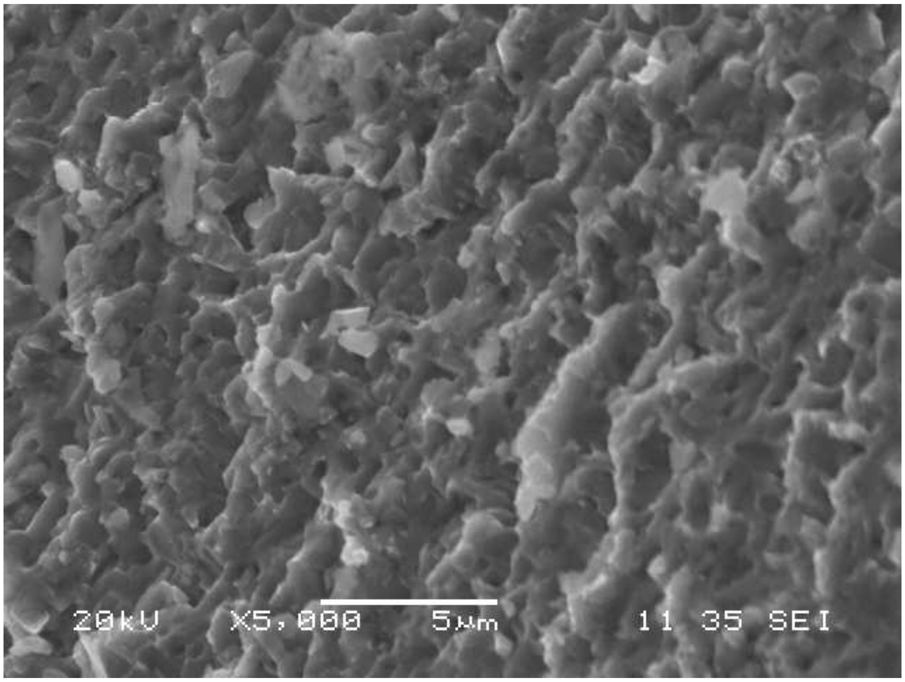

Figure 105: SEM image of the fracture surface along the recrystallized grain structure.

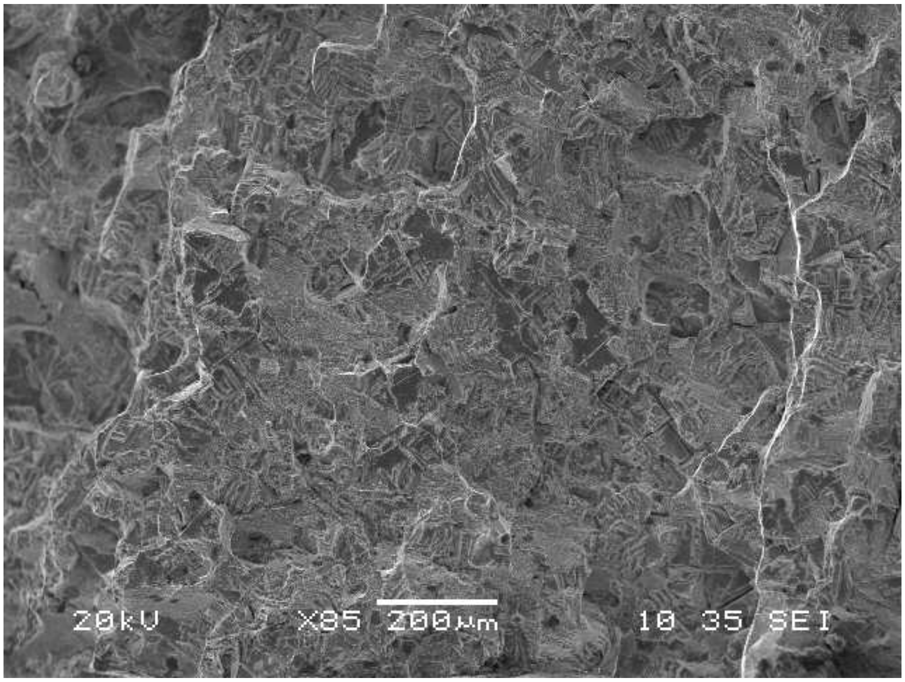

Figure 106: SEM image of the fracture surface along the parent material.

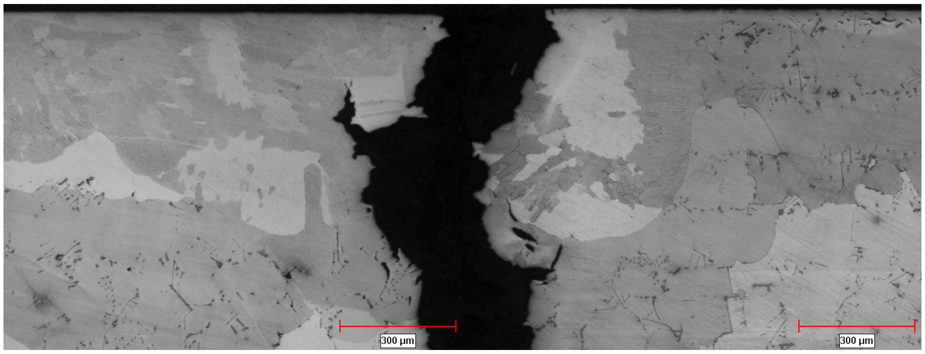

Figure 107: Optical micrographs of fracture through the fusion zone.

High magnification examination of the microstructure under the SEM revealed extensive cracking of carbides in the vicinity of the fracture surface. Due to the relatively low ductility of carbides and the localized strain and deformation by the crack propagation and specimen fracture, the carbide particles cracked perpendicular to the loading axis. Figure 108 is an SEM image showing a cracked carbide particle near the fracture surface with cracks extending in the surrounding parent material.

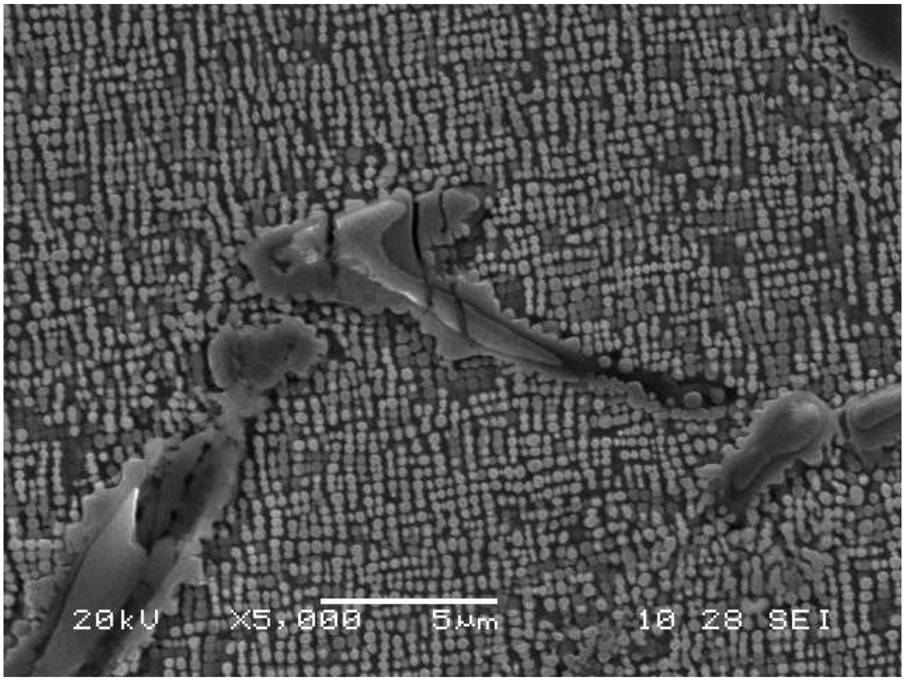

Figure 108: SEM image of cracks in carbide phase near fracture.

SEM examination of the parent material microstructure near the fracture surface showed the early stages of gamma prime rafting. As shown in Figure 109, the gamma prime particles have grown in a preferential direction due to a change in the local chemical potential energy caused by elastic strain in the specimen [64]. The observed growth and coalescence of gamma prime particles shown in Figure 109 are aligned perpendicular to the loading axis in the specimen and is consistent the mechanism of rafting under these conditions.

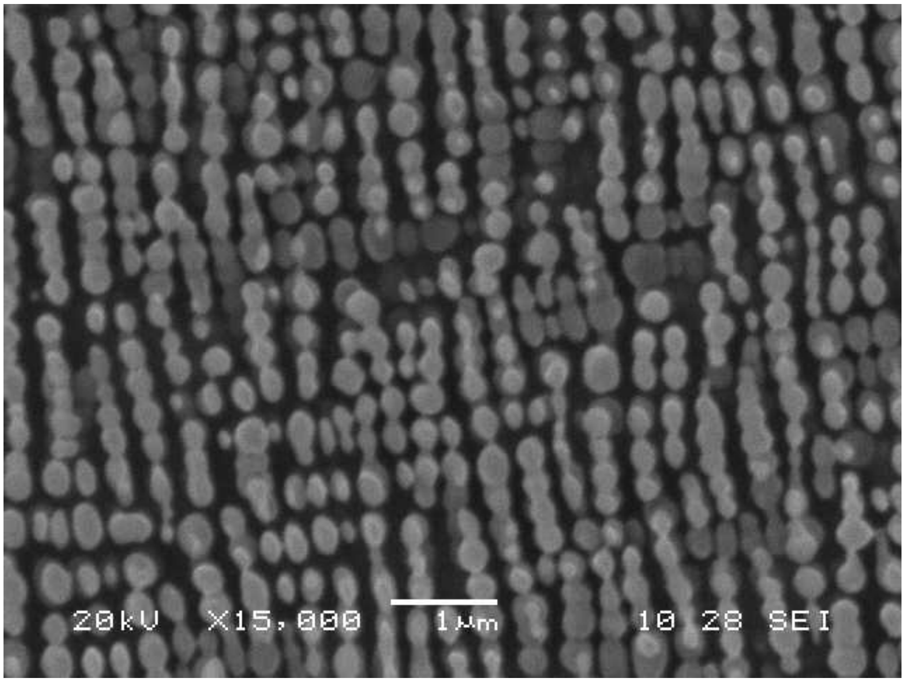

Figure 109: René 80 γ' morphology near crack surface, early stages of rafting

0.25% MECHANICAL STRAIN

One TMF specimen was tested under an applied strain of 0.25%. The specimen fractured after 4750 cycles and is shown in Figure 110. Similar to the TMF specimen tested at 0.2%, the 0.25 % strain specimen showed oxidation in the gauge section. Low magnification examination under the optical stereomicroscope showed a crack path through the weld fusion zone, recrystallized region and the parent material. The specimen facture surfaces appeared very similar to those of the 0.2% strain specimen with the exception that oxidation appeared to have occurred over the entire weld fusion zone fracture surface as shown in Figure 111. Also, the crack propagation took an intergranular path in the recrystallized regions as evidenced by the faceted grain structure being exposed.

Figure 110: Fractured 0.25% strain René 80 MF specimen

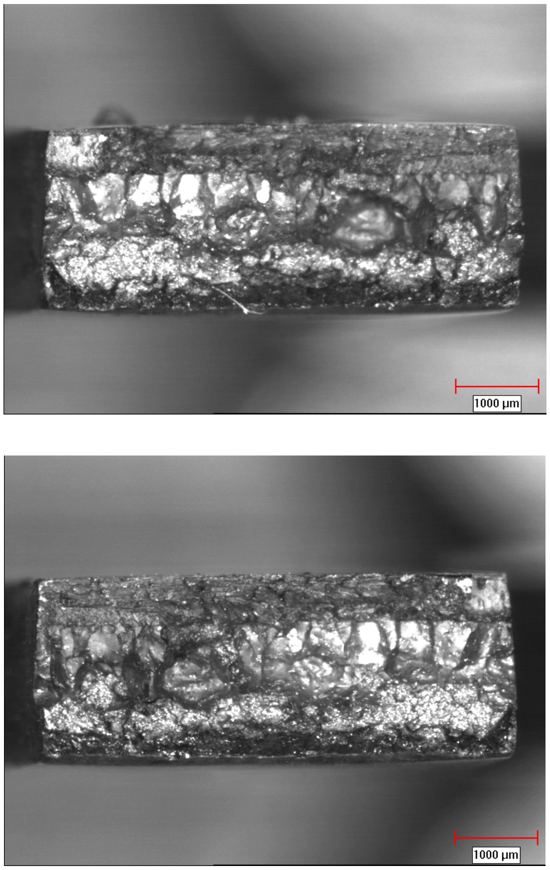

Figure 111: Fracture surfaces of 0.25% strain René 80 TMF specimen

Figures 112 and 113 are SEM images of the fracture surface along the weld fusion zone. The smoother and beach-mark regions near the specimen's top surface suggest that cracks initiated in these areas and propagated through the fusion zone and remainder of the specimen.   Recrystallized grains were visible across the entire specimen width along the weld root and subject to intergranular cracking along the boundary with the base material. As shown in Figure 114, the faceted surface of recrystallized grains is smooth with carbides visible over the general area.

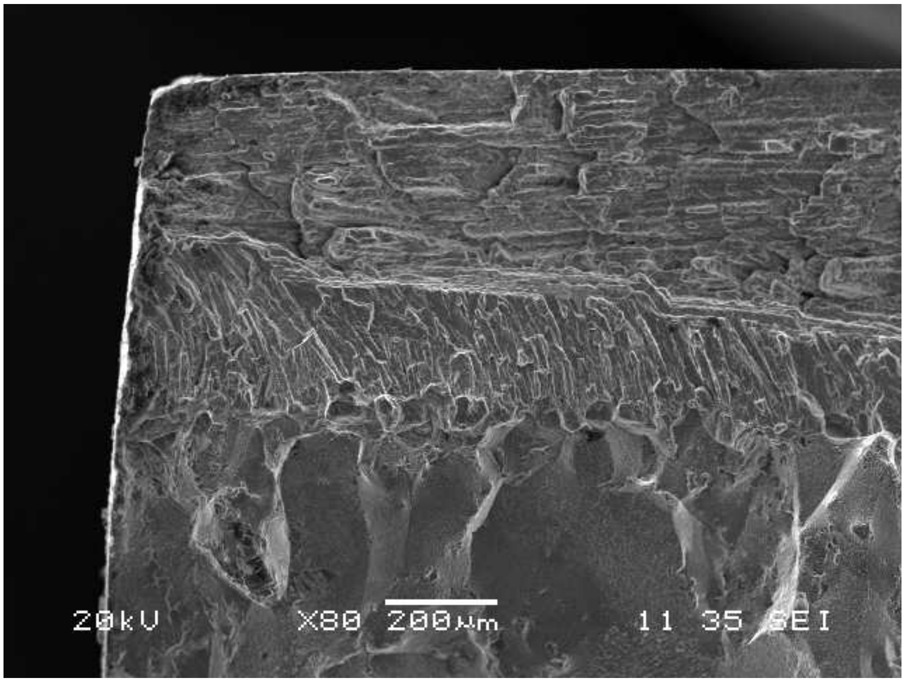

Figure 112: SEM image of the fracture surface near the specimen corner

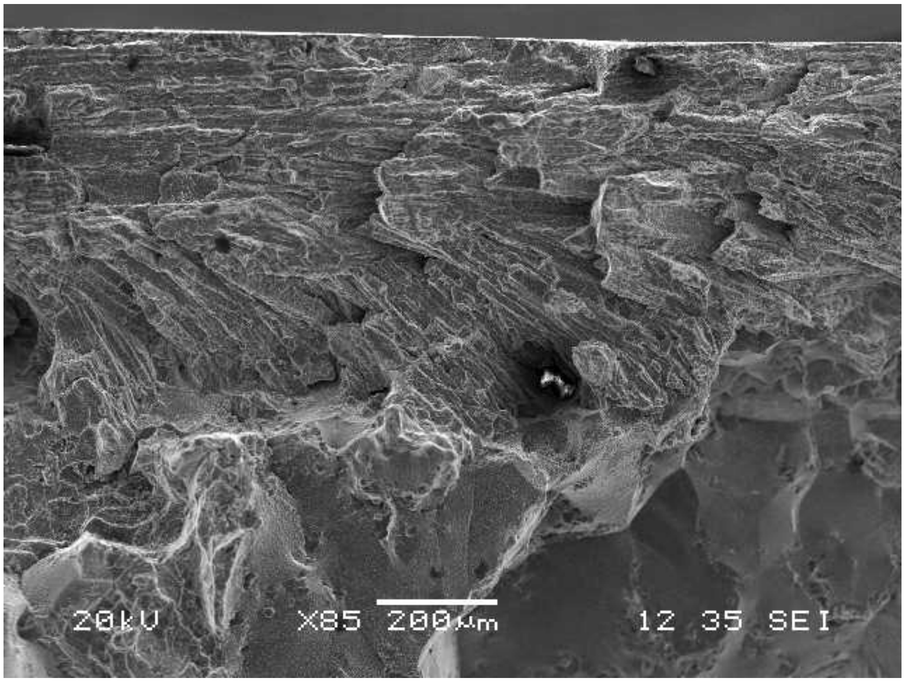

Figure 113: SEM image of fracture surface in the fusion zone near the specimen's edge

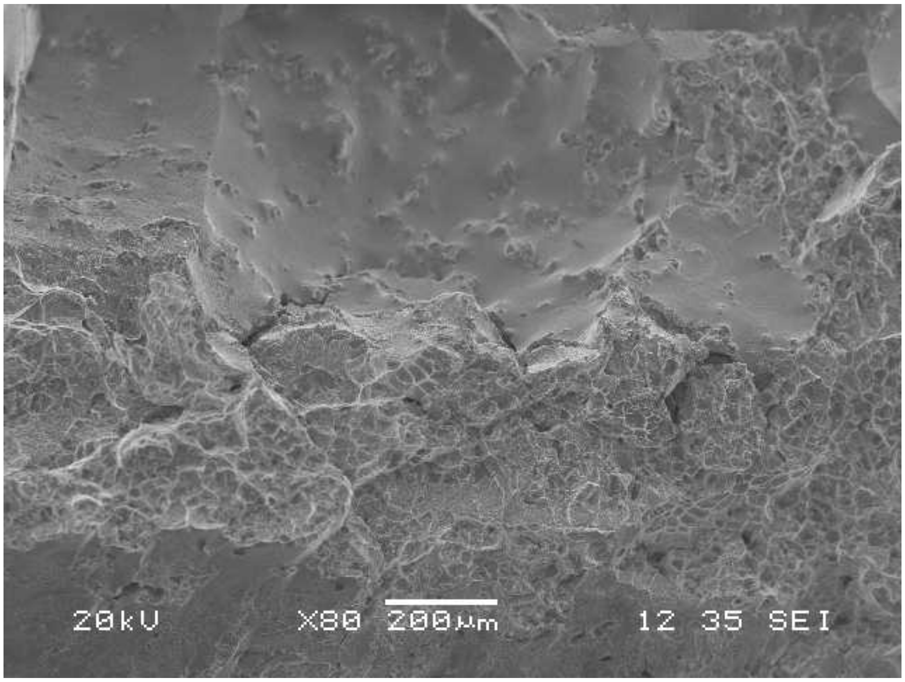

Figure 114: SEM image of fracture surface and intergranular cracking

Metallographic examination of the fusion microstructure revealed several intergranular cracks in the vicinity of the fracture. The weld fusion structure was found to be completely recrystallized after the post-weld STA heat treatment and consisted of both large and small grains. The primary crack initiated and propagated along the fusion zone and recrystallized zone. As shown in Figure 115, several intergranular cracks formed along the surface and throughout the weld fusion zone.

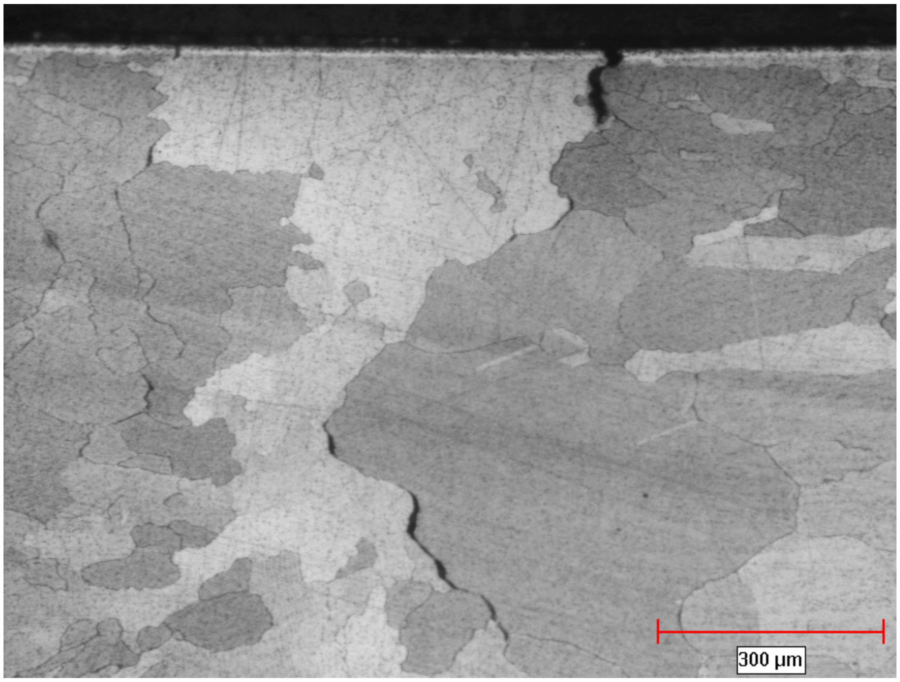

Figure 115: Micro-cracks in the weld fusion zone recrystallized microstructure.

Figures 116 and 117 are SEM images of the weld fusion zone showing the intergranular nature of cracks along the γ' phase present on the fusion zone grain boundaries. The polycrystalline structure of the fusion zone provided a path for cracks in a direction perpendicular to the loading axis. No other strengthening phases, such as carbides, were found on the grain boundaries in the fusion zone.

Surface oxidation of the TMF specimen was observed on all surface of the gauge section. The oxide film structure was comprised of a thin outer layer over a region of coarse oxide particles. Immediately adjacent to the oxide particles, was a layer of de-alloying 1 to 2 μm thick with no visible gamma prime as shown in Figure 118. Refer to Appendix O for EDS x-ray maps taken along the crack surface in the weld fusion zone.

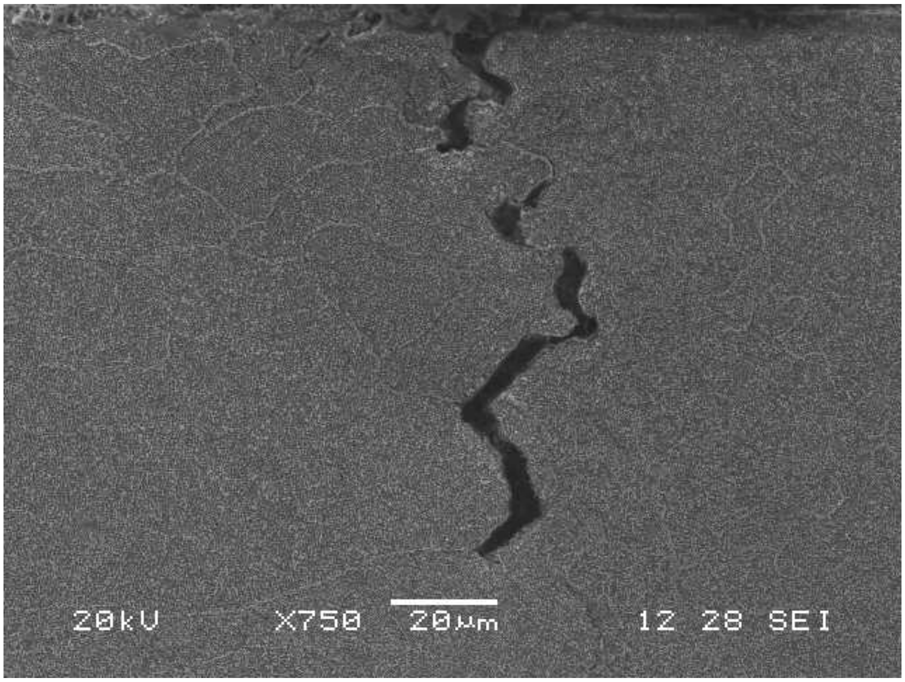

Figure 116: Micro-cracking in the fusion zone recrystallized microstructure.

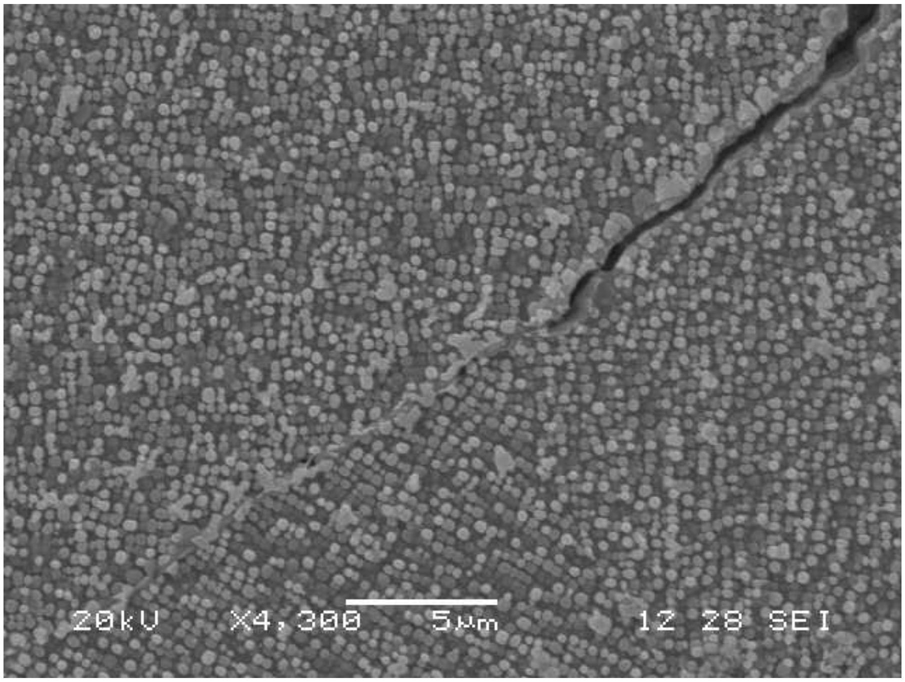

Figure 117: Intergranular crack tip in the weld fusion zone.

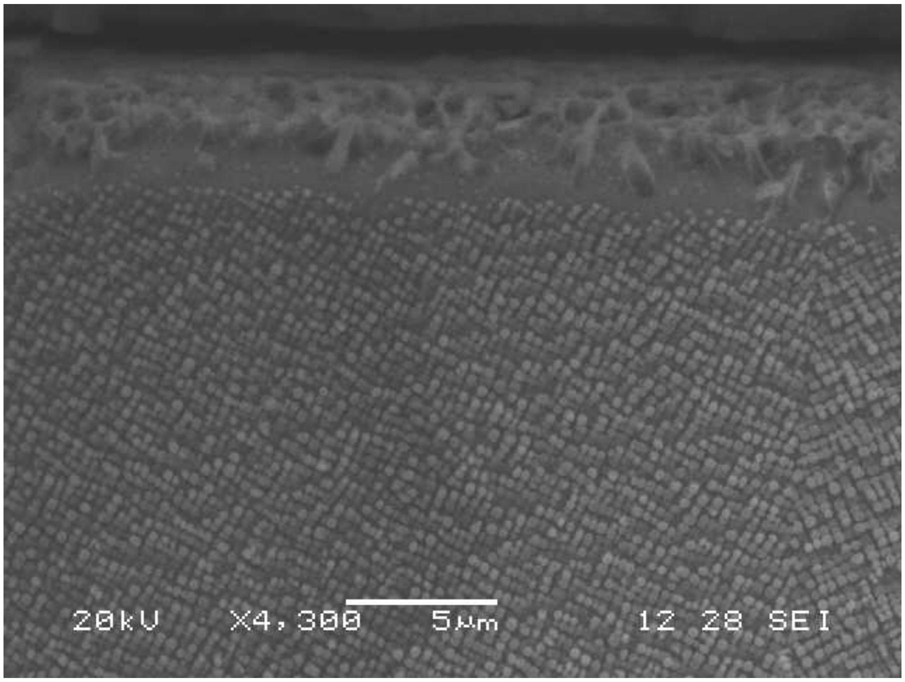

Figure 118: Surface oxidation and alloy depletion along the parent material surface.

Cracked carbides were visible in the vicinity of the fracture despite not being associated with the primary crack in the specimens. Refer to Figure 119 for an SEM image showing micro-cracked carbides in Inconel 738.

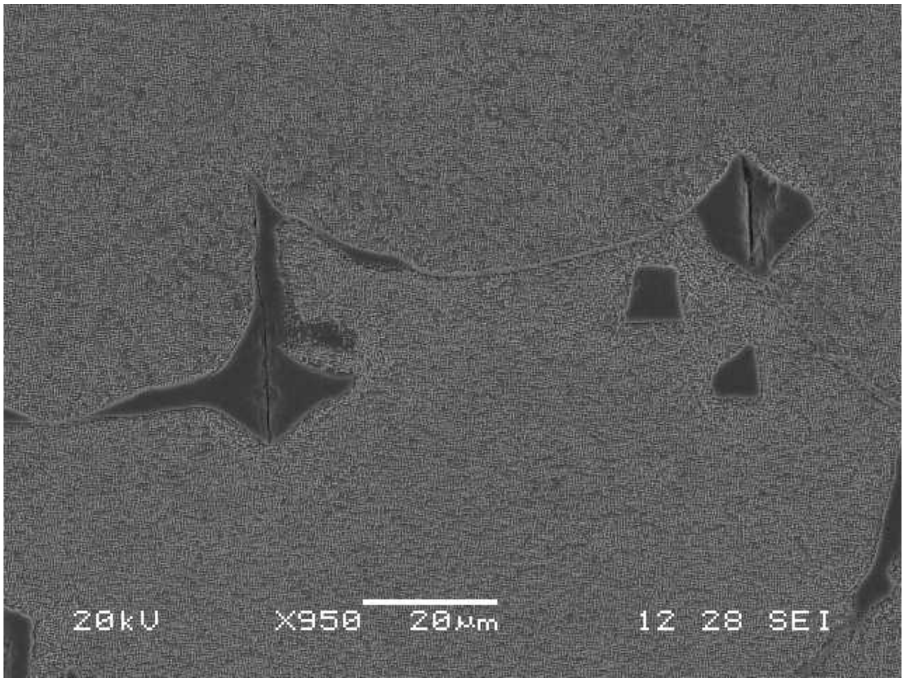

Figure 119: SEM image of cracks in the carbide phases near the fracture surface.

0.3% MECHANICAL STRAIN

The 0.3% strain specimen (Figure 120) ran for 2750 cycles until a crack was visible in the gauge length. As shown in Figure 121, the crack propagated across the specimen width to a depth of approximately 1 mm. As shown in Figure 122, the crack appears left of centre along the weld fusion zone. Metallographic assessment of the TMF specimen confirmed that the crack initiated in the fusion zone where it is widest, and propagated through to the recrystallized gains and parent material microstructures. The crack bisected the columnar grain structure of the parent material without significant change in direction and continued in a path oriented perpendicular to the loading axis on the specimen. Similar to the 0.1 and 0.2% strain specimens, the crack surface were oxidized and had an underlying layer of parent material free of γ' (Figure 123).

Figure 120: 0.3% strain René 80 TMF specimen

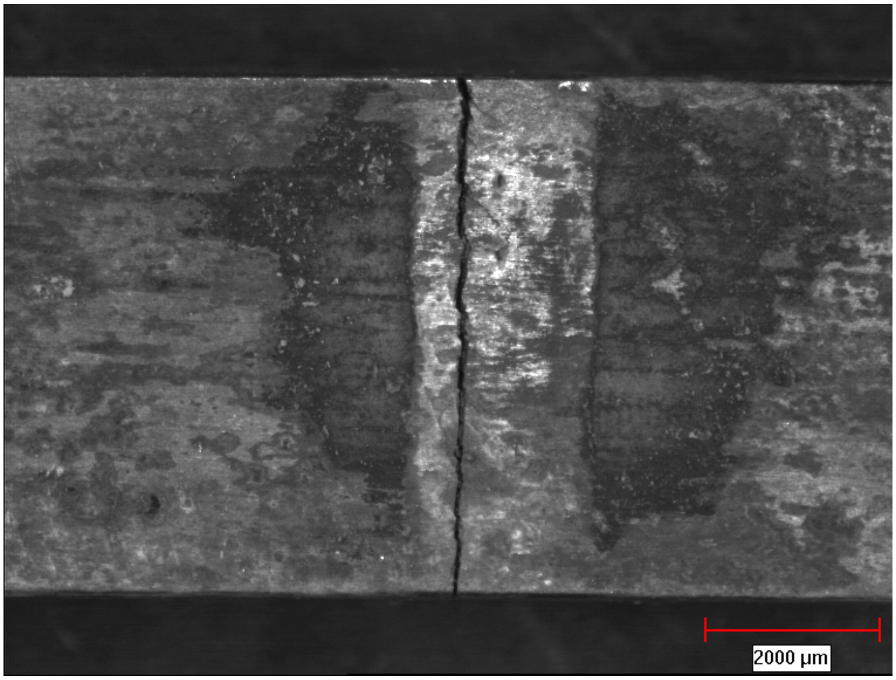

Figure 121: Crack along fusion zone, 0.3% strain René 80

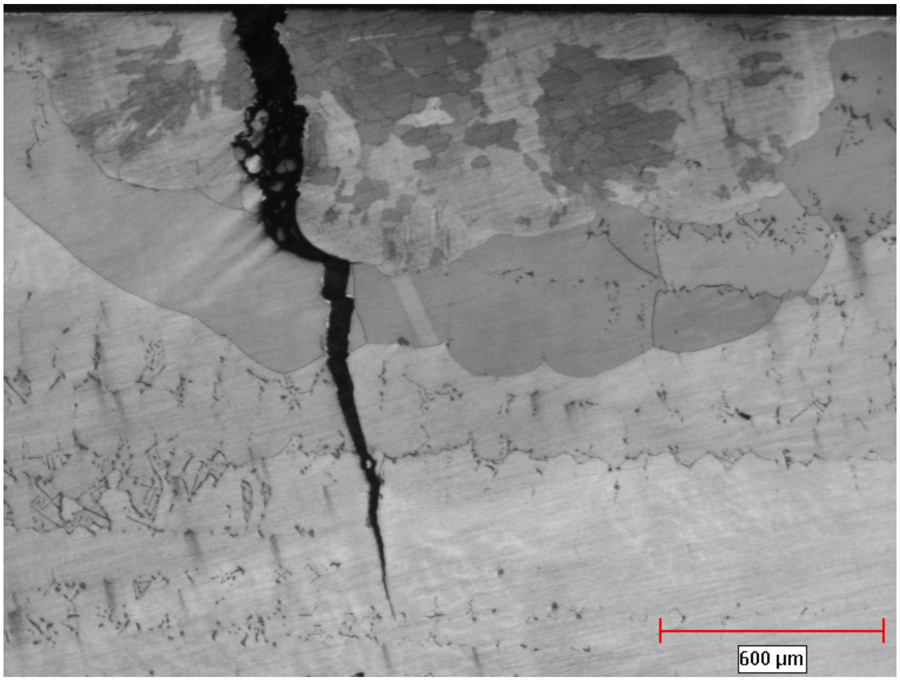

Figure 122: Optical micrograph of intergranular crack propagation through the weld fusion zone and extending in the base material

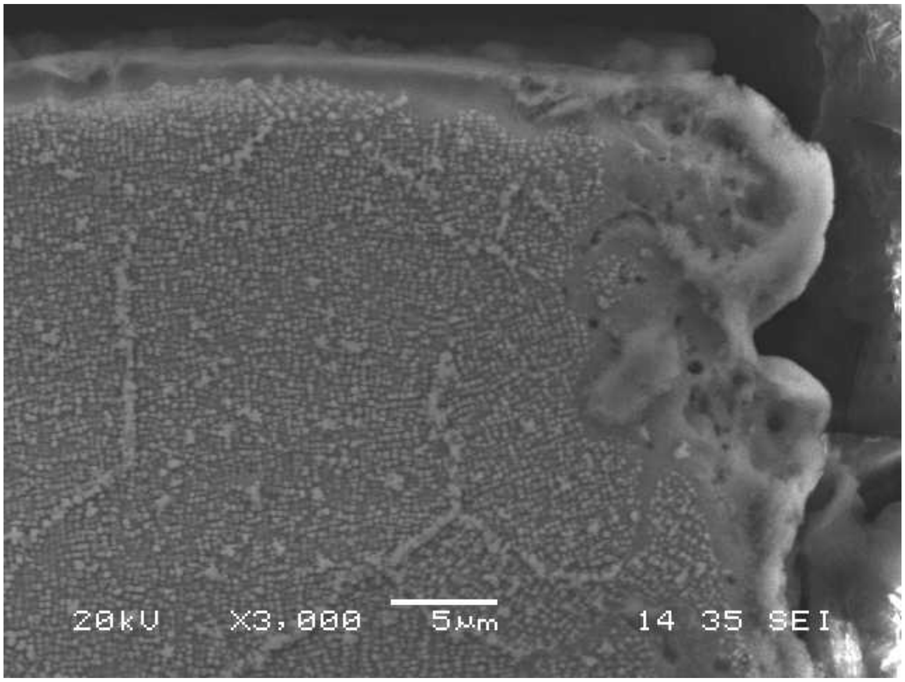

Figure 123: SEM image along crack opening in the weld fusion zone.

0.4% MECHANICAL STRAIN

The 0.4% strain specimen (Figure 124) ran for 750 cycles until a crack was detected in the gauge section. Figure 125 shows the specimen gauge section with a surface crack propagating over approximately half the width and to an approximate depth of 1 mm. Figure 126 is an optical stereomicroscope photograph showing the crack across the specimen's width.

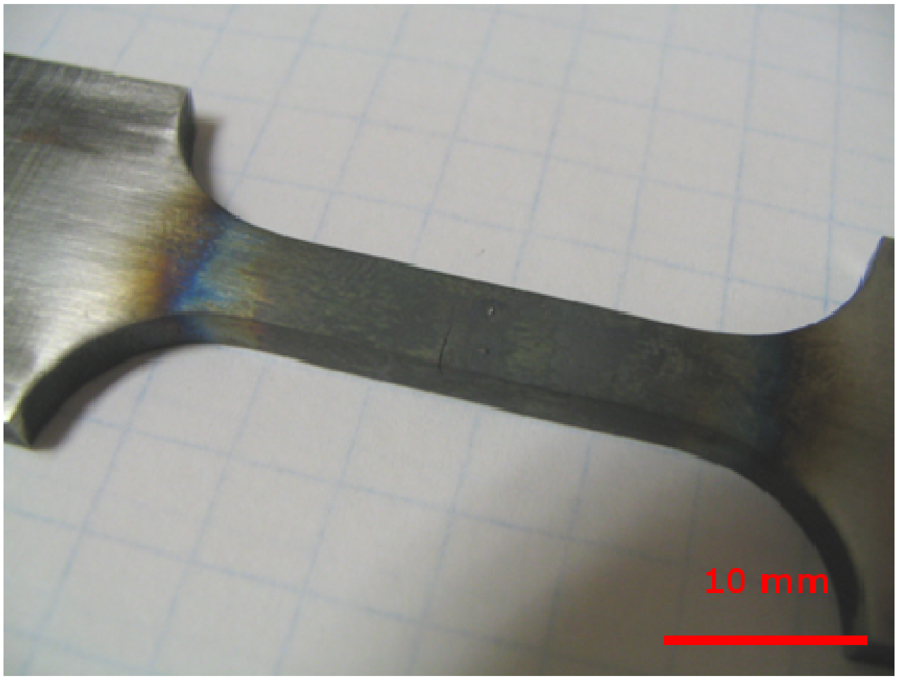

Figure 124: 0.4% strain René 80 TMF specimen

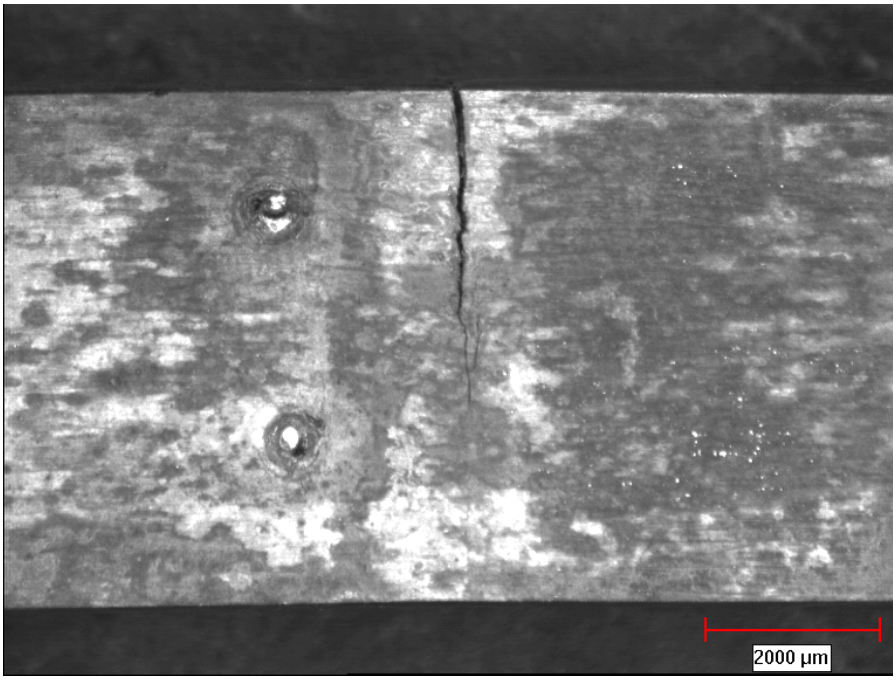

Figure 125: Crack in 0.4% strain René 80 TMF specimen along fusion zone

Metallographic examination of the gauge section revealed the crack initiation to be in the weld fusion zone, off the weld centre line, and propagating through the recrystallized grains and into the parent material. Figures 126 shows the intergranular crack path through the weld fusion zone and recrystallized grains in a René 80 specimen. Beyond the region of recrystallized grains, the crack propagates by transgranular fashion in a direction perpendicular to the loading axis as shown in Figure 127.

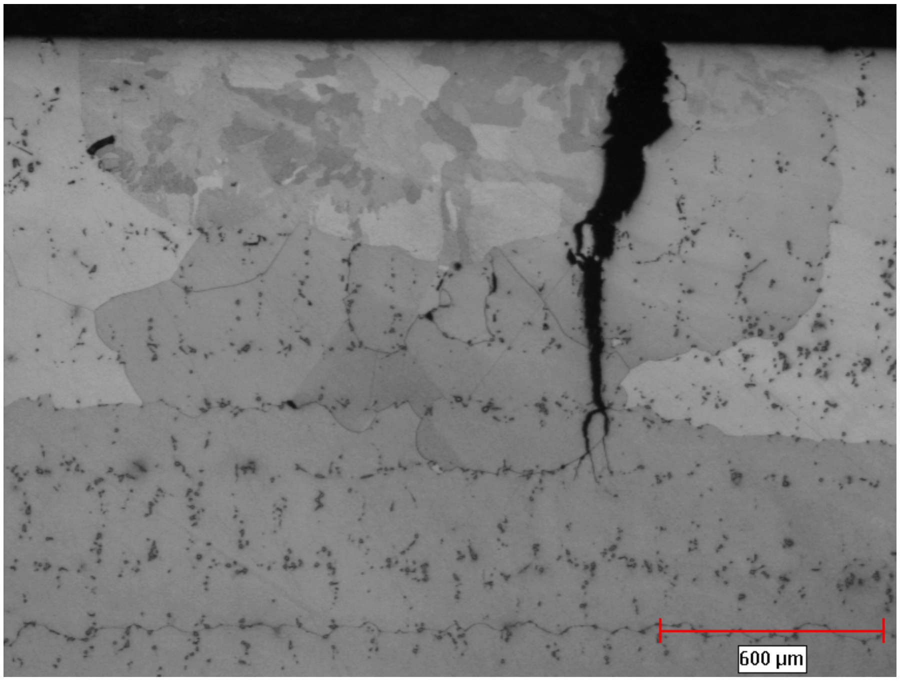

Figure 126: Optical micrograph of intergranular cracking in the weld fusion zone and recrystallized grains

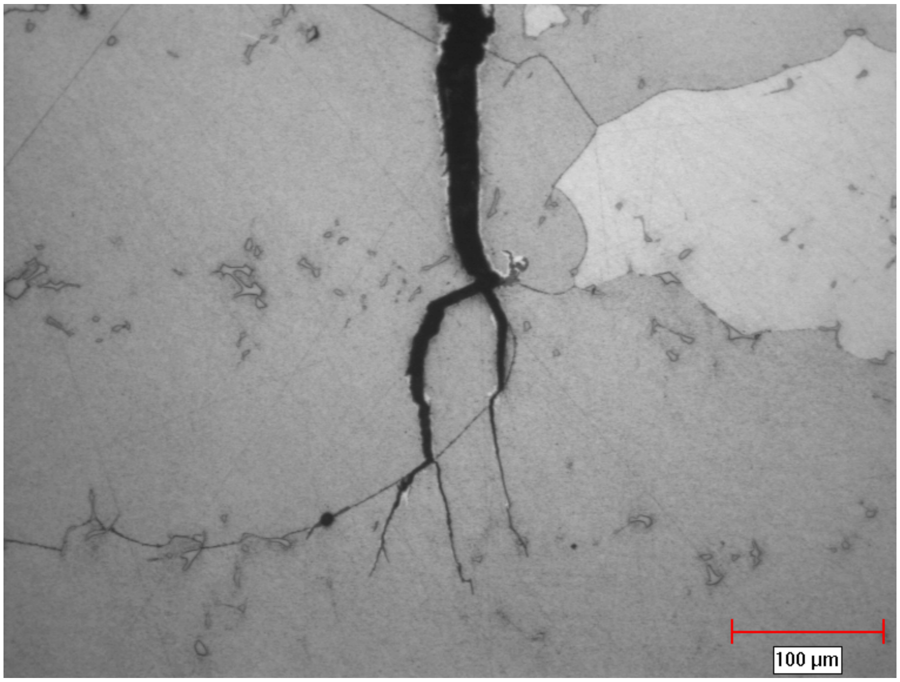

Figure 127: Optical micrograph of the branched crack in the base material

High magnification SEM examination of the crack tips in the parent material showed the presence of oxidation up to and ahead of the crack tip. Figure 128 shows an image with extensive oxidation along crack surfaces and a zone of de-alloying where the parent material is devoid of the gamma prime phase. No other significant microstructural changes were noted.

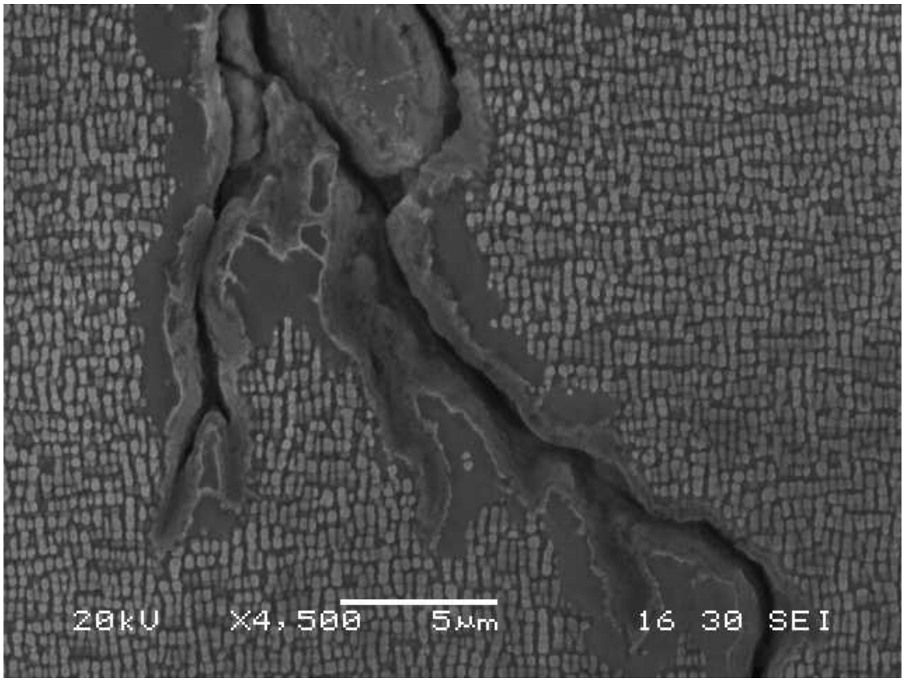

Figure 128: SEM image of the branched crack in René 80

5.6.3 René N5

0.2% MECHANICAL STRAIN

The 0.2% strain specimen did not fracture and ran the maximum allowed number of cycles (10,000). Microcracks were visible with the unaided on the specimen's top and side surfaces. Using a low magnification stereomicroscope, the cracks on the specimen's top surface were visible along the weld centerline and in the adjacent weld heat affected zone, see Figures 129 and 130. As shown in Figure 130, cracks on the specimen's edges were also visible along the weld centerline and extended through to the heat affected zone at the weld root. Crack branching along the specimen axis was also visible.

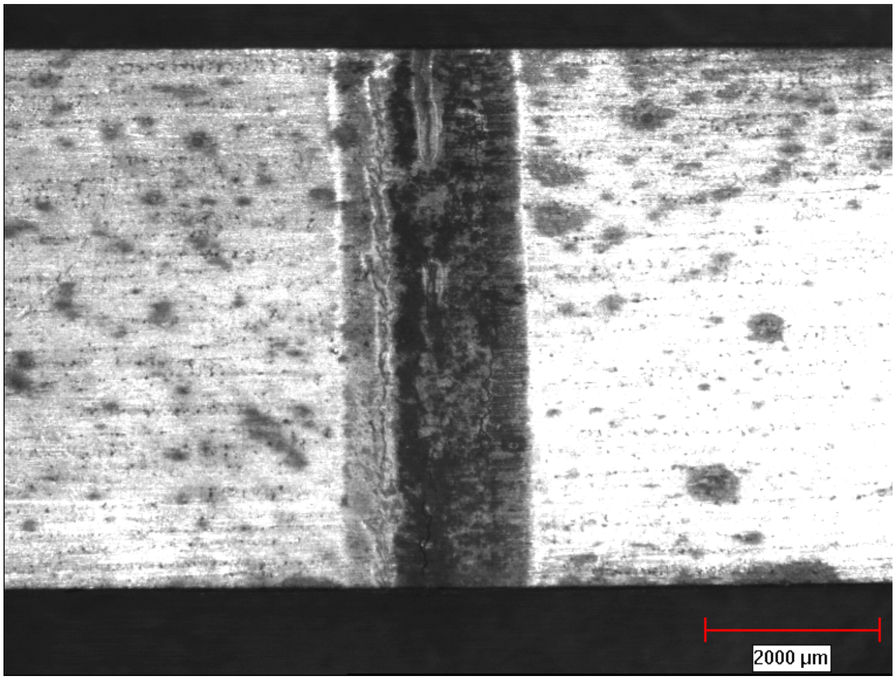

Figure 129: Top view of 0.2% strain specimen tested to 10,000 cycles (no fracture).

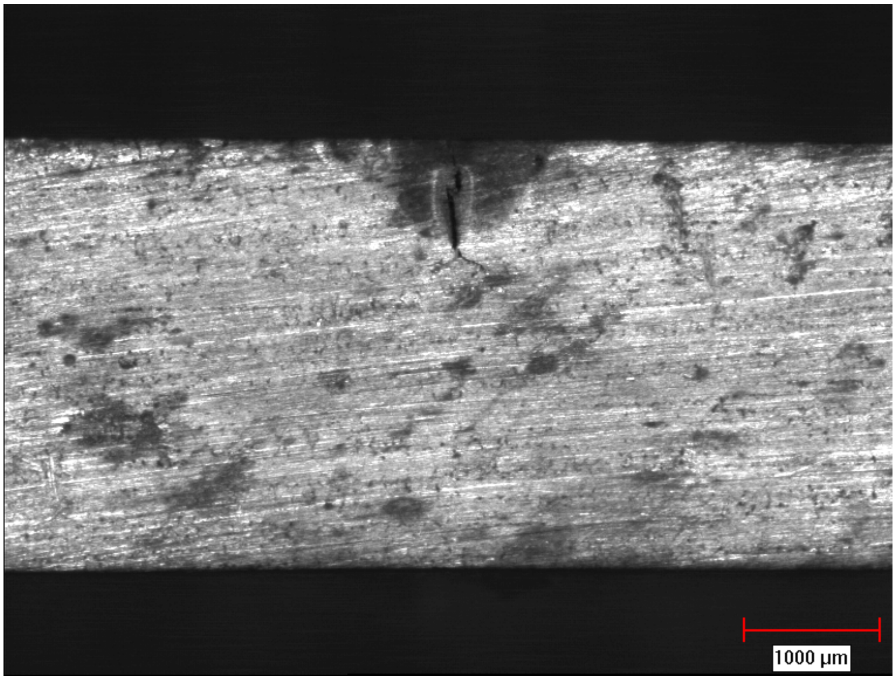

Figure 130: Side of 3mm thick 0.2 % strain specimen tested to 10,000 cycles.

Figure 131 is an optical micrograph showing that the crack initiated in the weld fusion zone near the centerline. Early crack propagation was at 45 degrees to the loading axis, along the plane of maximum shear stress. The crack propagated along the plane of maximum shear stress for approximately 150 µm and aligned itself perpendicular to the loading axis along the weld center line. The crack propagated completely through the fusion zone and eventually between recrystallized grains below the weld. The crack reached a triple point (two recrystallized grain boundaries and unchanged base material) and branched out along the recrystallized grain boundaries, parallel to the specimen axis.

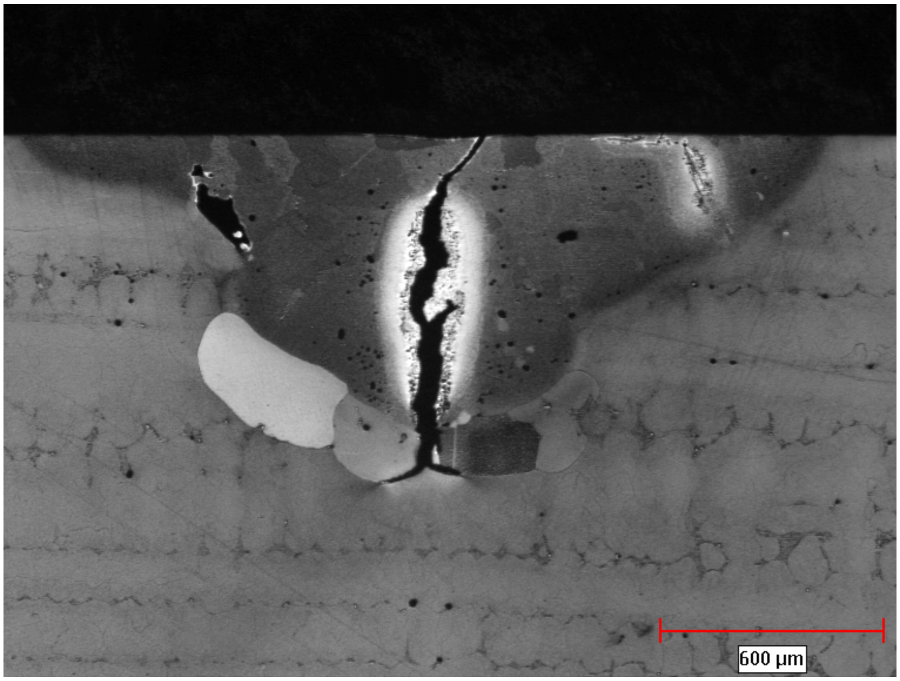

Figure 131: Optical micrograph showing cross-sectional view through crack along weld centerline (Kallings no.2 etchant).

Refer to Figures 132 and 133 for optical micrographs showing the crack propagation along the gamma prime grain boundary layer between recrystallized grains and the base material. The intergranular gamma prime layer between recrystallized grains changed morphology from blocky to large irregular gamma prime particles and are shown in Figure 134.

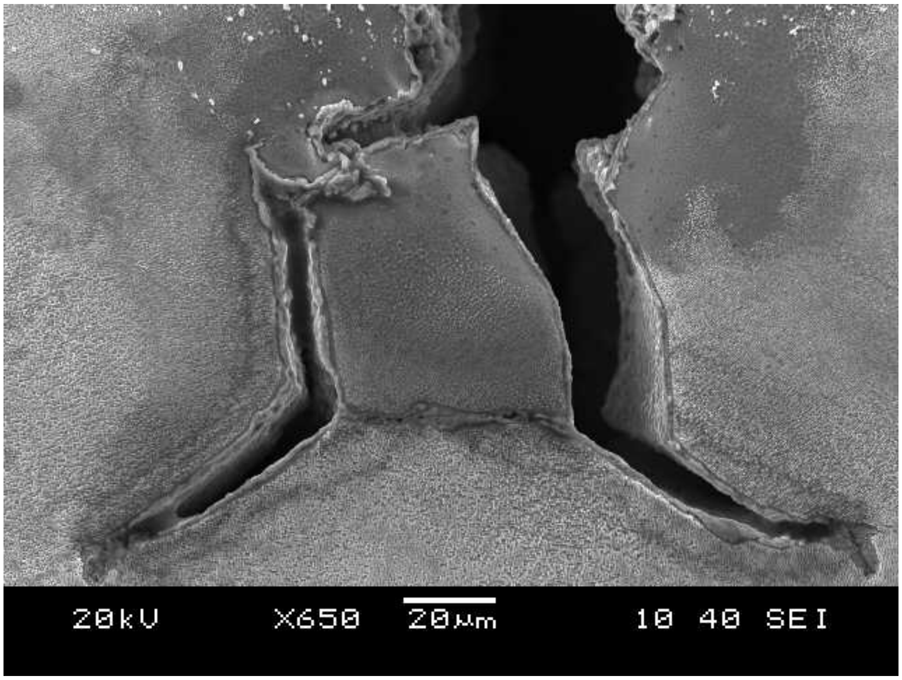

Figure 132: Intergranular cracking along between recrystallized grains in the weld heat affected zone

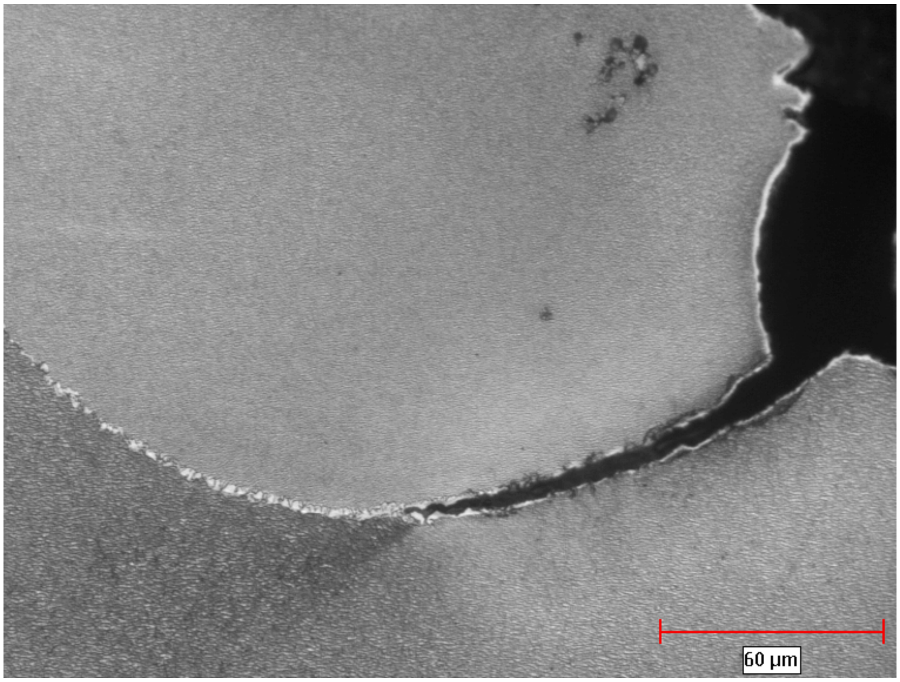

Figure 133: Crack tip along recrystallized grain boundary in the weld heat affected zone

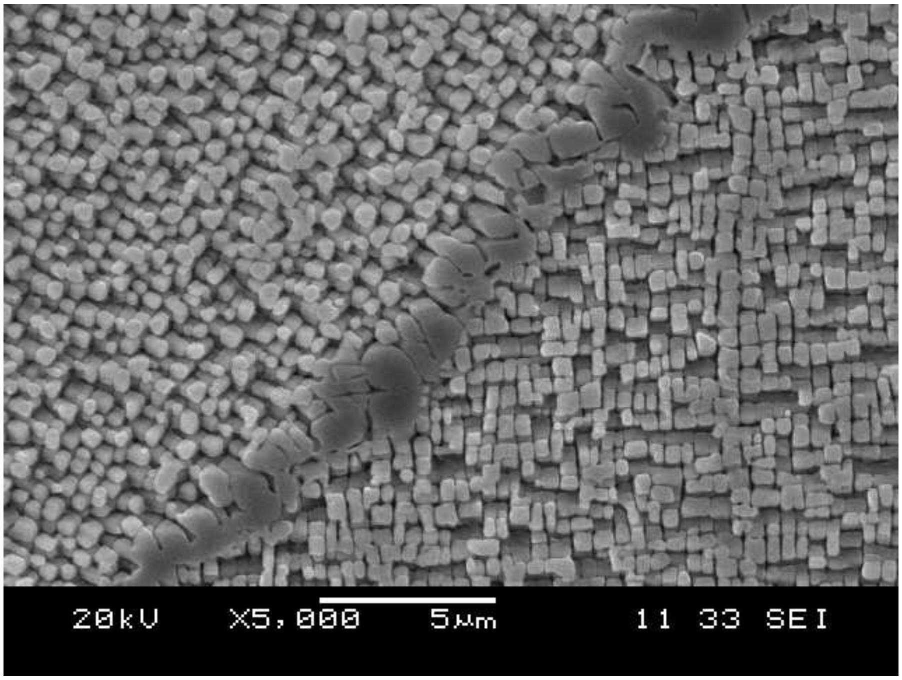

Figure 134: Typical gamma prime layer between recrystallized grains (left) and heat affected parent material (right)

Oxidation and the gamma prime depletion effect were visible up to the crack tip and the volume of material surrounding it. High magnification examination of the specimen cross-section using the scanning electron microscope revealed the presence of an oxide film on crack surfaces exposed to the test chamber atmosphere. Refer to Figures 135, 136 and 137 for SEM images showing oxidation of the crack surfaces near the specimen's surface, mid-depth and at the crack tip. Appendix Q shows EDS elemental x-ray maps for a view taken along the crack surface in the René N5 base alloy weld fusion zone.

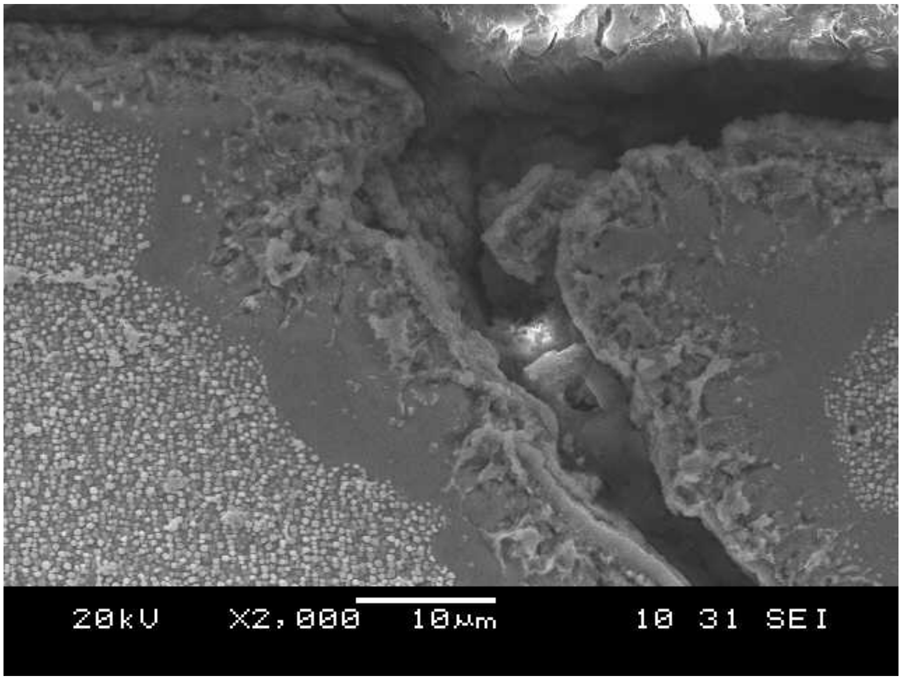

Figure 135: Crack initiation site in weld fusion zone showing oxidized surface layer and adjacent zone devoid of gamma prime phase

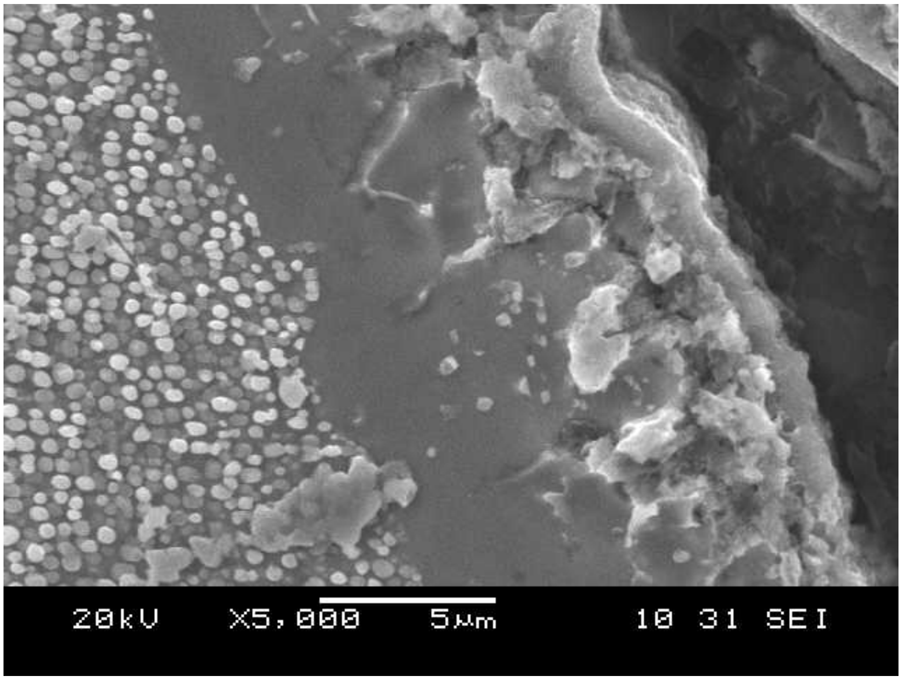

Figure 136: Higher magnification of fracture surface with oxide formation leading to dissolution of gamma prime (sharp effect).

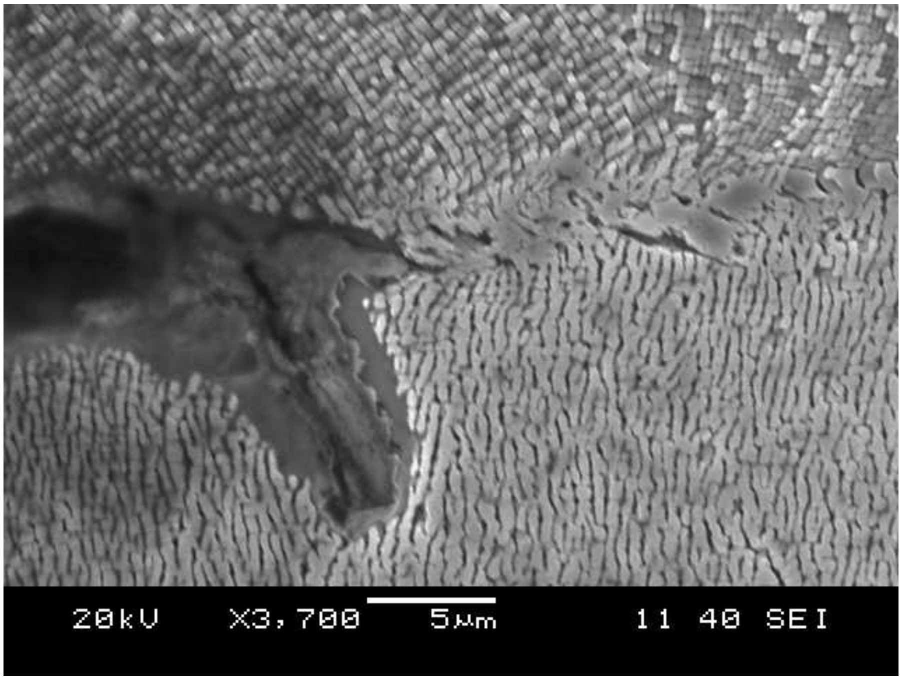

Figure 137: Typical crack tip along grain boundary.

0.3% MECHANICAL STRAIN

The 0.3% strain specimen ran to 1,450 cycles until a crack was visually detected. Using the low magnification stereomicroscope, cracks were visible through the weld centreline on the specimen's top and side surfaces, as shown in Figure 138. Small cracks were also visible in the weld heat affected zone. Under optimal microscope examination, the location of crack initiation was confirmed to be at the specimen surface in the weld fusion zone as shown in Figure 139. Similar to the 0.2% strain specimen, the initial crack orientation was 45 degrees to the specimen loading axis, along the plane of maximum shear stress. Beyond 100 µm, the crack was oriented perpendicular to the loading axis and extended through the weld fusion zone to the heat affected zone.

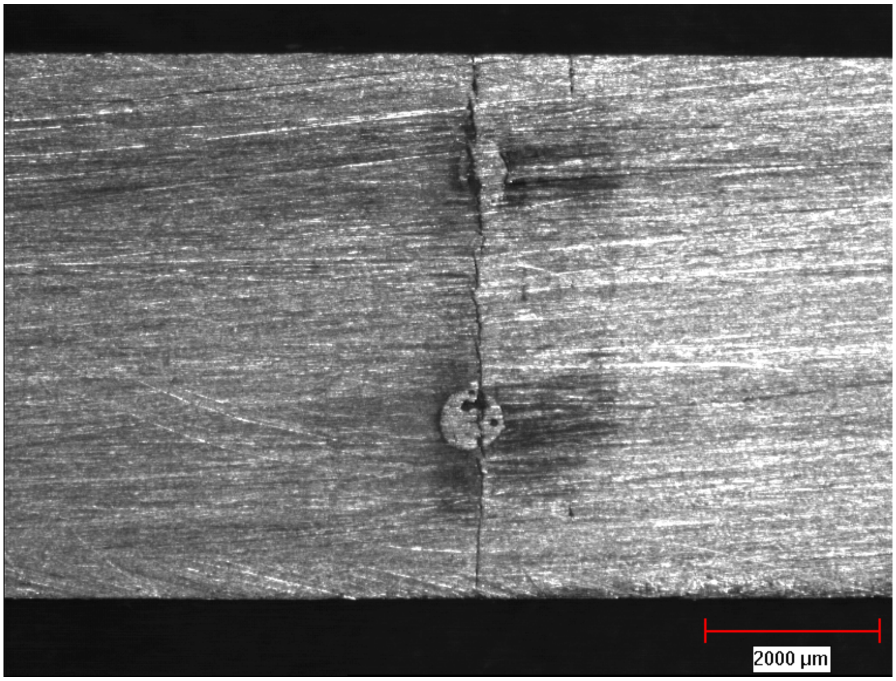

Figure 138: Top view of the 0.3% strain specimen tested to 1,450 cycles

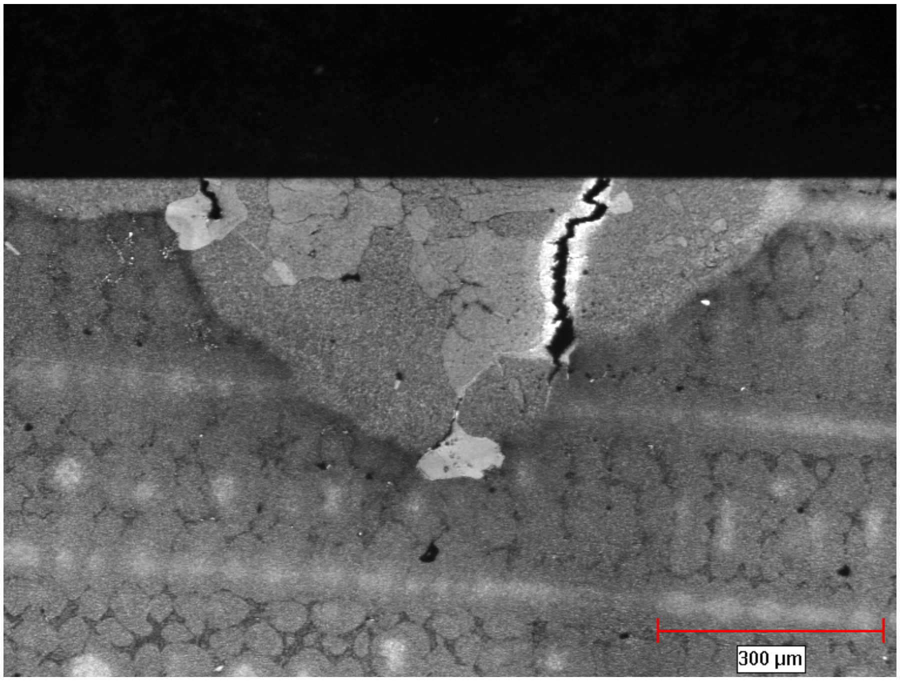

Figure 139: Optical micrograph showing cross-sectional view through crack along weld centerline

Figures 140 and 141 show SEM images of secondary cracks observed in a recrystallized grain in the weld heat affected zone. This crack is not connected to the primary crack that initiated in the weld fusion but propagated for approximately 75 µm along the brittle gamma prime intergranular layer.

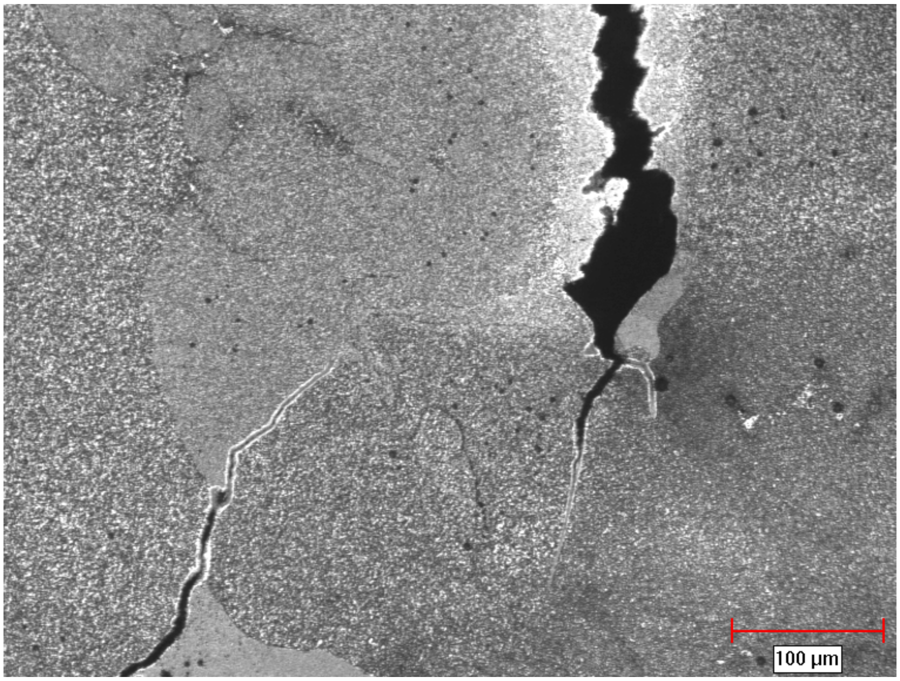

Figure 140: Crack propagation between recrystallized grains in the weld heat affected zone.

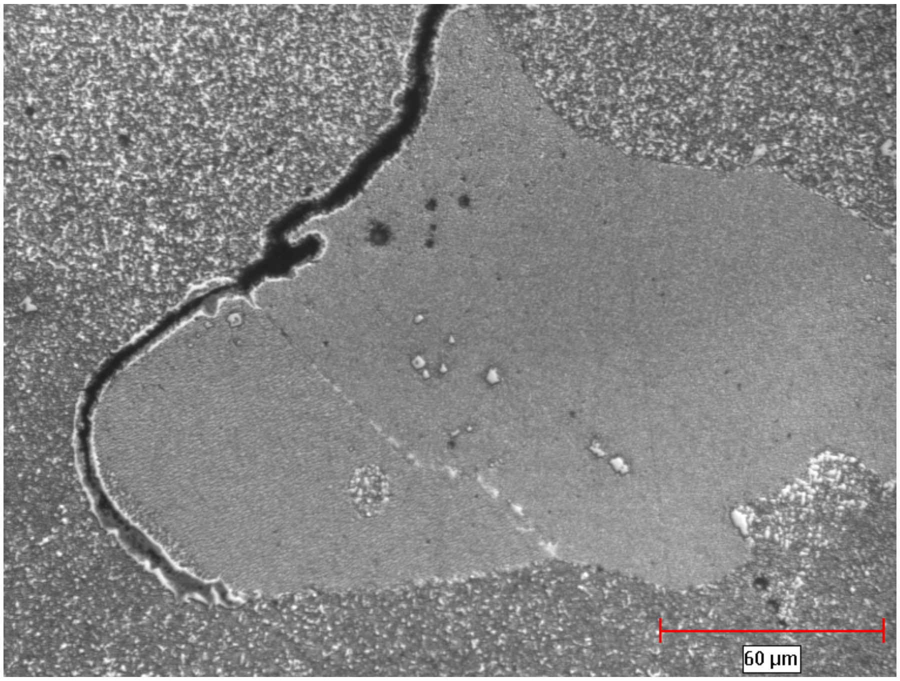

Figure 141: Crack tip along recrystallized grain boundary in the weld heat affected zone.

Molybdenum rich sulfocarbides and Cr-Mo rich borides were found in the weld fusion zone. The filler powder used for the welds was Praxair Ni-284-1 which is an equivalent to Inconel 738 in composition and therefore also susceptible to Mo-rich sulfocarbide and Cr-Mo rich boride formation. Figures 142 and 143 show SEM images of a sulfocarbide particle with neighbouring borides in the weld fusion zone. Refer to Appendix S for an EDS line scan across the sulfocarbide shown in Figure 142. A sharp increase in S concentration as compared to the surrounding material is evident.

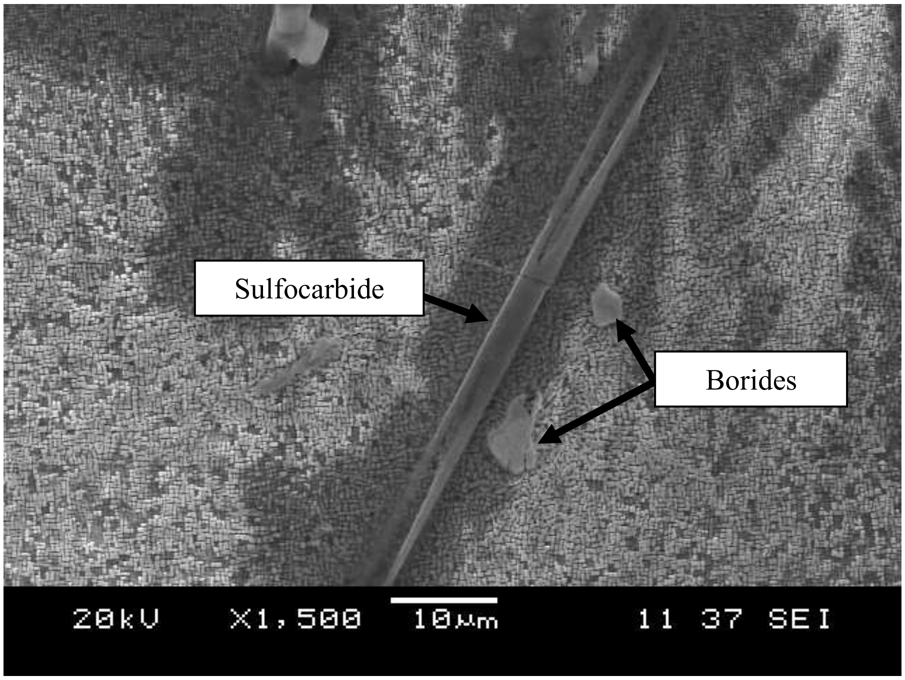

Figure 142: SEM image of sulfocarbide and borides in fusion zone.

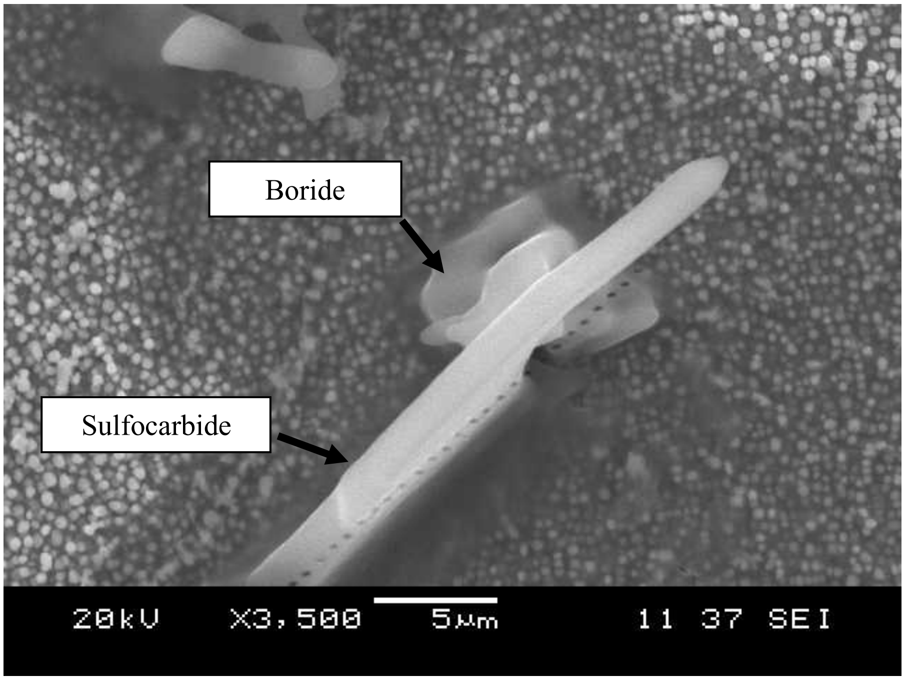

Figure 143: Sulfocarbide and chromium rich boride in weld fusion zone.

Due to shorter exposure to elevated temperatures (1,450 vs. 10,000 cycles) crack surfaces were oxidized to a lesser degree than the 0.2% strain specimen.

0.4% MECHANICAL STRAIN

Two 0.4% strain specimens were tested and fractured after 4750 and 6000 cycles. As shown in Figure 144, the specimen fractured though the weld fusion zone near the centerline.

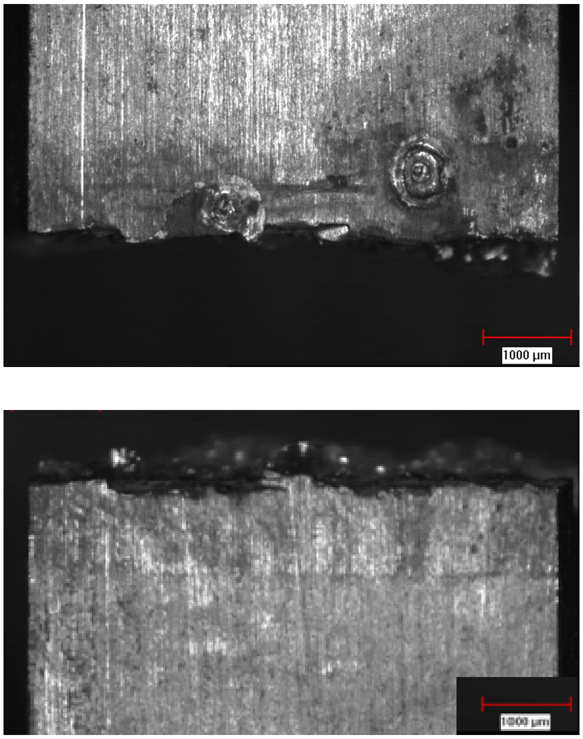

Figure 144: Top view of 0.4% strain René N5 TMF specimen

Fracture surface (end views) of both fractured surface displaying three distinct structures across the specimen width; the weld fusion zone (top), recrystallized grains in the HAZ (middle layer) and the unaltered base material (bottom) and are shown in Figure 145.

Using higher magnification on the stereomicroscope, the fracture surface was carefully examined in an attempt to determine the crack initiation site. The fracture surface displayed trans-granular topography across the weld fusion zone and unaltered base material. However, the fracture surface along the recrystallized grains followed an intergranular path with smooth and faceted surfaces as shown in Figure 146. Secondary cracks between the recrystallized grains and the untransformed base material were visible across the entire specimen width.

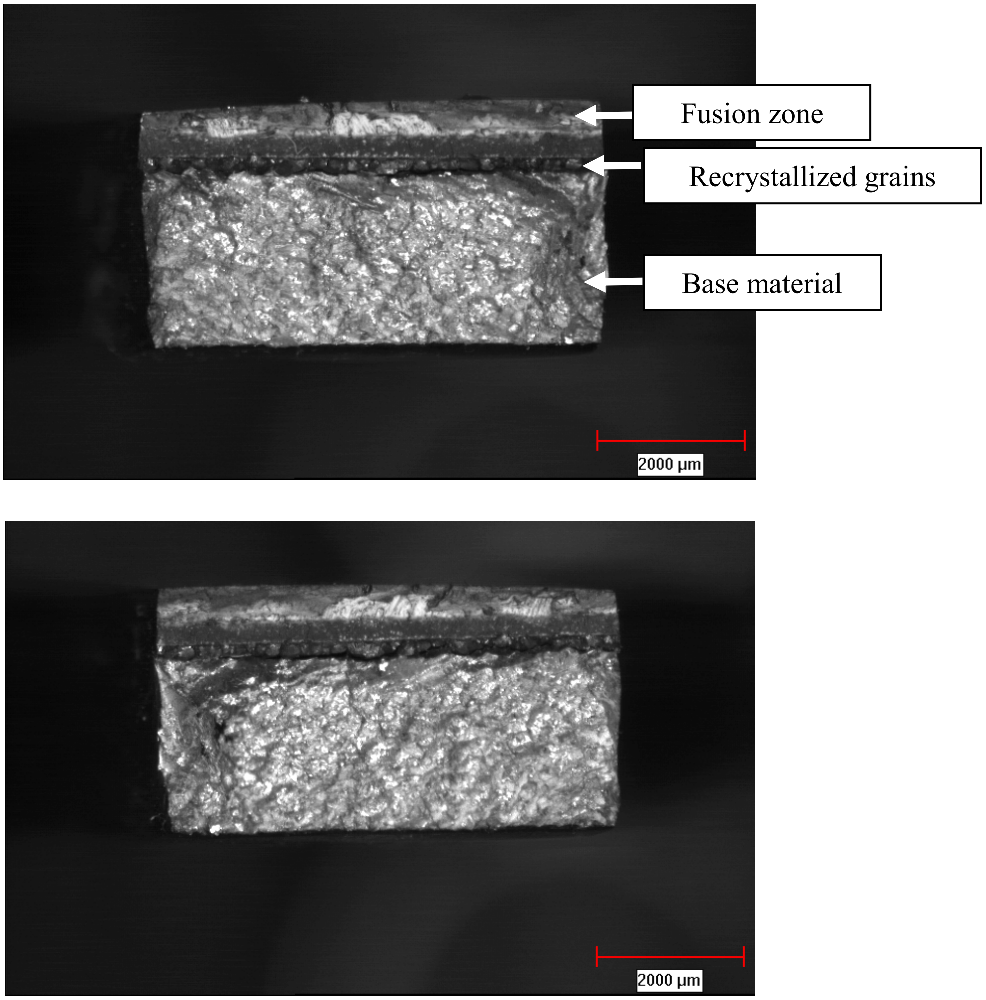

Figure 145: Fracture surfaces of 0.4% strain TMF specimen showing the weld fusion zone and recrystallized grains in the weld heat affected zone.

The difference in surface texture at the upper corners in the fusion zone shown in Figure 146 suggests that the cracks initiated at both corners and propagated across the specimens width before a re-direction along the specimen's thickness.

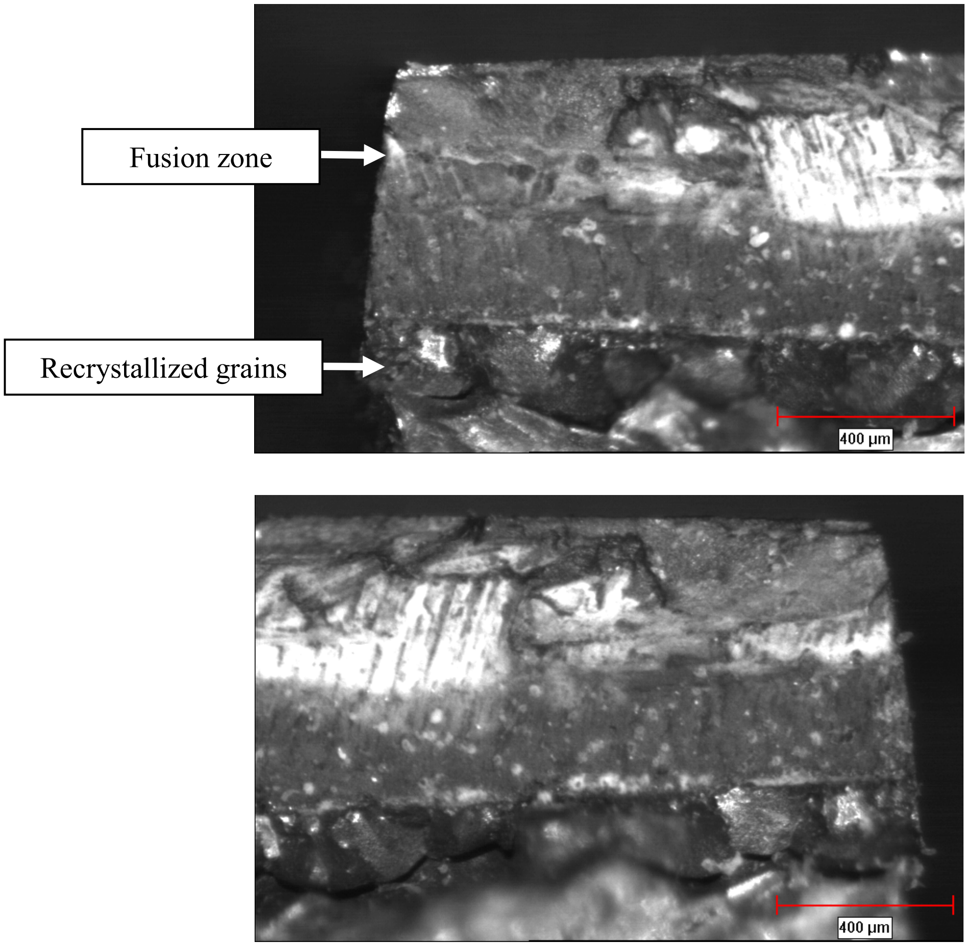

Figure 146: Crack initiation sites at corners in the weld fusion zone in 0.4 strain TMF specimen.

Examination under the optical microscope confirmed that crack initiation occurred in the weld fusion zone, approximately along the weld centerline. As shown in Figure 147, the crack propagated through the entire fusion zone and along the boundary of large recrystallized grains in the weld heat affected zone. Secondary cracks originated and propagated along the boundary between the recrystallized grain and the parent material sustaining localized intergranular cracking behaviour. The main crack followed another recrystallized grain boundary until it propagated further in the base material. The crack orientation in the unaltered base material was at approximately 45 degrees to the loading axis, along the plane of maximum shear stress for approximately 800µm prior to reorienting itself perpendicular to the loading axis until the point of fracture.

Fracture of this specimen likely occurred by the following steps:

- Initial crack formed in the weld fusion zone from a defect and propagated in a transgranular mode, perpendicular to the loading axis up to recrystallized grains (ductile)
- Crack path changed to intergranular along grain boundaries between neighbouring recrystallized grains and branched out parallel to the loading axis in the HAZ (brittle)
- The crack re-oriented itself in the parent material typical of ductile materials and eventually propagated perpendicular to the loading axis until fracture occurred

High magnification examination using the scanning electron microscope revealed a great level of detail on the facture surface. The weld fusion zone displayed a change in topography across the entire fracture surface. As shown in Figures 148 and 149, the upper half of the fusion zone primarily contained stray grains while the lower half entirely made up of epitaxial growth from planar-cellular-dendritic solidification parallel to the thermal gradient during post-weld cooling. Figure 149 shows the recrystallized grains along with a continuous crack between them and the base material.

High magnification examination of the fracture surface on recrystallized grains revealed the gamma prime layer along which the crack propagated in a brittle fashion. In contrast, the fracture surface in the parent material far from the HAZ exhibited a moderately ductile fracture mode by micro-void coalescence. Refer to Figures 150 and 151 for SEM images comparing the fracture surface along recrystallized grains and the parent material.

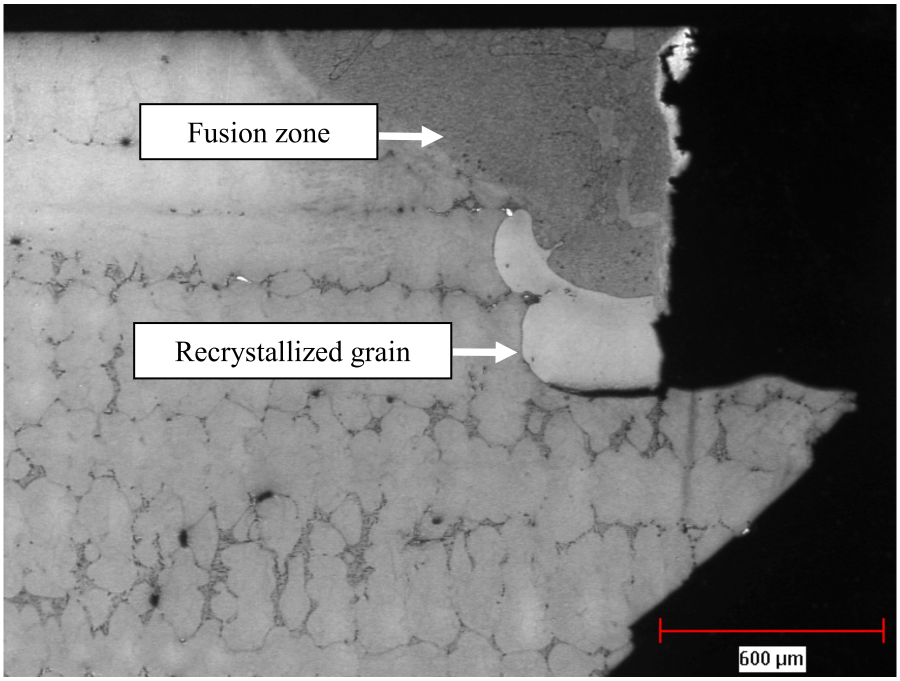

Figure 147: Optical micrograph showing crack through the weld fusion zone and extending in the weld heat affected zone. MTU etchant.

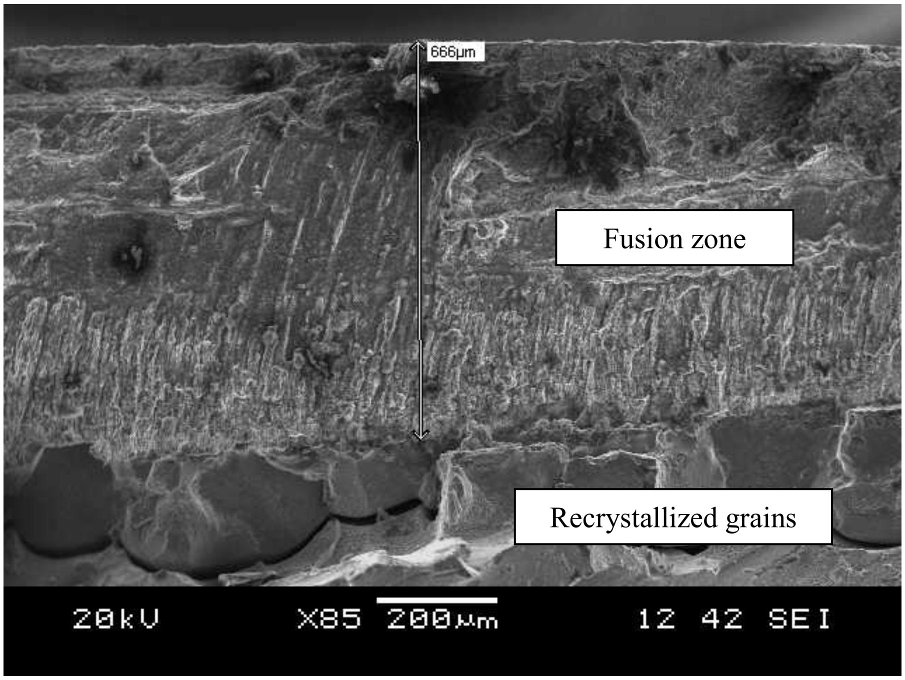

Figure 148: SEM image of crack through weld fusion zone and recrystallized grains

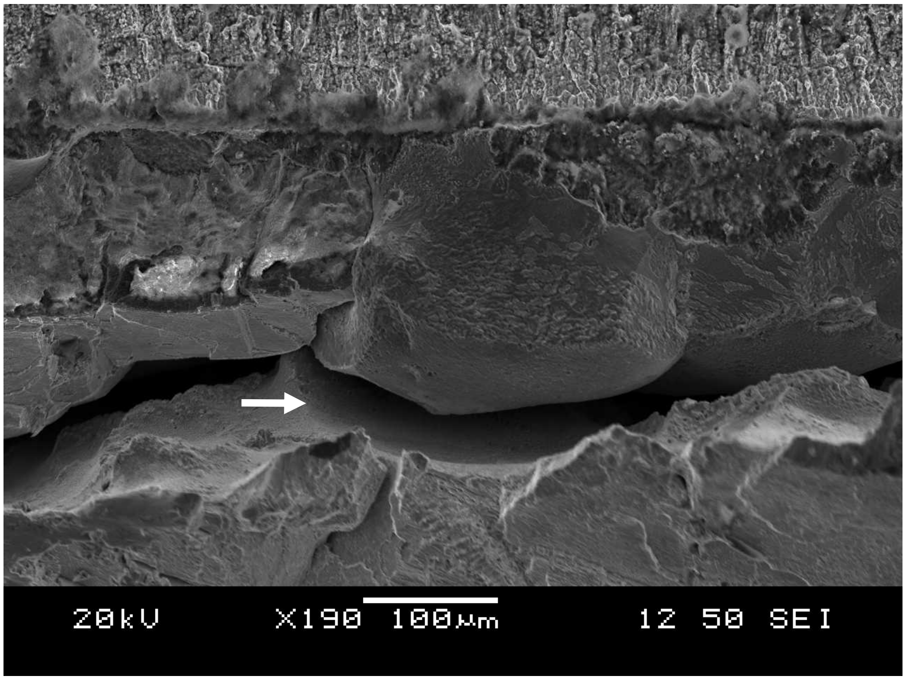

Figure 149: SEM image of intergranular cracking between recrystallized grains and the parent material

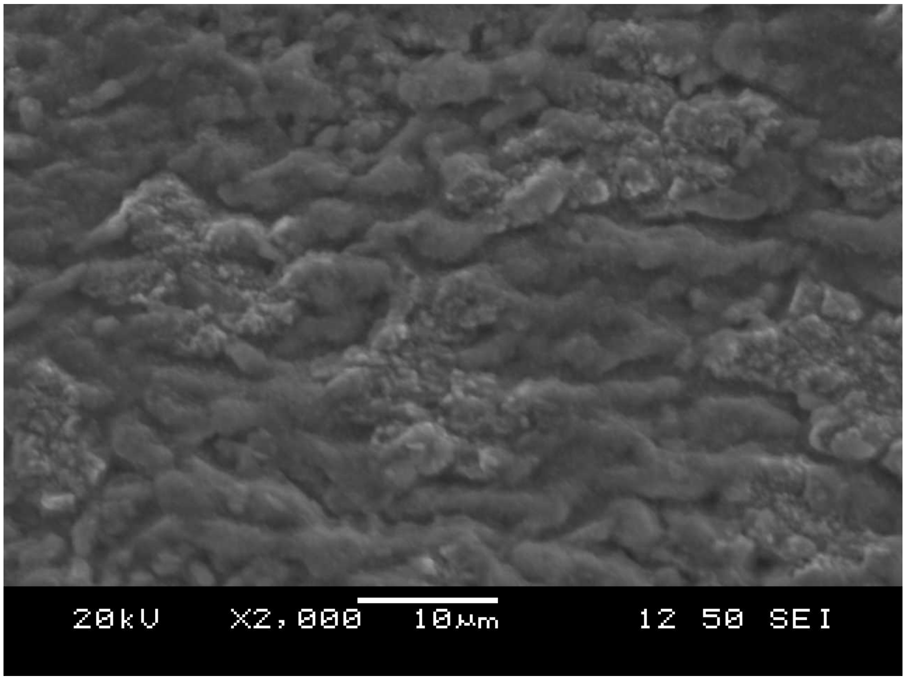

Figure 150: SEM image of fracture surface on recrystallized grains through the gamma prime film/layer

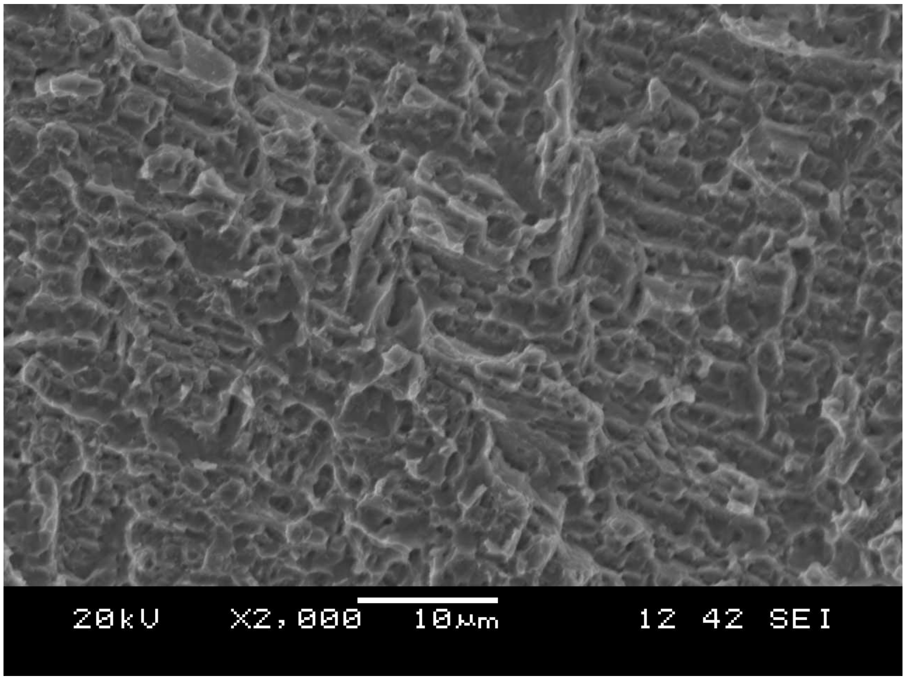

Figure 151: SEM image of fracture surface in parent material (more ductile in appearance)

5.6.4 Discussion of Results for Fractography

In this study, crack initiation in laser beam welded thermo-mechanical fatigue specimens occurred in the fusion zone for all three base alloys evaluated. In all cases, primary cracks originated in the fusion zone, along a random grain boundary in the equiaxed solidification microstructure. Fractured specimens showed evidence of crack initiation along the specimen top surface and corners with smooth and finely striated regions consistent with 'thumbnail' type of fatigue cracking initiation sites [65]. In addition to the primary crack which led to fracture in some specimens, several secondary cracks were observed in the fusion zone microstructure. As shown in Figure 115, several microcracks formed along fusion zone grain boundaries. Therefore, the initiation of primary fatigue cracks in the LBW specimens tested in this study was entirely related to random (high angle) grain boundaries in the weld fusion zone. Although the presence of stray grains did not cause cracking during the weld thermal cycle cooling and the subsequent post-weld STA heat treatment, the grain boundaries were susceptible to crack initiation and growth under cyclic thermo-mechanical fatigue conditions.

Surface oxidation of the fusion zone and base material was observed on LBW and baseline specimen with a corresponding zone free of the γ' strengthening phase. Nickel base superalloys form oxides from Al, Ti and Cr present in the base metal. Oxides are possible with many common alloying elements, but the standard free energies of formation for Al_3O_2, Ti_2O and Cr_2O_3 are the highest and will favour their formation as stable oxides at elevated temperatures [66]. Since Al, Ti and Cr are consumed in the formation of oxides at or near the alloy surface, the concentration of these elements is depleted to a depth dependent on the duration of exposure to the oxidizing atmosphere.

Energy dispersive x-ray spectroscopy (EDS) in the elemental mapping and line scan modes detected oxygen in high concentrations in the surface scales along with internal precipitate particles. Metallic elements such as aluminum, chromium and titanium were found to be in significantly higher concentrations in the regions of high oxygen concentration. Therefore, assuming stochiometric compositions, it is concluded that Al_2O_3, Cr_2O_3 and TiO_2 oxides were formed at or near the specimen surfaces exposed to the elevated temperature oxidizing environment of the Gleeble testing machine.

The formation of oxide species is explained by the second law of thermodynamics written in terms of the Gibbs free energy (G) as [66]:

$$G = H - T\ S$$

where H is the enthalpy and S' is the entropy of the system.

Under these conditions, the second law states that if:

$\Delta G < 0$	the reaction is spontaneous
$\Delta G = 0$	equilibrium is maintained
$\Delta G > 0$	no reaction occurs

As shown in Figure 152, at 900ºC the Gibbs free energy of formation of Al_2O_3, Cr_2O_3 and NiO are -860, -540 and -280 kJ/mol O_2, respectively. The stability of an oxide species is related to its relative position on the plot, with lower positions being more stable. The equilibrium oxygen partial pressure is determined by plotting a line from the point of origin in the upper left corner through the desired temperature on the species' line and extending it to the lower scale. Therefore at 900ºC, the equilibrium partial pressure for Al_2O_3, Cr_2O_3 and NiO are 10^{-38}, 10^{-24} and 10^{-12} atm O_2, respectively. Increasing the oxygen partial pressure above the equilibrium will form oxides while reducing the oxygen partial pressure below equilibrium will decompose the oxide.

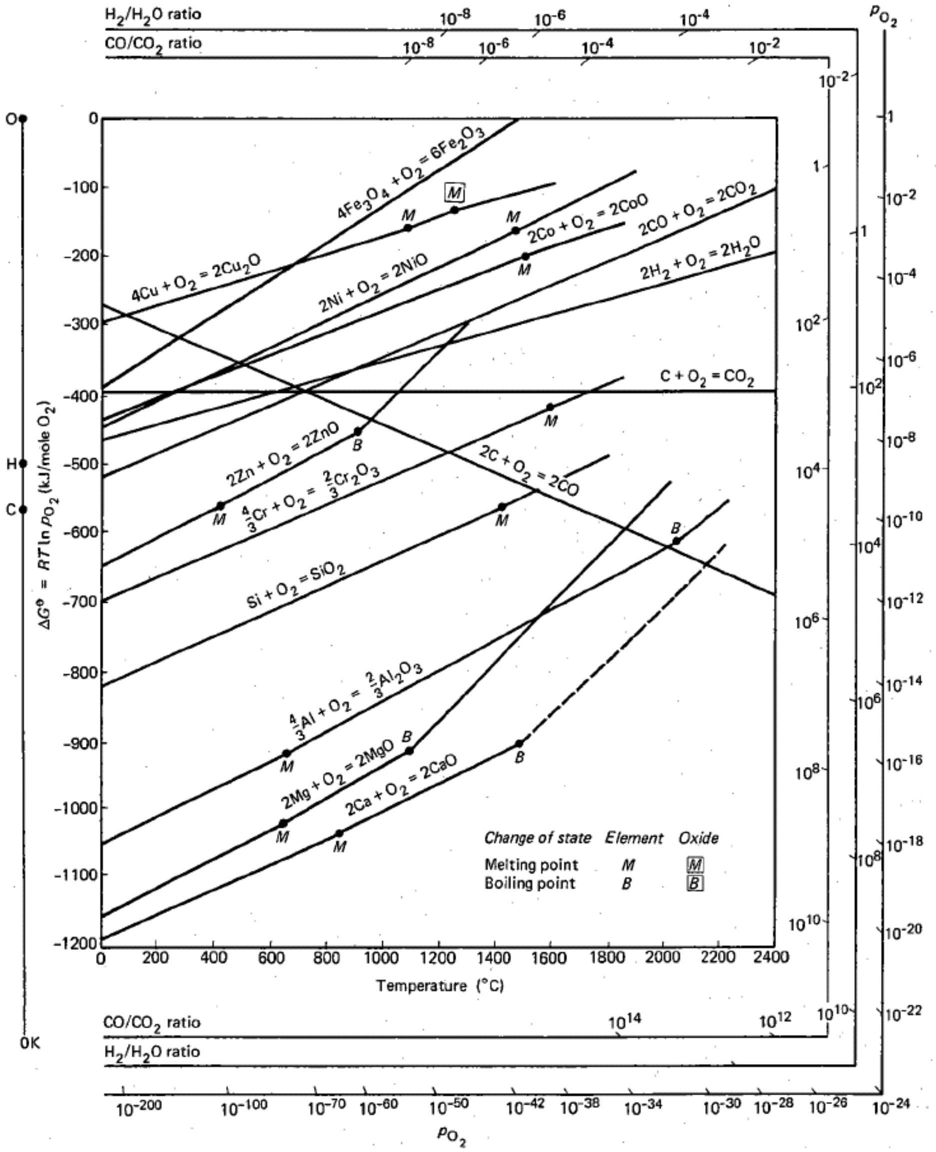

Figure 152: Standard free energy of formation for selected oxides as a function of temperature. © Reprinted with the permission of Cambridge University Press [66].

The formation of diffusion controlled oxide scales is affected by the relative diffusion coefficients of alloying elements in the γ matrix. Assuming that the γ matrix is predominantly nickel, the diffusion results for solute impurities in nickel listed by Burachynsky and Cahoon [67] can be used to explain the composition of protective scales.

From Leclaire's theory on impurity diffusion in metals [68], the difference in activation energy between solute and solvent self diffusion (ΔQ) is given by:

$$\Delta Q = \Delta H_2 + \Delta E = -\frac{\alpha Z_2 e^2 V_o e^{-(11qa/16)}}{11a/16}$$

where α is a parameter (~1 in value) dependent on Z

Z_2 is the excess charge of the solute impurity

e is the charge of an electron

V_o is the valence of the solvent

q is a calculated parameter related to the screening potential around the impurity atom

a is the jump distance between a solute or solvent atom and a vacancy

Titanium, aluminum and chromium also have significantly large negative ΔQ values and were found to be present in the protective scales.

With positive ΔQ values, molybdenum, tantalum and tungsten are relatively slow diffusers in nickel and were not present in the oxide scales. Refer to Figure 153 for a plot of relative differences in activation energy for diffusion of solute impurities in nickel compiled by Burachynsky and Cahoon [67].

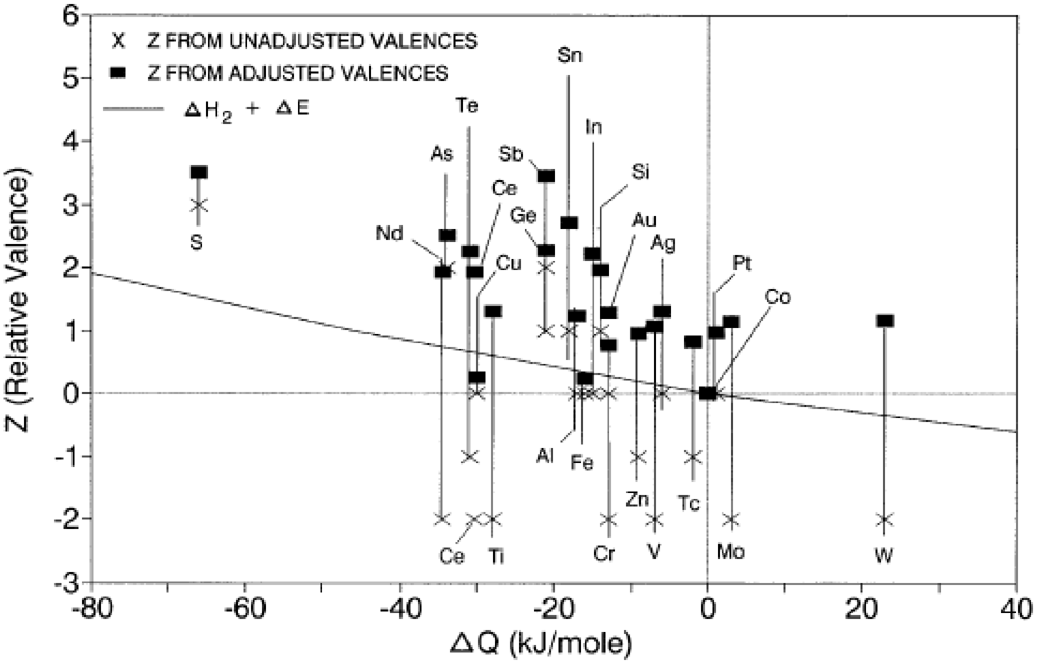

Figure 153: Activation energies for solute impurity diffusion in nickel. © Reprinted with kind permission from Springer Science and Business Media [67].

Therefore, localized alloy depletion resulting from surface oxidation in LBW specimens and baseline material was a dominant factor in the initiation of cracks. Thus, by providing oxidation resistance to the alloy surface (fusion and base material) by use of an aluminide-type or other elevated temperature resistant coating, it is reasonable to expect that the fatigue life of LBW nickel superalloys can be extended by preventing the formation of surface cracks along grain boundaries in the weld fusion zone.

The baseline specimens subjected to the same TMF testing parameters were evaluated and were found to have crack initiation sites associated with carbide particles. As shown in Figure 154, the thumbnail shaped fatigue crack initiation region originated from a carbide particle near the specimen surface. Figure 155 shows an SEM image of a cracked carbide particle in a René N5 baseline specimen with a major crack extending well into the parent material. Similar results were observed for all three base materials evaluated in this study as all contained extensive carbide phases in interdendritic regions throughout the microstructure. Cast nickel based superalloys are strengthened to an extent by formation of carbides along grain boundaries and interdendritic sites [56]. Therefore, since the alloys were already in the low carbon forms (common variant), the presence of carbides cannot be eliminated and it is reasonable to expect cracking under sufficient loading. The cracks in the carbide particles produce a notch effect in the material and the crack extends in the base material and eventually leads to fracture. The failure mechanism of the baseline materials was consistent with the results reported by Abrokwah for DS René 80 [50].

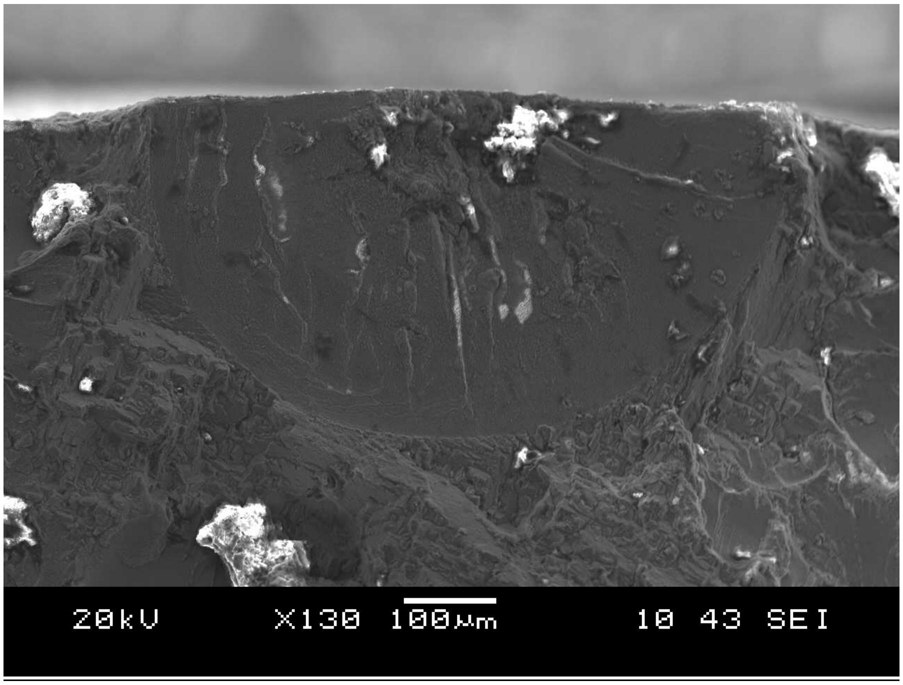

Figure 154: SEM fractograph image of fatigue crack initiation in René 80

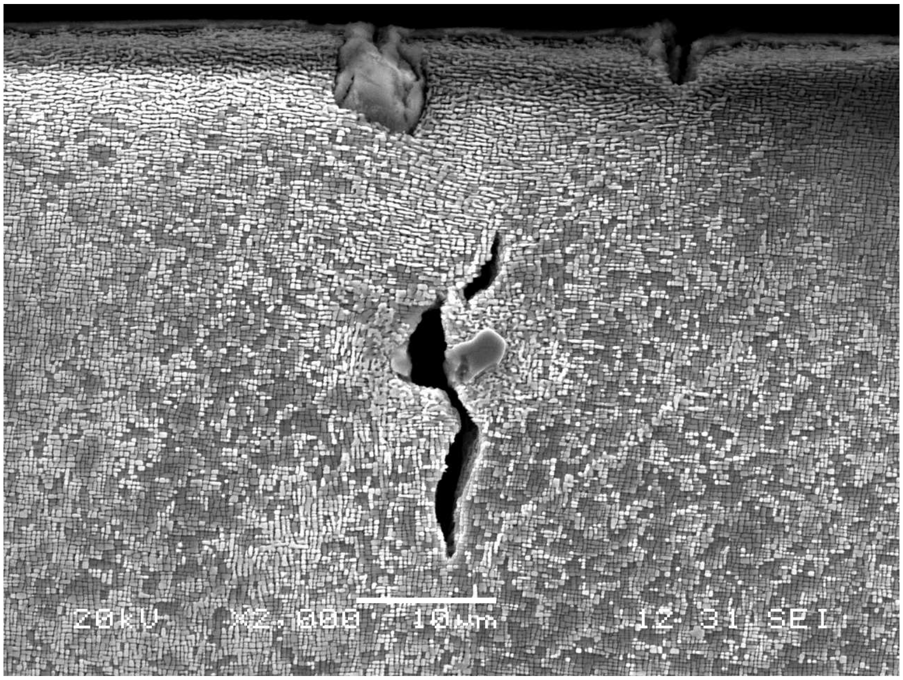

Figure 155: SEM image of cracked carbide and crack extending in René N5 parent material

The network of grain boundaries in the fusion zone of laser beam welded Inconel 738, René 80 and René N5 provided a path for the propagation of a primary crack through the fusion zone, perpendicular to the loading axis and into the base material.

Inconel 738 did not undergo recrystallization during the post-weld STA heat treatment. This is most likely as a result of the strain energy resulting from residual stresses in the HAZ not being sufficiently high to cause nucleation and growth of new defect-free grains in the polycrystalline alloy. The primary cracks in the weld fusion zone propagated along grain boundaries in the solidification structure and extended in the parent material along grain boundaries. Under these conditions, the crack surfaces were subject to oxidation and Al+Ti de-alloying from the base material to the very crack tip, reducing the material strength ahead of the advancing crack, exasperating the notch sensitivity of the material.

The absence of recrystallization in baseline René 80 and René N5 TMF specimens suggests that recrystallization observed in LBW specimens occurred during the post-weld heat treatment cycle and not during TMF tests. LBW René 80 and René N5 specimens underwent recrystallization in the weld heat affected zone with grains being formed in the base material microstructure. The grain boundaries of recrystallized grains in René 80 were dominated by a layer of γ’ and films of carbides undergoing degeneration while recrystallized grains in René N5 had a coherent layer of γ’ with discrete Cr-Mo-B rich particles. For LBW René 80 and René N5 specimens, the primary crack propagated along an intergranular path between recrystallized grains. Additional secondary cracks were found in the recrystallized region for René 80 and René N5 substrates. The smooth texture of the exposed recrystallized grains indicated a brittle fracture in the heat affected region. Beyond the recrystallized grains, the primary cracks extended in the base material across columnar grains in René 80 and across dendrites in René N5. The surface texture of the unaltered parent material was ductile for René 80 and René N5.

In summary, laser beam welding of Inconel 738 under the conditions described in this thesis did not reduce the TMF properties of the alloy. The fusion zone introduced a predominantly equiaxed structure in the polycrystalline cast structure. Minor HAZ cracking was found and considered to have had negligible effect on the TMF properties of LBW Inconel 738. The relative reduction in TMF of Inconel 738 as compared to René 80 and René N5 was as a result of the lower mechanical properties of the polycrystalline alloy due to the presence of grain boundaries perpendicular to the applied loading.

Laser beam welding René 80 and René N5 was detrimental to the resistance of crack initiation under thermo-mechanical fatigue testing. The equiaxed grain solidification structure in the fusion zone provided multiple crack initiation sites and a propagation path across the specimen thickness. The recrystallization phenomena observed in René 80 and René N5 provided a crack propagation path in the base material beyond the weld fusion zone. Both alloys yielded similar fatigue lives and were superior to Inconel 738 due the absence of grain boundaries beyond the fusion zone and recrystallized grains.

Using an over-ageing pre-weld heat treatment, near crack-free welds were achieved in Inconel 738 while crack free welds in René 80 and René N5 were produced. The weld microstructure was a mix of epitaxial growth and equiaxed grains with no cracks resulting from weld cooling or post-weld STA heat treatment. However the base material surface along equiaxed grain boundaries provided crack initiation sites due to local oxidation attack of the Inconel 738 filler alloy. Further studies in this field must consider the potential adverse effects of equiaxed grains and high angle grain boundaries in the weld fusion zone on the fatigue properties of material under study. The elimination of stray grains in the weld fusion zone would also eliminate the grain boundaries that were associated with crack initiation. An entirely epitaxial fusion zone would be susceptible to crack initiation from oxidation mechanism and would likely require testing under controlled atmospheric conditions.

Recrystallization of DS and SX nickel based superalloys during post-weld STA heat treatment presents a challenge and may be eliminated or reduced by changing the weld conditions. Since recrystallization is driven by strains in the weld HAZ, means of reducing residual stresses must be employed. By using a more ductile filler such a solid solution strengthened nickel based alloy, residual stresses in the weld HAZ will be reduced and accommodated by the filler. As shown by Banerjee et al. [2], the reduction in weld HAZ cracking was attributed to the increased ductility of the filler alloy which accommodated stresses during the weld cooling phase. Selecting a filler alloy with superior ductility and corrosion resistance may resolve the problems of recrystallization and intergranular crack initiation simultaneously. Further reduction in residual stresses may be achieved by use of lower heat input laser welding parameters and applying smaller deposits with each weld pass. By reducing the filler deposition rate, lower beam power would be required to sustain a molten weld pool and fusion with the base material. Therefore, a significant reduction in substrate heating is possible and could reduce residual stresses in the HAZ. Lastly, pre-heating the substrate prior to welding may also provide a significant reduction in HAZ residual stresses caused by the high thermal gradients generated by welding specimens at ambient temperature. However, the positive effects of pre-heating and lower thermal gradients would likely result in a completely equiaxed (stray grains) solidification structure in the weld fusion zone. Therefore, the combination of ductile filler alloys, lower heat input welding parameters and pre-heating the substrate may significantly reduce residual stresses in the HAZ and reduce or prevent nucleation and growth of new grains during the post-weld heat treatment.

6. CONCLUSIONS

Based on the metallographic and thermo-mechanical fatigue testing of laser beam welded CC Inconel 738, DS René 80 and SX René N5, the following conclusions are drawn:

- Laser beam welding produced near crack-free welds in polycrystalline Inconel 738. Using a v-notch preparation and low heat input welding parameters, only minor cracking occurred as a result of γ' liquation along grain boundaries at the weld fusion line.

- Crack free laser beam welds using a matched filler alloy were possible on DSRené 80 and SX René N5. René 80 and René N5 had higher hardness values than Inconel 738 in the pre-weld over-aged condition, yet they provided welds free from HAZ-cracking. Therefore, the hardness of the material cannot be used solely to predict whether HAZ micro-cracking will occur; the presence of grain boundaries along the weld fusion line must be considered. If few or no grain boundaries are present at the weld line, then the HAZ micro-cracking susceptibility will be lower provided that the heat input to the base alloy is relatively low as compared to GTAW.

- The fusion zone microstructure did not perfectly match that of the base material; stray grains and epitaxial growth were observed. The local thermal gradient conditions in the weld puddle and the crystallographic orientation of the base alloy along the fusion line dictated the direction of epitaxial growth. Thermal undercooling of the weld puddle led to the formation of stray grains in the weld core and cap. Complete epitaxial and dendritic solidification structure may be achieved by changing the weld parameters or solidification conditions such that a greater thermal gradient is maintained at the solidification front.

- Grain growth/recrystallization occurred during post-weld heat treatment (STA) in the heat affected zone of DS René 80 and SX René N5 as a result of plastic strains. Strains were sufficiently high to drive the nucleation and growth of new grains the base alloy HAZ.

- Crack initiation in LBW specimens occurred in the fusion zone by localized oxidation of grain boundaries between stray grains. Cracks propagated along an intergranular path in the fusion zone. Secondary cracks formed along other grain boundaries in the fusion zone and along recrystallized grain boundaries in DS René 80 and SX René N5.

- LBW welding of polycrystalline Inconel 738 did not have an adverse effect on the thermo-mechanical fatigue properties of the alloy. Despite minor HAZ liquation cracking, TMF results were comparable to the baseline condition. The epitaxial and equiaxed solidification structures in laser beam welded Inconel 738 did not reduce the TMF life of the alloy under the pre-weld material condition and welding parameters used in this thesis.

- The TMF resistance of LBW DS René 80 and SX René N5 specimens was lower than the baseline condition for these alloys. The formation of stray grains in the weld fusion zone and the low strength character of grain boundaries in the recrystallized zone were detrimental to the TMF life of LBW DS René 80 and SX René N5. TMF specimen cracks and fracture along recrystallized grain boundaries were brittle in nature.

- Crack initiation in the baseline alloys involved two mechanism:
    1. Fracture of carbides followed by crack propagation into the surrounding base alloy microstructure
    2. Surface oxidation at grain boundaries, near surface carbides or local depletion of γ’ from oxide spikes

- Oxidation protection is an essential consideration in order to eliminate the initiation of surface cracks along exposed grain boundaries, near surface carbides and localized spikes with a corresponding γ’ depletion. Preventing oxidation or reducing the rate of alloy oxidation during elevated temperature exposure is expected to increase the TMF properties of the alloys by delaying the initiation of surface cracks.

7. FUTURE WORK

Further investigations are necessary in order to minimize the adverse effect of recrystallized grain boundaries on the base material microstructure. A possible and likely solution will be the development of a post-weld heat treatment that alters the character of the resulting grain boundaries such that ductility is improved. Banerjee et al. [2] have shown that the use of a ductile filler alloy increases the ductility of the weld and reduces the extent of HAZ cracking by better accommodating strain ageing and thermal stresses during the weld cooling phase. Therefore by reducing the stresses in the weld HAZ, it is reasonable to expect that recrystallization may be eliminated or reduced. Lastly, the application of elevated temperature welding (at the expense of epitaxial fusion zone structure) may sufficiently reduce the stored mechanical energy in the weld heat affected zone and reduce/eliminate the nucleation of new grains during post-weld STA.

When considering the potential application of comparative TMF testing for the repair of gas turbine blades and nozzles, the application of protective coatings becomes relevant in terms of assessing the comparative TMF life of weld repairs. Hot section components in modern gas turbines have oxidation resistant coatings applied to surfaces exposed to exhaust gases. Therefore, the presence of a diffused aluminide coating is expected to protect the underlying base alloy (including weld repairs) from oxidation but the performance of the coating system/part combination must be assessed under TMF conditions. Based on the demonstrated performance of aluminide and other oxidation resistant coatings, the greatest improvement to thermal mechanical fatigue properties of LBW DS René 80 and SX René N5 would be realized by eliminating recrystallized grains in the weld heat affected zone or changing their character such that they better resist crack propagation.

8. REFERENCES

1. A. Thakur, N.L. Richards and M.C. Chaturvedi, “On crack free welding of cast Inconel 738”, International Journal for the Joining of Materials, volume 25, no. 4, pp. 21-25, 2003
2. K. Banerjee, N.L. Richards and M.C. Chaturvedi, “Effect of filler alloys on heat-affected zone cracking in pre-weld heat-treated IN738 LC gas tungsten arc welds”, Metallurgical and Materials Transactions A, volume 36, no. 7, 1881-1890, 2005
3. R.K. Sidhu, N.L. Richards and M.C. Chaturvedi, “Effect of aluminum concentration in filler alloys on HAZ cracking in TIG welded cast Inconel 738LC superalloy”, Materials Science and Technology, volume 21, no. 10, pp. 1119-1131, 2005
4. R.K. Sidhu, O.A. Ojo and M.C. Chaturvedi, “Microstructural analysis of laser-beam-welded directionally solidified Inconel 738”, Metallurgical and Materials Transactions A, volume 38, no. 4, pp. 858-870, 2007
5. R.K. Sidhu, O.A. Ojo and M.C. Chaturvedi, “Microstructural analysis of directionally solidified René 80 superalloy to gas-tungsten arc welding”, Metallurgical and Materials Transactions A, volume 40, no. 1, pp 150-162, 2009
6. J.M. Vitek, “The effect of welding conditions on stray grain formation in single crystal welds – Theoretical analysis”, Acta Materialia, volume 53, no. 1, pp 53-67, 2005
7. S. Mokadem, C. Bezençon, J.-M. Drezet, A. Jacot, J.-D. Wagnière and W. Kurz, “Microstructure control during single crystal laser welding and deposition of Ni-base superalloys”, Solidification Processes and Microstructures: A Symposium in Honour of Wilfried Kurz, pp 67 –76, 2004
8. L.Coffin, “A study of the effects of cyclic thermal stresses on a ductile metal”, AIME Transactions, volume 76, pp. 931-948, 1954
9. S.S. Manson, “Behaviour of materials under conditions of thermal stress”, NACA TN 2933, pp. 636-670, 1953

10. L.F. Coffin, “Cyclic-strain induced oxidation of high-temperature alloys”, ASM Transactions, volume 56, pp. 339-344, 1963
11. S. Pahlavanyali, G. Drew, A. Rayment, C.M.F. Rae, “Oxidation assisted thermomechanical fatigue failure of polycrystalline superalloys”, Materials Science and Technology, volume 23, no. 12, pp. 1454-1460, 2007
12. J. Kanesund, J.J. Moverare, S. Johansson, “The deformation and damage mechanisms during thermomechanical (TMF) in IN792”, Procedia Engineering, volume 10, pp. 189-194, 2011
13. F.L. Versynder: US Patent no. 3260505, 1966
14. W.H. Chang, “Tensile embrittlement of turbine blade alloys after high-temperature exposure”, Superalloys Processing: Proceedings of the second international conference, pp. 1-41, 1972
15. K. Rahmani, S. Nategh, “ Low cycle fatigue mechanisms of René 80 at high temperature-high strain”, Material Science and Engineering, volume 494, no. 1-2, pp. 385-390, 2008
16. M. Raguet, S.D. Antolovich and R.K. Payne, “Superalloys 1984”, Metallurgical Society of AIME, pp. 231-241, 1984
17. L. Remy, H. Bernard, J.L. Malpertu, F. Rezai-Arai: “Fatigue life prediction under thermal-mechanical loading in a Ni base superalloy”, ASTM Special Technical Publication, no. 1186, pp. 3-16; 1993
18. P.S. Karamched, A.J. Wilkinson, “High resolution electron back-scatter diffraction analysis of thermally and mechanically induced strains near carbide inclusion in a superalloy”, Acta Materialia, volume 59, no. 1, pp. 263-272, 2011
19. M. Herbig, A. King, P. Reischig, H. Proudhon, E.M. Lauridsen, J. Marrow, J.Y. Buffière and W. Ludwig, “3-D growth of a short fatigue crack within a polycrystalline microstructure studied using combined diffraction and phase-contrast x-ray tomography”, Acta Materialia, volume 59, no. 2, pp. 590-601, 2011

20. W. Schaef, M. Marx, H. Vehoff, A. Heckl, P. Randelzhofer, "A 3-D view on the mechanisms of short fatigue cracks interacting with grain boundaries", Acta Materialia, volume 59, no. 5, pp. 1849-1861, 2011
21. M. Okazaki, T. Tabata, S. Nohmi, "Intrinsic stage I crack growth of directionally solidified Ni-base superalloys during low-cycle fatigue at elevated temperature", Metallurgical Transactions A, volume 21A, no. 8, p. 2201-2208, 1990
22. D. A. Koss, K. S. Chan, "Fracture along planar slip bands", Acta Metallurgica, volume 28, no. 9, pp. 1245-1252, 1980
23. C.E. Feltner, C.Laird, "Cyclic stress-strain response of F.C.C. metals and alloys – Phenomenological experiments, Acta Metallurgica., volume 15, no. 9, pp. 1621-1632, 1967
24. R. Chieragatti, L. Remy, "Influence of orientation on the low cycle fatigue of MAR-M 200 single crystals at 650ºC. I. Fatigue life behaviour", Materials Science and Engineering A, volume A141, no. 1, pp. 1-9, 1991
25. F. Meyer-Olbersleben, C. Engler-Pinto Jr, F. Rezai-Aria, "On thermal fatigue of nickel-based superalloys", ASTM Special Technical Publication, no. 1263, pp. 41-55, 1996
26. J. Xu, S. Reuter, W. Rothkegal, "Tensile and bending thermo-mechanical fatigue testing on cylindrical and flat specimens of CMSX-4 for design of turbine blades", International Journal of Fatigue, volume 30, no. 2, pp. 363-371, 2008
27. E. Chataigner & L. Remy, "Thermomechanical fatigue behaviour of coated and bare nickel-based superalloys single crystals", ASTM Special Technical Publication, no. 1263, pp. 3-26, 1996
28. P.A.S. Reed, M.D. Miller, "Comparison of low cycle (notch) fatigue behaviour at temperature in single crystal turbine blade materials", Superalloys 2008 – Eleventh International Symposium on Superalloys, pp. 527-533, 2008

29. H.U. Hong, B.G. Choi, I.S. Kim, Y.S. Yoo & C.Y. Jo, “A comparative study on thermomechanical and low cycle fatigue failures of a single crystal nickel-based superalloy”, International Journal of Fatigue, volume 33, no. 12, pp. 1592-1599, 2011

30. H.U. Hong, B.G Choi, I.S. Kim, Y.S. Yoo & C.Y. Jo, “Characterization of deformation mechanisms during low cycle fatigue of a single crystal nickel-based superalloy”, Journal of Materials Science, volume 46, no. 15, pp. 5245-5251, 2011

31. J.J. Moverare, S. Johanson & R.C. Reed, “Deformation and damage mechanisms during thermal-mechanical fatigue of a single-crystal superalloy”, Acta Materialia, volume 57, no. 7, pp. 2266-2276, 2009

32. E. Fleury, L. Remy, “Behaviour of nickel-base superalloy single crystals under thermal-mechanical fatigue”, Metallurgical and Materials Transactions A, volume 25A, no. 1, pp. 99-109, 1994

33. G.M. Han, J.J. Yu, X.F. Sun, Z.Q.Hu, “Thermo-mechanical fatigue behaviour of a single crystal nickel-based superalloy”, Materials Science and Engineering: A, volume A528, no. 19-20, pp. 6217-6234, 2011

34. J.X Zhang, H. Harada, Y. Koizumi, T. Kobayashi, “Crack appearance of single crystal nickel-base superalloys after thermo-mechanical fatigue”, Scripta Materialia, volume 61, no. 12, pp. 1105-1108, 2009

35. Q.Z. Chen, N. Jones, D.M. Knowles, “Microstructures of modified RR2072 single crystal superalloys and their effects on LCF response at 950ºC”, Fatigue and Fracture of Engineering Materials and Structures, volume 26, no. 3, pp. 185-198, 2003

36. M. McLean, “Directionally solidified materials for high temperature service”, Metals Society, 1983

37. M.B. Henderson, D. Arrell, R. Larsson, M. Heobel, G. Marchant, “Nickel based superalloy welding practices for industrial gas turbine applications”, Science and Technology of Welding and Joining, volume 9, no. 1, pp. 13-21, 2004

38. R.K. Sidhu, N.L. Richards, M.C. Chaturvedi, “Post weld heat treatment cracking in autogenous GTA welded cast Inconel 738LC superalloy”, Materials Science and Technology, volume 23, no. 2, pp. 203-213, 2007

39. R.K. Sidhu, N.L. Richards, M.C. Chaturvedi, “Effect of filler alloy composition on post-weld heat treatment cracking in GTA welded cast Inconel 738LC superalloy”, Materials Science and Technology, volume 24, no. 5, pp. 529-539, 2008

40. R.K. Sidhu, O.A. Ojo, N.L. Richards and M.C. Chaturvedi, “Metallographic and OIM study of weld cracking in GTA build-up of polycrystalline, directionally solidified and single crystal Ni based superalloys”, Science and Technology of Welding and Joining, Volume 14, 2009, pp 125-131

41. S. Tsubota, M. Mega, K. Takahashi, Y. Uemura, N. Hirota, K. Yamagichi. “Application of YAG laser welding to gas turbine components”, Proceedings of Society for Optical Engineering, volume 4831, pp. 433-437, 2003

42. N.C. Sekhar, R.C. Reed, “Power beam welding of thick section nickel base alloys”, Science and Technology of Welding and Joining, volume 7, no. 2, pp. 77-87, 2002

43. G. Frederick, D. Gandy, J.T. Stover, “Laser repair of service exposed IN738 and GTD 111 buckets”, American Society of Mechanical Engineers, International Gas Turbine Institute, Turbo Expo (Publication) IGTI, volume 1, pp. 885-899, 2002

44. S. Gobbi, L. Zhang, J. Norris, K.H. Richter, J.H. Loreau, “High powder CO_2 and Nd-YAG laser welding of wrought Inconel 718”, Journal of Materials Processing Technology, volume 56, pp. 333-345, 1996

45. Z. Li, S.L. Gobbi, F. Bonollo, A. Tiziani, G. Fontana, “Metallurgical investigation of laser welds in wrought Waspaloy”, Science and Technology of Welding and Joining, volume 3, no. 1, pp. 1-7, 1998

46. M.T. Rush, P.A. Colegrove, Z. Zang, D. Broad, “Liquation and post-weld heat treatment cracking in René 80 laser repair welds”, Journal of Materials Processing Technology, volume 212, pp. 188-197, 2012

47. M.M. Biela, H.W. Kerr, D.C. Weckman, “Effect of process variables on cracking of pulsed laser beam welds in IN600”, Fifth International Conference: Trends in Welding Reasearch; Pine Mountain, GA, USA, pp. 769-774, 1998

48. Y.L. Wang, O.A. Ojo, R.G. Ding, M.C. Chaturvedi, “Weld metal cracking in laser beam welded single crystal nickel base superalloys”, Materials Science and Technology, volume 25, no.1, pp. 68-75, 2009

49. C. Churchman, E.A. Bonifaz, N.L. Richards, “Comparison of single crystal Ni based superalloy repair by gas tungsten arc and electron beam processes”, Materials Science and Technology, volume 27, number 4, pp. 811-817, 2011

50. E.O. Abrokwah, O.A. Ojo, N.L. Richards, “Failure mechanisms in thermo-mechanical fatigue of DS superalloy René 80”, Canadian Metallurgy Quarterly, volume 51, no.3, pp. 356-366, 2012

51. E.A. Bonifaz, N.L. Richards, “Modelling cast IN-738 superalloy gas tungsten arc welds”, Acta Materialia, volume 57, no. 6, pp. 1785-1794, 2009

52. E.A. Bonifaz, N.L. Richards, “Stress-strain evolution in cast IN-738 superalloy single fusion welds”, International Journal of Applied Mechanics, volume 2, no. 4, pp. 807-826, 2010
53. H.U. Hong, B.G. Choi, L.S. Kim, Y.S. Yoo, C.Y. Jo, “Characterization of deformation mechanisms during low cycle fatigue crystal nickel-based superalloys”, Journal of Material Science, volume 64, no. 15, pp. 5245-5251, 2011
54. C. Zhang, L. Li, A. Deceuster, “Thermo-mechanical analysis of multi-bead pulsed laser powder deposition of a nickel based superalloy”, Journal of Materials Processing Technology, volume 211, no. 9, pp. 1478-1487, 2011
55. G. Feng, D. Nowak, “Low cycle fatigue behavior of cast GTD-222 weld joint at elevated temperatures”, Fatigue. David L. Davidson Symposium Proceedings, pp. 217-226, 2002
56. C.T. Sims, “Superalloys II”, Wiley Publishing, pp. 61-213, 1987
57. F. Weinberg, “Tools and Techniques in Physical Metallurgy”, M. Dekker, 1970
58. Y. Amouyal, D.N Seidman, “The role of hafnium in the formation of misoriented defects in Ni-based superalloys: An atom-probe tomographic study”, Acta Materialia, volume 59, no. 9, pp. 3321-3333, 2011
59. R. Sellamuthu, A.F. Giamei, “Measurement of segregation and distribution coefficients in MAR-M200 and hafnium-modified MAR-M200 superalloys”, Metallurgical Transactions A, volume 17A, no. 3, pp. 419-428, 1986
60. W. Kurz, D.J. Fisher, “Fundamentals of Solidification”, Fourth Edition, Trans Tech Publications, USA, 1998

61. R. Burgel, P.D. Portella, J. Preuhs, “Recrystallization in single crystals of nickel base superalloys”, SUPERALLOYS 2000 - Proceedings of the Ninth International Symposium on Superalloys, pp. 229-238, 2000
62. Y. Li, Y. Han, “Recrystallization of Ni_3Al base single crystal alloy IC6SX with different surface mechanical processes”, Journal of Materials Science and Technology, volume 26, no. 10, pp. 883-888, 2010
63. G.E. Dieter, “Mechanical Metallurgy”, Third Edition, McGraw Hill, USA, 1986
64. J.C. Chang, S.M. Allen, “Elastic energy changes accompanying gamma-prime rafting in nickel-base superalloys”, Journal of Materials Research, volume 6, no. 9, pp. 1843-1855, 1991
65. ASM International, “Failure Analysis and Prevention”, ASM Handbook, volume 11, pp. 627-640, 2002
66. N.Birks, G.H. Meier, “Introduction to High Temperature Oxidation of Metals”, Edward Arnold (Publishers), USA, 1983
67. V. Burachynsky, J.R. Cahoon, “A theory for solute diffusion, which considers Engel-Brewer valences, balancing the Fermi energy levels of solvent and solute, and differences in zero point energy”, Metallurgical and Material Transactions A, volume 28A, no. 3, pp. 563-582, 1997
68. A.D. Le Claire, “On the theory of impurity diffusion in metals”, National Metal Congress, Philadelphia, 1960
69. E. Abrokwah, “Microstructural studies on failure mechanisms in thermo-mechanical fatigue of repaired DS R80 and IN738 superalloy”, Master of Science thesis., University of Manitoba, 2012

9. APPENDICES

APPENDIX A: PCC Airfoils report no. B046591 for Inconel 738
APPENDIX B: PCC Airfoils report no. B046174 for René 80
APPENDIX C: PCC Airfoils report no. B046740 for René N5
APPENDIX D: Praxair specification PS 036108 for Ni-284-1 powder
APPENDIX E: Laser beam welding parameter development
APPENDIX F: SEM EDS linescan across of S-Ti-Zr rich phase in Inconel 738 in the as-received condition
APPENDIX G: SEM EDS linescan of cellular solidification structure in fusion zone of Inconel 738
APPENDIX H: SEM EDS line scan across crack tip in Inconel 738 TMF specimen
APPENDIX I: SEM EDS line scan of TMF crack edge in base alloy Inconel 738,
APPENDIX J: SEM EDS linescan across liquated MC carbide in René 80, as-welded condition
APPENDIX K: SEM EDS linescan across MC carbide in base alloy René 80, as-welded condition
APPENDIX L: SEM EDS linescan across Zr-Ti rich sulfocarbide in René 80, as-received condition
APPENDIX M: SEM EDS linescan across recrystallized grain boundary in PWHT René 80 base alloy
APPENDIX N: SEM EDS linescan across recrystallized grain boundary in PWHT René 80 base alloy
APPENDIX O: SEM EDS mapscan of surface scale of René 80 TMF specimen
APPENDIX P: SEM EDS linescan across Cr-Mo-C-B rich along recrystallized grains in René N5 PWHT
APPENDIX Q: SEM EDS x-ray maps along crack surface in René N5
APPENDIX R: TMF test results for Inconel 738, René 80 and René N5
APPENDIX S: SEM EDS line scan across sulfocarbides particle in the weld fusion zone

APPENDIX A: PCC Airfoils report no. B046591 for Inconel 738

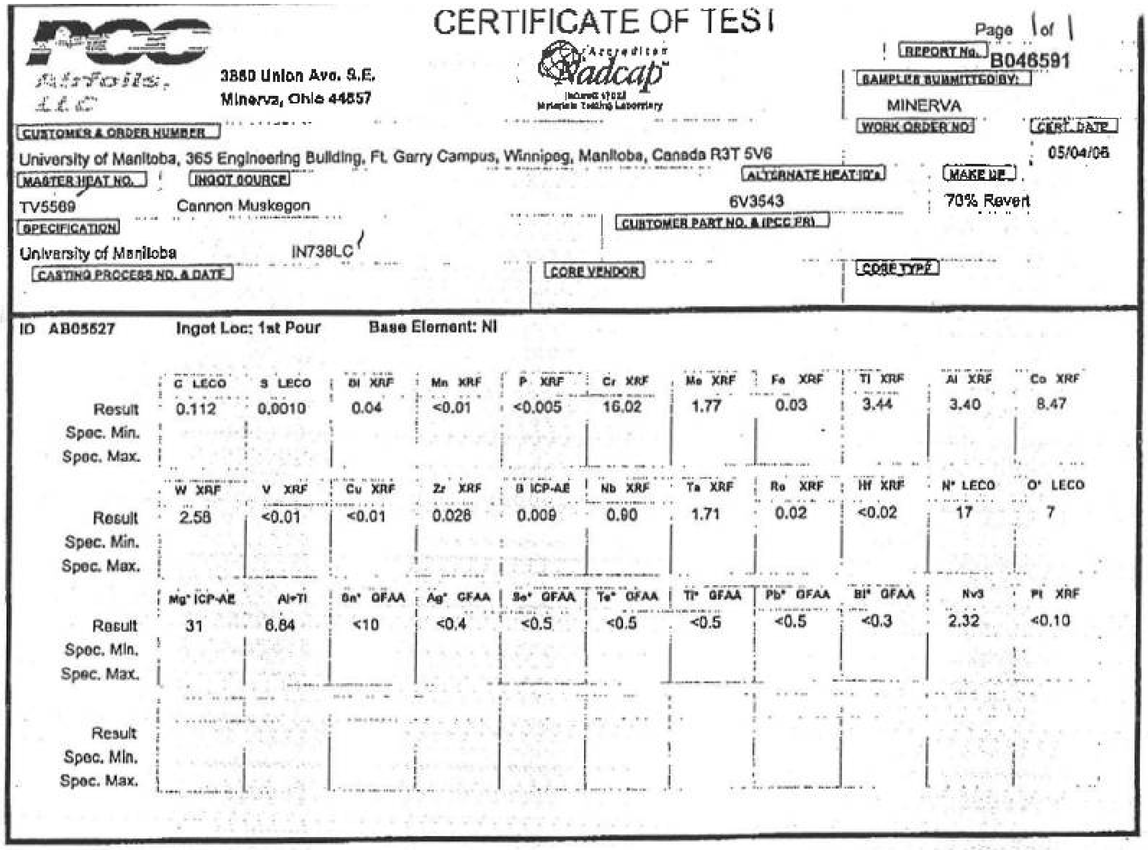

PCC Airfoils, LLC
3880 Union Ave. S.E.
Minerva, Ohio 44657

CERTIFICATE OF TEST

Accredited Nadcap Materials Testing Laboratory

Page 1 of 1

REPORT No. B046591

SAMPLES SUBMITTED BY: MINERVA

WORK ORDER NO

CERT. DATE 05/04/06

CUSTOMER & ORDER NUMBER
University of Manitoba, 365 Engineering Building, Ft. Garry Campus, Winnipeg, Manitoba, Canada R3T 5V6

MASTER HEAT NO. TV5569

INGOT SOURCE Cannon Muskegon

ALTERNATE HEAT ID's 6V3543

MAKE UP 70% Revert

SPECIFICATION
University of Manitoba IN738LC

CUSTOMER PART NO. & (PCC PR)

CASTING PROCESS NO. & DATE

CORE VENDOR

CORE TYPE

ID AB05527 Ingot Loc: 1st Pour Base Element: Ni

	C LECO	S LECO	Si XRF	Mn XRF	P XRF	Cr XRF	Mo XRF	Fe XRF	Ti XRF	Al XRF	Co XRF
Result	0.112	0.0010	0.04	<0.01	<0.005	16.02	1.77	0.03	3.44	3.40	8.47
Spec. Min.											
Spec. Max.											

	W XRF	V XRF	Cu XRF	Zr XRF	B ICP-AE	Nb XRF	Ta XRF	Re XRF	Hf XRF	N* LECO	O* LECO
Result	2.58	<0.01	<0.01	0.028	0.009	0.90	1.71	0.02	<0.02	17	7
Spec. Min.											
Spec. Max.											

	Mg* ICP-AE	Al+Ti	Sn* GFAA	Ag* GFAA	Se* GFAA	Te* GFAA	Tl* GFAA	Pb* GFAA	Bi* GFAA	Nv3	Pt XRF
Result	31	6.84	<10	<0.4	<0.5	<0.5	<0.5	<0.5	<0.3	2.32	<0.10
Spec. Min.											
Spec. Max.											

Result											
Spec. Min.											
Spec. Max.											

APPENDIX B: PCC Airfoils report no. B046174 for René 80

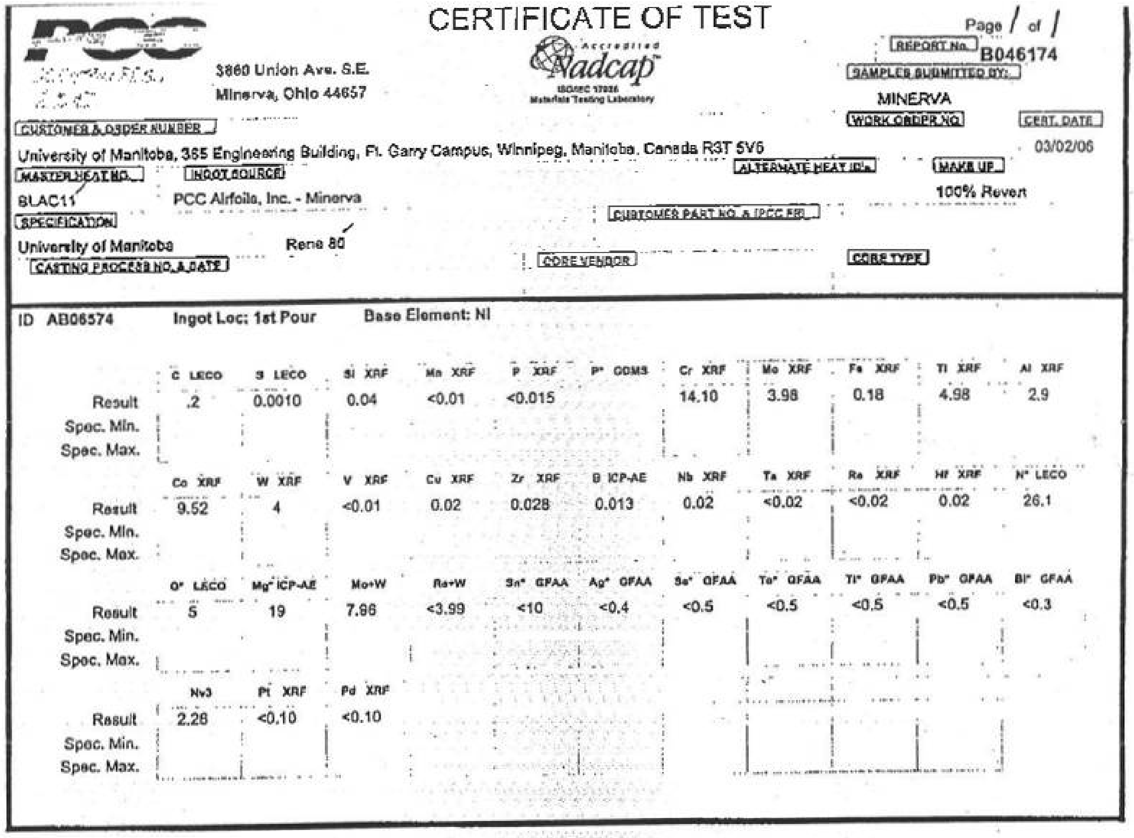

CERTIFICATE OF TEST

Accredited Nadcap
ISO/IEC 17025
Materials Testing Laboratory

PCC
3860 Union Ave. S.E.
Minerva, Ohio 44657

Page 1 of 1

REPORT No. B046174

SAMPLES SUBMITTED BY: MINERVA

WORK ORDER NO

CERT. DATE 03/02/06

CUSTOMER & ORDER NUMBER
University of Manitoba, 365 Engineering Building, Ft. Garry Campus, Winnipeg, Manitoba, Canada R3T 5V6

MASTER HEAT NO. 8LAC11

INGOT SOURCE PCC Airfoils, Inc. - Minerva

ALTERNATE HEAT ID's

MAKE UP 100% Revert

CUSTOMER PART NO. & (PCC P/N)

SPECIFICATION University of Manitoba Rene 80

CASTING PROCESS NO. & DATE

CORE VENDOR

CORE TYPE

ID AB06574 Ingot Loc: 1st Pour Base Element: Ni

	C LECO	S LECO	Si XRF	Mn XRF	P XRF	P* GDMS	Cr XRF	Mo XRF	Fe XRF	Ti XRF	Al XRF
Result	.2	0.0010	0.04	<0.01	<0.015		14.10	3.98	0.18	4.98	2.9
Spec. Min.											
Spec. Max.											

	Co XRF	W XRF	V XRF	Cu XRF	Zr XRF	B ICP-AE	Nb XRF	Ta XRF	Re XRF	Hf XRF	N* LECO
Result	9.52	4	<0.01	0.02	0.028	0.013	0.02	<0.02	<0.02	0.02	26.1
Spec. Min.											
Spec. Max.											

	O* LECO	Mg* ICP-AE	Mo+W	Re+W	Sn* GFAA	Ag* GFAA	Se* GFAA	Te* GFAA	Tl* GFAA	Pb* GFAA	Bi* GFAA
Result	5	19	7.98	<3.99	<10	<0.4	<0.5	<0.5	<0.5	<0.5	<0.3
Spec. Min.											
Spec. Max.											

	Nv3	Pt XRF	Pd XRF
Result	2.28	<0.10	<0.10
Spec. Min.			
Spec. Max.			

APPENDIX C - PCC Airfoils report no. B046740 for René N5

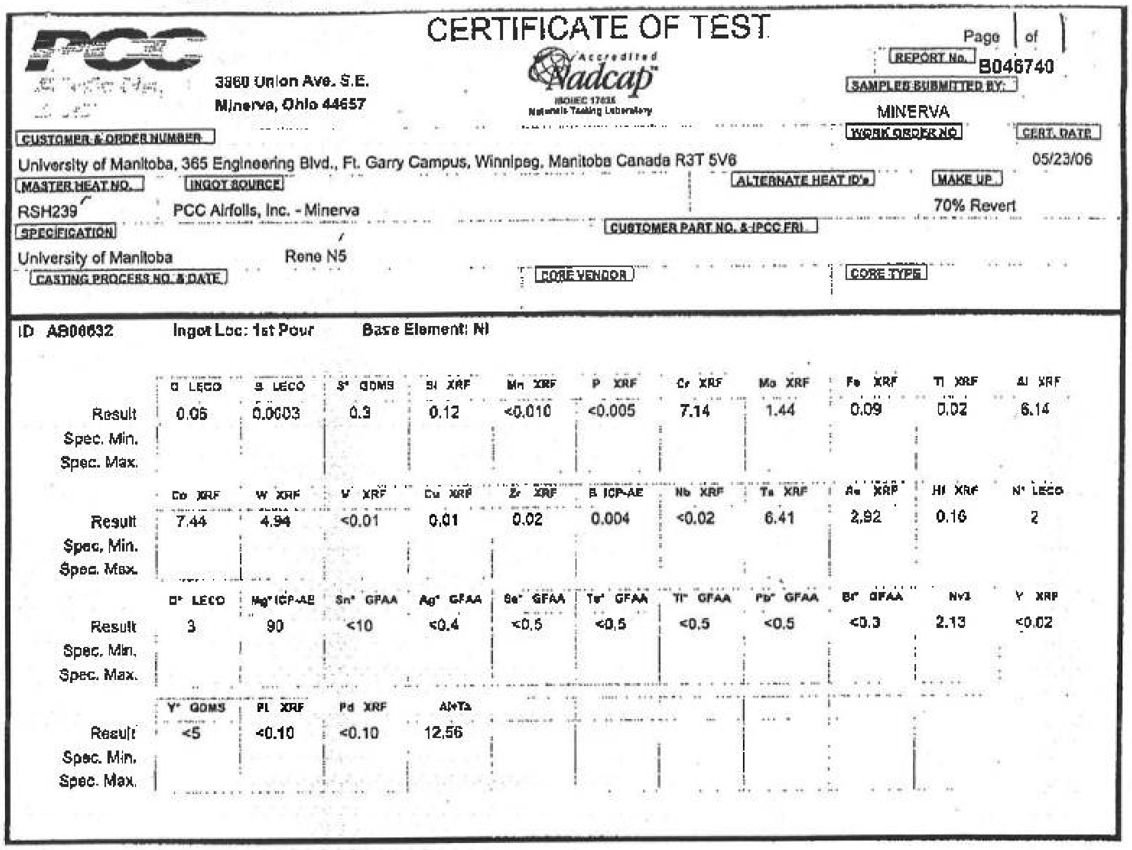

PCC

3360 Union Ave. S.E.
Minerva, Ohio 44657

CERTIFICATE OF TEST

Accredited Nadcap
ISO/IEC 17025
Materials Testing Laboratory

Page | of |

REPORT No. B046740

SAMPLES SUBMITTED BY: MINERVA

WORK ORDER NO

CERT. DATE 05/23/06

CUSTOMER & ORDER NUMBER
University of Manitoba, 365 Engineering Blvd., Ft. Garry Campus, Winnipeg, Manitoba Canada R3T 5V6

MASTER HEAT NO. RSH239

INGOT SOURCE PCC Airfoils, Inc. - Minerva

ALTERNATE HEAT ID's

MAKE UP 70% Revert

SPECIFICATION University of Manitoba Rene N5

CUSTOMER PART NO. & IPCC FRI

CASTING PROCESS NO. & DATE

CORE VENDOR

CORE TYPE

ID AB06632 Ingot Loc: 1st Pour Base Element: Ni

	C LECO	S LECO	S* GDMS	Si XRF	Mn XRF	P XRF	Cr XRF	Mo XRF	Fe XRF	Ti XRF	Al XRF
Result	0.06	0.0003	0.3	0.12	<0.010	<0.005	7.14	1.44	0.09	0.02	6.14
Spec. Min.											
Spec. Max.											

	Co XRF	W XRF	V XRF	Cu XRF	Zr XRF	B ICP-AE	Nb XRF	Ta XRF	Re XRF	Hf XRF	N* LECO
Result	7.44	4.94	<0.01	0.01	0.02	0.004	<0.02	6.41	2,92	0.16	2
Spec. Min.											
Spec. Max.											

	O* LECO	Mg* ICP-AE	Sn* GFAA	Ag* GFAA	Se* GFAA	Te* GFAA	Tl* GFAA	Pb* GFAA	Bi* GFAA	Nv3	Y XRF
Result	3	90	<10	<0.4	<0,5	<0,5	<0.5	<0.5	<0.3	2.13	<0.02
Spec. Min.											
Spec. Max.											

	Y* GDMS	Pt XRF	Pd XRF	Al+Ta
Result	<5	<0.10	<0.10	12,56
Spec. Min.				
Spec. Max.				

APPENDIX D - Praxair specification PS 036108 for Ni-284-1 powder

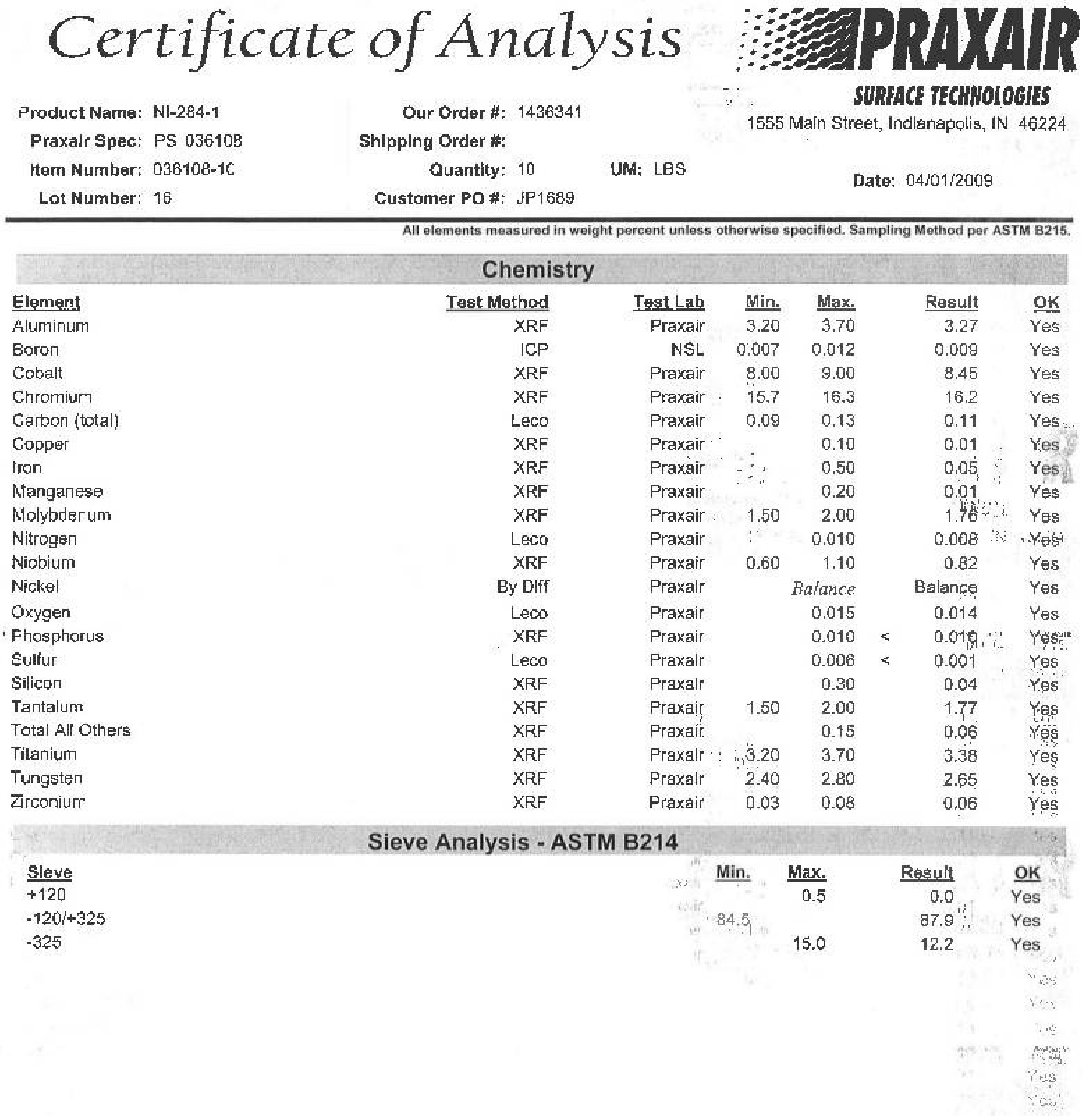

Certificate of Analysis

PRAXAIR
SURFACE TECHNOLOGIES
1555 Main Street, Indianapolis, IN 46224

Product Name:	NI-284-1	**Our Order #:**	1436341		
Praxair Spec:	PS 036108	**Shipping Order #:**			
Item Number:	036108-10	**Quantity:**	10	**UM:**	LBS
Lot Number:	16	**Customer PO #:**	JP1689	**Date:**	04/01/2009

All elements measured in weight percent unless otherwise specified. Sampling Method per ASTM B215.

Chemistry

Element	Test Method	Test Lab	Min.	Max.		Result	OK
Aluminum	XRF	Praxair	3.20	3.70		3.27	Yes
Boron	ICP	NSL	0.007	0.012		0.009	Yes
Cobalt	XRF	Praxair	8.00	9.00		8.45	Yes
Chromium	XRF	Praxair	15.7	16.3		16.2	Yes
Carbon (total)	Leco	Praxair	0.09	0.13		0.11	Yes
Copper	XRF	Praxair		0.10		0.01	Yes
Iron	XRF	Praxair		0.50		0.05	Yes
Manganese	XRF	Praxair		0.20		0.01	Yes
Molybdenum	XRF	Praxair	1.50	2.00		1.76	Yes
Nitrogen	Leco	Praxair		0.010		0.008	Yes
Niobium	XRF	Praxair	0.60	1.10		0.82	Yes
Nickel	By Diff	Praxair		*Balance*		Balance	Yes
Oxygen	Leco	Praxair		0.015		0.014	Yes
Phosphorus	XRF	Praxair		0.010	<	0.010	Yes
Sulfur	Leco	Praxair		0.006	<	0.001	Yes
Silicon	XRF	Praxair		0.30		0.04	Yes
Tantalum	XRF	Praxair	1.50	2.00		1.77	Yes
Total All Others	XRF	Praxair		0.15		0.06	Yes
Titanium	XRF	Praxair	3.20	3.70		3.38	Yes
Tungsten	XRF	Praxair	2.40	2.80		2.65	Yes
Zirconium	XRF	Praxair	0.03	0.08		0.06	Yes

Sieve Analysis - ASTM B214

Sieve	Min.	Max.	Result	OK
+120		0.5	0.0	Yes
-120/+325	84.5		87.9	Yes
-325		15.0	12.2	Yes

APPENDIX D: Praxair specification PS 036108 for Ni-284-1 powder (continued)

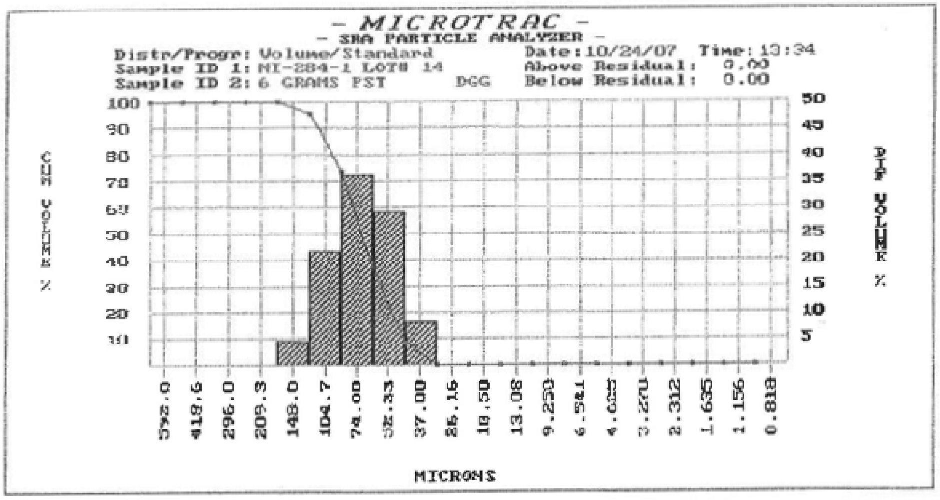

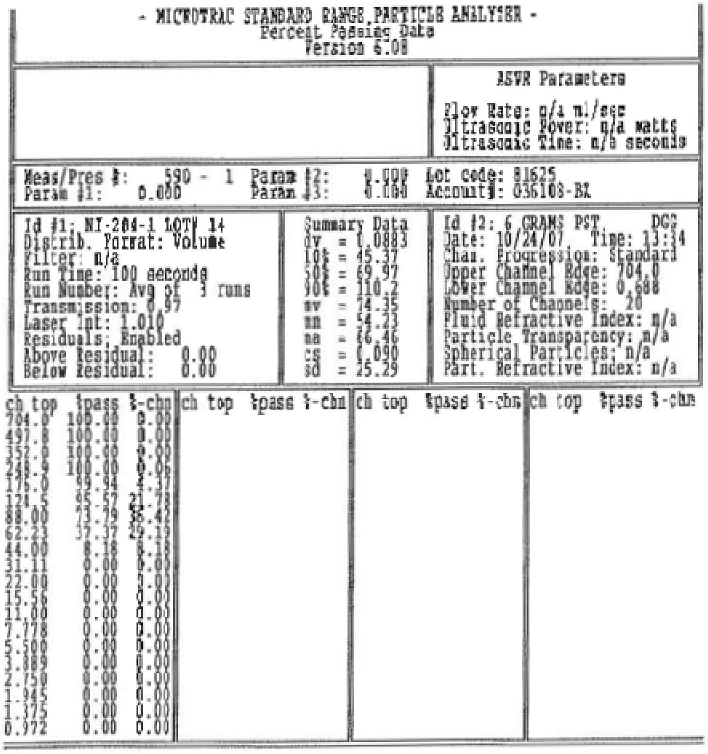

```
- MICROTRAC STANDARD RANGE PARTICLE ANALYSER -
Percent Passing Data
Version 6.08

ASVR Parameters

Flow Rate: n/a ml/sec
Ultrasonic Power: n/a watts
Ultrasonic Time: n/a seconds

Meas/Pres #:    590 - 1   Param #2:    0.000   Lot code: 81625
Param #1:    0.000        Param #3:    0.000   Account#: 036108-BX

Id #1: NI-284-1 LOT# 14         Summary Data       Id #2: 6 GRAMS PST        DGG
Distrib. Format: Volume         dv  = 0.0883       Date: 10/24/07   Time: 13:34
Filter: n/a                     10% = 45.37        Chan. Progression: Standard
Run Time: 100 seconds           50% = 69.97        Upper Channel Edge: 704.0
Run Number: Avg of  3 runs      90% = 110.2        Lower Channel Edge: 0.688
Transmission: 0.97              mv  = 74.35        Number of Channels:  20
Laser Int: 1.010                mn  = 54.23        Fluid Refractive Index: n/a
Residuals: Enabled              ma  = 66.46        Particle Transparency: n/a
Above Residual:    0.00         cs  = 0.090        Spherical Particles: n/a
Below Residual:    0.00         sd  = 25.29        Part. Refractive Index: n/a

ch top   %pass  %-chn  ch top  %pass %-chn  ch top  %pass %-chn  ch top  %pass %-chn
704.0   100.00   0.00
497.8   100.00   0.00
352.0   100.00   0.00
248.9   100.00   0.06
175.0    99.94   4.37
124.5    95.57  21.78
88.00    73.79  36.42
62.23    37.37  29.19
44.00     8.18   8.18
31.11     0.00   0.00
22.00     0.00   0.00
15.56     0.00   0.00
11.00     0.00   0.00
7.778     0.00   0.00
5.500     0.00   0.00
3.889     0.00   0.00
2.750     0.00   0.00
1.945     0.00   0.00
1.375     0.00   0.00
0.972     0.00   0.00
```

APPENDIX E: Laser beam welding parameter development

Trial 1	Power (W)	Freq. (Hz)	Speed (mm/sec)	Nozzle Setting (mm)	De-Focus ** (mm)	Nozzle Stand-off (mm)	Robot Z Pos'n (mm)
1	510	5,000	6.4	-8.9	8.0	15.0	7.2
2	600	5,000	6.4	-8.9	8.0	15.0	7.2
3	710	5,000	6.4	-8.9	8.0	15.0	7.2
Modified program to apply 4 consecutive passes w/o pause ("CLDGRV1") sequence: pass 1 (root/centre), pass 2 (RHS), 3 (LHS), 4 (centre)							
4	520	5,000	6.4	-8.9	8.0	15.0	7.2
5	520	5,000	6.4	-8.9	8.0	15.0	7.2
Adjustable nozzle used; standoff from surface = 16.5 mm (0.650") when F=0, dial=0 and nozzle setting = 0							
6	520	5,000	6.4	-8.9	8.0	14.8	7.2
7	520	5,000	6.4	-8.9	8.0	14.8	7.2
Change sequences: pass 1 (root/centre), pass 2 (RHS), 3 (centre), 4 (LHS)							
8	520	5,000	6.4	-8.9	8.0	14.8	7.2
9	520	5,000	6.4	-8.9	8.0	14.8	7.2
10	615	5,000	6.4	-8.9	8.0	15.6	7.2 (surface)
11	615	5,000	6.4	-6.4	5.5	15.6	4.7 (surface)

APPENDIX E: Laser beam welding parameter development (continued)

Trial	Powder RPM	Carrier Gas Flow (L/min)	Nozzle Gas Flow (L/min)	Comments	Microstructure
1	12	3	40	3 passes, +/-0.5 mm apart centre, right, left pass	LOF on root pass, surface underfill, 4th pass needed
2	12	3	40	3 passes, +/-0.5 mm apart centre, right, left pass	similar result to R80-1, LOF & underfill
3	12	3	40	3 passes, +/-0.5 mm apart centre, right, left pass	better penetration than R80-1/-2 but still some LOF at root pass
4	12	3	40	sharper F=5.0 for root pass, remaining 3 passes at F=8.0	deeper root penetration (no LOF), but some LOF at interface with 4th pass
5	8 12	3 3	40	root pass at F=6.5, powder=8 remaining at F=8.0, powder=12 pass spacing = +/- 0.5 mm	very slight LOF at root, still LOF on 4th pass interface
6	8 12	4 4	40	root pass at F=5.5, powder=8 pass 2 & 3 F=8.0, powder=12 pass 4 at F=6.5, powder=12 pass spacing = +/- 0.5 mm	sharpened focus for pass 4: still approx. .010" LOF/pore at root of pass 4 possible HAZ microcracks
7	8 12	4 4	40	root pass at F=5.5, powder=8 pass 2 & 3 F=8.0, powder=12 pass 4 at F=8.0, powder=12 pass spacing = +/- 0.7 mm	reduced focus back to 8.0 for pass 4, & increased pass spacing for 2 & 3 still LOF/porosity between pass 4 and 2/3, but smaller (< .005")
8	12	4	40	root pass at F=5.5, pass 2-4 at F=8.0, sequence: right/centre/left pass spacing= +/-0.55 mm powder=12 for all passes	LOF at root of 1st pass, and on 4th pass
9	12	4	40	same as Trial 8 except pass spacing= +/-0.75 mm powder=12 for all passes	LOF worse due to increased spacing
10	10	4	40	similar to Trial 8, but increased power 100W, less powder pass spacing= +/-0.55 mm	minor LOF at pass 1 root (greatly reduced) approx. .005" LOF at pass 4 root
11	10	4	40	same as Trial 8, except root pass F=5.0, all others F=5.5 Plasma occurred - all passes	spatter & slight underfill due to plasma deeper penetration, complete root fusion minor oxide/LOF at pass 4 root

APPENDIX F: SEM EDS line scan across typical S-Ti-Zr rich phase in Inconel 738, as-received condition

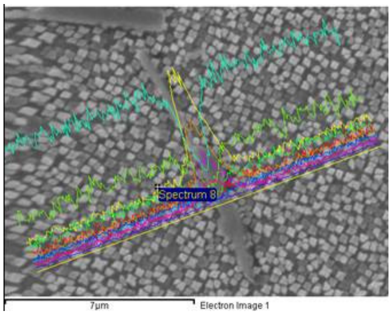

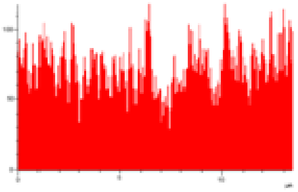
Al

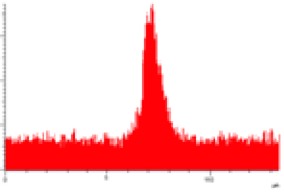
S

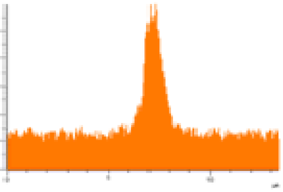
Ti

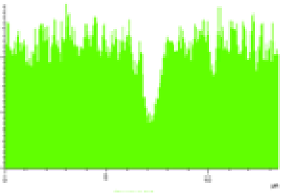
Cr

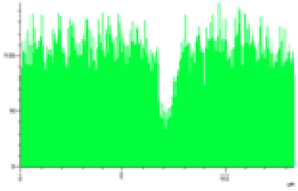
Co

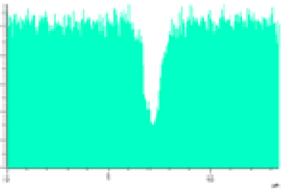
Ni

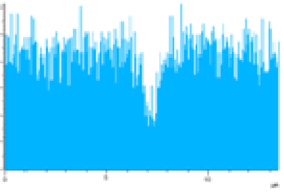
W

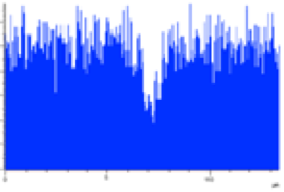
Ta

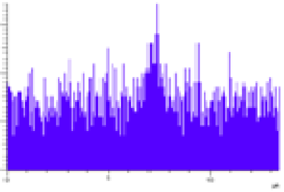
Hf

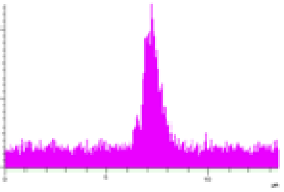
Zr

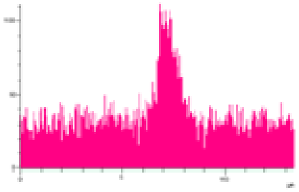
Nb

APPENDIX G: SEM EDS line scan of cellular solidification structure in fusion zone of Inconel 738

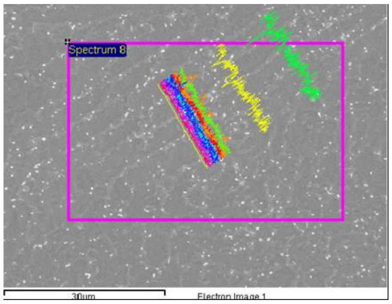

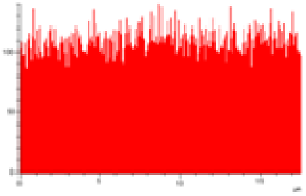

Al

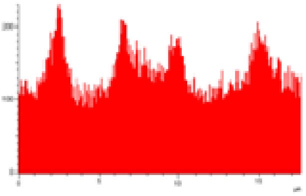

Cr

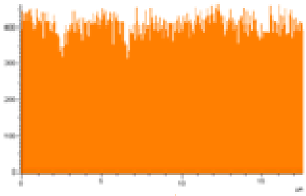

Ti

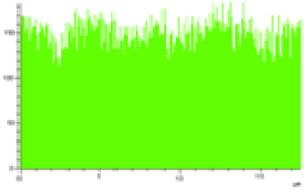

Co

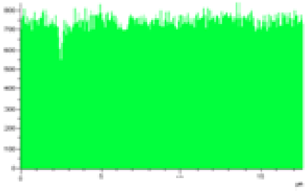

Ni

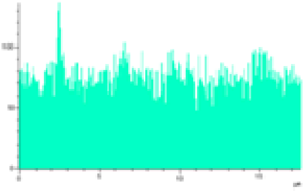

Mo

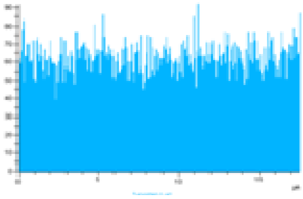

W

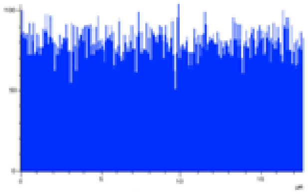

Ta

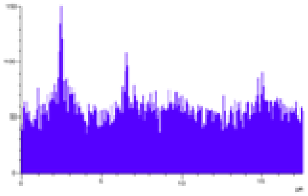

Nb

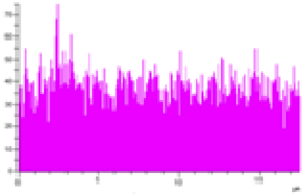

Zr

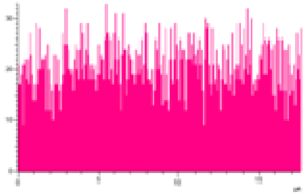

Hf

APPENDIX H: SEM EDS line scan across crack tip in Inconel 738 TMF specimen

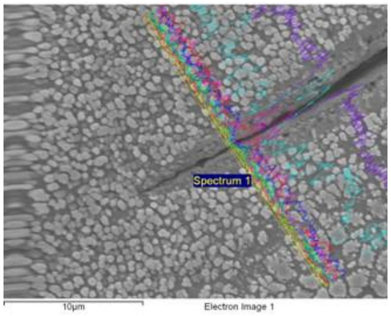

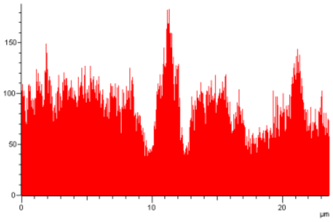

Ti

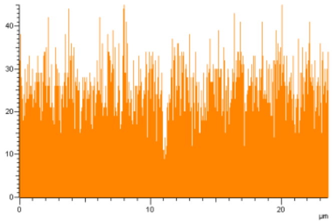

Zr

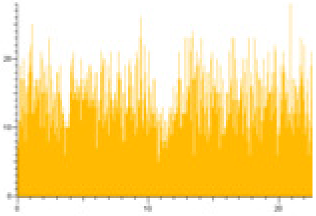

Hf

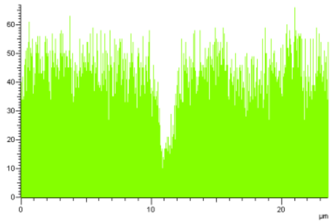

Ta

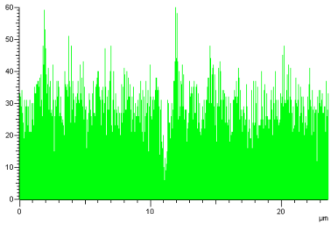

Nb

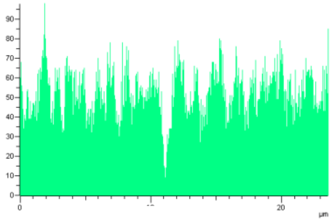

W

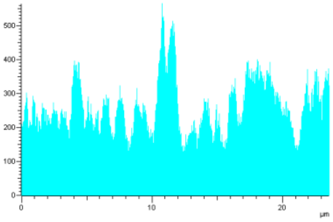

Cr

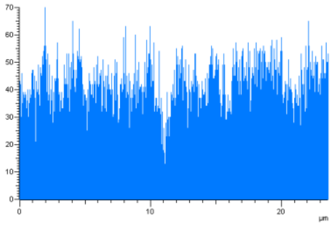

Mo

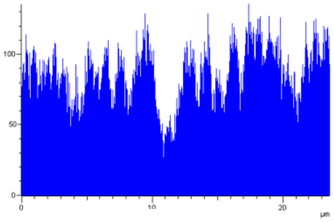

Co

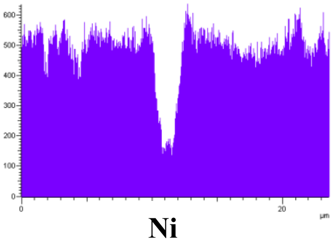

Ni

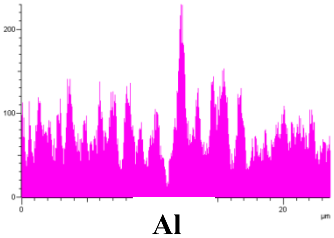

Al

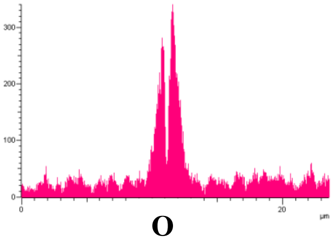

O

APPENDIX I: SEM EDS line scan of crack edge in parent material Inconel 738

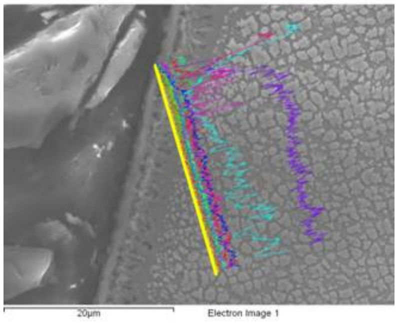

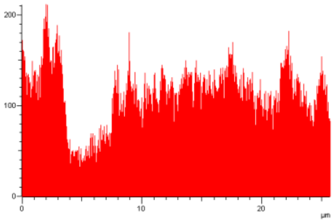

Ti

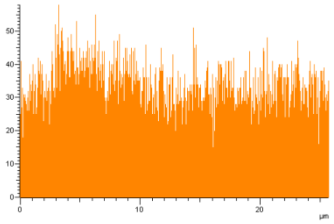

Zr

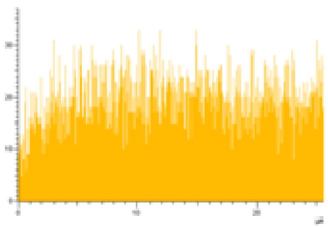

Hf

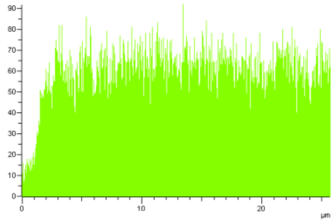

Ta

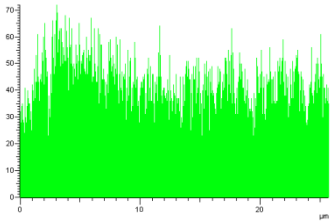

Nb

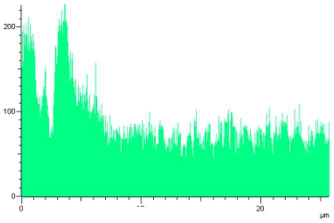

W

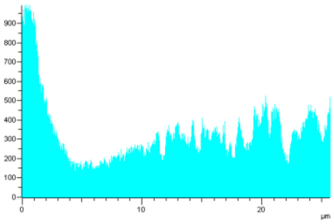

Cr

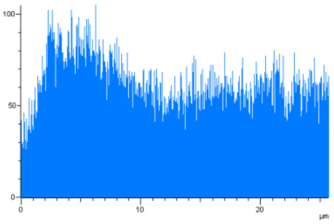

Mo

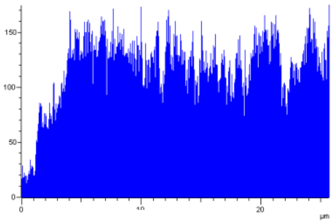

Co

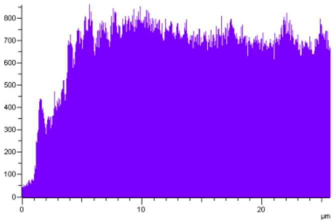

Ni

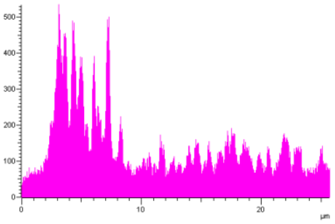

Al

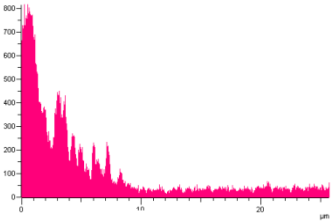

O

APPENDIX J: SEM EDS linescan across liquated MC carbide in René 80 in the as-welded condition

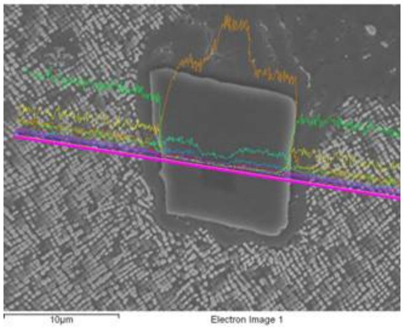

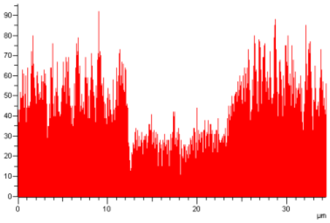

Al

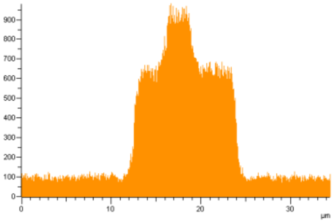

Ti

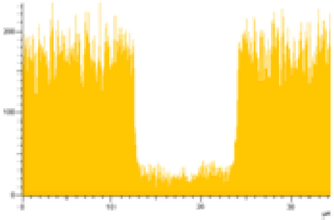

Cr

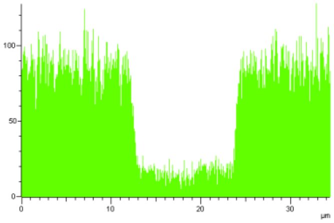

Co

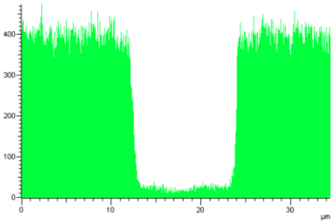

Ni

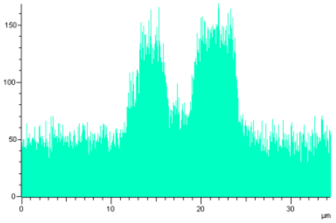

Mo

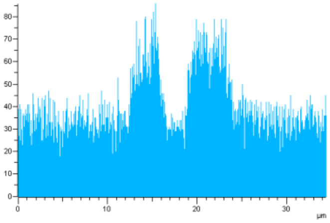

W

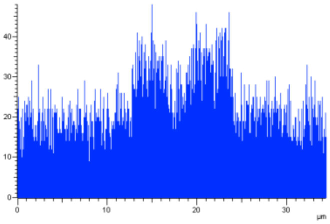

Zr

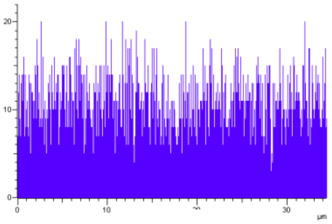

Hf

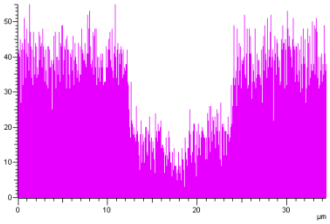

Ta

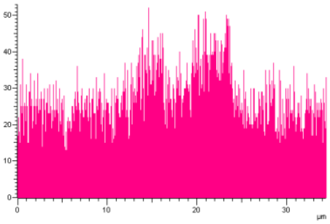

Nb

APPENDIX K: SEM EDS line scan analysis of MC carbide in René 80, as-received condition

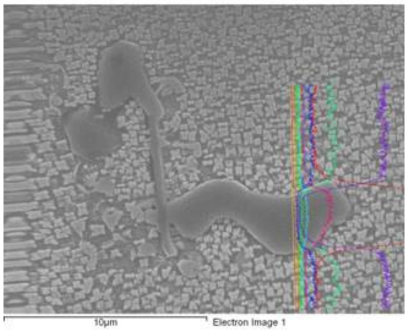

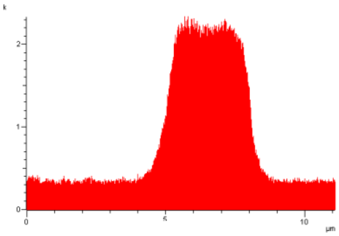

Ti

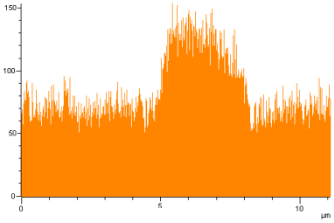

Zr

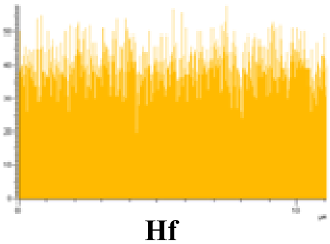

Hf

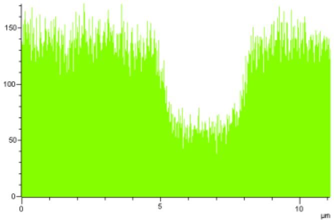

Ta

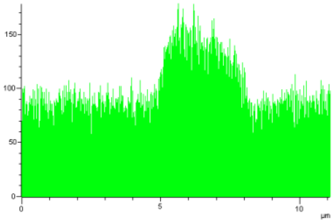

Nb

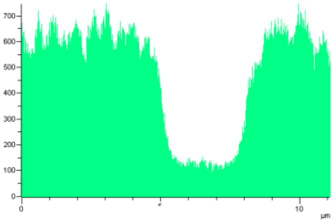

Cr

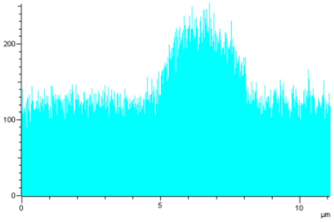

W

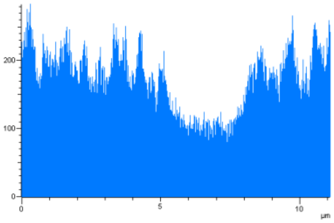

Al

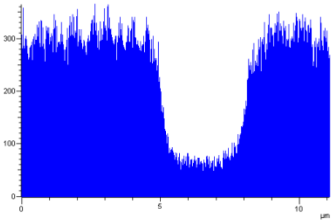

Co

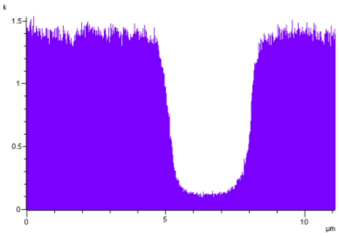

Ni

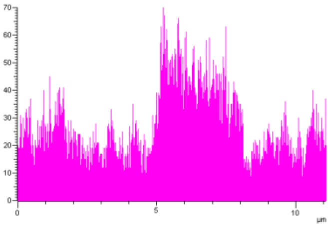

B

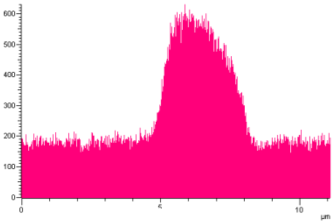

Mo

APPENDIX L: SEM EDS line scan across Zr-Ti rich sulfocarbide phase in René 80 in the as-received condition

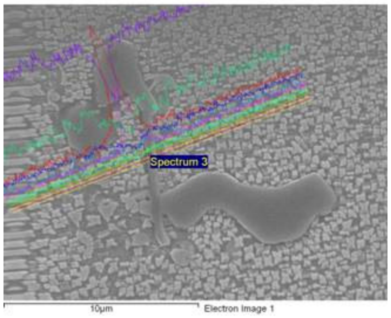

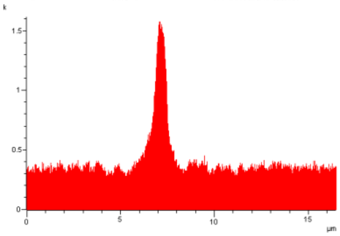

Ti

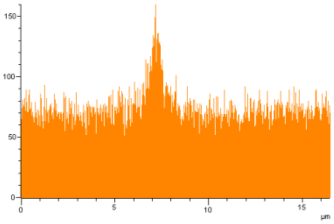

Zr

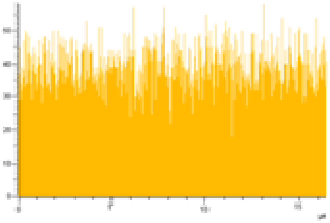

Hf

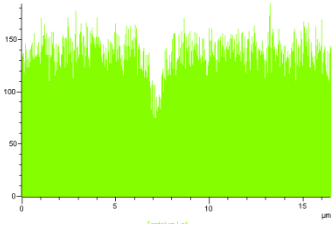

Ta

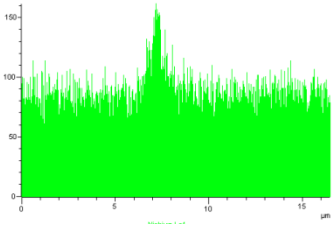

Nb

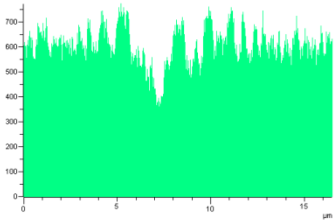

Cr

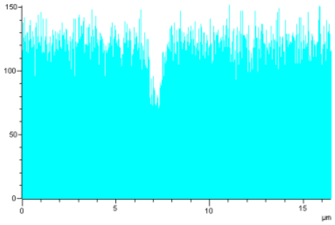

W

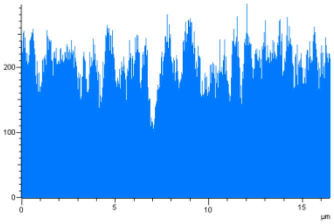

Al

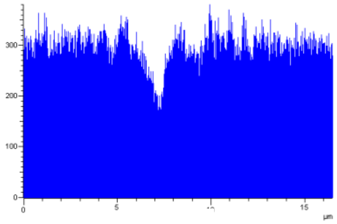

Co

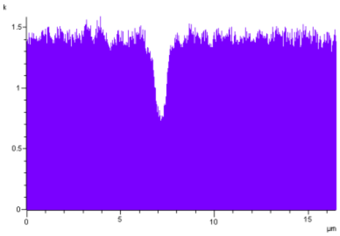

Ni

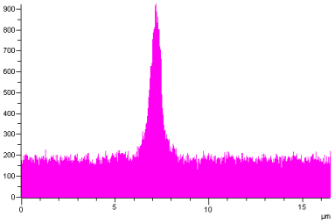

S

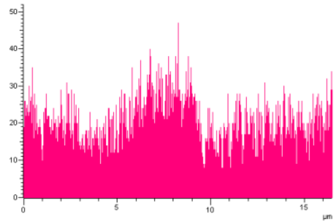

B

APPENDIX M: SEM EDS linescan across recrystallized grain boundary in PWHT René 80 base alloy

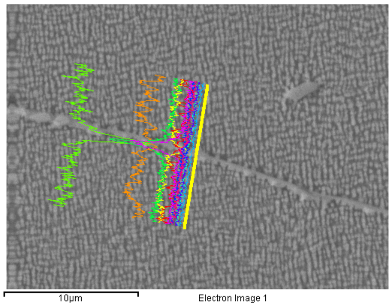

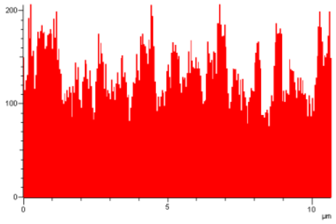

Al

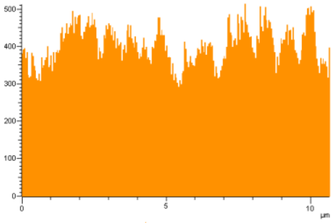

Cr

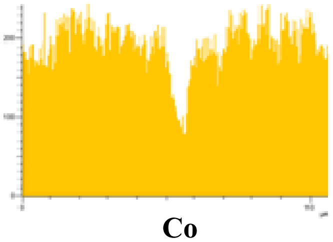

Co

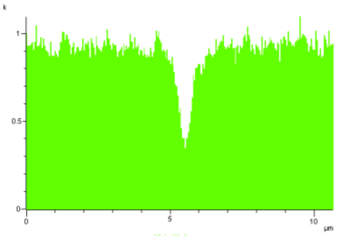

Ni

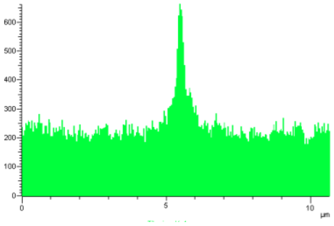

Ti

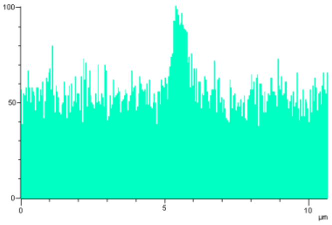

Zr

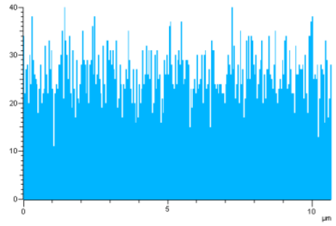

Hf

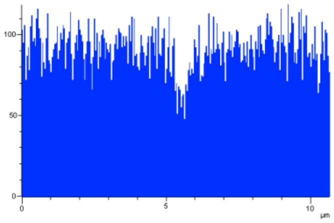

Ta

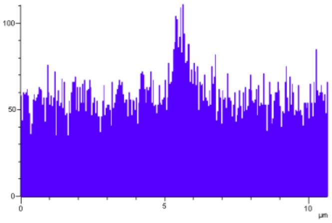

Nb

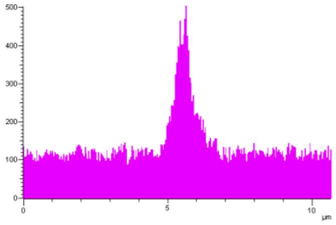

Mo

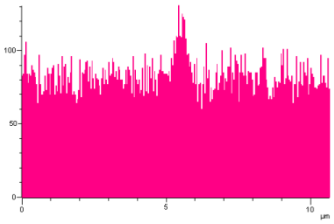

W

APPENDIX N: SEM EDS linescan across recrystallized grain boundary in PWHT René 80 base alloy

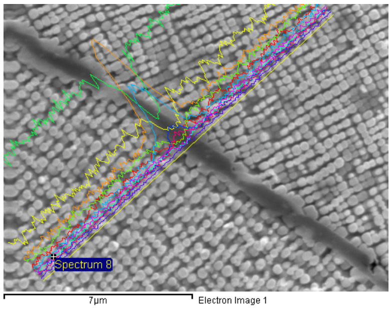

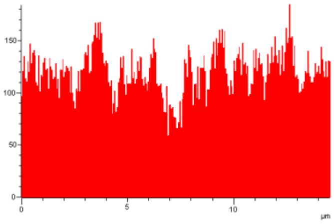

Al

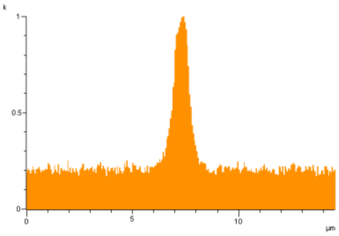

Ti

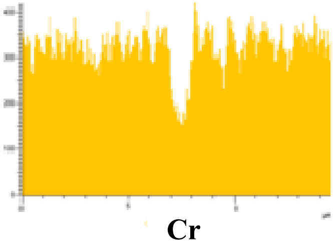

Cr

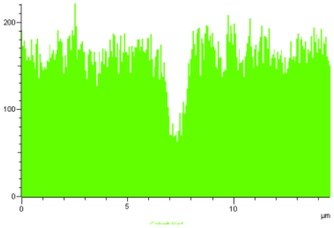

Co

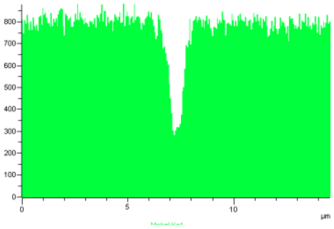

Ni

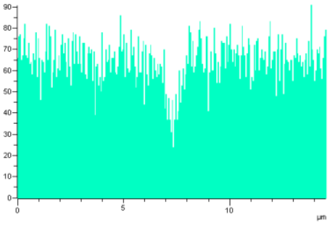

W

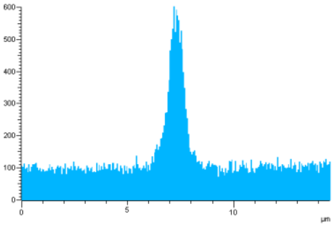

Mo

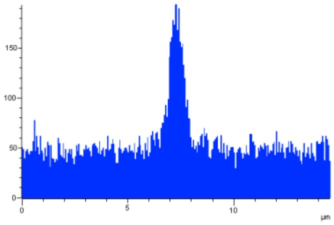

Zr

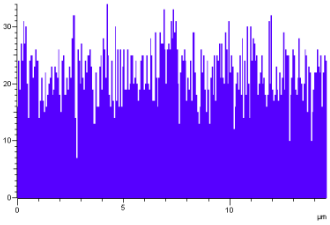

Hf

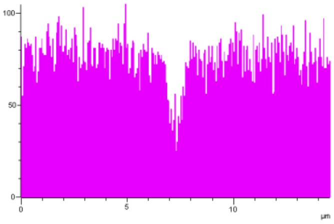

Ta

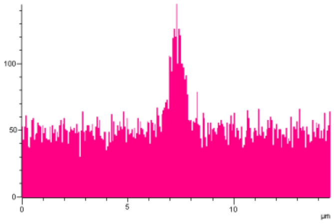

Nb

APPENDIX O: SEM EDS mapscan of surface scale of René 80 TMF specimen

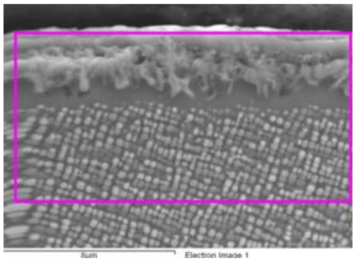

B Ka1_2

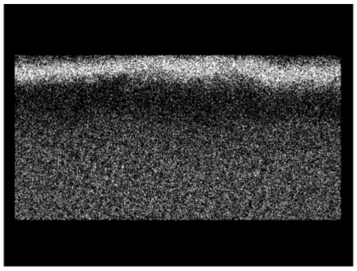

Cr Ka1

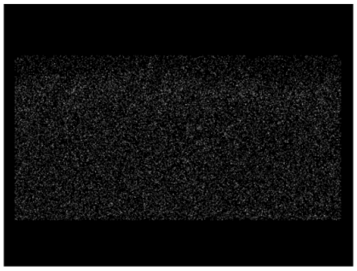

Mo La1

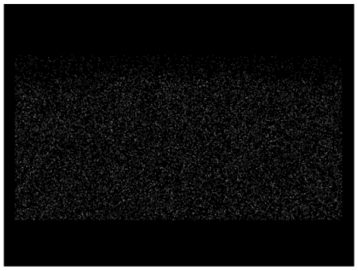

W La1

Ta La1

Nb La1

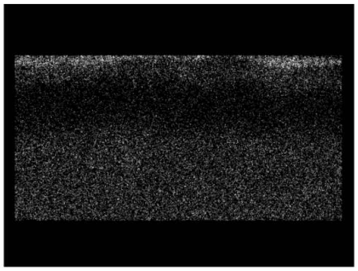

Ti Ka1

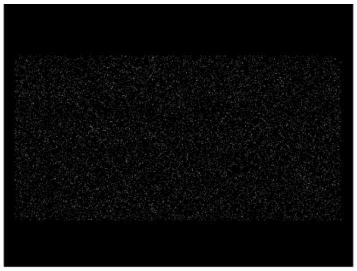

Zr La1

Hf La1

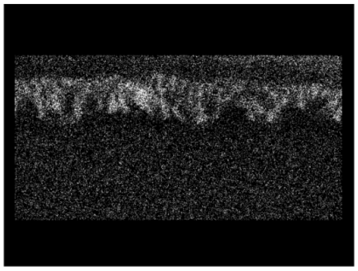

Al Ka1

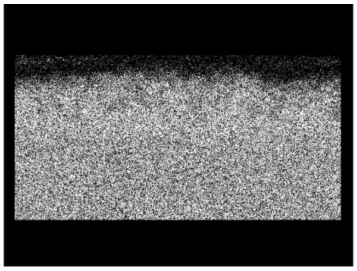

Ni Ka1

APPENDIX P: SEM EDS linescan across Cr-Mo-C-B rich along recrystallized grains in René N5 PWHT

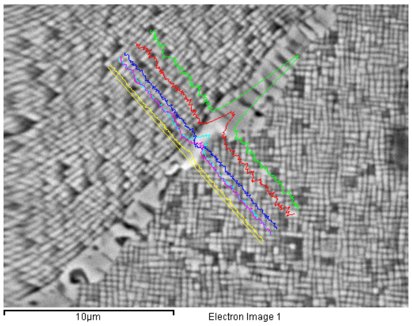

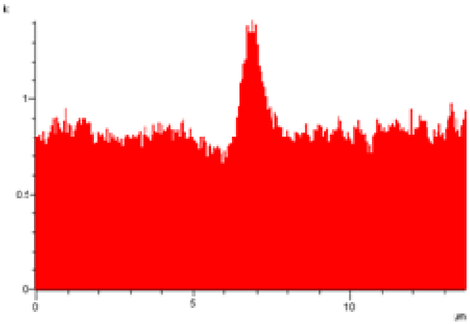

Cr

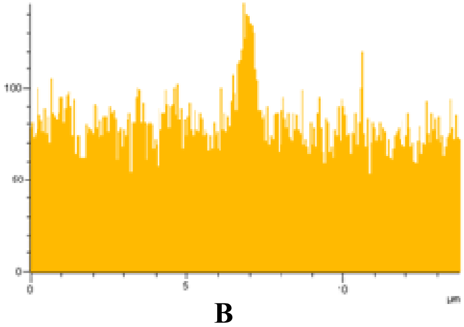

B

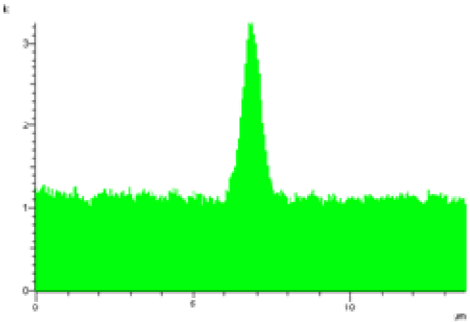

W

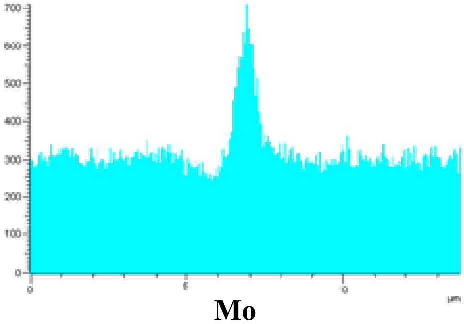

Mo

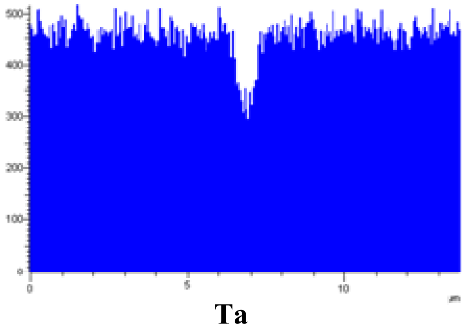

Ta

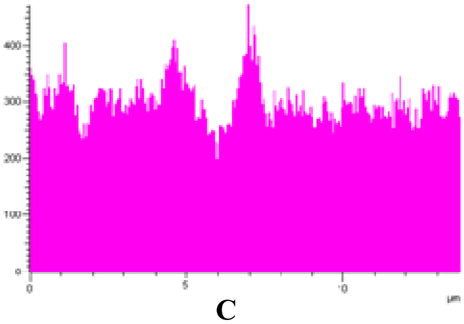

C

APPENDIX Q: SEM EDS x-ray maps along crack surface in René N5

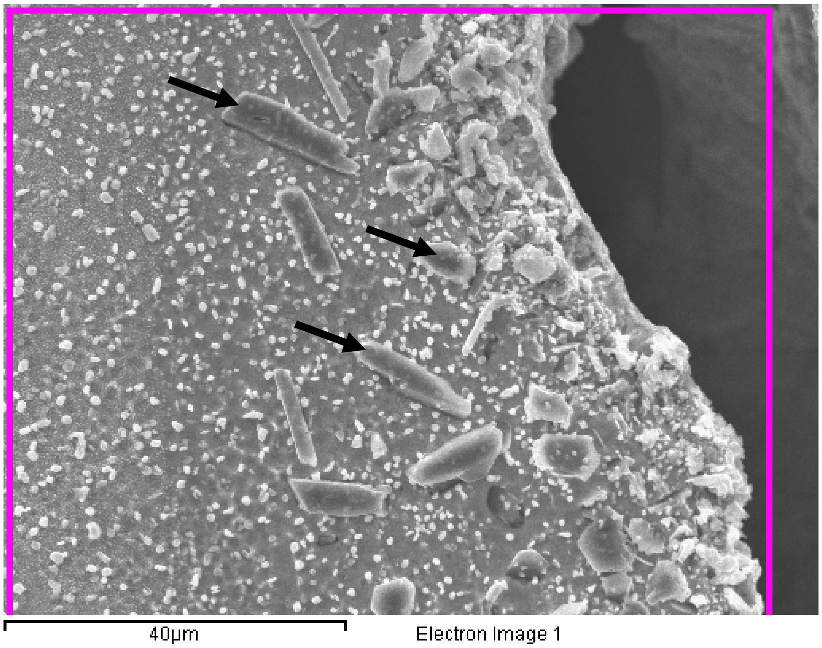

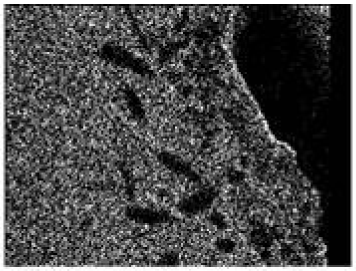

Cr

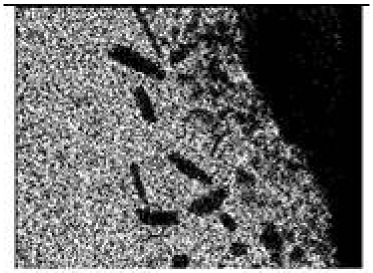

Ni

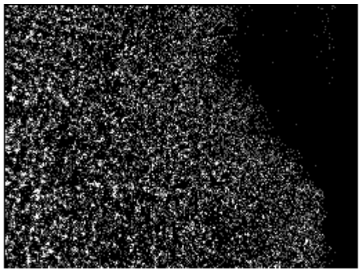

Ti

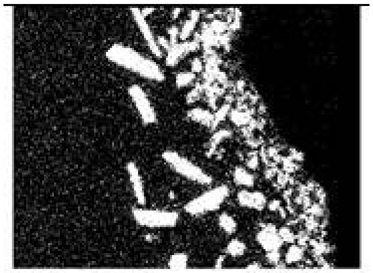

Al

APPENDIX R: Thermo-mechanical fatigue test results

CC Inconel 738

Baseline	
Strain (%)	Cycles
0.1	5250
0.2	1250
0.3	500
0.6	130
0.8	50

LBW	
Strain (%)	Cycles
0.1	10000
0.1	8750
0.2	925

GTAW	
Strain (%)	Cycles
0.1	10000
0.2	3000
0.3	500
0.35	750

DS Rene 80

Baseline	
Strain (%)	Cycles
0.4	7334
0.6	2900
0.8	257
0.8	148

LBW	
Strain (%)	Cycles
0.2	10000
0.2	3950
0.25	4750
0.3	2750
0.4	750

GTAW	
Strain (%)	Cycles
0.2	10000
0.4	2360
0.45	1000
0.6	175

SX Rene N5

Baseline	
Strain (%)	Cycles
0.6	9300
0.8	2350
1	750
1.5	67

LBW	
Strain (%)	Cycles
0.2	10000
0.3	1450
0.35	10000
0.4	250

GTAW	
Strain (%)	Cycles
0.4	10000
0.5	250
0.5	24
1	750

APPENDIX S: SEM EDS line scan across sulfocarbides particle in the weld fusion zone

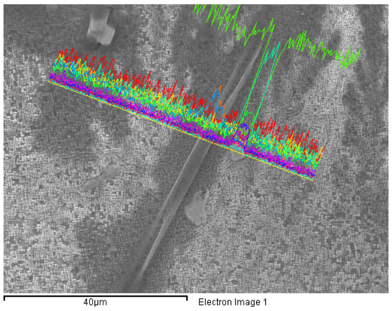

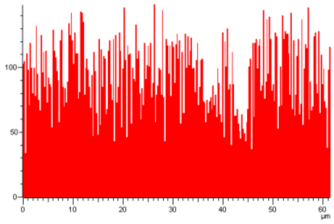

Al

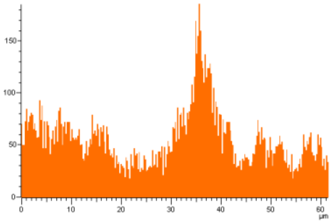

S

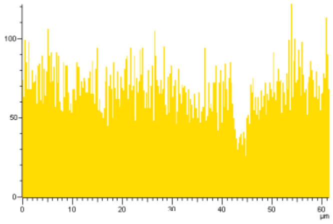

Cr

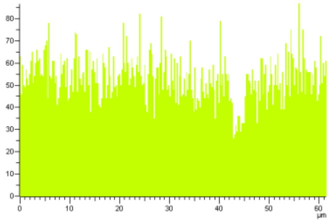

Co

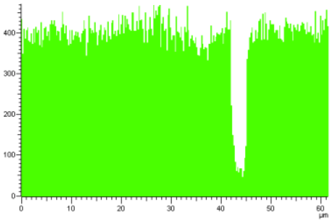

Ni

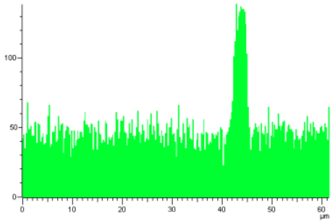

Ta

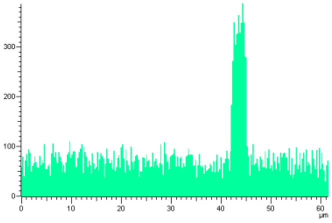

W

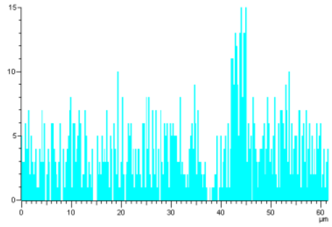

B

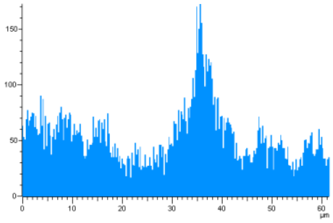

Mo

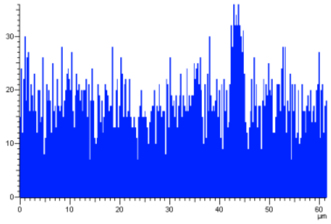

Ni

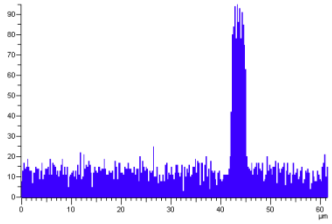

Hf

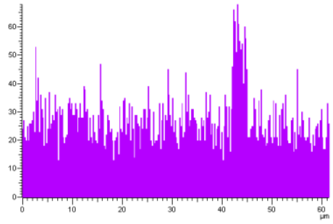

Zr

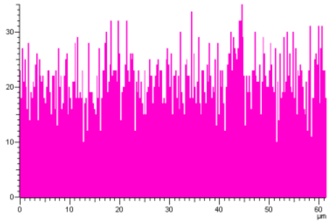

Ti

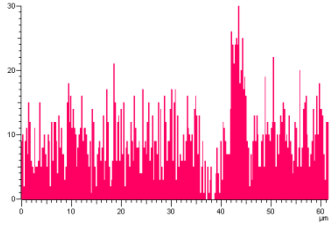

C